MOX-Report No. 38/2016

The Cardiovascular System: Mathematical Modeling, Numerical Algorithms, Clinical Applications

Quarteroni, A.; Manzoni, A.; Vergara, C.

MOX, Dipartimento di Matematica
Politecnico di Milano, Via Bonardi 9 - 20133 Milano (Italy)

mox-dmat@polimi.it http://mox.polimi.it

The Cardiovascular System: Mathematical Modeling, Numerical Algorithms, Clinical Applications

A. Quarteroni[1], A. Manzoni[1], C. Vergara[2]

October 29, 2016

[1] Chair of Modelling and Scientific Computing, École Polytechnique Fédérale de Lausanne, Switzerland, {alfio.quarteroni,andrea.manzoni}@epfl.ch
[2] MOX, Dipartimento di Matematica, Politecnico di Milano, Italy, christian.vergara@polimi.it

Keywords: Blood flow simulation, fluid-structure interaction, heart function, parameter estimation, uncertainty

Abstract

Mathematical and numerical modeling of the cardiovascular system is a research topic that has attracted a remarkable interest from the mathematical community because of the intrinsic mathematical difficulty and due to the increasing impact of cardiovascular diseases worldwide. In this review article, we will address the two principle components of the cardiovascular system, the arterial circulation and the heart function. We systematically go through the complete pipeline from data imaging acquisition, setting the basic physical principles, analyzing the associated mathematical models that comprise PDEs and ODEs systems, proposing sound and efficient numerical methods for their approximation, simulating both benchmark problems and clinically inspired (driven) problems. Mathematical modeling itself features tremendous challenges, due to the amazing complexity of the cardiocirculatory system, the multiscale nature of the involved physiological processes, and the need of devising computational methods that are stable, reliable, and efficient. A critical issue is about filtering the data, identifying the parameters of mathematical models, devising optimal treatments, accounting for uncertainties. For this reason, we will devote the last part of the paper to control and inverse problems, including parameter estimation, uncertainty quantification and the development of reduced order models that are of paramount importance when solving problems with high complexity, that would be out of reach otherwise.

Contents

1 Introduction

This is a review paper on the mathematical and numerical modeling of the cardiovascular system (CS), a research topic that has attracted remarkable interest from both the mathematical and bioengineering communities over the past 25 years. The driving motivation for such interest is the increasing impact of cardiovascular diseases (CVD) in our lives. According to [384], CVD are the major cause of death worldwide, leading to more than 17.3 million deaths per year, a number that is expected to grow to more than 23.6 million by 2030. In Europe, nowadays they correspond to nearly half of all deaths (47%).

In this paper we focus on the two principal components of the CS, the *arterial circulation* and the *heart function* with its electrical and mechanical activities. Geometric complexity, lack of data to feed the mathematical models, multiphysics and multiscale nature of the processes at hand, represent major challenges when trying to reproduce both function and malfunction.

Due to its composite nature, the CS is first modeled by means of stand-alone *core components* describing a single functionality, like e.g. the artery fluid-dynamics, the heart electrical activity, the fluid dynamics in the left ventricle, etc. Each core model needs to be properly analyzed mathematically and efficiently approximated numerically, often by specifically devised methods. The next step is the integration of the core models into global, coupled integrated models apt at describing a meaningful and coherent part of the (or even the entire) CS system. This step requires the introduction of suitable coupling

conditions and of (novel) numerical strategies for a stable, reliable, and computationally effective solution of the global problem.

Clinical data play a decisive role for CS models and, at the same time, they represent a formidable challenge. Clinical radiological images (such as *Computer Tomography* and *Magnetic Resonance Imaging*) are necessary to construct the computational domains. The procedure of geometric reconstruction is difficult and, especially for the heart, requires advanced mathematical and numerical tools. Standard radiological images can sometimes be useless: some cardiovascular components may have a size smaller than the spatial resolution featured by the imaging device (this is e.g. the case of the Purkinje network); in other cases the elevated brightness gap between fluid and vessel wall, makes the detection of the latter very hard. Boundary data are also difficult to obtain. When the computational domain results from an artificial truncation, specific physical quantities (e.g. fluid velocity or pressure) should be provided at those locations of the arterial tree corresponding to the artificial boundaries. However, this would require invasive measurements that cannot be easily carried out. Finally, the huge inter- and intra-patient data variability and uncertainty represent further sources of concern toward model calibration and validation.

In spite of all these difficulties, a wealth of models has already been successfully applied to address both physiological and pathological instances. The aim is from one side a better understanding of the physical and quantitative processes governing the CS, and on the other side the opening of new frontiers in therapeutic planning and the design of implantable devices (such as e.g. medical stents and cardiac defibrillators).

The literature about the mathematical and numerical modeling of CS is huge (as the reader would realize by browsing this paper's references, a tiny subset of the overall existing ones). In the forthcoming sections we will try to provide an outlook to the main contributions in this field. Here, among the several books, monographes, and review papers published so far, we mention [188, 540, 482] for the circulatory system and [448, 521, 118, 468, 470] for the heart.

This review paper consists of three main parts, i.e. i) modeling the *arterial circulation* (Sects. 2, 3 and 4), ii) modeling the *heart function* (Sects. 5, 6 and 7), and iii) solving *inverse problems* and including *uncertainty* (Sects. 8, 9, 10 and 11). Both parts 1 and 2 are composed by an introductory section on physiology (Sects. 2 and 5), a section describing the available data and their use (Sects. 3 and 6), and a final section on the mathematical and numerical modeling (Sects. 4 and 7). Regarding the third part, in an introductory section we underline the need of going beyond a single (forward) simulation in some applications (Sect. 8). This represents the common denominator of three topics recently applied to cardiovascular mathematics: *control and optimization* (Sect. 9), *parameter estimation* (Sect. 10), and *uncertainty quantification* (Sect. 11).

When appropriate (in particular in Sects. 4, 7, 9, 10 and 11), we report some numerical results to highlight the effectiveness of the numerical strategies here presented. Unless otherwise specified, all our numerical results have been obtained using the Finite Element library *LifeV*, see `www.lifev.org` for more details.

Part I
THE ARTERIAL CIRCULATION

2 Basic facts on quantitative physiology

The cardiovascular system is a close circuit that carries oxygenated blood to all the tissues and organs of the body. Functionally, it can be regarded as made by three compartments: the *heart*, the *systemic* and *pulmonary circulations*, and the *microvasculature*. In this section we will recall the most important features about the physiology of the systemic circulation characterizing the mathematical models that will be introduced later on. We will also highlight the main peculiarities of the pulmonary circulation. Heart physiology will be addressed in Section 5.

The systemic circulation is composed by the arteries, that carry the oxygenated blood ejected by the left heart to the living tissues, and the veins that allow the non-oxygenated blood to returning to the right heart. The exchange of oxygen between blood and the body tissues occurs in the microvasculature, which in fact separates the systemic arterial tree from the venous systems. In the pulmonary circulation, non-oxygenated blood ejected by the right heart flows in the pulmonary arteries towards the lungs where it becomes oxygenated and goes back to the left heart through the pulmonary veins.

Blood is composed by *plasma* (about 55% of its total volume) which consists of water (about 92% of plasma volume), proteins and ions. The remaining part of blood corresponds to the blood cells, whose 97% of volume is occupied by *erythrocytes* (red blood cells) that carry the oxygen in oxygenated blood. The other cells are *leukocytes* (white blood cells) and *platelets*. The diameter of blood cells is approximately $10^{-3}\,cm$, whereas that of the smallest arteries/veins is about $10^{-1}\,cm$. This is the reason why blood in the systemic and pulmonary circulations is often considered as Newtonian, i.e. characterized by a linear relationship between internal forces and velocity gradients [443, 188] However, in the smallest arteries, such as coronaries (the arteries perfusing the heart and the corresponding veins, see Figure 1, right), or in presence of a vessel narrowing (stenosis), a non-Newtonian blood rheology is more appropriately assumed, see, e.g., [93] and references therein.

Thanks to the heart contraction, the blood flow is pulsatile and blood is pumped into the two circulations by means of discrete pulses with a pressure usually varying during an heartbeat in the ranges $70-130\,mmHg$ and $20-30\,mmHg$ for the systemic and pulmonary networks, respectively ($1\,mmHg \simeq 133.3\,Pa = 1333\,g/(cm\,s^2)$).

In the systemic circulation, blood first enters the *aorta* (the largest artery with diameter equal to about $2.5\,cm$ in adults, see Figure 1, left) and then flows through a network of hundreds of branching arteries of decreasing size, reaching all the regions of the body. Dimensions and numbers of veins are comparable with those of arteries. The waveform of the flow rate as a function of time is characterized by different peak values when moving downstream towards the smallest arteries. In particular, the flow rate peak value is about $200\,cm^3/s$ in aorta, $80\,cm^3/s$ in the abdominal aorta, $15\,cm^3/s$ in the carotids (the arteries supplying blood to the brain, see Figure 1, middle), and $1\,cm^3/s$ in coronaries

(corresponding to a maximum blood velocity of about $150\,cm/s$ in aorta, $100\,cm/s$ in the abdominal aorta, $80\,cm/s$ in the carotids, and $40\,cm/s$ in coronaries). Also the shape of the waveforms changes while moving downstream, see Figure 2, left. In particular, in the ascending aorta, after the systolic peak the flow rate decelerates assuming null or even negative values, whereas in the abdominal aorta and in carotids is more spread out and always positive. In any case, we can distinguish the *systolic phase*, i.e. the interval of acceleration and deceleration of blood flow, and the *diastolic phase*, i.e. the interval of almost constant or negative flow [1]. A different situation occurs in coronaries, where the peak flow rate is reached during diastole, see Figure 2, right. Coronaries are not directly fed by the heart; indeed, blood in the proximal part of the aorta (the sinuses of Valsalva from which coronaries originate) during diastole is allowed to enter the coronaries thanks to the elastic response of the aorta (see below for more details).

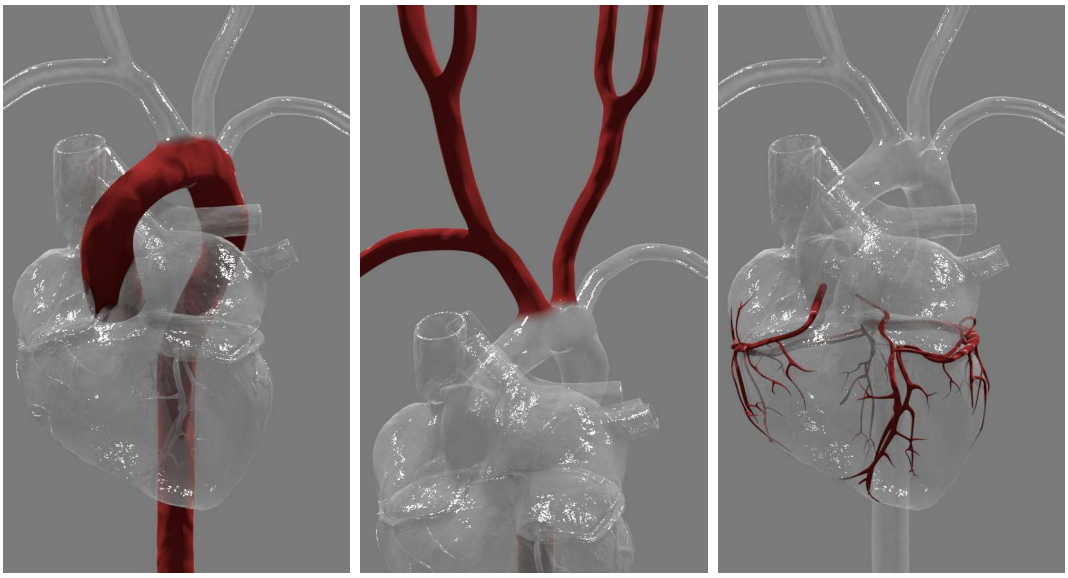

Figure 1: Visualization of the aorta (left), carotids (middle), and coronaries (right)

In the pulmonary circulation blood first enters the *pulmonary artery* (diameter equal to about $3.0\,cm$ in adults) and then flows into another network of branching arteries of decreasing size reaching the lungs. The waveforms and peak intensities are similar to those of systemic arteries.

The different characteristics of blood flow in the arteries of the systemic circulation result in different values of the *Reynolds number* $Re = \frac{\rho_f D U}{\mu}$ (ρ_f being the blood density, D and U characteristic vessel dimension and blood velocity, respectively, and μ the fluid viscosity), a dimensionless quantity which quantifies the importance of the inertial terms over the viscous ones. In particular, $Re \simeq 4000$ in the aorta and $Re \simeq 400$ in coronaries,

[1] The previous definition of systole and diastole is formulated from the point of view of the arteries. An almost equivalent definition could be given from the point of view of the heart, see Section 5.

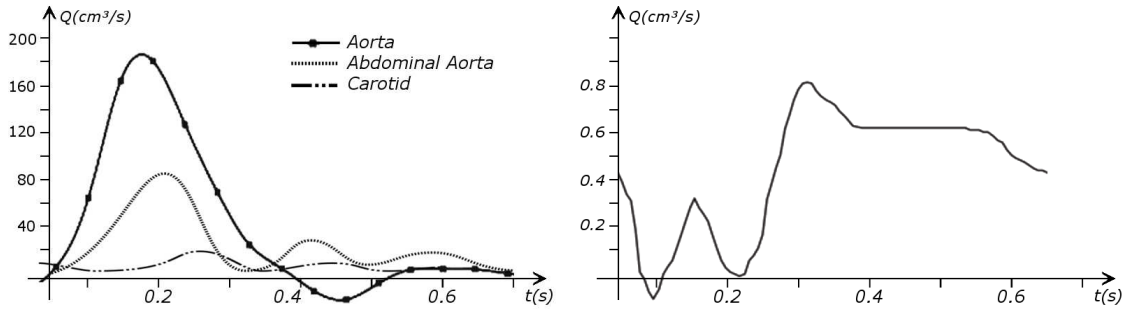

Figure 2: Typical flow rate waveforms in ascending aorta, abdominal aorta and carotids (left), and in coronaries (right)

with intermediate values when moving downstream the aorta. Thus, blood covers a range of Reynolds numbers where both the inertial and the viscous components of the flow are relevant. Although in the aorta Re is higher than the critical value of 2000 above which the flow would not be laminar any longer in a straight pipe, the pulsatile nature of blood flow does not allow fully transition to turbulence to develop. It is debated whether in aorta at least transitional-to-turbulence effects may occur. In this respect, some authors speculate that the helicoidal velocity pattern in aorta induced by the torsion of the heart contraction inhibits any transition to turbulence, thus supporting the thesis that in healthy conditions turbulence is never observed in the cardiovascular system [383]. This is not necessary the case for some pathological conditions, such as carotid stenosis, yielding a narrowing of the vessel lumen and an increased complexity of the geometry together with higher Reynolds numbers, see, e.g., [2, 326, 288, 316]. As for the *Womersley number* $W = \sqrt{\frac{2\,A\,f}{\mu}}$ (A and f being characteristic cross-section vessel area and time frequency of the flow rate signal, respectively), a dimensionless number quantifying the pulsatility of flow, we have decreasing values in the systemic circulation moving downstream ($W \simeq 10$ in aorta, $W \simeq 3$ in carotids). Similar values of Re and W are found in the pulmonary arteries.

As for the veins of the systemic circulation, comparable values with respect to arteries of flow rate, Reynolds and Womersley numbers are found, the only difference being that the blood flow waveform is more spread out with respect to the corresponding arteries. Another major difference is given by blood pressure values. In the arteries the range of pressure is almost the same, independently of the location in the tree ($70 - 130\,mmHg$), whereas in the veins it falls down assuming a mean value of about $10\,mmHg$. This is due to the big resistances that blood flow experiences at the microvasculature. The latter is composed by thousands of *arterioles* and *venules* and billions of *capillaries*. The blood velocity and vessel dimensions are here greatly reduced (about $10^{-1}\,cm/s$ the first one and $10^{-2}\,cm$ the second ones). This means that Re is very small in comparison with the systemic circulation so that viscous forces completely dominate the inertial ones. As a result, the highest resistance to flow is found in microvasculature, thus provoking a big

decrease in the blood pressure. Since the typical dimension of capillaries is comparable to that of erythrocites, a multiphase model looks appropriate for their mathematical descriptions [156]. Finally, we observe that, unlike arteries, veins can be supplied by valves that prevent backflow of blood and venous flow highly depends on the muscle contraction and respiratory effects.

As observed, blood pressure assumes the same range of values ($70 - 130\, mmHg$) along the entire systemic arterial tree. More precisely, a negligible dissipation is experienced by the pressure signal in large and medium sized vessels before reaching small vessels and microvasculature. Of course, at a given instant the pressure is not constant-in-space along the tree. Indeed, a time shift characterizes the pressure waveforms at different locations which generate gradient pressures between proximal and distal regions facilitating the blood movement. These spatial gradients are due to the propagating nature of the pressure which is in fact a wave traveling along the arterial network. The wave speed ranges from about $500\, cm/s$ in the aorta to $1200\, cm/s$ in coronaries. The presence of bifurcations or high resistance regions (such as the microvasculature) produces wave reflections propagating backward to the heart.

The propagation of a pressure wave along the vascular tree is due to the vessels *compliance*, i.e. the ability of the vessel to distend under the forces exerted by the blood pressure. Vessel wall displacements are quite large, reaching up the value of 10% of the lumen diameter. This is possible thanks to the structure of the vessel walls: their total thickness is about 10% of the lumen diameter and are composed by three layers, the *intima*, the *media*, and the *adventitia*. The inner part of the intima is the *endothelium* (facing the blood), whereas the remaining part is composed by connective tissue. The media and the adventitia mainly have a major role in characterizing the mechanical response of the vessel wall from the mechanical point of view. Their main structural components are *elastin* and *collagen*. The media is also formed by *smooth muscle cells* which provide the tone to the vessel wall. Elastin forms complex networks that are very distensible, providing the elasticity of the vessel wall at small strain. Instead, collagen forms stiff fibers oriented in a helical form that provide tensile strenght at large strain. Thus, the artery vessel wall is characterized by highly non-linear elastic properties. The quantity of elastin and collagen decreases going downstream along the arterial network, whereas the quantity of smooth muscle cells increases. This allows the arteries more proximal to the heart, in particular the aorta, to be very extendible and, thanks to the high peripheral resistances due to the elevated tone of the distal arteries and to the microvasculature, to store during systole about 50% of the entering blood. This blood reserve is then discharged during diastole owing to the vessel wall elastic response (*windkessel effect*). This is responsible for the smoothing of the blood flow waveform discussed above going downstream along the arterial network, which guarantees a nearly continuous peripheral blood flow and thus an almost continuous exchange of oxygen with the tissues. Also pulmonary arteries walls are extendible (with muscular tone increasing going downstream), their thickness being however only about 1% of the lumen diameter.

As already observed, there is mutual exchange of energy between blood and extendible vessel walls: the latter accumulate elastic potential energy under the forces exerted by the blood pressure, which is then transfered to the blood as kinetic energy. From the

mechanical point of view, this gives rise to a *fluid-structure interaction* problem. This process occurs at short time scales, proportional to the duration of a heartbeat ($\sim 1\,s$). Other interaction mechanisms may take place at larger time scales yielding a wall modification of vessel properties. This occurs in the case of several arterial diseases, such as *atherosclerosis* and *aneurysm* formation. In the first case, an increased permeability of vessel wall to lipoprotein provokes a cascade of events at the cellular level which leads to the accumulation of fatty material in the intima, just below the endothelium, and then to plaque formation in the media. Preferential sites of atherosclerotic plaque formation are the carotids and the coronaries. The main complications are the partial occlusion of the lumen with consequent (cerebral or heart) ischemia, or even the total occlusion resulting in (cerebral or cardiac) infarction. An aneurysm consists in the dilatation of the vessel wall with formation of a (possibly huge) bulge, mainly in aorta and cerebral arteries, due to a loss of elastin and to the consequent remodeling of collagen, resulting in a weakening of the arterial wall. 80-90% of ruptured abdominal aortic aneurysms and 45% of ruptured cerebral aneurysms result in death. The role of blood fluid-dynamics has been recognized to be crucial for the development of both these diseases [215, 27]. In particular, *wall shear stresses*, i.e. the viscous/friction forces exerted by the blood on the endothelium, although about 100 times smaller in magnitude than pressure, regulate the permeability of the wall to lipopotrein and the loss of elastin, thus playing an important role in atherosclerosis and aneurysm development. For both these arterial diseases, this supplementary interaction between fluid and structure occurs at time scales of several years.

More on the physiology of the systemic and pulmonary circulations and microvasculature in view of mathematical modeling is available in, e.g., [401, 478, 188].

3 Landscape on data

The ultimate and ambitious goal of mathematical models in medicine is to provide quantitative results for enhancing the understanding of biophysical processes and provide clinicians with useful indications in support of their diagnostic and therapeutic procedures. To these aims, it is mandatory to consider data that are *patient-specific* (according to the bioengineering jargon), i.e. related to real patients. Obtaining and processing patient-specific data is a major issue which alone deserves specific review papers. Here, we provide a brief overview of the most common techniques for acquisition and analysis of "clinical" data. This data *preprocessing* is essential prior to the set up of a numerical simulation.

In this section, we address the case of data related to the arterial (or venous) circulation, whereas in Section 6 we will discuss cardiac data. In arteries we have two processes interplaying with one another, the blood flow in the *vessel lumen* (the region occupied by the blood, which is referred to as the *fluid domain*) and the displacement of the *vessel wall* (referred to as *structure*). We need *geometric*, *boundary*, and *biological* data, which are discussed in what follows.

3.1 Geometric vascular data

Geometric data are necessary to build the geometry of the computational domains wherein the differential problems are numerically solved. At the end of the geometric preprocessing step, we should obtain the fluid computational domain for the blood fluid-dynamics problem, and the structure computational domain, for the vessel wall displacement problem.

The processing of geometric data for blood flow simulations is a major task since vessels exhibit high morphological variability due, e.g., to the noticeable vessel tortuosity and the presence of several bifurcations. Moreover, in unhealthy cases, this variability is further emphasized, because of the possible presence of calcifications, stenoses, aneurysms, or even prostheses (such as stents).

The geometric preprocessing consists of the following steps, which are usually performed in sequence [11, 10]: acquisition of clinical images, image enhancement, image segmentation, and generation of the computational mesh. These items are addressed below.

3.1.1 Acquisition of clinical images

Angiography is an imaging technique successfully used to "identify" the vessel lumen. It exploits the property that a liquid inside the vessel appears brighter than the vessel wall and the surrounding tissue. Angiographies are usually acquired as two dimensional (2D) images, corresponding to different slices of the domain of interest, but also three dimensional (3D) acquisitions of volumes are possible.

One of the most common techniques to obtain an angiography is *X-ray imaging*, based on the projection of X-ray beams through the body onto suitable screens, and on the contrast produced on the 2D image by the different absorption properties of the body structures. To highlight the vessel lumen, a radio-opaque dye is inserted into the blood stream through the arterial system. To reconstruct tortuous geometries, a *rotational angiography* (RA) is performed, where X-ray sources and detectors are rapidly rotated around the patient, allowing one to acquire many projections within few seconds. The excellent spatial resolution of projection angiography (about $0.2\,mm$, $0.4\,mm$ for RA) makes this technique the gold standard for most vascular imaging applications. Another X-ray angiography technique, widely used for blood flow simulation, is based on the *computed tomography* (CT) technology, where multiple X-ray sources and detectors are rotated rapidly around the patient, allowing one to acquire 3D images with an excellent spatial resolution (less than $1\,mm$, computed tomography angiography, CTA). Unlike projection angiography, another advantage of CTA is the possibility of using intravenous instead of arterial injections. Recently, temporally-resolved CTA imaging (4D-CTA) became feasible. This allows one to obtain several (15-20) 3D images during an heartbeat.

Difficulties may arise for the presence of metal artifacts due to metallic prostheses such as peacemakers, which results in streaks on the images obscuring anatomical details, see e.g. [493, 167] for possible mathematical treatments.

Another, widely used technique to obtain angiographies is *Magnetic Resonance* (MR), based on the different decay rate featured by body structures after the application of a

radiofrequency (RF) energy. This is called *Magnetic Resonance Angiography* (MRA). The generated contrast in the images could be tuned by selecting different RF stimuli. This allows MRA to be suitably indicated to detect soft tissues. Another advantage of MRA is that angiography could be generated without using exogenous agents. However, usually an intravenous injection of a paramagnetic contrast agent is used to improve the blood signal and reduce the acquisition time (*Contrast-Enhanced (CE)-MRA*).

Finally, we mention *Ultrasound* (US) imaging, based on the reflections of high frequency sound waves (few MHz) transmitted into the body. US is the least expensive and invasive among the techniques here discussed, and allows one for real-time acquisition of 2D images. In contrast, the spatial resolution is the poorest one. Recently, also 3D images could be acquired by means of 3D US, by reconstructing a 3D volume from 2D slices.

On the other side, only a few techniques allow one to obtain vessel wall images nowadays. Among them, we cite *Black Blood* (BB)-MRI, by which the vessel wall and the surrounding tissue can be viewed as well, and *Intravascular Ultrasound* (IVUS), which is however very invasive since the transducer is placed directly in the artery (typically a coronary) via a catheter.

No matter which technique is being used, from a mathematical standpoint we can assume that at the end of the acquisition step we obtain a vector $\boldsymbol{I}^{clin}$, whose $j-th$ component, I_j^{clin}, corresponds to the intensity of the image at the point $\boldsymbol{x}_j$ in a gray-scale representing the contrast generated by the imaging technique. The collection of the points $\boldsymbol{x}_j$, $j = 1, \ldots, N^{clin}$, assembles the lattice $\mathcal{L}^{clin}$, N^{clin} being the total numbers of acquisition points (in practice, either pixels or voxels) where the image contrast has been evaluated. Here and in what follows, a lattice is a simple collection of points determined by the points coordinates. It may be useful to associate to the image intensity vector $\boldsymbol{I}^{clin}$ a corresponding image intensity (scalar) function, that is typically obtained by interpolation. We will denote it by $I^{clin}(\boldsymbol{x})$.

3.1.2 Image enhancement

Medical images are often affected by noise and artifacts that may interfere with the quality of the final results of the preprocessing step. Thus, prior to the reconstruction of the 3D geometry, an imaging enhancement is usually performed.

A popular enhancement technique is *resampling*, consisting in suitably changing the resolution of the images in one or more directions. In practice, an interpolation of image intensity values $\boldsymbol{I}^{clin}$ onto a different (more refined) lattice is performed. The most commonly used methods are constant interpolation, first order composite Lagrangian interpolation, B-spline [555], and windowed sinc interpolation.

The noise in the medical images may be due to thermal effects in the signal processing electronics or to other undesired sources. Reduction of noise could be obtained by means of a *smoothing filter* which does not require any prior information about the nature of the noise and has a regularizing effect on the image. This technique is the most commonly used both for CT and MR images. A very popular filter is the *Gaussian* one, consisting in performing a discrete convolution with a Gaussian kernel over the lattice $\mathcal{L}^{clin}$ of the image intensity $\boldsymbol{I}^{clin}$. Unfortunately, together with the noise, smoothing could filter also

significant high frequency image contents. Moreover, since the image is separated by the background by sharp boundaries, characterized by high frequency content, the smoothing filtering could blur and move the boundaries. To prevent this, *anisotropic diffusion filtering* has been introduced [445]: the heat equation is solved for a new image intensity function, with diffusion coefficient decreasing for increasing values of the gradient magnitude of intensity. By so doing, the filtering is not performed at the boundaries where the gradient is large.

Another technique, called *multiscale vessel enhancement* [196], exploits the specific tubular shape of vascular geometries and, accordingly, assumes that the smallest modulus of the eigenvalues of the Hessian matrix of the image intensity function I^{clin} is small, while the other two are large and of equal sign.

At the end of this substep, we obtain a new image intensity vector $\boldsymbol{I}^{en}$ whose $j-th$ component, I_j^{en}, represents the intensity of the enhanced image in a gray-scale at the point $\boldsymbol{x}_j, 1, \ldots, N^{en}$, belonging to the lattice $\mathcal{L}^{en}$ (and, correspondingly an associated enhanced image intensity function $I^{en}(\boldsymbol{x})$ through interpolation). Here, N^{en} is the total number of points where the enhanced image intensity vector is available. Usually, $N^{en} > N^{clin}$.

3.1.3 Image segmentation

Image segmentation is the cornerstone of the preprocessing step. It consists in the construction of the shape of a vascular district from the image obtained after the enhancement substep. In particular, the segmentation allows one to detect those points of the lattice $\mathcal{L}^{en}$ which are supposed to belong to the boundary of the vessel lumen. The precise definition of the boundary of the lumen is a challenging task which requires, in general, a great user's experience.

The first technique we describe is *thresholding*, consisting in selecting a threshold k to identify the points $\boldsymbol{x}_j \in \mathcal{L}^{en}$ such that $I_j^{en} > k$. This is motivated by the assumption that k separates different anatomical structures, in our case the vessel lumen (characterized by intensity values larger than k) and the background, obtained by the collection of points for which $I_j^{en} \leq k$. The value of k is determined either manually or through a suitable algorithm. In the latter case, one commonly used strategy is the *full width at half maximum* (FWHM) consisting in setting the threshold halfway between the peak intensity within the lumen and the intensity of the background. For the segmentation of special structures, such as calcifications or stents, higher-bound thresholds are used [69].

A more sophisticated class of segmentation methods than thresholding is given by *front propagation methods*, where the propagation of a suitable wavefront is tracked. The speed of the wave is small in regions where $\boldsymbol{I}^{en}$ changes rapidly and high for the other regions, so that the wavefront is supposed to slow down when approaching the boundary. The most popular front propagation method is the *fast marching method* which provides an efficient solution to the Eikonal problem

$$\|\nabla T(\boldsymbol{x})\| = \frac{1}{V(I^{en}(\boldsymbol{x}))}, \quad \boldsymbol{x} \in \mathcal{D}^{en},$$

where $\mathcal{D}^{en} \subset \mathbb{R}^3$ is a region that contains all $\boldsymbol{x}_j \in \mathcal{L}^{en}$, and where suitable boundary

conditions on a selected boundary where the propagation starts are prescribed [612]. In the previous equation, V is the speed of the wavefront and $T(\boldsymbol{x})$ the first arrival time at point $\boldsymbol{x}$. In fact, T are iso-contours, representing a collection of surfaces describing the shape of the waveform. The vessel boundary is then represented by the points $\boldsymbol{x}_j \in \mathcal{L}^{en}$ such that $T(\boldsymbol{x}_j) = T^b$ (up to a given tolerance), where T^b is a suitable value selected by the user.

Another class of segmentation methods is given by *deformable models*, where a suitable energy is minimized, allowing the deformation of the body (in our case the boundary of the vessel lumen) to reach a final state with smallest energy, accounting for external terms derived from the image and internal terms constraining the boundary to be regular. The most used class of deformable models is the *level set method*, where a deformable surface is represented implicitly as the zero-level of a higher dimensional embedding function [517]. Deformable models, e.g. based on cylindrically parametrized surface meshes, incorporate anatomical knowledge of the vessel shape [196, 607].

As for the segmentation of the vessel wall, in [525], starting from BB-MRI images, the vessel wall outer boundary was segmented using the same deformable model used for the vessel lumen segmentation. Usually, BB-MRI or other images detecting the vessel wall are not routinely acquired in the clinical practice. In this case, a reasonable approach to obtain the vessel wall is to extrude the reconstructed boundary lumen along the outward unit vector by using a suitable function specifying the vessel wall thickness in the different regions of the district of interest.

In those cases where the image intensity vectors $\boldsymbol{I}^{clin}$ and $\boldsymbol{I}^{en}$ refer to 2D slices, the application of the previous segmentation strategies leads to identify several vessel boundaries (contours), one for each slice, which now needs to be connected to obtain the 3D boundary surface. This operation is called *surface reconstruction*. A simple procedure consists in connecting successive contours by straight lines defining surface triangle edges. This strategy is not suited in presence of changes of shape such as in bifurcations. A better surface reconstruction is provided by least-square fitting of polynomial surfaces to the contour set [586]. This strategy is suitable to manage bifurcations whose branches are fitted separately with a successive extension into the parent vessel. A variant of this approach has been proposed in [204], where contours are first filled with triangles which are then connected to the triangles of the adjacent contours by means of tethraedra. The final lumen surface is then represented by the boundary of this tetrahedral mesh (formed by triangles). We mention also *shape based interpolation* where, for each contour, a characteristic function with positive (respectively, negative) values for points located inside (respectively, outside) the contour is built. The final lumen boundary surface is then represented by the zero level-set of the interpolation of all these characteristic functions [486]. Finally, we briefly describe interpolation by means of *radial basis functions* (RBF), that provide a flexible way of interpolating data in multi-dimensional spaces, even for unstructured data where interpolation nodes are scattered and/or do not form a regular grid, and for which it is often impossible to apply polynomial or spline interpolation [84, 193]. The coefficients in the linear combination with respect to the RBF basis are determined by solving a suitable linear system, which is invertible under very mild conditions [438].

A special mention is deserved by *centerline* reconstruction. The centerline is a one-

dimensional curve centered inside the vessel lumen. Many segmentation tools use the centerline as starting point making the assumption that the shape of the section is known around each centerline location [419]. Centerline reconstruction allows a complete reconstruction of the computational domain when using *one-dimensional modeling* of blood flow, see Section 4.5.1.

In any case, at the end of the segmentation step we obtain the lattice $\mathcal{L}^{surf}$ which collects the points $\boldsymbol{x}_j, 1, \ldots, N^{surf}$, classified as belonging to the lumen vessel surface or to the outer wall, N^{surf} being the total numbers of points of the surface lattice.

3.1.4 Building the computational mesh

Once the final boundary lattice $\mathcal{L}^{surf}$ (made of points standing on the lumen boundary) is made available, we are ready to build the volumetric mesh $\mathcal{T}^{vol}$ in the lumen. This mesh usually consists of unstructured tetrahedra, because of their flexibility to fill volumes of complex shape.

Unstructured volumetric meshes are constructed starting from an analytical expression, say $\mathcal{S}(\boldsymbol{x})$, representing the surface associated to the boundary lattice $\mathcal{L}^{surf}$. This expression can derive from an explicit representation, for instance a bivariate parametric function built as a collection of adjacent polygons. The latter are typically triangles, generated by Lagrangian shape functions, or patches, generated by high degree polynomial such as NURBS [532]. Alternatively, the surface is represented implicitly as the iso-surface of an embedding function. Notice that some of the segmentation strategies described above, such as deformable models and those used for the surface reconstruction, provide directly an analytical expression $\mathcal{S}(\boldsymbol{x})$ of the lumen boundary surface.

For the construction of unstructured volumetric meshes $\mathcal{T}^{vol}$, we mention here two possible approaches. In the first one, a boundary surface mesh $\mathcal{T}^{surf}$ is first generated. To this aim, we start from a lattice $\widetilde{\mathcal{L}}^{surf}$ (in principle different than $\mathcal{L}^{surf}$) composed by points of $\mathcal{S}$. Then, the *Voronoi diagram* for $\widetilde{\mathcal{L}}^{surf}$ is constructed. This is a partition of $\mathcal{S}$ into non-overlapping regions, each one containing exactly one point (node) of $\widetilde{\mathcal{L}}^{surf}$ and being composed by all the points of $\mathcal{S}$ that are closer to that node than to any other node. Starting from the Voronoi diagram, it is possible to obtain a mesh $\mathcal{T}^{surf}$ by joining with straight lines nodes in regions sharing an edge (*Delaunay mesh generation*). We underline that the vertices of the mesh $\mathcal{T}^{surf}$ do not necessarily coincide with the points of the lattice $\widetilde{\mathcal{L}}^{surf}$. Popular algorithms to generate a Delaunay mesh have been proposed, e.g., in [590, 591]. Once a surface mesh $\mathcal{T}^{surf}$ is made available, the volumetric mesh $\mathcal{T}^{vol}$ is generated. The latter could be obtained by, e.g., *advancing front* methods, where, starting from the triangles of the surface mesh, a front composed by internal nodes is generated. These new nodes allow one to identify tetrahedra, whose validity is verified by checking that they do not intersect the front [46].

The second approach relies on directly generating the volumetric mesh $\mathcal{T}^{vol}$, e.g., by means of a Delaunay 3D mesh generation, where a starting volumetric lattice $\widetilde{\mathcal{L}}^{vol}$ is obtained by locating the nodes in the volume $\mathcal{V}(\boldsymbol{x})$ contained in $\mathcal{S}(\boldsymbol{x})$. One of the main problems related to this approach is that boundary meshing is often difficult, since the related surface triangulation could not be of Delaunay type. An alternative approach is

given by *octree mesh generation*, where $\mathcal{V}(\boldsymbol{x})$ is embedded in a box and successive subdivisions are performed until the smallest cells permit to accurately describe the boundary. Although being faster, this strategy generates meshes with poor quality near the boundary.

When a volumetric mesh $\mathcal{T}^{vol}$ is obtained, a further step (*mesh optimization*) prior to the generation of the final mesh could be introduced, so as to improve its quality. This prevents mesh distortion, e.g. the presence of very small angles, which could deteriorate the convergence of algorithms for the solution of the PDE of interest and thus their accuracy. Mesh optimization leads to an *optimal mesh*, which produces the best accuracy for a given number of nodes. This is obtained by selecting (a priori or a posteriori through error estimates) a lower bound for the mesh size (in case assuming different values in different regions of $\mathcal{V}(\boldsymbol{x})$). Mesh optimization is incorporated in the strategies described above. For example, in octree mesh generation, this is obtained by splitting a cell only if its children have a size larger than the lower bound.

A mesh is deemed valid for blood flow simulations if it allows to recover outputs of physical interest. In arteries, the mesh should be fine enough to capture Wall Shear Stresses (WSS) [86], and, to this aim, the construction of a boundary layer mesh is essential, even at low Reynolds numbers [53]. WSS expresses the magnitude of tangential viscous forces exerted by the fluid on the lumen boundary Σ^t, defined by

$$WSS = \mu \sqrt{\sum_{j=1}^{2} \left(\nabla \boldsymbol{v}\, \boldsymbol{n} \right) \cdot \boldsymbol{\tau}^{(j)} \big)^2} \qquad \text{on } \Sigma^t,$$

where $\boldsymbol{v}$ is the fluid velocity, $\boldsymbol{n}$ the outward unit vector, and $\boldsymbol{\tau}^{(j)}$ the tangential unit vectors, $j = 1, 2$. Note that WSS is a scalar function of $\boldsymbol{x} \in \Sigma^t$ and $t > 0$. In componentwise notation,

$$WSS = \mu \left(\sum_{j=1}^{2} \left(\sum_{i,k=1}^{3} \left(\frac{\partial v_i}{\partial x_k} n_k \right) \tau_i^{(j)} \right)^2 \right)^{1/2} \qquad \text{on } \Sigma^t.$$

As for the structure domain, hexahedral meshing is preferable so as to prevent the locking phenomenon, whereas tetrahedral meshes are used when conforming meshes at the boundary lumen interface are needed in view of fluid-structure interaction problems (see Section 4.3). Usually, three or four layers of elements are enough to obtain an accurate result [609].

For recent reviews on geometric reconstruction for blood flow simulation, see [10, 510, 332].

3.2 Boundary vascular data

The differential problems we will treat in the next sections need appropriate boundary conditions. For our problems (incompressible Navier-Stokes equations for the fluid and finite elasticity for the structure), we anticipate the kind of boundary conditions that should ideally be prescribed:

$$\boldsymbol{v} = \boldsymbol{g}_f \quad \text{on } \Gamma_f^{D,t}, \qquad -p\boldsymbol{n} + \mu \left(\nabla \boldsymbol{v} + (\nabla \boldsymbol{v})^T \right) \boldsymbol{n} = \boldsymbol{h}_f \quad \text{on } \Gamma_f^{N,t},$$

for the fluid problem and

$$\boldsymbol{d} = \boldsymbol{g}_s \quad \text{on } \Gamma_s^{D,t}, \qquad \boldsymbol{T}_s\boldsymbol{n} = \boldsymbol{h}_s \quad \text{on } \Gamma_s^{N,t},$$

for the structure problem. In the previous equations, the Dirichlet and Neumann boundaries, $\Gamma_j^{D,t}$ and $\Gamma_j^{N,t}$, respectively, are such that $\Gamma_j^{D,t} \cap \Gamma_j^{N,t} = \emptyset$, $\Gamma_j^{D,t} \cup \Gamma_j^{N,t} = \partial\Omega_j^t$, $j = f, s$, Ω_f^t and Ω_s^t being the fluid and structure domains at time t, see Figure 3. Moreover, p denotes the fluid pressure, $-p\boldsymbol{n} + \mu\left(\nabla\boldsymbol{v} + (\nabla\boldsymbol{v})^T\right)\boldsymbol{n}$ is the fluid normal Cauchy stress, $\boldsymbol{d}$ the structure displacement, $\boldsymbol{T}_s$ the Cauchy stress tensor of the wall material, and $\boldsymbol{g}_f$, $\boldsymbol{g}_s$, $\boldsymbol{h}_f$, $\boldsymbol{h}_s$ given data, see Section 4. In the previous definitions of domains and boundaries, the superscript ^{t} means that they possibly change in time.

As we will see in the following, the boundary of the computational domain (either the fluid or the structure one) will be composed of two parts, namely the *physical boundary* and the *artificial boundary*. On the physical boundary, often suitable conditions are suggested by physical principles. For example, for the fluid problem, *no-slip* Dirichlet conditions should be prescribed at the lumen boundary, since it is assumed that the fluid particles perfectly adhere to the vessel wall. This leads to a homogeneous Dirichlet condition ($\boldsymbol{v} = \boldsymbol{0}$) in the case of rigid walls, and to a kinematic interface condition ($\boldsymbol{v} = \dot{\boldsymbol{d}}$) for fluid-structure interaction problems (see Section 4.3). As for the structure problem, at the internal physical boundary (that is at the lumen boundary) often the fluid pressure is prescribed. This leads to a Neumann boundary condition ($\boldsymbol{T}_s\boldsymbol{n} = -P\boldsymbol{n}$, P being a measurement of the fluid pressure) for a pure structure problem, and to a dynamic interface condition ($\boldsymbol{T}_s\boldsymbol{n} = -p\boldsymbol{n} + \mu\left(\nabla\boldsymbol{v} + (\nabla\boldsymbol{v})^T\right)\boldsymbol{n}$) for fluid-structure interaction. On the outer wall boundary Γ_{ext}, the interaction with the surrounding tissue should be considered. This is often modeled by means of a Robin boundary condition of type

$$\alpha_{ST}\boldsymbol{d} + \boldsymbol{T}_s\boldsymbol{n} = P_{ext}\boldsymbol{n} \quad \text{on } \Gamma_{ext}, \tag{1}$$

which assimilates the surrounding tissue to a sequence of elastic springs with rigidity α_{ST} and where P_{ext} is the external pressure [380].

On a different side, the artificial sections are those introduced by the truncation of the computational domains, see Figure 3. Truncation is done in order to focus on a specific domain of interest. Ideally, the boundary conditions to be used on artificial sections should derive from clinical measurements.

The technique mainly used to obtain boundary data on artificial boundaries is US. This is because of its non-invasiveness and the fact that it is daily used in the clinical practice. If the US beam is swept (unlike in geometric acquisitions where it is kept fixed) through a plane or sector, it is possible to measure the blood velocity in a single point of a cross-section Γ^t in the direction of the US beam by exploiting the Doppler effect. The velocity is then converted into a flow rate measure Q across Γ^t for each time (this is the principle of the so-called *Echo-Color-Doppler* technique [509]) and can then be used to prescribe at each time a *flow rate condition*

$$\rho_f \int_{\Gamma^t} \boldsymbol{v} \cdot \boldsymbol{n}\, d\gamma = Q. \tag{2}$$

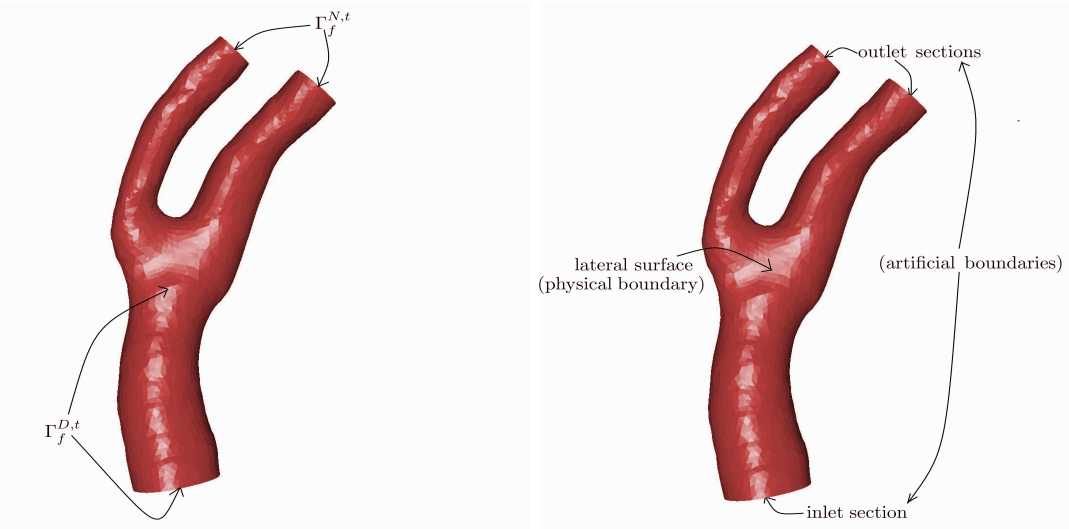

Figure 3: Possible choices of the Dirichlet and Neumann boundaries (left) and physical and artificial boundaries (right) for a carotid domain in the fluid stand-alone problem (reconstructed from MRA images)

The previous condition is *defective* since it is not enough to ensure well-posedness of the fluid problem. The treatment of defective conditions will be addressed in Section 4.4. Another technique which allows one to measure cross-sectional flow rates is based on the acquisition of thermal images [349]. Another quantity easily measurable by means of US is the lumen area $\int_{\Gamma^t} d\gamma$. This information could be used to prescribe a defective condition for the vessel wall.

More sophisticated techniques could acquire velocity measures in several points on the same cross-section, thus in principle leading to a Dirichlet boundary condition (possibly after a suitable regularization). This is the case of *Phase Contrast* (PC)-MRA, where the blood velocities are encoded into images for several instants of the heartbeat [383]. The spatial resolution of modern PC-MRA are of the order of $1-2\,mm$ on each cross section and $4\,mm$ along the longitudinal axis. The required mesh size is often less than $1\,mm$ so that interpolation is however needed to obtain a usable Dirichlet condition. The temporal resolution is of about $0.03\,s$.

If the lumen artificial cross section is orthogonal to the axial direction, then the viscous terms in the fluid normal Cauchy stress are very small [248]. In this case, a measure of the pressure $P(t)$ could be used to prescribe a Neumann boundary condition. This could be obtained for the arterial system non-invasively by means of a *sphygmomanometer*, which usually measures the pressure at the level of the radial aorta (remember that the pressure peak could be considered constant along the arterial tree, at least until the capillary net, see Section 2). To have a continuous monitoring of the pressure (for example during hospital recovery) or to have a measure in the venous system (where the pressure falls down) a catheter with a transducer could be placed in the district of interest. In any case,

the average pressure over the cross section is measured. This leads at each time to the following defective boundary condition for the normal component of the normal Cauchy stress of the fluid

$$\frac{1}{|\Gamma^t|}\int_{\Gamma^t}\left(p\boldsymbol{n}-\mu\left(\nabla\boldsymbol{v}+(\nabla\boldsymbol{v})^T\right)\boldsymbol{n}\right)\cdot\boldsymbol{n}\,d\gamma=P. \tag{3}$$

Unfortunately, no measurement is available at the artificial sections of the structure, so that "empirical" and "practical" choices are made (see Section 4.4).

Finally, we observe that measurements acquired at several instants during an heartbeat could be used in principle also for physical boundaries. For example, from 4D-CTA the boundary lumen displacement could be used as Dirichlet condition for the structure problem, whereas from PC-MRA the blood velocity at the boundary lumen could be used to prescribe a Dirichlet condition for the fluid problem. Since at the physical boundaries the physical principles are used to prescribe boundary conditions, these "extra" data could be used in view of a validation of the numerical results or in a *parameter estimation* fashion, as described in Section 10. PC-MRA allows one to acquire also internal measures of blood velocity. This could be used again for a validation or in a parameter estimation context.

3.3 Biological vascular data

Finally, we need to know the values of physical parameters appearing in the differential problems. For the fluid, two parameters characterize the problem, namely blood *density* and blood *viscosity*. Although density is in principle easily measurable, no patient-specific acquisition is in general made because its value does never significantly depart from an average value of $1.06\,g/cm^3$. The range of variability of viscosity is instead larger. Indeed, its value depends on the shear rate (non-Newtonian behavior) and on the physical state of the patient. When the assumption of Newtonian fluid (holding for medium and large healthy vessels) is made, typical values of the viscosity ranges in the interval $(0.03 - 0.04\,Poise(=1\,g/(cm\,s)))$. Again, no patient-specific viscosity measures are usually made and, unless for pathological situations, a value in the previous range is selected.

The parameters characterizing the vessel wall depend (also in number) by the constitutive law used to represent its behavior. More typically, they are the density, the *elasticity* (or compliance) and the degree of *incompressibility*. For linear elasticity models, the latter two are quantified by the *Young modulus* and *Poisson modulus*, respectively. The density value is very similar to that of blood, the range most commonly used reaching values up to $1.2\,g/cm^3$. The compliance of the vessel could be qualitatively seen as the ratio between the volume and pressure variations [401]. Patient-specific measures could be obtained by the simultaneous (invasive) measures of pressure and cross-sectional area at different locations, by measuring the rate of propagation of flow waves [63], or by *elastography* where the elasticity properties are analyzed by images before and after the application of a deformation [418]. The range of variability of vessel compliance is quite wide ($200 - 800\,kPa$ in normal conditions), with a great dependence on the location and on possible presence of aneurysms or calcifications. As for the Poisson modulus, only ex-vivo measurements are possible. An acceptable value used by the community is 0.49, meaning that vessels could be considered as quasi-incompressible. Finally, let us mention that the coefficient α_{ST} in

(1) can be regarded as representative of the Young modulus of the surrounding tissue. As such, it thus could be measured, even though this is a difficult endeavor. Estimates have been provided, e.g., in [339].

When not available from measurements, patient-specific values of biological data could be alternatively obtained by means of parameter estimation mathematical techniques. This will be the topic of Section 10.

4 Modeling blood flow

4.1 The fluid problem

In large and medium sized arteries, those more typically affected by vascular diseases, blood can be modeled by means of the Navier-Stokes (NS) equations for incompressible homogeneous Newtonian fluids [444, 541, 542, 188]. For non-Newtonian rheological models necessary to describe some specific flow processes, such as clotting or sickle cell diseases, or more generally flow in capillaries, we refer e.g. to [492, 169].

For the mathematical formulation of the problem, we write the fluid equations with respect to an Eulerian frame of reference, and we denote by $\Omega_f^t = \Omega_f(t) \subset \mathbb{R}^3$ the time-varying arterial lumen, at time $t > 0$ (see Figure 4, left).

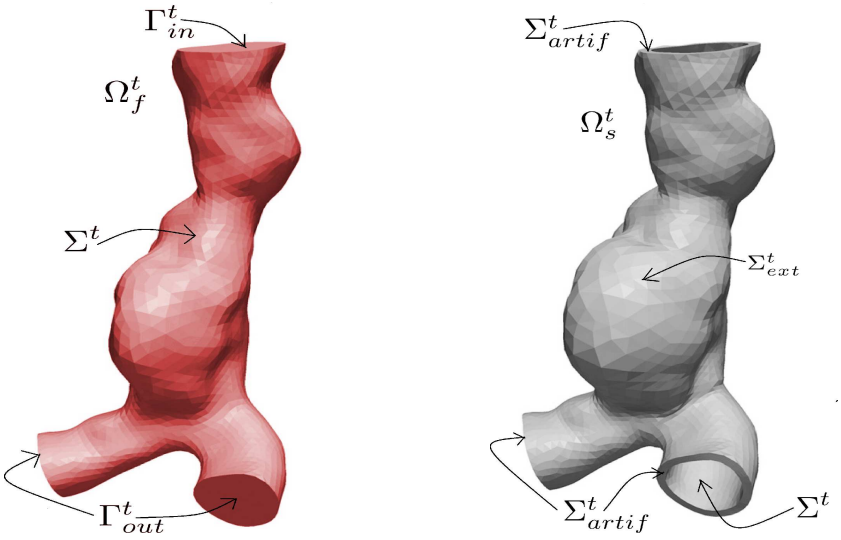

Figure 4: Representation of the fluid domain on the left and structure domain on the right. The fluid domain here illustrated is that of an abdominal aorta in presence of aneurysm, reconstructed from CTA images. The structure domain has been obtained by extrusion of the fluid one

Then, at each time $t > 0$, we look for fluid velocity $\boldsymbol{v}$ and fluid pressure p such that

$$\rho_f \left(\frac{\partial \boldsymbol{v}}{\partial t} + \rho_f (\boldsymbol{v} \cdot \nabla) \boldsymbol{v} \right) - \nabla \cdot \boldsymbol{T}_f(\boldsymbol{v}, p) = \boldsymbol{0} \qquad \text{in } \Omega_f^t, \tag{4a}$$

$$\nabla \cdot \boldsymbol{v} = 0 \qquad \text{in } \Omega_f^t. \tag{4b}$$

Notice that volumetric forces acting in the fluid domain (e.g. due to gravity) were set to zero since they are quite often neglected. Moreover,

$$\boldsymbol{T}_f(\boldsymbol{v}, p) = -p\boldsymbol{I} + \mu \left(\nabla \boldsymbol{v} + (\nabla \boldsymbol{v})^T \right) \tag{5}$$

is the fluid Cauchy stress tensor, μ being the blood viscosity. As we consider only Newtonian rheology here, μ is assumed to be constant.

Finally, problem (4) is completed by the initial condition

$$\boldsymbol{v}|_{t=0} = \boldsymbol{v}_0 \quad \text{in } \Omega_f,$$

where $\Omega_f = \Omega_f^0$, and boundary conditions. The latter typically prescribe no-slip conditions on the physical boundary Σ^t,

$$\boldsymbol{v} = \boldsymbol{\phi} \quad \text{on } \Sigma^t, \tag{6}$$

the upstream velocity on the proximal boundaries, say Γ_{in}^t,

$$\boldsymbol{v} = \boldsymbol{v}_{up} \quad \text{on } \Gamma_{in}^t, \tag{7}$$

and traction conditions on the distal boundaries, say Γ_{out}^t,

$$\boldsymbol{T}_f \boldsymbol{n} = \boldsymbol{h}_f \quad \text{on } \Gamma_{out}^t. \tag{8}$$

Here, $\boldsymbol{v}_0$, $\boldsymbol{v}_{up}$, $\boldsymbol{\phi}$ and $\boldsymbol{h}_f$ are suitable functions with the required regularity [479]. Notice that the lumen boundary displacement $\boldsymbol{\phi}$ at this level is a known function of space and time. For rigid boundaries, we have $\boldsymbol{\phi} = \boldsymbol{0}$.

When patient-specific measures are available, other conditions might be prescribed. However, measures seldom provide a complete data set to be used in the computation, see our previous discussion in Section 3.2; this prompts the issue of solvability of Navier-Stokes equations, that we address in Section 4.4.

For each $t > 0$ (a.e. $t > 0$), the weak form of (4) together with the boundary conditions (6)-(7)-(8) reads: Find $\boldsymbol{v} = \boldsymbol{v}(t) \in [H^1(\Omega_f^t)]^3$, $\boldsymbol{v} = \boldsymbol{v}_{up}$ on Γ_{in}^t, $\boldsymbol{v} = \boldsymbol{\phi}$ on Σ^t, $\boldsymbol{v} = \boldsymbol{v}_0$ for $t = 0$ in Ω_f, and $p = p(t) \in L^2(\Omega_f^t)$ such that

$$\rho_f \int_{\Omega_f^t} \frac{\partial \boldsymbol{v}}{\partial t} \cdot \boldsymbol{w} \, d\omega + \mathcal{A}_f^t(\boldsymbol{v}, \boldsymbol{v}, \boldsymbol{w}) + \mathcal{B}^t(p, \boldsymbol{w}) = \int_{\Gamma_{out}^t} \boldsymbol{h}_f \cdot \boldsymbol{n} \, d\gamma, \tag{9a}$$

$$\mathcal{B}^t(q, \boldsymbol{v}) = 0, \tag{9b}$$

for all $\boldsymbol{w} \in \boldsymbol{V}^t = \{[H^1(\Omega_f^t)]^3 : \boldsymbol{w} = \boldsymbol{0} \text{ on } \partial\Omega \setminus \Gamma_{out}^t\}$ and $q \in L^2(\Omega_f^t)$, and where we have set

$$\mathcal{A}_f^t(\boldsymbol{z}, \boldsymbol{v}, \boldsymbol{w}) = \rho_f \int_{\Omega_f^t} (\boldsymbol{z} \cdot \nabla) \boldsymbol{v} \cdot \boldsymbol{w} \, d\omega + \mu \int_{\Omega_f^t} \left(\nabla \boldsymbol{v} + (\nabla \boldsymbol{v})^T \right) : \nabla \boldsymbol{w} \, d\omega,$$

and

$$\mathcal{B}^t(q, \boldsymbol{w}) = -\int_{\Omega_f^t} q\nabla \cdot \boldsymbol{w}\, d\omega.$$

Existence of a global in time weak solution of the previous problem has been proven in [331] for the case $\Omega_f = \mathbb{R}^3$ and in [260] for the case of bounded domain. The uniqueness has been proven only for the two-dimensional case [338]; for the three-dimensional case, only locally in time uniqueness results are available [462].

4.2 Mechanical wall models

The problem that models the deformation of vessel walls is given by the elasto-dynamics equation that is usually written in a reference domain $\Omega_s = \Omega_s(0) \subset \mathbb{R}^3$ using a Lagrangian framework. For any $t > 0$, the material domain $\Omega_s^t = \Omega_s(t)$ (depicted in Fig. 4, right) is the image of Ω_s by a proper Lagrangian map $\mathcal{L} : \Omega_s \to \Omega_s^t$. We use the abridged notation $\widehat{g} = g \circ \mathcal{L}$ to denote in Ω_s any function g defined in the current solid configuration Ω_s^t.

For the sake of simplicity, we assume the arterial wall to obey a (possibly nonlinear) finite elastic law relating stress to strain in the arterial tissue; for more complex behaviors of arterial walls see, e.g., [257, 259]. In more realistic settings, stress is a function of the strain but also of the past loading history [200].

The problem we consider reads: Find, at each time $t > 0$, the structure displacement $\boldsymbol{d}$ such that

$$\rho_s \frac{\partial^2 \widehat{\boldsymbol{d}}}{\partial t^2} - \nabla \cdot \widehat{\boldsymbol{T}}_s(\widehat{\boldsymbol{d}}) = \boldsymbol{0} \quad \text{in } \Omega_s, \tag{10}$$

where ρ_s is the structure density. Notice that volumetric forces acting in the solid domain (e.g. due to muscle forces) were set to zero since they are quite often neglected.

The previous equation has been written in terms of the first Piola-Kirchhoff tensor $\widehat{\boldsymbol{T}}_s(\widehat{\boldsymbol{d}})$ which is related to the Cauchy tensor $\boldsymbol{T}_s(\boldsymbol{d})$ thanks to the relation $\widehat{\boldsymbol{T}}_s = J\boldsymbol{T}_s\boldsymbol{F}^{-T}$. Here, $\boldsymbol{F} = \nabla \boldsymbol{x}$ is the deformation tensor, the gradient being taken with respect to the reference space coordinates and $\boldsymbol{x}$ being the coordinates of points in the current configuration. Correspondingly, $J = \det(\boldsymbol{F})$ represents the change of volume between the reference and the current configurations; notice that $\boldsymbol{F}$ (and thus J) depends on the current configuration Ω_s^t.

For a *hyperelastic* material, the first Piola-Kirchhoff stress tensor is obtained by differentiating a suitable Strain Energy Density Function Θ,

$$\widehat{\boldsymbol{T}}_s = \frac{\partial \Theta}{\partial \boldsymbol{F}}. \tag{11}$$

Several non-linear elastic energy functions have been proposed for arteries. For the *Saint Venant-Kirchhoff* material,

$$\Theta(\boldsymbol{C}) = \frac{E\nu}{2(1+\nu)(1-2\nu)} \left(tr\left(\frac{1}{2}(\boldsymbol{C}^T - \boldsymbol{I})\right)\right)^2 + \frac{E}{2(1+\nu)} tr\left(\left(\frac{1}{2}(\boldsymbol{C}^T - \boldsymbol{I})\right)^2\right), \tag{12}$$

where $\boldsymbol{C} = \boldsymbol{F}^T\boldsymbol{F}$, E is the *Young modulus* and ν the *Poisson modulus* of the vessel wall. More complex and accurate functions widely used for arteries are based on separating the isotropic and elastic behaviour due to the *elastin* and the anisotropic one accounting for the stiffening increment at large displacements due to the *collagen*,

$$\Theta = \Theta^{iso} + \Theta^{aniso}. \tag{13}$$

A common choice for the isotropic part is the *Neo-Hookean* law

$$\Theta^{iso}(\boldsymbol{C}) = \frac{G}{2}\left(tr(\boldsymbol{C}) - 3\right), \tag{14}$$

whereas for the anisotropic part, an exponential law is often considered:

$$\Theta^{aniso}(\boldsymbol{C}) = \frac{k_1}{2k_2}\left(e^{\left(k_2(\boldsymbol{a}\cdot(\boldsymbol{C}\boldsymbol{a})-1)^2\right)} - 1\right), \tag{15}$$

where $\boldsymbol{a}$ is the unit vector identifying the preferred direction of the collagen fibers, G the *shear modulus*, k_1, k_2 material parameters where k_2 characterizes the stiffness of the material for large displacements [199, 257, 484]. More complete laws also account for the symmetrical helical arrangement of the collagen fibers, introducing a second predominant direction of fibers [259]. When not available from medical images, the fibers directions are computed by means of suitable algorithms under the assumption that their orientation is mainly governed by the principal stresses, see, e.g., [242, 307]. For distal arteries of muscular type, viscoelastic and pseudoelastic terms are also considered [256].

Sometimes, the arterial tissue is considered as incompressible by enforcing to the strain energy function the incompressibility constraint $J = 1$ by means of a Lagrange multipliers approach [255]

$$\Theta^{inc} = \Theta + p_s(J - 1). \tag{16}$$

Here p_s is the hydrostatic pressure related to the vessel wall displacement, which plays the role of Lagrange multiplier for the incompressibility constraint. Correspondingly, the Cauchy stress tensor is augmented as follows

$$\boldsymbol{T}_s^{inc}(\boldsymbol{d}, p_s) = \boldsymbol{T}_s(\boldsymbol{d}) + p_s\boldsymbol{I},$$

where $\boldsymbol{T}_s$ is the component arising from the energy Θ. However, experimental studies showed that the arterial tissue has in fact a *nearly incompressible* behavior [83]. This means that the strain energy function could be decomposed into two terms

$$\Theta(\boldsymbol{C}) = \Theta_{vol}(J) + \Theta_{isoc}(\bar{\boldsymbol{C}}),$$

where $\bar{\boldsymbol{C}} = J^{-2/3}\boldsymbol{C}$, $det\bar{\boldsymbol{C}} = 1$. The *isochoric* part Θ_{isoc} is given by the general function (13) provided that $\boldsymbol{C}$ is substituted by $\bar{\boldsymbol{C}}$ and characterizes the mechanical response of the material to incompressible deformations. The *volumetric* part is usually given by

$$\Theta_{vol}(J) = \frac{\kappa}{2}\left(J - 1\right)^2,$$

where κ (*bulk modulus*) is a penalty parameter to enforce the incompressibility constraint $J = 1$ [336]. In this case, the related Cauchy stress tensor is the same of the compressible case. For a review of arterial vessel wall models we refer the reader to [259].

Problem (10) has to be completed by the initial conditions

$$\boldsymbol{d}|_{t=0} = \boldsymbol{d}_0, \qquad \frac{\partial \boldsymbol{d}}{\partial t}\Big|_{t=0} = \boldsymbol{d}_1 \quad \text{in } \Omega_s,$$

and boundary conditions. The latter typically prescribe on the artificial sections Γ^t_{artif} either

$$\boldsymbol{d} = \boldsymbol{0} \quad \text{on } \Gamma^t_{artif} \tag{17}$$

(fixed boundary) or $\boldsymbol{d} \cdot \boldsymbol{n} = 0$ together with $(\boldsymbol{T}_s\, \boldsymbol{n}) \cdot \boldsymbol{\tau}^{(j)} = \boldsymbol{0}$, $j = 1, 2$, $\boldsymbol{\tau}^{(j)}$ being the unit tangential directions (displacement allowed in the tangential direction), whereas at the internal physical boundary Σ^t they prescribe the solid traction

$$\boldsymbol{T}_s \boldsymbol{n} = \boldsymbol{h}_s \quad \text{on } \Sigma^t. \tag{18}$$

In the previous conditions, $\boldsymbol{d}_0$, $\boldsymbol{d}_1$ and $\boldsymbol{h}_s$ are suitable given functions. When considering the Fluid-Structure (FS) coupling, $\boldsymbol{h}_s$ is of course provided by the normal Cauchy stress from the fluid side, see Section 4.3. To account for the effect of the tissues surrounding the artery, the algebraic law (1) is often prescribed at the external lateral surface Γ_{ext} of Ω_s, to mimic the elastic behavior of this tissue [380].

For each time $t > 0$, the weak form of (10) together with the boundary conditions (1)-(17)-(18), in the case of fixed boundaries, reads: Find $\widehat{\boldsymbol{d}} = \widehat{\boldsymbol{d}}(t) \in \boldsymbol{D}$, $\widehat{\boldsymbol{d}} = \boldsymbol{0}$ on Γ_{artif}, $\widehat{\boldsymbol{d}} = \boldsymbol{d}_0$ and $\frac{\partial \widehat{\boldsymbol{d}}}{\partial t} = \boldsymbol{d}_1$ for $t = 0$ in Ω_s, such that

$$\rho_s \int_{\Omega_s} \frac{\partial^2 \widehat{\boldsymbol{d}}}{\partial t^2} \cdot \widehat{\boldsymbol{e}}\, d\omega + \int_{\Omega_s} \widehat{\boldsymbol{T}}_s\left(\widehat{\boldsymbol{d}}\right) : \nabla \widehat{\boldsymbol{e}}\, d\omega + \int_{\Gamma_{ext}} \alpha_{ST} \widehat{\boldsymbol{d}} \cdot \widehat{\boldsymbol{e}}\, d\sigma = \int_{\Gamma_{ext}} P_{ext} \widehat{\boldsymbol{n}} \cdot \widehat{\boldsymbol{e}}\, d\sigma + \int_{\Sigma} \widehat{\boldsymbol{h}}_s \cdot \widehat{\boldsymbol{e}}\, d\sigma, \tag{19}$$

for all $\widehat{\boldsymbol{e}} \in \boldsymbol{D} = \boldsymbol{D}^0$, where $\boldsymbol{D}^t = \{\boldsymbol{e} \in [H^1(\Omega_s^t)]^3 : \boldsymbol{e} = \boldsymbol{0} \text{ on } \Gamma^t_{artif}\}$.

The existence of strong (steady) solutions of the previous problems could be proven using the theory developed in [29]. For example, this is the case of the Saint Venant-Kirchhoff constitutive law given in (12) [107]. The existence and uniqueness of weak solutions are guaranteed by the coercivity and convexity of the energy Θ [106, 127]. However, a convex strain energy function is not able in general to describe instabilities such as buckling [28]. Thus, to avoid the use of convex functions, the property of *polyconvexity* has been introduced [29]. Its fulfillment guarantees physically admissible solutions [127]. Both the neo-Hookean law (14) and the exponential one (15) satisfy the polyconvexity property [32].

4.2.1 Modeling the structure as a 2D membrane

In some circumstances, because of the small thickness of the vessel wall, a non-linear shell model has been proposed, see, e.g., [333, 611]. In this case, the structure problem

is described by two-dimensional equations defined with respect to the middle surface, consisting of the computation of the deformation of this surface.

A simpler equation may be obtained if the structure is modeled as a 2D *membrane* whose position in space at any time exactly coincides with internal boundary Σ^t, yielding the so-called *generalized string model* [478]

$$\rho_s H_s \frac{\partial^2 \widehat{d}_r}{\partial t^2} - \nabla \cdot (\boldsymbol{P} \nabla \widehat{d}_r) + \chi H_s \widehat{d}_r = \widehat{f}_s \quad \text{in } \Sigma. \tag{20}$$

Here Σ represents the reference membrane configuration, d_r is the radial displacement, H_s the structure thickness; the tensor $\boldsymbol{P}$ accounts for *shear deformations* and, possibly, for *prestress*, $\chi = \frac{E}{1-\nu^2}(4\rho_1^2 - 2(1-\nu)\rho_2)$, where $\rho_1(\boldsymbol{x})$ and $\rho_2(\boldsymbol{x})$ are the *mean* and *Gaussian curvatures* of Σ, respectively, [413], and f_s the forcing term, given by a measure of the fluid pressure. Equation (20) is derived from the *Hooke law* for linear elasticity under the assumptions of small thickness, *plane stresses*, and negligible *elastic bending terms* [613]. To account for the effect of the surrounding tissue, the term χ in (20) needs to be augmented by the elastic coefficient of the tissue α_{ST} [189].

A further simplification arises when Σ represents the lateral surface of a cylinder. By discarding any dependence on the circumferential coordinate, model (20) reduces to

$$\rho_s H_s \frac{\partial^2 \widehat{d}_r}{\partial t^2} - kGH_s \frac{\partial^2 \widehat{d}_r}{\partial z^2} + \frac{EH_s}{(1-\nu^2)R_0^2} H_s \widehat{d}_r = \widehat{f}_s \quad \text{in } \Sigma, \tag{21}$$

k being the *Timoshenko correction factor*, G the *shear modulus*, R_0 the initial cylinder radius, and z the axial coordinate. Often, in the latter case, also a *visco-elastic term* of the form $\gamma_v \frac{\partial^3 d_r}{\partial^2 z \partial t}$ is added, with γ_v representing a suitable visco-elastic parameter [478].

4.3 The coupled fluid-structure interaction problem

Blood flow in the vessel lumen and deformation of the vessel wall are intimately connected through a fluid-solid interaction (FSI). In particular, fluid and structure interact through the fluid-solid (FS) interface Σ^t which coincides with the physical fluid boundary and the internal vessel wall boundary introduced in the previous sections. The coupled problem is obtained by combining at each $t > 0$ (4) and (10) as follows:

$$\rho_f \left(\frac{\partial \boldsymbol{v}}{\partial t} + (\boldsymbol{v} \cdot \nabla)\boldsymbol{v} \right) - \nabla \cdot \boldsymbol{T}_f(\boldsymbol{v}, p) = \boldsymbol{0} \qquad \text{in } \Omega_f^t, \tag{22a}$$

$$\nabla \cdot \boldsymbol{v} = 0 \qquad \text{in } \Omega_f^t, \tag{22b}$$

$$\boldsymbol{v} = \frac{\partial \boldsymbol{d}}{\partial t} \qquad \text{at } \Sigma^t, \tag{22c}$$

$$\boldsymbol{T}_s(\boldsymbol{d})\,\boldsymbol{n} = \boldsymbol{T}_f(\boldsymbol{v}, p)\,\boldsymbol{n} \qquad \text{at } \Sigma^t, \tag{22d}$$

$$\rho_s \frac{\partial^2 \widehat{\boldsymbol{d}}}{\partial t^2} - \nabla \cdot \widehat{\boldsymbol{T}}_s(\widehat{\boldsymbol{d}}) = \boldsymbol{0} \qquad \text{in } \Omega_s, \tag{22e}$$

$$\boldsymbol{d}_f = \boldsymbol{d} \qquad \text{at } \Sigma^t, \tag{22f}$$

together with the boundary conditions (1),(7),(8),(17), and where $\boldsymbol{d}_f$ is the displacement of the fluid domain Ω_f^t at the FS interface and we have used the convenction that $\boldsymbol{n}$ is the structure outward unit normal. The matching conditions (22c)-(22d) enforced at the fluid-solid interface express the *continuity of velocities* (kinematic condition) and the *continuity of normal stresses* (dynamic condition), respectively, whereas condition (22f) guarantees the geometry adherence between the fluid and structure domains (geometric condition). The well-posedness analysis of the coupled problem (22) (supplemented with the relevant boundary conditions) has been carried out under several regularity assumptions. We refer to, e.g., [44, 220, 62, 348], for a comprehensive description of this topic.

For each time $t > 0$, the weak formulation of the FSI problem (22) together with its boundary conditions (for the sake of simplicity, we set $\boldsymbol{v}_{up} = \boldsymbol{0}$ in (7)) reads: Find $(\boldsymbol{v}(t), \widehat{\boldsymbol{d}}(t)) \in \boldsymbol{W}^t = \{(\boldsymbol{w}, \widehat{\boldsymbol{e}}) \in [H^1(\Omega_f^t)]^3 \times [H^1(\Omega_s)]^3 : \ (\boldsymbol{w}, \widehat{\boldsymbol{e}}) = (\boldsymbol{0}, \boldsymbol{0}) \text{ on } \Gamma_{in}^t \times \Gamma_{artif} \text{ and } \boldsymbol{w} = \boldsymbol{e} \text{ on } \Sigma^t\}$, $\boldsymbol{v} = \boldsymbol{v}_0$ for $t = 0$ in Ω_f, $\widehat{\boldsymbol{d}} = \boldsymbol{d}_0$ and $\frac{\partial \widehat{\boldsymbol{d}}}{\partial t} = \boldsymbol{d}_1$ for $t = 0$ in Ω_s, and $p(t) \in L^2(\Omega_f^t)$, such that

$$
\begin{aligned}
&\rho_f \int_{\Omega_f^t} \frac{\partial \boldsymbol{v}}{\partial t} \cdot \boldsymbol{w} \, d\omega + \mathcal{A}_f^t(\boldsymbol{v}, \boldsymbol{v}, \boldsymbol{w}) + \mathcal{B}^t(p, \boldsymbol{w}) + \rho_s \int_{\Omega_s} \frac{\partial^2 \widehat{\boldsymbol{d}}}{\partial t^2} \cdot \widehat{\boldsymbol{e}} \, d\omega + \int_{\Omega_s} \widehat{\boldsymbol{T}}_s \left(\widehat{\boldsymbol{d}} \right) : \nabla \widehat{\boldsymbol{e}} \, d\omega \\
&\quad + \int_{\Gamma_{ext}} \alpha_{ST} \widehat{\boldsymbol{d}} \cdot \widehat{\boldsymbol{e}} \, d\sigma = \int_{\Gamma_{out}^t} \boldsymbol{h}_f \cdot \boldsymbol{n} \, d\gamma + \int_{\Gamma_{ext}} P_{ext} \widehat{\boldsymbol{n}} \cdot \widehat{\boldsymbol{e}} \, d\sigma, \\
&\mathcal{B}^t(q, \boldsymbol{v}) = 0, \\
&\boldsymbol{d}_f = \boldsymbol{d} \qquad \text{at } \Sigma^t,
\end{aligned}
\tag{23}
$$

for all $(\boldsymbol{w}, \widehat{\boldsymbol{e}}) \in \boldsymbol{W}^t$ and $q \in L^2(\Omega_f^t)$. Notice that in the previous weak formulation, the two terms arising after integration by parts and involving the normal Cauchy stresses $\boldsymbol{T}_f \boldsymbol{n}$ and $\boldsymbol{T}_s \boldsymbol{n}$ at the interface Σ^t cancel out, thanks to (22d) and to the special choice of the test functions in $\boldsymbol{W}^t$.

After introducing the following total energy for the FSI problem

$$
\mathcal{E}_{3D}(t) = \frac{\rho_f}{2} \int_{\Omega_f^t} |\boldsymbol{v}|^2 \, d\omega + \int_{\Omega_s} \frac{\rho_s}{2} \left| \dot{\widehat{\boldsymbol{d}}} \right|^2 \, d\omega + \int_{\Omega_s} \Theta(\widehat{\boldsymbol{d}}) \, d\omega + \int_{\Gamma_{ext}} \alpha_{ST} \left| \widehat{\boldsymbol{d}} \right|^2 \, d\gamma, \tag{24}
$$

the following conservation property holds true for the case of homogeneous boundary conditions [183, 189]:

$$
\frac{d}{dt} \mathcal{E}_{3D}(t) + \frac{\mu}{2} \int_{\Omega_f^t} \left(\nabla \boldsymbol{v} + (\nabla \boldsymbol{v})^t \right)^2 d\omega = 0.
$$

When the membrane model (20) is used instead of (22e), the matching conditions (22c)-(22d) are replaced by:

$$
\begin{aligned}
&\boldsymbol{v} \cdot \boldsymbol{n} = \frac{\partial d_r}{\partial t} && \text{at } \Sigma^t, \\
&\boldsymbol{T}_f(\boldsymbol{v}, p) \boldsymbol{n} \cdot \boldsymbol{n} = -f_s && \text{at } \Sigma^t,
\end{aligned}
$$

where d_r is the membrane displacement written in the current configuration and f_s is the forcing term of the membrane equation, see (20), acting only at the FS interface; in this

case it also plays the role of structure stress exerted at the FS interface. Owing to (20) itself, we can rewrite the previous interface conditions as follows:

$$\boldsymbol{v} \cdot \boldsymbol{n} = \frac{\partial d_r}{\partial t} \qquad \text{at } \Sigma^t, \tag{26a}$$

$$\boldsymbol{T}_f(\boldsymbol{v}, p)\boldsymbol{n} \cdot \boldsymbol{n} = -\left(\rho_s H_s \frac{\partial^2 d_r}{\partial t^2} - \nabla \cdot (\boldsymbol{P} \nabla d_r) + \chi H_s d_r\right) \qquad \text{at } \Sigma^t. \tag{26b}$$

Since the coupling only occurs in the radial direction, we have to complete the conditions at Σ^t for the fluid problem in the tangential directions by prescribing further equations on the fluid variables, e.g., homogeneous Dirichlet or Neumann conditions [409].

In [178] an effective formulation to solve the FSI problem with a membrane structure is proposed, whereas in [113] the accuracy of the FSI-membrane problem is discussed in comparison to a full 3D/3D simulation. In particular, for the Hooke law, the wall shear stresses computed with these two FSI models are in good agreement for a distal arterial tract such as a femoropopliteal bypass. Instead, when larger displacements are considered such as in the ascending aorta, the discrepancies between the two FSI models increase.

4.4 The boundary issue

According to the mathematical theory of the incompressible Navier-Stokes equations, three scalar conditions need to be prescribed at each point of the boundary. This however is seldom realistic in clinical practice. For instance, PC-MRI provides velocity data, but this technique is not routinely used and ad-hoc studies are mandatory [383]. Alternatively, the flow rate $Q = Q(t)$ can be obtained across a boundary cross section Γ^t, by proper post-processing of data retrieved by Echo-Cholor-Doppler or by thermal images, see Section 3.2. This yields the flow rate condition (2). In other situations, at both the inlet and outlet cross sections, pressure measurements $P = P(t)$ may be considered as representative of an average estimate, leading to condition (3).

From a mathematical perspective, (2) and (3) are *defective* conditions as they prescribe only one scalar function over the entire section Γ^t [184]. Several strategies have been proposed so far to supplement (2) or (3) with other conditions that allow to "close" the system. For the sake of clarity, we can classify them according to three different strategies, which are reported hereafter.

4.4.1 Conjecturing velocity and pressure profiles

A common trick to effectively prescribe the flow rate condition (2) consists in prescribing a velocity profile

$$\boldsymbol{v}(t) = \boldsymbol{g}(t) \qquad \text{on } \Gamma^t, \tag{27}$$

where $\boldsymbol{g} = \boldsymbol{g}(t, \boldsymbol{x})$ is chosen in such a way to satisfy (2), that is

$$\rho_f \int_{\Gamma^t} \boldsymbol{g}(t) \cdot \boldsymbol{n} \, d\gamma = Q(t). \tag{28}$$

The flow rate condition (2) is therefore replaced by the standard (vectorial) Dirichlet condition (27). A classical choice for $\boldsymbol{g}$ is a parabolic profile (for example for flow simulations in the carotids [82]), a constant profile (often used for the ascending aorta [380]), or that obtained from the Womersley solution [245]. Both the parabolic and Womersley profiles require a circular section to be prescribed on, while non-circular sections require an appropriate morphing [245].

In spite of its straightforward implementation, this choice has a major impact on the solution, in particular in the neighborhood of the section Γ^t and for elevated values of the Reynolds number [562]. To reduce the sensitivity of the results on the arbitrary choice of the profile, the computational domain can be artificially elongated by operating what is called a *flow extension* [381].

A similar approach could be applied to the mean normal Cauchy stress condition (3) as well. In the case at hand, we can postulate that the pressure on Γ^t is constant and that the viscous stress can be neglected, that is we can prescribe

$$p\boldsymbol{n} - \mu \left(\nabla \boldsymbol{v} + (\nabla \boldsymbol{v})^T \right) \boldsymbol{n} = P\boldsymbol{n} \quad \text{on } \Gamma^t. \tag{29}$$

Notice that the previous condition in particular satisfies the defective condition (3). Condition (29) is generally acceptable because the pressure changes in arteries mainly occur along the axial direction and the viscous stresses are negligible on orthogonal cross-sections.

Since $P\boldsymbol{n}$ plays the role of boundary normal Cauchy stress when implemented in the framework of finite element approximations, no further action than just assembling the matrix for Neumann conditions is required. For this reason, this treatment has been given the name of "*do-nothing*" approach [248]. As pointed out in [559, 558], this procedure in fact is not completely "innocent". The do-nothing approach corresponds to the following weak formulation (for the sake of simplicity we assume homogeneous Dirichlet conditions, $\boldsymbol{v}_{up} = \boldsymbol{0}$): Find for each $t > 0$, $\boldsymbol{v} \in \widetilde{\boldsymbol{V}}^t$, $\boldsymbol{v} = \boldsymbol{v}_0$ for $t = 0$ in Ω_f, and $p \in L^2(\Omega_f^t)$ such that

$$\begin{aligned} &\rho_f \int_{\Omega_f^t} \frac{\partial \boldsymbol{v}}{\partial t} \cdot \boldsymbol{w}\, d\omega + \mathcal{A}_f^t(\boldsymbol{v}, \boldsymbol{v}, \boldsymbol{w}) + \mathcal{B}^t(p, \boldsymbol{w}) = \int_{\Gamma_{out}^t} \boldsymbol{h}_f \cdot \boldsymbol{n}\, d\gamma - P \int_{\Gamma^t} \boldsymbol{w} \cdot \boldsymbol{n}\, d\gamma, \\ &\mathcal{B}^t(q, \boldsymbol{v}) = 0, \end{aligned}$$

for all $\boldsymbol{w} \in \widetilde{\boldsymbol{V}}^t = \{[H^1(\Omega_f^t)]^3 : \boldsymbol{w} = \boldsymbol{0} \text{ on } \partial\Omega \setminus \left(\Gamma_{out}^t \cup \Gamma^t\right)\}$ and $q \in L^2(\Omega_f^t)$.

A do-nothing formulation for the flow rate conditions is possible too, see [248, 559].

Notice that, alternatively to (3), other defective conditions involving the fluid pressure could be considered as well. This is the case, for example, of *mean pressure conditions* [248] or conditions involving the total pressure [189], defined by $p_{tot} = p + \frac{\rho_f}{2}|\boldsymbol{v}|^2$. For comprehensive review of these conditions, we refer the interested reader to [482].

4.4.2 Augmented formulation

An alternative approach consists in regarding the flow rate boundary condition (2) as a constraint for the solution of the fluid problem and then enforcing it by a Lagrange multiplier approach. Being a scalar constraint, we need a scalar multiplier $\lambda = \lambda(t)$ at

each time, resulting in the following weak formulation (we consider again the case of homogeneous Dirichlet conditions): Find for each $t > 0$, $\boldsymbol{v} \in \widetilde{\boldsymbol{V}}^t$, $\boldsymbol{v} = \boldsymbol{v}_0$ for $t = 0$ in Ω_f, $p \in L^2(\Omega_f^t)$, and $\lambda \in \mathbb{R}$ such that

$$\begin{aligned} &\rho_f \textstyle\int_{\Omega_f^t} \dfrac{\partial \boldsymbol{v}}{\partial t} \cdot \boldsymbol{w}\, d\omega + \mathcal{A}_f^t(\boldsymbol{v}, \boldsymbol{v}, \boldsymbol{w}) + \mathcal{B}^t(p, \boldsymbol{w}) + \mathcal{C}^t(\lambda, \boldsymbol{w}) = \displaystyle\int_{\Gamma_{out}^t} \boldsymbol{h}_f \cdot \boldsymbol{w}\, d\gamma, \\ &\mathcal{B}^t(q, \boldsymbol{v}) = 0, \\ &\mathcal{C}^t(\psi, \boldsymbol{v}) = \psi\, \frac{Q}{\rho_f}, \end{aligned} \tag{30}$$

for all $\boldsymbol{w} \in \widetilde{\boldsymbol{V}}^t$, $q \in L^2(\Omega_f^t)$, and $\psi \in \mathbb{R}$, and where we have set

$$\mathcal{C}^t(\psi, \boldsymbol{w}) = \psi \int_{\Gamma^t} \boldsymbol{w} \cdot \boldsymbol{n}\, d\gamma,$$

see [184, 561], where the well-posedness of this problem is also analyzed.

Besides prescribing the flow rate condition (2), the previous augmented formulation enforces at each time a constant-in-space normal Cauchy stress on Γ^t aligned with its normal direction, which precisely coincides with the Lagrange multiplier λ, that is

$$-p\boldsymbol{n} + \mu \left(\nabla \boldsymbol{u} + (\nabla \boldsymbol{v})^T \right) \boldsymbol{n} = \lambda \boldsymbol{n} \quad \text{on } \Gamma^t.$$

This method is particularly suited when the artificial cross section is orthogonal to the longitudinal axis, so that vector $\boldsymbol{n}$ is truly aligned along the axial direction.

Since the velocity spatial profile is not prescribed a priori, this technique has been used to improve the parabolic-based law implemented in the Doppler technology for the estimation of the flow rate starting from the peak velocity [457, 568, 458].

The extension of the augmented formulation to the case of compliant walls is addressed in [191] and to the quasi-Newtonian case in [159].

An augmented formulation has been proposed in [184] to prescribe condition (3) as well. However, as noticed in [184], in this case it yields at each time the condition

$$\boldsymbol{v} = \lambda \boldsymbol{n} \quad \text{at } \Gamma^t,$$

where $\lambda = \lambda(t)$ is again the constant-in-space Lagrange multiplier. This is a non-homogeneous Dirichlet boundary condition for the fluid velocity, which is in general incompatible with the no-slip condition $\boldsymbol{v} = \boldsymbol{\phi}$ prescribed at the physical boundary Σ^t. For this reason, this approach is not followed any longer.

4.4.3 A control-based approach

A different strategy for the fulfillment of condition (2) is based on the minimization of the mismatch functional

$$J(\boldsymbol{v}) = \frac{1}{2} \left(\int_{\Gamma^t} \boldsymbol{v} \cdot \boldsymbol{n}\, d\gamma - Q \right)^2, \tag{31}$$

constrained by the fact that $\boldsymbol{v}$ satisfies the incompressible Navier-Stokes equations [190]. This PDE-constrained optimization – which can be regarded as the dual of the previous augmented strategy – yields a system of optimality conditions (also referred to as Karush-Kuhn-Tucker (KKT) system) to be fulfilled, see Sect. 9.1.2 for further details. In particular, in [190] the normal component of the normal Cauchy stress on Γ^t is used as control variable for the minimization of the mismatch functional. This approach has been considered for the compliant case in [191], whereas in [324, 201, 202] the non-Newtonian, quasi-Newtonian, and visco-elastic cases are addressed.

The same approach can also be used to fulfill the defective condition (3) provided that a suitable functional to be minimized is introduced [190]. This allows to prescribe (3) on a section oblique with respect to the longitudinal axis too. In this case the control variable is the complete normal Cauchy stress vector, that is also the direction of the normal Cauchy stress is a priori unknown.
Boundary data may be lacking for the cross sectional of the vessel wall as well. In this case we end up with defective BC issues for the vessel wall, see, e.g. [482].

4.5 Geometric reduced models and multiscale approach

4.5.1 The 1D and 0D models

Numerical modeling of the entire cardiovascular system by means of 3D models is currently not affordable because of the complexity of the computational domain, which is composed by thousands of arteries and veins and billions of arterioles, capillaries, and venules [401]. In many applications, reduced dimensional models are used instead, either as stand-alone models or coupled with the 3D ones.

The first one-dimensional (1D) model was introduced almost 250 years ago by L. Euler [162]. More recently, this approach has been brought into the engineering environment by [38, 265, 267]. These models allow the description of blood flow in a compliant vessel where the only space coordinate is that of the vessel axis.

1D models may be derived from 3D models by making simplifying assumptions on the behavior of the flow, the structure, and their interaction [469, 439]. The starting fluid domain is represented by a truncated cone, see Figure 5. Referring to cylindrical coordinates (r, φ, z), we make the following simplifying assumptions: (i) the axis of the cylinder is fixed; (ii) for any z, the cross section $\mathcal{S}(t, z)$ is a circle with radius $R(t, z)$; (iii) the solution of both fluid and structure problems does not depend on φ; (iv) the pressure is constant over each section $\mathcal{S}(t, z)$; (v) the axial fluid velocity v_z dominates the other velocity components; (vi) only radial displacements are allowed, so that the structure deformation takes the form $\boldsymbol{d} = d\boldsymbol{e}_r$, $\boldsymbol{e}_r$ being the unit vector in the radial direction and $d(t, z) = R(t, z) - R_0(z)$, where $R_0(z)$ is the reference radius at the equilibrium; (vii) the fluid is supposed to obey the Poiseuille law, so that the viscous effects are modeled by a linear term proportional to the flow rate; (viii) the vessel structure is modeled as a membrane with constant thickness.

We introduce the following quantities: $A(t, z) = |\mathcal{S}(t, z)| = \pi R(t, z)^2$ (lumen section area), $\bar{v}(t, z) = A^{-1} \int_{\mathcal{S}(t,z)} v_z(t, z) dS$ (mean velocity), $s(r/R)$ such that $v_z(t, r, z) =$

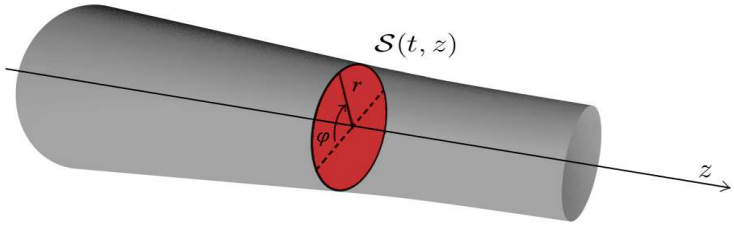

Figure 5: Fluid domain for the derivation of the 1D model

$\bar{v}(t,z)s\,(r/R(t,z))$ (velocity profile), $Q(t,z) = \rho_f \int_{\mathcal{S}(t,z)} v_z\, dS = \rho_f A(t,z)\bar{v}(t,z)$ (flow rate), $P(t,z) = A^{-1} \int_{\mathcal{S}(t,z)} p(t,z)\, dS$ (mean pressure).

As for the structure and its interaction with the fluid, we need to introduce a membrane law, which in fact prescribes a relation between the pressure and the lumen area (which is determined by d_r) of the following form

$$P(t,z) = P_{ext} + \psi(A(t,z), A_0(z), \boldsymbol{\beta}(z)), \tag{32}$$

where ψ is a given function satisfying $\frac{\partial \psi}{\partial A} > 0$, $\psi(A_0) = 0$. Here $\boldsymbol{\beta}$ is a vector of parameters describing the mechanical properties of the membrane.

By integrating over the sections $\mathcal{S}$ the momentum fluid equation (22a) in the $z-$direction and the mass conservation law (22b), we obtain the following system

$$\frac{\partial \boldsymbol{U}}{\partial t} + \mathrm{H}(\boldsymbol{U})\frac{\partial \boldsymbol{U}}{\partial z} + \boldsymbol{B}(\boldsymbol{U}) = \boldsymbol{0} \qquad z \in (0,L),\, t > 0, \tag{33}$$

where $\boldsymbol{U} = [A\ Q]^T$ is the vector of the unknowns, $\alpha = \frac{\int_S u_z^2}{A\bar{v}^2} = \frac{1}{A}\int_0^1 s^2(y)dy$ is the *Coriolis coefficient*, $K_r = -2\pi\mu s'(1)$ is the *friction parameter*, $c_1 = \sqrt{\frac{A}{\rho_f}\frac{\partial \psi}{\partial A}}$, while

$$\mathrm{H}(\boldsymbol{U}) = \begin{bmatrix} 0 & 1 \\ c_1^2 - \alpha\left(\frac{Q}{A}\right)^2 & 2\alpha\frac{Q}{A} \end{bmatrix}, \tag{34a}$$

$$\boldsymbol{B}(\boldsymbol{U}) = \begin{bmatrix} 0 \\ K_r\frac{Q}{A} + \frac{A}{\rho_f}\frac{\partial \psi}{\partial A_0}\frac{\partial A_0}{\partial z} + \frac{A}{\rho_f}\frac{\partial \psi}{\partial \boldsymbol{\beta}}\frac{\partial \boldsymbol{\beta}}{\partial z} \end{bmatrix} \tag{34b}$$

represent the flux matrix and the dissipation vector term, respectively. A complete derivation of the model can be found e.g. in [437, 265, 439]. Classical choices of the velocity profile s are the flat one ($\alpha = 1$) and the parabolic one ($\alpha = 4/3$).

The term $\frac{\partial A_0}{\partial z}$ in $\boldsymbol{B}$ is typically non-positive, accounting for the vessel "tapering", i.e. the reduction of the area of the lumen when proceeding from proximal to distal arteries. The term $\frac{\partial \boldsymbol{\beta}}{\partial z}$ originates from possibly different mechanical properties along the vessel, to describe, for example, the presence of atherosclerotic plaques or vascular prostheses.

If $A > 0$, system (33) has two real distinct eigenvalues (see, e.g., [469])

$$\lambda_{1,2} = \alpha\bar{v} \pm \sqrt{c_1^2 + \bar{v}^2\alpha(\alpha - 1)}, \tag{35}$$

hence it is *strictly hyperbolic* (see e.g. [334]). Under physiological conditions, $c_1 \gg \alpha\bar{v}$, yielding $\lambda_1 > 0$ and $\lambda_2 < 0$, thus we have two waves traveling in opposite directions, that are associated to corresponding characteristic variables. An explicit expression of these variables as a function of the physical variables could be in general derived

$$W_i = \zeta_i(A, Q), \quad i = 1, 2. \tag{36}$$

A simple membrane law (32) can be obtained by the following algebraic relation [185, 189],

$$\psi(A, A_0, \eta) = \eta\frac{\sqrt{A} - \sqrt{A_0}}{A_0}, \quad \text{with} \quad \eta = \frac{\sqrt{\pi}H_s E}{1 - \nu^2}, \tag{37}$$

where ν is the Poisson modulus of the membrane, E its Young modulus , and H_s its thickness, yielding $c_1 = \sqrt{\frac{\eta\sqrt{A}}{2\rho_f A_0}}$. This simple law, stating that the membrane radial displacement d_r is linearly proportional to the fluid pressure, is successfully considered in many applications, see, e.g., [524, 367, 223]. Other laws have been proposed to account for additional features of arterial walls, such as visco-elasticity, wall-inertia, and longitudinal pre-stress [478, 185].

Remark 1. *1D models do not allow one to describe secondary flows, such as vortices or recirculation regions. However, they provide average quantities about the axial component of the velocity, the radial vessel wall displacements, and the pressure of a complex network at computational costs that are orders of magnitude lower than those of the corresponding 3D FSI models [306, 250, 60, 68, 351].*

The accuracy of the solution provided by 1D models is addressed, e.g., in [20, 524, 490], where the numerical results of different networks are successfully compared with clinical measurements, and in [367, 386], where a comparison with in vitro measurements is performed for a complete network of the cardiovascular system.

A further geometrical reduction is represented by the so-called *lumped parameters models*, which are zero-dimensional (0D) models obtained by integrating the 1D problem over the axial direction. These are typically used to describe the peripheral part of the arterial and venous tree, such as the capillaries and the arterioles.

In this case, only dependence on time is allowed and nominal values of the unknowns are used as representative of the entire compartment. To this aim, we introduce the *average* flow rate and pressure in the district at hand, defined respectively as

$$\widehat{Q}(t) = \frac{1}{l}\int_{z_p}^{z_d} Q(t, z)\, dz = \frac{\rho_f}{l}\int_{z_p}^{z_d}\int_{\mathcal{S}(t,z)} v_z(t, z)\, dSdz,$$

$$\widehat{P}(t) = \frac{1}{l}\int_{z_p}^{z_d} P(t, z)dz = \frac{1}{V}\int_{z_p}^{z_d}\int_{\mathcal{S}(t,z)} p(t, z)\, dSdz,$$

where z_p and z_d are the proximal and longitudinal abscissas of the segment, respectively, l its length and V the volume. The convective term is dropped since in the peripheral sites the velocity is small.

If we take the longitudinal average of the momentum equation given by the first of (33) and we combine it with (37), we obtain the following ordinary differential equation (ODE) [439]

$$\frac{\rho_f l}{A_0}\frac{d\widehat{Q}}{dt} + \frac{\rho_f K_R l}{A_0^2}\widehat{Q} + \widehat{P}_d - \widehat{P}_p = 0, \tag{38}$$

where $\widehat{P}_d$ and $\widehat{P}_p$ are the distal and proximal pressure, respectively. When taking the longitudinal average of the mass conservation law given by the second of (33) and using (37), we obtain [439]:

$$\frac{\sqrt{A_0}l}{\eta}\frac{d\widehat{P}}{dt} + \widehat{Q}_d - \widehat{Q}_p = 0, \tag{39}$$

where $\widehat{Q}_d$ and $\widehat{Q}_p$ are the distal and proximal flow rate, respectively.

The two ODE's (38)-(39) can be regarded as the starting point toward a 0D description of a compartment model of an arterial tract. In fact, the term $L\dfrac{d\widehat{Q}}{dt}$, with $L = \dfrac{\rho_f l}{A_0}$, corresponds to the blood acceleration, $R\widehat{Q}$, with $R = \dfrac{\rho_f K_R l}{A_0^2}$, stems from the blood resistance due to the viscosity, while $C\dfrac{d\widehat{P}}{dt}$, with $C = \dfrac{\sqrt{A_0}l}{\eta}$, is due to the compliance of the vessel wall. Usually, an electric analogy is used to easily interpret 0D models. In particular, the flow rate plays the role of the current, whereas the pressure is the potential. Accordingly, the acceleration term is represented by an inductance, the viscosity term by a resistance, and the compliance term by a capacitance.

To close the system (38)-(39) (featuring 4 unknowns) we need to include also the boundary conditions originally prescribed to the 1D model. For instance, we can assume a Dirichlet condition at the inlet and a Neumann condition at the outlet. Thus, we may localize the unknown pressure $\widehat{P}$ at the proximal section, ($\widehat{P} \approx \widehat{P}_p$), assuming that the distal pressure $\widehat{P}_d$ is given. Similarly we assume that the flow rate $\widehat{Q}$ is approximated by $\widehat{Q}_d$ and that the proximal flow rate $\widehat{Q}_p$ is given. Then, from (38)-(39), we obtain

$$\begin{aligned} &\widehat{P} - L\frac{d\widehat{Q}}{dt} - R\widehat{Q} = \widehat{P}_d, \\ &C\frac{d\widehat{P}}{dt} + \widehat{Q} = \widehat{Q}_p, \end{aligned} \tag{40}$$

corresponding to the electrical circuit drawn in Fig. 6. Other sequences corresponding to different boundary conditions and then to different state variables are possible too, see, e.g. [482]. Even though these schemes are equivalent in terms of functionality, they play a different role when coupled with higher dimensional models, see, e.g., [482].

For a description of more complex vascular districts, we may combine several 0D elementary tracts, by gluing them owing to classical continuity arguments. However, the

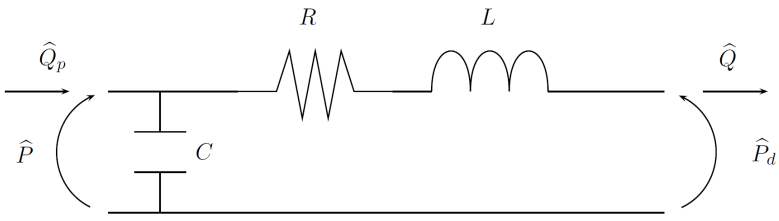

Figure 6: Example of lumped parameter scheme for an arterial tract

lumped parameters models have been mainly used to provide suitable boundary conditions at the distal artificial sections of 3D and 1D models. In this case, one simple compartment is enough to describe the entire arterial system downstream the region of interest. Examples are provided by the *windkessel model* [594], featuring an average resistance and capacitance, the *3-element windkessel* [594], where a second resistance is added before the windkessel compartment, and the *4-element windkessel model* [526, 527], where an inductance element is added to the 3-element windkessel model. A 0D model given simply by a resistance is used to provide absorbing boundary conditions at the outlets of the fluid domain in FSI simulations, see, e.g., [413]. Instead, more sophisticated approaches account for the propagative dynamics associated with the peripheral circulation, such as the *structured tree* model [420], which assumes an asymmetric self-similar structure for the peripheral network.

4.5.2 The geometric multiscale coupling

The geometrical multiscale approach, first introduced in [480], consists in the coupling among 3D, 1D, and 0D models. The idea is to use higher dimensional models in those regions where a description with a great detail is required, and lower dimensional models in the remaining part of the region of interest. This allows one to describe a wide portion of the circulatory system.

As discussed earlier, 0D models are typically used to provide boundary conditions for 3D and 1D models. For this reason, the coupling between 3D or 1D models with an extended 0D network has been rarely considered in applications. Instead, the 3D-1D coupling has received a great deal of attention. For this reason, we detail here only the latter case, while referring to, e.g., [472, 481, 574, 297, 372, 239] for the 3D-0D coupling, and [187, 175] for the 1D-0D coupling.

As reported in Figure 7, we consider a 3D/FSI problem (22) in a 3D cylindrical domain together with initial conditions and boundary conditions at the proximal boundaries and at the external structure.

At the distal boundaries, the 3D problem is coupled with the 1D model (33) written in the domain $z \in [0, L]$, together with initial conditions and a boundary condition at the distal boundary. We name $\Gamma^t = \Gamma^t_f \cup \Gamma^t_s$ the coupling interface from the 3D side, which corresponds to the point $z = 0$ from the 1D side (see Fig. 7).

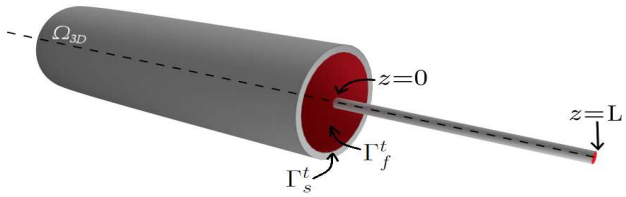

Figure 7: Schematic representation of the reference 3D-1D coupled model

A major mathematical issue is how to couple 3D and 1D models at the common interface. Several strategies can be pursued, yielding to many (alternative) sets of interface conditions. For a rigorous derivation of the 3D-1D problem and a detailed discussion of the interface conditions, we refer the interested reader to the recent review article [482].

Instead, here we follow the guiding principle described in [189], where suitable interface conditions are derived from a global energy estimate. In particular, we introduce, together with the 3D energy (24), the 1D energy [183]

$$\mathcal{E}_{1D}(t) = \frac{\rho_f}{2}\int_0^L A\,\bar{v}^2\,dx + \int_0^L \chi(A)\,dx,$$

where $\chi(A) = \displaystyle\int_{A_0}^{A} \psi(\tau)\,d\tau$, ψ being the vessel law (see (32)), Notice that the stand-alone 1D problem satisfies bounds for this energy functional as proved in [183].

Let $P_{tot} = \psi(A) + \dfrac{\rho_f}{2}\bar{v}^2$ be the total pressure for the 1D model, and $p_{tot} = p + \dfrac{\rho_f}{2}|\boldsymbol{v}|^2$ that of the 3D model. Then, we have the following result [189].

Proposition 1. *For the interface coupling conditions holding at Γ^t let us assume that the following inequality holds*

$$\int_{\Gamma_f^t} \boldsymbol{T}_f(\boldsymbol{v}, p_{tot})\boldsymbol{n}\cdot\boldsymbol{v}\,d\gamma + \int_{\Gamma_s^t} \boldsymbol{T}_s(\boldsymbol{d})\boldsymbol{n}\cdot\dot{\boldsymbol{d}}\,d\gamma + Q|_{z=0}\,P_{tot}|_{z=0} \le 0. \tag{41}$$

Then, for all $t > 0$, the coupled 3D-1D problem (22)-(33) *with homogeneous boundary conditions satisfies the energy decay property*

$$\frac{d}{dt}\left(\mathcal{E}^{3D}(t) + \mathcal{E}^{1D}(t)\right) \le 0.$$

The previous result provides an indication on how to find suitable interface conditions for the 3D-1D coupled problem. In particular, for inequality (41) to be fulfilled it is sufficient that the following interface conditions

$$\rho_f \int_{\Gamma_f^t} \boldsymbol{v}\cdot\boldsymbol{n}\,d\gamma = Q|_{z=0}, \tag{42a}$$

$$\left(\boldsymbol{T}_f(\boldsymbol{v}, p_{tot})\boldsymbol{n}\right)|_{\Gamma_f^t} = -P_{tot}|_{z=0}\boldsymbol{n} \tag{42b}$$

hold for the fluid, together with

$$\boldsymbol{T}_s(\boldsymbol{d})\boldsymbol{n} = \boldsymbol{0} \quad \text{on } \Gamma_s^t \tag{43}$$

for the structure [186, 189]. Similarly, inequality (41) holds if relation (43) is replaced by

$$\begin{aligned} &\boldsymbol{d}\cdot\boldsymbol{n} = \boldsymbol{0} && \text{on } \Gamma_s^t, \\ &(\boldsymbol{T}_s(\boldsymbol{d})\boldsymbol{n})\times\boldsymbol{n} = \boldsymbol{0} && \text{on } \Gamma_s^t. \end{aligned} \tag{44}$$

The interface conditions (42) prescribe the continuity of the flow rate (kinematic condition) and a dynamic condition involving the total pressures. Note that (43) and (44) are in fact independent of the 1D model, resulting in boundary conditions for the 3D structure problems only. This allows a discontinuity to manifest in the displacement between the 3D and the 1D model.

Usually, dynamic interface conditions involving the pressure (instead of the total pressure) are considered in place of (42b), such as

$$\frac{1}{|\Gamma_f^t|}\int_{\Gamma_f^t} \boldsymbol{T}_f(\boldsymbol{v},p)\boldsymbol{n}\,d\gamma = -\psi(A|_{z=0})\boldsymbol{n}. \tag{45}$$

However, the previous condition does not satisfy the compatibility condition (41). More precisely, in this case we have

$$\frac{d}{dt}\left(\mathcal{E}^{3D}(t)+\mathcal{E}^{1D}(t)\right) = \frac{\rho_f}{2}\left(\frac{(Q(t)|_{z=0})^3}{(A(t)|_{z=0})^2} - \int_{\Gamma_f^t}|\boldsymbol{v}(t)|^2\boldsymbol{v}(t)\cdot\boldsymbol{n}\,d\gamma\right).$$

Even though the right hand side is not necessarily (always) negative, numerical evidence indicates that condition (45) leads to stable results for hemodynamic applications, see [351]. This interface condition is indeed the most commonly used among the dynamic ones.

4.6 Numerical strategies

In this section, we comment on the numerical solution of the problems presented in the previous subsections. We do not have the ambition to be exhaustive, due to the problem complexity. Rather, we review some of the methods which are among the most suited in hemodynamics. In particular, for the space discretization, we will focus on Galerkin-type methods, such as Finite Elements, Spectral Elements, and Discontinuous Galerkin methods.

We will use the following notation. Let Δt and h be the time and space discretization parameters. In our examples Δt is assumed to be fixed, but adaptive strategies could be considered as well, see, e.g., [564]. Correspondingly, the discrete time instants are $t^n = n\Delta t$. h is instead defined as usual as a representative value of the mesh size, for example $h = \min_{\mathcal{K}} h_K$, where $\mathcal{K}$ are the tetrahedra of the mesh and h_K the radius of the sphere inscribed in $\mathcal{K}$. Given the functions $w(t)$ and $z(\boldsymbol{x})$, we denote by w^n the approximation of $w(t^n)$ and by $z_h(\boldsymbol{x})$ the Galerkin approximation of $z(\boldsymbol{x})$.

4.6.1 Numerical methods for the fluid problem

We start to review some numerical methods for the fluid problem (4) together with its initial and boundary conditions.

As for the time discretization, usually implicit methods with a semi-implicit treatment of the convective term and (in case of moving domain) of the fluid domain are considered. The problem is solved at the discrete time t^{n+1} in the domain Ω_f^* and with convective term $\rho_f(\boldsymbol{v}^* \cdot \nabla)\boldsymbol{v}^{n+1}$, where Ω_f^* and $\boldsymbol{v}^*$ are suitable extrapolations of Ω_f^{n+1} and $\boldsymbol{v}^{n+1}$ of the same order of the time discretization. This choice introduces a CFL-like restriction on the time step to preserve absolute stability [479]. However, this condition is very mild in hemodynamic applications, since, for accuracy purposes, the pulsatility of the blood signal and the quick dynamics around systole can only be accommodated by choosing a small Δt. Usually, a second order approximation is considered a good choice in hemodynamics; in this respect, BDF2 and Crank-Nicolson are the mostly used methods [475].

The first class of methods we present is based on a decomposition of the semi-discrete problem at the spatial continuous level (*differential splitting* or *projection* methods). The basic idea underlying these methods is to split the computation of velocity and pressure, with a final step aiming at recovering the incompressibility constraint. We detail in what follows the Chorin-Teman method [104, 543], originally proposed for homogeneous Dirichlet conditions and fixed domain, which is the progenitor of these methods. We only detail the case of the Backward Euler discretization.

Chorin Temam method. For $n \geq 0$, at time t^{n+1}

1. solve in Ω_f the advection-reaction-diffusion problem with homogeneous Dirichlet condition for the intermediate unknown velocity $\widetilde{\boldsymbol{v}}^{n+1}$

$$\rho_f \frac{\widetilde{\boldsymbol{v}}^{n+1} - \boldsymbol{v}^n}{\Delta t} - \mu \left(\nabla \widetilde{\boldsymbol{v}}^{n+1} + \left(\nabla \widetilde{\boldsymbol{v}}^{n+1} \right)^T \right) + \rho_f (\boldsymbol{v}^n \cdot \nabla) \widetilde{\boldsymbol{v}}^{n+1} = \boldsymbol{0};$$

2. solve in Ω_f the pressure problem with homogeneous Neumann conditions

$$\triangle p^{n+1} = \frac{\rho_f}{\Delta t} \nabla \cdot \widetilde{\boldsymbol{v}}^{n+1};$$

3. correct the velocity

$$\boldsymbol{v}^{n+1} = \widetilde{\boldsymbol{v}}^{n+1} - \frac{\Delta t}{\rho_f} \nabla p^{n+1}.$$

This splitting method is based on the *Ladhyzhenskaja theorem* [214], stating that a vector function belonging to $[L^2(\Omega_f)]^3$ can be always decomposed as the sum of a solenoidal part and of a gradient term. In fact, the correction step corresponds to project the intermediate velocity onto $\boldsymbol{H} = \{\boldsymbol{w} \in [L^2(\Omega_f)]^3 : \nabla \cdot \boldsymbol{w} = 0, \boldsymbol{w} \cdot \boldsymbol{n}|_{\partial\Omega_f} = 0\}$. Thus, it is possible to show that $\boldsymbol{v}^{n+1}$ and p^{n+1} are in fact solution of the original semi-discrete problem. The Chorin-Temam method is very effective since it overcomes the saddle-point nature of the problem and solve two standard uncoupled elliptic problems. However, it suffers from

inaccuracies at the boundary. In particular, the tangential velocity cannot be controlled (see the definition of $\boldsymbol{H}$) and spurious pressure values appear as a consequence of the artificial Neumann condition for the pressure problem [485]. This has an effect on the accuracy of the semi-discrete solution, in particular the following error estimate holds true [485]:

$$\|\boldsymbol{v}(t^n,\boldsymbol{x})-\boldsymbol{v}^n(\boldsymbol{x})\|_{[H^1]^3}+\|p(t^n,\boldsymbol{x})-p^n(\boldsymbol{x})\|_{L^2}\lesssim\sqrt{\Delta t}.$$

The use of higher order time approximations leads to the same accuracy.

An improvement of the previous method is given by the *rotational incremental* variant of the Chorin-Temam scheme [545]. We detail in what follows the case of BDF2 and second order extrapolation of the convective term, since the first order approximation does not lead to any improvement.

Rotational-incremental Chorin-Temam method. For $n\geq 0$, at time t^{n+1}

1. solve in Ω_f the advection-reaction-diffusion problem with homogeneous Dirichlet condition in the intermediate unknown velocity $\widetilde{\boldsymbol{v}}^{n+1}$:

$$\rho_f\frac{3\widetilde{\boldsymbol{v}}^{n+1}-4\boldsymbol{v}^n+\boldsymbol{v}^{n-1}}{2\Delta t}-\mu\left(\nabla\widetilde{\boldsymbol{v}}^{n+1}+\left(\nabla\widetilde{\boldsymbol{v}}^{n+1}\right)^T\right)+\rho_f((2\boldsymbol{v}^n-\boldsymbol{v}^{n-1})\cdot\nabla)\widetilde{\boldsymbol{v}}^{n+1}+\nabla p^n=\boldsymbol{0};$$

2. solve the pressure problem

$$\begin{aligned}\triangle p^{n+1}&=\triangle p^n+\left(\frac{3\rho_f}{2\Delta t}-\mu\right)\nabla\cdot\widetilde{\boldsymbol{v}}^{n+1} && \boldsymbol{x}\in\Omega_f,\\ \frac{\partial p^{n+1}}{\partial\boldsymbol{n}}&=\mu\left(\nabla\times\nabla\times\widetilde{\boldsymbol{v}}^{n+1}\right)\cdot\boldsymbol{n} && \boldsymbol{x}\in\partial\Omega_f,\end{aligned}$$

3. correct the velocity

$$\boldsymbol{v}^{n+1}=\widetilde{\boldsymbol{v}}^{n+1}-\frac{2}{3}\frac{\Delta t}{\rho_f}\nabla\left(p^{n+1}-p^n+\mu\nabla\cdot\widetilde{\boldsymbol{v}}^{n+1}\right).$$

Unlike the classical Chorin-Temam scheme, in the previous method the boundary conditions for the pressure problem are consistent and no numerical boundary layer for the pressure is observed. This is confirmed by the improved error estimate [232]

$$\|\boldsymbol{v}(t^n,\boldsymbol{x})-\boldsymbol{v}^n(\boldsymbol{x})\|_{[H^1]^3}+\|p(t^n,\boldsymbol{x})-p^n(\boldsymbol{x})\|_{L^2}\lesssim\Delta t^{3/2}.$$

The previous two methods belong to the general class of *pressure-correction* methods, see also, e.g., [111, 229, 230]. A different class is obtained by switching the role of velocity and pressure in the splitting, i.e. the viscous term is now ignored or treated explicitly in the first step and the velocity is then corrected accordingly (*velocity-correction* schemes, [421, 285]). These schemes feature the same non-optimal error estimates of the pressure-correction schemes due to artificial Neumann conditions for the pressure problem. Again, an improvement could be obtained by considering a rotational-incremental variant [231].

In hemodynamics it is often the case that Neumann boundary conditions are prescribed at some artificial section. The extension of the differential splitting methods to this case is addressed in [228]: on the Neumann boundary we have an artificial Dirichlet condition for the pressure, which again deteriorates the optimal rate of convergence with respect to Δt.

In view of the next methods we are going to review, it is convenient to introduce the algebraic problem arising from the application of a Galerkin-like method to the semi-discrete-in-time problem. First of all we notice that the solvability of the discretized-in-space problem is guaranteed by a suitable compatible choice of the approximation spaces for the velocity and the pressure in order to satisfy the discrete *inf-sup stability condition* [479]. As it is well known, an example for Finite Elements (FE) for a tetrahedral mesh is provided by piecewise polynomials of order 2 for the velocity approximation and of order 1 for the pressure approximation. This choice guarantees the existence and uniqueness of the solution to the linearized fully discrete problem and are often used to provide a stable solution in hemodynamics. In this case, we have the following optimal error estimate

$$\|\boldsymbol{v}^n(\boldsymbol{x}) - \boldsymbol{v}_h^n(\boldsymbol{x})\|_{[H^1]^3} + \|p^n(\boldsymbol{x}) - p_h^n(\boldsymbol{x})\|_{L^2} \lesssim h^2,$$

provided that $\boldsymbol{v}^n$ and p^n are regular enough. (For other stable choices see [479, 64]). Alternatively, suitable stabilization terms could be added to the problem, circumventing the inf-sup condition and allowing the use of polynomials of equal order. In this case, additional terms are added to the mass conservation equation and, in case, to the momentum conservation equation. Usually, these techniques allow one to stabilize also convected-dominated problems arising when the Reynolds number is high, for example in aorta or in stenotic carotids. One technique is *Streamline Upwind-Petrov Galerkin* (SUPG) [385]. A generalization of SUPG is the *variational multiscale* (VMS) method [266, 268], which is based on the decomposition of the unknown into two terms, one accounting for the large scales and another one for the small scales. The same decomposition is used for the test functions, so that a system of two coupled problems is obtained. VMS is also useful since it allows one to model the transitional to turbulence effects which may occur in some pathological conditions such as stenoses [3]. For an application to hemodynamics, see [195].

We introduce in what follows the algebraic problem related to the fully discretized linearized problem. For the sake of exposition, we limit ourselves to the cases without stabilization terms. We refer the interested reader to, e.g., [154, 48] for the more general case. At each time step we have

$$\begin{bmatrix} A & B^T \\ B & 0 \end{bmatrix} \begin{bmatrix} \boldsymbol{V} \\ \boldsymbol{P} \end{bmatrix} = \begin{bmatrix} \boldsymbol{F}_f \\ \boldsymbol{0} \end{bmatrix},$$

where $\boldsymbol{V}$ and $\boldsymbol{P}$ are the vectors collecting the velocity and pressure unknowns, $A = \rho_f \frac{\alpha}{\Delta t} M_f + \rho_f N(\boldsymbol{V}^*) + \mu K$ (with M_f the mass matrix, N the matrix related to the linearized convective term, K the stiffness matrix), $\boldsymbol{F}_f$ accounts for non-homogeneous Dirichlet and Neumann conditions and the terms coming from time discretization, α depends on the time discretization scheme, and where we have omitted the current temporal index $^{n+1}$.

The previous non-symmetric linear system can be solved by a Krylov method, e.g. by the GMRES method. Suitable preconditioners are mandatory. A classical choice is given by block-preconditioners which again split in fact the solution of the velocity and of the pressure, e.g.

$$P = \begin{bmatrix} P_A & B^T \\ 0 & -P_\Sigma \end{bmatrix}.$$

If $P_A = A$ and $P_\Sigma = \Sigma = BA^{-1}B^T$ (*Schur complement*), then the solution is achieved in three GMRES iterations [154]. In fact, this choice is equivalent to formally solve the momentum equation for the velocity and to substitute its expression in the mass equation. However, in practice this preconditioner is not efficient, since the linear system involving the Schur complement is too onerous, Σ being a full matrix whose explicit construction requires the knowledge of A^{-1}. Efficient preconditioners can be obtained by approximating Σ (and, in case, A). For low Reynolds numbers (say, less than 10), an effective choice is given by $P_\Sigma = \frac{1}{\mu}M_P$, where M_P is the pressure mass matrix (or even its diagonal) [155]. Thus, this is a good choice in hemodynamics for small vessels. For increasing Reynolds numbers, the convergence properties of this preconditioner deteriorates since it does not account for the convective term. A better choice for medium and large vessels is given by $P_\Sigma = A_P F_P^{-1} M_P$, where A_P is the pressure stiffness matrix and $F_P = \mu A_P + \rho_f N_P(\boldsymbol{V}^*)$, N_P being the matrix related to the convective term defined on the pressure space (*pressure convection-diffusion* preconditioner, [154, 48]). As for the solution of the velocity problem, suitable preconditioners for the advection-reaction-diffusion problem could be introduced. Alternatively, fast solutions such as V-cycle multigrid can be considered as well [553].

Another class of preconditioners is obtained by an inexact block LU factorization of the fluid matrix. The starting point is the exact factorization

$$\begin{bmatrix} A & B^T \\ B & 0 \end{bmatrix} = \begin{bmatrix} A & 0 \\ B & -\Sigma \end{bmatrix} \begin{bmatrix} I & A^{-1}B^T \\ 0 & I \end{bmatrix}.$$

Again, different preconditioners are obtained by suitable approximations $\widehat{A}_1$ and $\widehat{A}_2$ of A and $\widehat{\Sigma}$ of Σ, leading to

$$P = \begin{bmatrix} \widehat{A}_1 & 0 \\ B & -\widehat{\Sigma} \end{bmatrix} \begin{bmatrix} I & \widehat{A}_2^{-1}B^T \\ 0 & I \end{bmatrix}.$$

A convenient choice is $\widehat{A}_1 = \widehat{A}_2 = D_A$ and $\widehat{\Sigma} = BD_A^{-1}B^T$, where D_A is the diagonal of A (*SIMPLE* preconditioner, [432, 335]). Notice that in this case $\widehat{\Sigma}$ is sparse and could be explicitly assembled. This is an effective choice when the fluid matrix is diagonally dominant, i.e. when small values of Δt are used. Another choice is *Yosida* preconditioner, where $\widehat{\Sigma} = \frac{\Delta t}{\rho_f \alpha} B M_f^{-1} B^T$, $\widehat{A}_1 = A$ and $\widehat{A}_2 = \frac{\rho_f \alpha}{\Delta t} M_f$ [560]. Again, the efficiency deteriorates for increasing Δt. The Yosida preconditioner had been originally introduced as a solver in [477, 476]. This lead to a splitting of the velocity and of the pressure computation, which could be seen as the algebraic counterpart of the Chorin-Temam method (*algebraic pressure-correction* methods). In particular, we have the following steps:

1. $A\widetilde{\boldsymbol{V}} = \boldsymbol{F}_f$ (computation of the velocity);

2. $\Delta t B M_f^{-1} B^T \boldsymbol{P} = B\widetilde{\boldsymbol{V}}$ (computation of the pressure);

3. $\boldsymbol{V} = \widetilde{\boldsymbol{V}} - \frac{\Delta t}{\rho_f \alpha} M_f^{-1} B^T \boldsymbol{P}$ (correction of the velocity).

Again, an incremental version of the algebraic pressure-correction methods could be considered as well [477]. An extension to spectral methods is provided in [209].

For a recent comparison of the performance of different preconditioners (all described above) used for hemodynamic applications, see [139].

In healthy conditions, blood flow is mainly laminar. Transitional flow may develop in some pathological instances, or under the assistance of devices. In these circumstances, suitable mesh refinement, possibly accompanied by the use of turbulence models, are often employed. We mention the case of stenotic carotids, where Reynolds-average Navier Stokes (RANS) models are used in [529, 224], *Direct Numerical Simulations (DNS)* in [326, 180, 99], and *Large Eddy Simulations (LES)* in [487, 316]. In [41] the VMS formulation is used to describe transitional effect in the ascending aorta under the effect of the Left Ventricular Assist Device (LVAD).

In Figure 8 we report some examples of numerical results obtained in four real geometries reconstructed from radiological images (see the caption for details). These results highlight the complex pattern of blood flow induced by the geometry and by the heart pulsatility. To highlight the transitional effects in stenotic carotids, we plotted in one of the figures the Q criterion, defined as

$$Q = -\frac{1}{2} \sum_{i,j} S_{ij}^2 - \Omega_{ij}^2,$$

where $\boldsymbol{S} = \nabla \boldsymbol{u} + (\nabla \boldsymbol{u})^T$ and $\boldsymbol{\Omega} = \nabla \boldsymbol{u} - (\nabla \boldsymbol{u})^T$ [326]. Positive values of Q indicate locations where rotations dominates strain and shear.

4.6.2 Numerical methods for the vessel wall problem

In this section we review some of the most commonly used numerical approaches for the solution of problem (10), endowed with its initial and boundary conditions.

As for the time discretization, a popular family of schemes is *Newmark*'s, which is characterized by two parameters θ and ζ [399]. The special combination $\theta = 1/2$ and $\zeta = 1/4$ yields the following semi-discrete form of (19) (set $P_{ext} = 0$ and $\boldsymbol{h}_s = \boldsymbol{0}$ for the sake of simplicity):

$$\begin{aligned} \rho_s \int_{\Omega_s} \frac{4\widehat{\boldsymbol{d}}^{n+1} - 4\widehat{\boldsymbol{d}}^{n}}{\Delta t^2} \cdot \widehat{\boldsymbol{e}}\, d\omega + \int_{\Omega_s} \widehat{\boldsymbol{T}}_s \left(\widehat{\boldsymbol{d}}^{n+1}\right) : \nabla \widehat{\boldsymbol{e}}\, d\omega + \int_{\Gamma_{ext}} \alpha_{ST} \widehat{\boldsymbol{d}}^{n+1} \cdot \widehat{\boldsymbol{e}}\, d\sigma \\ = \rho_s \int_{\Omega_s} \left(\frac{4\widehat{\boldsymbol{w}}^n}{\Delta t} + \widehat{\boldsymbol{a}}^n \right) \cdot \widehat{\boldsymbol{e}}\, d\omega, \end{aligned} \tag{46}$$

$$\widehat{\boldsymbol{w}}^{n+1} = \frac{2}{\Delta t} \left(\widehat{\boldsymbol{d}}^{n+1} - \widehat{\boldsymbol{d}}^{n} \right) - \widehat{\boldsymbol{w}}^n, \quad \widehat{\boldsymbol{a}}^{n+1} = \frac{4}{\Delta t^2} \left(\widehat{\boldsymbol{d}}^{n+1} - \widehat{\boldsymbol{d}}^{n} \right) - \frac{4}{\Delta t} \widehat{\boldsymbol{w}}^n - \widehat{\boldsymbol{a}}^n,$$

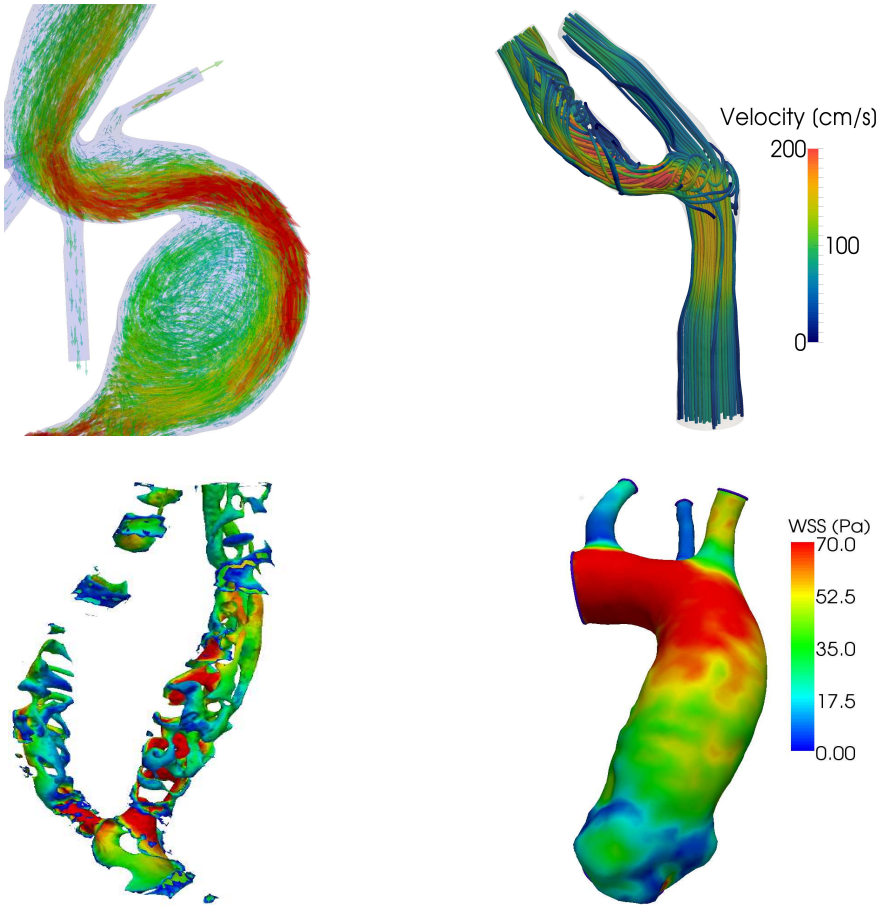

Figure 8: Top left: velocity vectors in the aneurysm of an abdominal aorta (CT images from the Vascular-surgery and Radiology Divisions at Fondazione IRCSS Cà Granda, Ospedale Maggiore Policlinico, Milan, Italy). Top right: velocity streamlines in a stenotic carotid (MRI images from the Vascular-surgery and Radiology Divisions at Ospedale Maggiore Policlinico, Milan). Bottom left: coherent vortical structures by Q criterion in a stenotic carotid (we report only the regions with $Q > 50000$ painted by the velocity magnitude, CT images from the Vascular-surgery and Radiology Divisions at Ospedale Maggiore Policlinico, Milan). Bottom right: wall shear stress in an ascending aorta (MRI images from the Cardio-surgery and Radiology Divisions at Ospedale Borgo Trento, Verona, Italy). These numerical results are obtained using the finite element library *LifeV*, $P2/P1$ Finite Elements , the backward Euler scheme for the time discretization with a semi-implicit treatment of the nonlinear term, and the Yosida preconditioner. For the stenotic carotids a LES model has been used

where $\widehat{\boldsymbol{w}}^{n+1}$ and $\widehat{\boldsymbol{a}}^{n+1}$ represent approximations of vessel wall velocity and acceleration, respectively. This method is unconditionally absolutely stable and second order accurate with respect to Δt. An extension of Newmark schemes is provided by the *generalized-alpha* method [105], see, e.g., [277] for an application to hemodynamics.

Space discretization is typically based on Finite Elements. Whatever the implicit temporal scheme chosen, a system of non-linear algebraic equations is obtained after space and time discretization, reading

$$\frac{\rho_s \beta}{\Delta t^2} M_s \boldsymbol{D} + \boldsymbol{\Gamma}(\boldsymbol{D}) + \alpha_{ST} M_s^{ext} \boldsymbol{D} = \boldsymbol{G}_s,$$

where β depends on the time discretization (e.g., $\beta = 4$ for the Newmark method (46)), $\boldsymbol{D}$ is the vector collecting the vessel wall displacement unknowns, M_s is the mass matrix, M_s^{ext} the boundary mass matrix related to Σ_{ext}, $\boldsymbol{\Gamma}$ is the non-linear operator defined by $\Gamma_i = \int_{\Omega_s} \widehat{\boldsymbol{T}}_s \left(\widehat{\boldsymbol{d}}\right) : \nabla \widehat{\boldsymbol{e}}_i \, d\omega$, $\widehat{\boldsymbol{e}}_i$ being the $i-th$ basis function, and $\boldsymbol{G}_s$ the vector related to the right hand side of the discretized-in-time equation. Notice that we have suppressed the temporal index that is understood. The previous system is linearized by means of the Newton method, obtaining at each time step a sequence of linear systems of the form

$$\left(\frac{\rho_s \beta}{\Delta t^2} M_s + T\left(\boldsymbol{D}_{(k-1)}\right) + \alpha_{ST} M_s^{ext}\right) \delta \boldsymbol{D}_{(k)} = \\ \boldsymbol{G}_s - \frac{\rho_s \beta}{\Delta t^2} M_s \boldsymbol{D}_{(k-1)} - \boldsymbol{\Gamma}\left(\boldsymbol{D}_{(k-1)}\right) - \alpha_{ST} M_s^{ext} \boldsymbol{D}_{(k-1)},$$

with $k \geq 1$ the Newton iterations index, to be solved until convergence. Here $\delta \boldsymbol{D}_{(k)} = \left(\boldsymbol{D}_{(k)} - \boldsymbol{D}_{(k-1)}\right)$, T is the matrix related to the linearization of the first Piola-Kirchhoff tensor, i.e. $(T)_{ij} = \int_{\Omega_s} \left(D_F \widehat{\boldsymbol{T}}_s \left(\widehat{\boldsymbol{d}}_{(k-1)}\right) : \nabla \widehat{\boldsymbol{e}}_j\right) : \nabla \widehat{\boldsymbol{e}}_i$, D_F being the Gâteaux derivative with respect to $\boldsymbol{F}$.

For the solution of the previous linear system, Domain Decomposition (DD) methods are often used as efficient preconditioners for iterative Krylov methods. Since matrix T is symmetric, the Coniugate Gradient method is usually considered for iterations. Among DD preconditioners, *FETI* methods [168] are very often used in structural mechanics. In particular, *all floating* FETI methods have been considered for vessel wall problems, e.g., in [17]. Like in classical FETI methods, Lagrange multipliers are introduced to glue the solution at the subdomain interfaces. In addition, Lagrange multipliers are also used to prescribe Dirichlet boundary conditions. This simplifies the implementation of FETI method since all the subdomains are treated in the same way. A variant successfully used for arterial vessel walls is the so-called *Dual-Primal FETI* method, see, e.g., [31]. Finally, we mention as yet another class of DD methods considered for this problem: a two-level overlapping Schwarz method with an energy minimization coarse space, see [145].

In Figure 9 we report a coupled of examples of numerical results obtained in real geometries reconstructed from radiological images (see the caption for details). These results highlight the anisotropic internal stresses characterizing vascular vessel walls.

4.6.3 Numerical methods for the fluid-structure interaction problem

The numerical solution of the coupled FSI problem (22) requires to manage three sources of non-linearities, i.e.:

i) the fluid domain is unknown (*geometric non-linearity*);

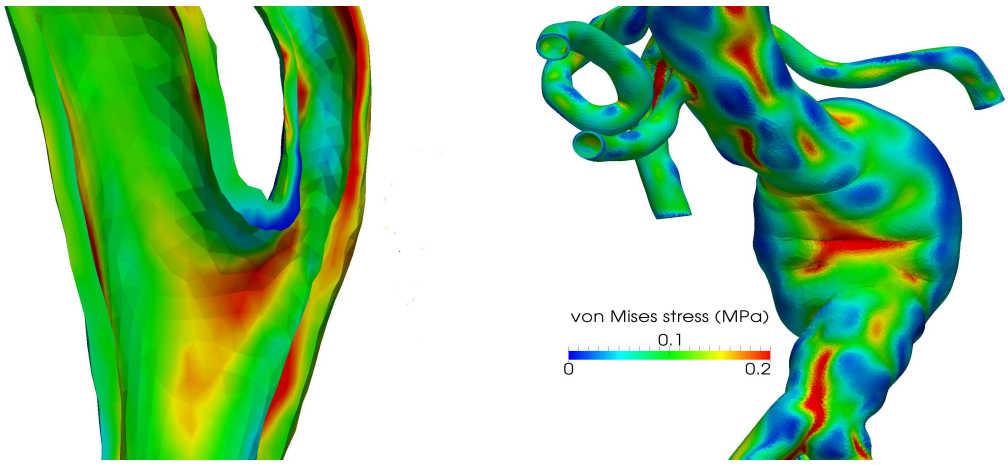

Figure 9: Left: von Mises internal stresses in a carotid (MRI images from the Vascular-surgery and Radiology Divisions at Ospedale Maggiore Policlinico, Milan, Italy). Right: von Mises stresses in an abdominal aortic aneurysm (right, mesh from http://www.vascularmodel.com/sandbox/doku.php?id=start). These numerical results are obtained using *LifeV* (carotid) and the Finite Element library *redbKIT v2.1* (github.com/redbKIT/redbKIT/releases) (AAA), $P2$ Finite Elements, a Newmark unconditionally stable scheme for the time discretization and an exponential vessel wall law

ii) the fluid subproblem is non-linear (*fluid constitutive non-linearity*);

iii) the vessel displacement subproblem is non-linear (*structure constitutive non-linearity*), together with two different kinds of coupling, i.e.:

iv) the displacement of the fluid domain at the FS interface needs to match the vessel wall one (*geometric adherence*, see condition (22f));

v) the fluid and vessel displacement subproblems are coupled by means of the kinematic and dynamic conditions (22c)-(22d) (*physical coupling*).

Arbitrary-Lagrangian formulation. As for points i) and iv), a classical numerical strategy relies on extending the FS interface displacement $\boldsymbol{d}_f = \boldsymbol{d}|_{\Sigma^t}$ in the whole fluid domain, thus associating a displacement also to its internal points. This is obtained by solving an extra problem for the fluid mesh displacement, usually an harmonic extension of the FS interface datum $\boldsymbol{d}_f$, with homogeneous Dirichlet conditions at $\partial\Omega_f^t \setminus \Sigma^t$. The fluid domain displacement is then used to move the points of the fluid mesh accordingly, obtaining the new computational fluid domain. With this aim, the Navier-Stokes equations are reformulated on a frame of reference which moves with the fluid mesh. This is neither a Lagrangian description (where the frame moves with the fluid particles) nor an Eulerian description (where a fixed frame would be used). For this reason, it is called *Arbitrary Lagrangian-Eulerian* (ALE) approach [253, 148]. To write the Navier-Stokes equations in ALE configuration, the Reynolds transport formula to express the ALE material time

derivative $\frac{\delta}{\delta t}$ of a function $\boldsymbol{z}$ with respect to the Eulerian one is used, i.e.

$$\frac{\delta \boldsymbol{z}}{\delta t} = \frac{\partial \boldsymbol{z}}{\partial t} + (\boldsymbol{v}_f \cdot \nabla)\boldsymbol{z},$$

$\boldsymbol{v}_f = \dot{\boldsymbol{d}}_f$ being the velocity of the points of the fluid mesh. Thus, the FSI problem together with its initial and boundary conditions becomes:

$$\rho_f \left(\frac{\delta \boldsymbol{v}}{\delta t} + ((\boldsymbol{v} - \boldsymbol{v}_f) \cdot \nabla)\boldsymbol{v} \right) - \nabla \cdot \boldsymbol{T}_f(\boldsymbol{v}, p) = \boldsymbol{0} \qquad \text{in } \Omega_f^t, \tag{47a}$$

$$\nabla \cdot \boldsymbol{v} = 0 \qquad \text{in } \Omega_f^t, \tag{47b}$$

$$\boldsymbol{v} = \frac{\partial \boldsymbol{d}}{\partial t} \qquad \text{on } \Sigma^t, \tag{47c}$$

$$\boldsymbol{T}_s(\boldsymbol{d})\boldsymbol{n} = \boldsymbol{T}_f(\boldsymbol{v}, p)\boldsymbol{n} \qquad \text{on } \Sigma^t, \tag{47d}$$

$$\rho_s \frac{\partial^2 \widehat{\boldsymbol{d}}}{\partial t^2} - \nabla \cdot \widehat{\boldsymbol{T}}_s \left(\widehat{\boldsymbol{d}} \right) = \boldsymbol{0} \qquad \text{in } \Omega_s, \tag{47e}$$

$$\widehat{\boldsymbol{d}}_f = \widehat{\boldsymbol{d}} \qquad \text{on } \Sigma, \tag{47f}$$

$$-\triangle \widehat{\boldsymbol{d}}_f = \boldsymbol{0} \qquad \text{in } \Omega_f. \tag{47g}$$

This choice is particularly suited when Finite Elements are considered for the space discretization. Indeed, the terms involving spatial derivatives are as usual expressed with respect to the current configuration, whereas the (material) time derivative term is written in the reference configuration. In particular, given the nodal basis functions $\boldsymbol{\phi}_j$, we have

$$\frac{\delta(\boldsymbol{v}_h(t, \boldsymbol{x}))}{\delta t} = \frac{\delta}{\delta t} \left(\sum_j v_h^j(t) \boldsymbol{\phi}_j(\boldsymbol{x}(t)) \right) = \sum_j \frac{dv_h^j(t)}{dt} \boldsymbol{\phi}_j(\boldsymbol{x}(t)),$$

since the time variations of the basis functions with respect to the reference domain vanish. This makes the computation of the fluid velocity on the nodes of the fluid mesh easy, see e.g. [409].

For time discretization of (47), a common choice is to discretize the fluid and the vessel wall problems with two schemes of equal order (let us say of order p), e.g., BDF2 or Crank-Nicolson for the fluid and the Newmark scheme (46) for the vessel problem.

Treatment of geometric coupling, geometric adherence, and fluid non-linearity. As for issue ii) above (constitutive fluid non-linearity), following the approach commonly used for a stand-alone fluid problem, the convective field is usually treated explicitly, by using a suitable extrapolation $\boldsymbol{v}^* - \boldsymbol{v}_f^*$ of order p from previous time steps. This choice introduces a CFL-like condition for Δt to preserve absolute stability, which however is always satisfied for the values of Δt usually considered in hemodynamics. Another common choice in hemodynamics is the explicit treatment of the geometric coupling and adherence (issues i) and iv) above). In particular, the fluid problem coupled with the structure one is solved in a domain Ω_f^* obtained by a suitable extrapolation from previous time steps

of order p and the fluid geometry problem is then solved in sequence [536, 174, 26, 413]. Again, a limitation on Δt is required to ensure absolute stability. In particular, in [174] it is proven for a model problem that stability is guaranteed under a CFL-like condition. Numerical evidence in real scenarios highlighted that also this is a mild condition in the hemodynamics regime, see, e.g. [380, 411]. Based on the considerations above, the following temporal discretization of the FSI problem (47) can be considered:

Explicit scheme for the geometric coupling and adherence. For $n \geq 1$, at time step t^n:

1. solve the FSI problem:

$$\frac{\rho_f \alpha}{\Delta t}\boldsymbol{v}^n + \rho_f((\boldsymbol{v}^* - \boldsymbol{v}_f^*)\cdot\nabla)\boldsymbol{v}^n - \nabla\cdot\boldsymbol{T}_f\left(\boldsymbol{v}^n, p^n\right) = \boldsymbol{g}_f^n \qquad \text{in } \Omega_f^*, \tag{48a}$$

$$\nabla\cdot\boldsymbol{v}^n = 0 \qquad \text{in } \Omega_f^*, \tag{48b}$$

$$\boldsymbol{v}^n = \frac{\alpha}{\Delta t}\boldsymbol{d}^n + \boldsymbol{g}_{fs}^n \qquad \text{on } \Sigma^*, \tag{48c}$$

$$\boldsymbol{T}_s\left(\boldsymbol{d}^n\right)\boldsymbol{n}^* = \boldsymbol{T}_f\left(\boldsymbol{v}^n, p^n\right)\boldsymbol{n}^* \qquad \text{on } \Sigma^*, \tag{48d}$$

$$\frac{\rho_s \beta}{\Delta t^2}\widehat{\boldsymbol{d}}^n - \nabla\cdot\widehat{\boldsymbol{T}}_s\left(\widehat{\boldsymbol{d}}^n\right) = \widehat{\boldsymbol{g}}_s^n \qquad \text{in } \Omega_s, \tag{48e}$$

   where α still depends on the time discretization scheme and $\boldsymbol{g}_f^n = \boldsymbol{g}_f^n(\boldsymbol{v}^{n-1}, \boldsymbol{v}^{n-2}, ...)$, $\boldsymbol{g}_s^n = \boldsymbol{g}_s^n(\boldsymbol{d}^{n-1}, \boldsymbol{d}^{n-2}, ...)$, and $\boldsymbol{g}_{fs}^n = \boldsymbol{g}_{fs}^n(\boldsymbol{d}^{n-1}, \boldsymbol{d}^{n-2}, ...)$ account for the terms at previous time steps coming from time discretizations of order p of the corresponding equations (47a),(47e), and (47c), respectively;

2. then, solve the fluid geometry problem:

$$-\triangle\widehat{\boldsymbol{d}}_f^n = \boldsymbol{0} \qquad \text{in } \Omega_f, \tag{49a}$$

$$\widehat{\boldsymbol{d}}_f^n = \widehat{\boldsymbol{d}}^n \qquad \text{on } \Sigma, \tag{49b}$$

   and then build Ω_f^* accordingly.

In the previous substeps, the FSI problem (48) is still coupled by means of the physical coupling given by the interface conditions (48c)-(48d), see issue v) above. For the solution of this problem, both *partitioned* and *monolithic* procedures have been successfully considered so far in hemodynamics. In partitioned schemes, the fluid and vessel wall subproblems are solved separately, one or more times per time step. Each of the two problems is equipped with a suitable boundary condition at the FS interface Σ^* derived by splitting the physical interface conditions (48c)-(48d).

Partitioned algorithms of explicit type. From the computational point of view, an attractive class of partitioned schemes is that of the *loosely-coupled algorithms* where the two subproblems are solved only once per time step. The most classic loosely-coupled algorithm, widely used in aerodynamics [455], is the *explicit Dirichlet-Neumann* scheme, where condition (48c) is prescribed explicitly as a Dirichlet condition to the fluid subproblem, whereas condition (48d) is prescribed as a Neumann condition to the vessel wall

subproblem, leading to the following

Explicit Dirichlet-Neumann scheme. For $n \geq 1$, at time step t^n:

1. solve the fluid Oseen problem with a Dirichlet condition at the FS interface:

$$\frac{\rho_f \alpha}{\Delta t}\boldsymbol{v}^n + \rho_f((\boldsymbol{v}^* - \boldsymbol{v}_f^*)\cdot\nabla)\boldsymbol{v}^n - \nabla\cdot\boldsymbol{T}_f(\boldsymbol{v}^n, p^n) = \boldsymbol{g}_f^n \qquad \text{in } \Omega_f^*, \tag{50a}$$

$$\nabla\cdot\boldsymbol{v}^n = 0 \qquad \text{in } \Omega_f^*, \tag{50b}$$

$$\boldsymbol{v}^n = \frac{\alpha}{\Delta t}\boldsymbol{d}^{n-1} + \boldsymbol{g}_{fs}^{n-1} \qquad \text{on } \Sigma^*; \tag{50c}$$

2. then, solve the non-linear vessel wall problem with a Neumann condition at the FS interface:

$$\frac{\rho_s \beta}{\Delta t^2}\widehat{\boldsymbol{d}}^n - \nabla\cdot\widehat{\boldsymbol{T}}_s\left(\widehat{\boldsymbol{d}}^n\right) = \widehat{\boldsymbol{g}}_s^n \qquad \text{in } \Omega_s, \tag{51a}$$

$$\widehat{\boldsymbol{T}}_s\left(\widehat{\boldsymbol{d}}^n\right)\widehat{\boldsymbol{n}} = \widehat{\boldsymbol{T}}_f\left(\widehat{\boldsymbol{v}}^n, \widehat{p}^n\right)\widehat{\boldsymbol{n}} \qquad \text{on } \Sigma. \tag{51b}$$

Notice that the discretized-in-time kinematic condition (50c) differs from (48c) since now we are considering an explicit Dirichlet condition for the fluid subproblem, so that the right hand side is computed at the previous time step.

A "parallel" version of the previous scheme is obtained by substituting $\widehat{\boldsymbol{T}}_f\left(\widehat{\boldsymbol{v}}^n, \widehat{p}^n\right)\widehat{\boldsymbol{n}}$ with $\widehat{\boldsymbol{T}}_f\left(\widehat{\boldsymbol{v}}^{n-1}, \widehat{p}^{n-1}\right)\widehat{\boldsymbol{n}}$ in (51b). Notice that in the monolithic FSI problem (48), the dynamic continuity condition (48d) is written in the current configuration Σ^*, whereas for the structure subproblem alone (51) is written in the reference configuration Σ. Accordingly, in what follows the structure interface quantities will be written in the current configuration in monolithic FSI problems and in the reference configuration when the structure problem is uncoupled in view of a partitioned scheme.

Unfortunately, the explicit Dirichlet-Neumann scheme can be unconditionally absolutely unstable. In particular, in [85] it is proven that this happens if the fluid and structure densities are comparable, which is precisely the case of hemodynamics (high *added mass effect*, see also [194] for a discrete analysis and [414] for an analysis of the added mass effect arising from a temporal discretization of order $p \geq 2$).

Stable loosely-coupled algorithms have been recently introduced. To this aim, replace in the FSI problem (48) the interface conditions (48c)-(48d) with two linear independent combinations

$$\sigma_f\boldsymbol{v}^n + \boldsymbol{T}_f\left(\boldsymbol{v}^n, p^n\right)\boldsymbol{n}^* = \sigma_f\left(\frac{\alpha}{\Delta t}\boldsymbol{d}^n + \boldsymbol{g}_{fs}^n\right) + \boldsymbol{T}_s\left(\boldsymbol{d}^n\right)\boldsymbol{n}^* \qquad \text{on } \Sigma^*, \tag{52a}$$

$$\sigma_s\left(\frac{\alpha}{\Delta t}\boldsymbol{d}^n + \boldsymbol{g}_{fs}^n\right) + \boldsymbol{T}_s\left(\boldsymbol{d}^n\right)\boldsymbol{n}^* = \sigma_s\boldsymbol{v}^n + \boldsymbol{T}_f\left(\boldsymbol{v}^n, p^n\right)\boldsymbol{n}^* \qquad \text{on } \Sigma^*, \tag{52b}$$

where $\sigma_f \neq \sigma_s$ are, in general, two functions of space and time. This naturally leads to the following

Explicit Robin-Robin scheme. For $n \geq 1$, at time step t^n:

1. solve the Oseen problem with a Robin condition at the FS interface:

$$\frac{\rho_f \alpha}{\Delta t}\boldsymbol{v}^n + \rho_f((\boldsymbol{v}^* - \boldsymbol{v}_f^*)\cdot\nabla)\boldsymbol{v}^n - \nabla\cdot\boldsymbol{T}_f(\boldsymbol{v}^n, p^n) = \boldsymbol{g}_f^n \qquad \text{in } \Omega_f^*, \quad (53a)$$

$$\nabla\cdot\boldsymbol{v}^n = 0 \qquad \text{in } \Omega_f^*, \quad (53b)$$

$$\sigma_f\boldsymbol{v}^n + \boldsymbol{T}_f\left(\boldsymbol{v}^n, p^n\right)\boldsymbol{n}^* = \sigma_f\left(\frac{\alpha}{\Delta t}\boldsymbol{d}^{n-1} + \boldsymbol{g}_{fs}^{n-1}\right) + \boldsymbol{T}_s\left(\boldsymbol{d}^{n-1}\right)\boldsymbol{n}^* \qquad \text{on } \Sigma^*; \quad (53c)$$

2. then, solve the non-linear vessel wall problem with a Robin condition at the FS interface:

$$\frac{\rho_s \beta}{\Delta t^2}\widehat{\boldsymbol{d}}^n - \nabla\cdot\widehat{\boldsymbol{T}}_s\left(\widehat{\boldsymbol{d}}^n\right) = \widehat{\boldsymbol{g}}_s^n \qquad \text{in } \Omega_s, \quad (54a)$$

$$\frac{\sigma_s \alpha}{\Delta t}\widehat{\boldsymbol{d}}^n + \widehat{\boldsymbol{T}}_s\left(\widehat{\boldsymbol{d}}^n\right)\widehat{\boldsymbol{n}} = \sigma_s\widehat{\boldsymbol{v}}^n + \widehat{\boldsymbol{T}}_f\left(\widehat{\boldsymbol{v}}^n, \widehat{p}^n\right)\widehat{\boldsymbol{n}} - \sigma_s\widehat{\boldsymbol{g}}_{fs}^n \qquad \text{on } \Sigma. \quad (54b)$$

In [80], a Discontinuous Galerkin (DG)-like mortaring of the interface coupling conditions (48c)-(48d) is proposed. The corresponding block Gauss-Seidel explicit algorithm could be reinterpreted as an explicit Dirichlet-Robin scheme, where in (53c)-(54b) we have $\sigma_f = +\infty$, $\sigma_s = -\frac{\gamma\mu}{h}$, γ being the DG penalty parameter. It is shown that the DG interface penalty and the viscous dissipation are not able to control the pressure fluctuations at the FS interface appearing in the discrete energy estimate. For this reason, it is proposed to add to the fluid problem a consistent stabilization term penalizing the pressure fluctuations, that is proven to be absolutely stable under a CFL-like condition. A stable explicit Robin-Robin scheme has been introduced in [34], where the parameters in the Robin interface conditions (53c)-(54b) were set after analyzing the incoming and outcoming characteristic variables of the vessel wall problem. In particular, they are defined in terms of the outgoing characteristic variable for the fluid subproblem and in terms of the incoming characteristic variable for the vessel wall subproblem. For linear elasticity, the following values are obtained: $\sigma_{f,norm} = \sqrt{\rho_s(\mu_1 + 2\mu_2)}$ and $\sigma_{f,tang} = \sqrt{\rho_s\mu_2}$ in the normal and tangential direction, respectively (μ_1 and μ_2 being the Lamé constants), and $\sigma_s = -\sigma_f$. This choice allows the traveling information brought by the characteristic variables to provide a more tightly coupling of the fluid and structure problems than the one enforced by (48c)-(48d).

Partitioned algorithms of semi-implicit type. In [174], it is proven that to achieve stability without stabilization terms for the Dirichlet-Neumann scheme, at least an implicit coupling between the fluid pressure and the vessel wall displacement is mandatory. In particular, a projection scheme is used where the fluid ALE-advection-diffusion step is solved explicitly, whereas the fluid pressure and vessel wall subproblems are coupled and solved in an iterative framework until convergence (see also [15] for a convergence analysis):

Semi-implicit pressure-vessel wall coupled scheme. For $n \geq 1$, at time step t^n:

1. solve the ALE-advection-diffusion problem with a Dirichlet condition at the FS interface:

$$\frac{\rho_f \alpha}{\Delta t}\widetilde{\boldsymbol{v}}^n + \rho_f((\boldsymbol{v}^* - \boldsymbol{v}_f^*)\cdot\nabla)\widetilde{\boldsymbol{v}}^n - \nabla\cdot\mu\left(\nabla\widetilde{\boldsymbol{v}}^n + (\nabla\widetilde{\boldsymbol{v}}^n)^T\right) = \boldsymbol{g}_f^n \qquad \text{in } \Omega_f^*, \quad (55a)$$

$$\widetilde{\boldsymbol{v}}^n = \frac{\alpha}{\Delta t}\boldsymbol{d}^{n-1} + \boldsymbol{g}_{fs}^{n-1} \qquad \text{on } \Sigma^*; \quad (55b)$$

2. then, solve the coupled pressure-vessel wall problem. To this aim, introduce the following iterations on index $k \geq 1$:

   a) solve the pressure problem with a Neumann condition at the FS interface:

$$\begin{aligned} \triangle p_{(k)}^n &= \frac{\rho_f \alpha}{\Delta t}\nabla\cdot\widetilde{\boldsymbol{v}}_{(k)}^n && \text{in } \Omega_f^*, \\ \frac{\partial p_{(k)}^n}{\partial \boldsymbol{n}^*} &= \frac{\alpha}{\Delta t}\boldsymbol{d}_{(k-1)}^n + \boldsymbol{g}_{fs}^n && \text{on } \Sigma^*; \end{aligned}$$

   b) then, solve the non-linear vessel wall problem with a Neumann condition at the FS interface:

$$\begin{aligned} \frac{\rho_s \beta}{\Delta t^2}\widehat{\boldsymbol{d}}_{(k)}^n - \nabla\cdot\widehat{\boldsymbol{T}}_s\left(\widehat{\boldsymbol{d}}_{(k)}^n\right) &= \widehat{\boldsymbol{g}}_s^n && \text{in } \Omega_s, \\ \widehat{\boldsymbol{T}}_s\left(\widehat{\boldsymbol{d}}_{(k)}^n\right)\widehat{\boldsymbol{n}} &= \widehat{\boldsymbol{T}}_f\left(\widehat{\widetilde{\boldsymbol{v}}}^n, \widehat{p}_{(k)}^n\right)\widehat{\boldsymbol{n}} && \text{on } \Sigma. \end{aligned}$$

In [13], the DG-mortaring approach is applied to this projection scheme, leading to a Robin-Robin-like scheme. An algebraic version of the projection scheme proposed in [174] is introduced in [26].

Partitioned algorithms of implicit type. More in general, a fully implicit treatment of (48c)-(48d) (or more in general of (52)) by means of partitioned algorithms is often considered. In this case, the fluid and vessel wall subproblems are solved iteratively until the whole interface conditions are satisfied within a prescribed tolerance. A general scheme is given by the following

Implicit Robin-Robin scheme. For $n \geq 1$, $k \geq 1$, at time step t^n/iteration k:

1. solve the Oseen problem with a Robin condition at the FS interface:

$$\frac{\rho_f \alpha}{\Delta t}\boldsymbol{v}_{(k)}^n + \rho_f((\boldsymbol{v}^* - \boldsymbol{v}_f^*)\cdot\nabla)\boldsymbol{v}_{(k)}^n - \nabla\cdot\boldsymbol{T}_f(\boldsymbol{v}_{(k)}^n, p_{(k)}^n) = \boldsymbol{g}_f^n \qquad \text{in } \Omega_f^*, \quad (58a)$$

$$\nabla\cdot\boldsymbol{v}_{(k)}^n = 0 \qquad \text{in } \Omega_f^*, \quad (58b)$$

$$\sigma_f\boldsymbol{v}_{(k)}^n + \boldsymbol{T}_f\left(\boldsymbol{v}_{(k)}^n, p_{(k)}^n\right)\boldsymbol{n}^* = \sigma_f\left(\frac{\alpha}{\Delta t}\boldsymbol{d}_{(k-1)}^n + \boldsymbol{g}_{fs}^n\right) + \boldsymbol{T}_s\left(\boldsymbol{d}_{(k-1)}^n\right)\boldsymbol{n}^* \qquad \text{on } \Sigma^*; \quad (58c)$$

2. then, solve the non-linear vessel wall problem with a Robin condition at the FS interface:

$$\frac{\rho_s \beta}{\Delta t^2} \widehat{\boldsymbol{d}}^n_{(k)} - \nabla \cdot \widehat{\boldsymbol{T}}_s \left(\widehat{\boldsymbol{d}}^n_{(k)} \right) = \widehat{\boldsymbol{g}}^n_s \qquad \text{in } \Omega_s, \tag{59a}$$

$$\frac{\sigma_s \alpha}{\Delta t} \widehat{\boldsymbol{d}}^n_{(k)} + \widehat{\boldsymbol{T}}_s \left(\widehat{\boldsymbol{d}}^n_{(k)} \right) \widehat{\boldsymbol{n}} = \sigma_s \widehat{\boldsymbol{v}}^n_{(k)} + \widehat{\boldsymbol{T}}_f \left(\widehat{\boldsymbol{v}}^n_{(k)}, \widehat{p}^n_{(k)} \right) \widehat{\boldsymbol{n}} - \sigma_s \widehat{\boldsymbol{g}}^n_{fs} \qquad \text{on } \Sigma. \tag{59b}$$

As proven in [85], a small relaxation parameter is needed to achieve convergence in the implicit Dirichlet-Neumann scheme (corresponding to setting $\sigma_f = +\infty$, $\sigma_s = 0$ in (58c)-(59b)). In practice, often an Aitken relaxation procedure is used to dynamically estimate an efficient relaxation parameter [136, 313]. A better situation is obtained by properly selecting the parameters in the Robin interface conditions (58c)-(59b). In particular, the choice $\sigma_f = \frac{\rho_s H_s}{\Delta t} + \frac{E H_s \Delta t}{(1-\nu^2) R^2}$, $\sigma_s = 0$ (where, as usual, E and ν are the Young modulus and the Poisson ratio for the vessel material at small deformations, H_s and R representative thickness and radius of the vessel) yields fast convergence without any relaxation (*Robin-Neumann* scheme, [23, 410]). An optimization of σ_s is performed in [207, 211], leading to a further improvement in the convergence history. A Dirichlet-Robin scheme is derived in [610] by means of a *generalized fictitious* method, where the coefficients of the fluid pressure and vessel wall acceleration are changed to account for the added mass effect. This allows one to obtain again good convergence properties for hemodynamic parameters without any relaxation. Another class of implicit methods with good convergence properties for high added mass effect is based on adding a suitable *interface artificial compressibility* (IAC) consistent term to the fluid problem, proportional to the jump of pressure between two successive iterations [131]. In [130], it is showed that for a finite volume approximation, IAC method based on Dirichlet-Neumann iterations is equivalent to a Robin-Neumann scheme for a suitable choice of the parameter σ_f.

Partitioned algorithms for the FSI problem with a membrane structure. Recently, several papers have analyzed algorithms for FSI problems featuring a reduced membrane model for the vessel wall. In this case, the FSI problem is given by the fluid problem (22a), by the kinematic continuity condition (26a) and by the membrane equation (26b), which in this case plays also the role of dynamic continuity condition. Moreover, homogeneous Dirichlet or Neumann conditions in the tangential direction need to be prescribed for the fluid problem at the interface Σ. By considering an implicit time discretization of (26b) and an explicit treatment of the geometry coupling, we obtain at each time step the following linearized FSI problem:

$$\frac{\rho_f \alpha}{\Delta t} \boldsymbol{v}^n + \rho_f ((\boldsymbol{v}^* - \boldsymbol{v}^*_f) \cdot \nabla) \boldsymbol{v}^n - \nabla \cdot \boldsymbol{T}_f (\boldsymbol{v}^n, p^n) = \boldsymbol{g}^n_f \qquad \text{in } \Omega^*_f, \tag{60a}$$

$$\nabla \cdot \boldsymbol{v}^n = 0 \qquad \text{in } \Omega^*_f, \tag{60b}$$

$$\boldsymbol{v}^n \cdot \boldsymbol{n}^* = \frac{\alpha}{\Delta t} {d_r}^n + g^n_{fs} \qquad \text{on } \Sigma^*, \tag{60c}$$

$$\boldsymbol{v}^n - (\boldsymbol{v}^n \cdot \boldsymbol{n}^*) \boldsymbol{n}^* = \boldsymbol{0} \qquad \text{on } \Sigma^*, \tag{60d}$$

$$\frac{\rho_s H_s \beta}{\Delta t^2} d^n_r - \nabla \cdot (\boldsymbol{P} \nabla d^n_r) + \chi H_s d^n_r = -\boldsymbol{T}_f (\boldsymbol{v}^n, p^n) \boldsymbol{n}^* \cdot \boldsymbol{n}^* + g^n_s \qquad \text{on } \Sigma^*, \tag{60e}$$

where, as usual, $\boldsymbol{g}_f^n$, g_s^n and g_{fs}^n account for the terms at previous time steps coming from time discretization.

The explicit Dirichlet-Neumann scheme applied to the previous monolithic problem reads:

Explicit Dirichlet-Neumann scheme for the FSI problem with membrane structure. Given the quantities at previous time steps, at time step t^n:

1. solve the Oseen problem with a Dirichlet condition at the FS interface:

$$\begin{aligned}
&\frac{\rho_f \alpha}{\Delta t}\boldsymbol{v}^n + \rho_f((\boldsymbol{v}^* - \boldsymbol{v}_f^*)\cdot\nabla)\boldsymbol{v}^n - \nabla\cdot\boldsymbol{T}_f(\boldsymbol{v}^n, p^n) = \boldsymbol{g}_f^n && \text{in } \Omega_f^*,\\
&\nabla\cdot\boldsymbol{v}^n = 0 && \text{in } \Omega_f^*,\\
&\boldsymbol{v}^n\cdot\boldsymbol{n}^* = \frac{\alpha}{\Delta t}d_r^{n-1} + g_{fs}^{n-1} && \text{on } \Sigma^*,\\
&\boldsymbol{v}^n - (\boldsymbol{v}^n\cdot\boldsymbol{n}^*)\boldsymbol{n}^* = \boldsymbol{0} && \text{on } \Sigma^*;
\end{aligned}$$

2. then, solve the membrane problem:

$$\frac{\rho_s H_s \beta}{\Delta t^2}\widehat{d}_r^n - \nabla\cdot(\boldsymbol{P}\nabla\widehat{d}_r^n) + \chi H_s \widehat{d}_r^n = -\widehat{\boldsymbol{T}}_f\left(\widehat{\boldsymbol{v}}^n, \widehat{p}^n\right)\widehat{\boldsymbol{n}}\cdot\widehat{\boldsymbol{n}} + \widehat{g}_s^n \qquad \text{on } \Sigma.$$

As in the case of scheme (50)-(51), unfortunately this scheme is unconditionally absolutely unstable in the hemodynamic regime [85].

Different algorithms are obtained by linearly combining the interface conditions (60c) and (60e) and by substituting the new condition to (60c). In this case, we have to solve a coupled problem consisting of:

Robin-Neumann coupling for the FSI problem with membrane structure. Given the quantities at previous time steps, at time step t^n:

1. solve the Oseen problem with a Robin condition at the FS interface:

$$\begin{aligned}
&\frac{\rho_f \alpha}{\Delta t}\boldsymbol{v}^n + \rho_f((\boldsymbol{v}^* - \boldsymbol{v}_f^*)\cdot\nabla)\boldsymbol{v}^n - \nabla\cdot\boldsymbol{T}_f(\boldsymbol{v}^n, p^n) = \boldsymbol{g}_f^n && \text{in } \Omega_f^*, && \text{(62a)}\\
&\nabla\cdot\boldsymbol{v}^n = 0 && \text{in } \Omega_f^*, && \text{(62b)}\\
&\left(\sigma_f\boldsymbol{v}^n + \boldsymbol{T}_f\left(\boldsymbol{v}^n, p^n\right)\boldsymbol{n}^*\right)\cdot\boldsymbol{n}^* = \\
&\sigma_f\left(\frac{\alpha}{\Delta t}d_r^n + g_{fs}^n\right) - \left(\frac{\rho_s H_s\beta}{\Delta t^2}d_r^n - \nabla\cdot(\boldsymbol{P}\nabla d_r^n) + \chi H_s d_r^n\right) && \text{on } \Sigma^*, && \text{(62c)}\\
&\boldsymbol{v}^n - (\boldsymbol{v}^n\cdot\boldsymbol{n}^*)\boldsymbol{n}^* = \boldsymbol{0} && \text{on } \Sigma^*; && \text{(62d)}
\end{aligned}$$

2. solve the membrane problem:

$$\frac{\rho_s H_s \beta}{\Delta t^2}\widehat{d}_r^n - \nabla\cdot(\boldsymbol{P}\nabla\widehat{d}_r^n) + \chi H_s \widehat{d}_r^n = -\widehat{\boldsymbol{T}}_f\left(\widehat{\boldsymbol{v}}^n, \widehat{p}^n\right)\widehat{\boldsymbol{n}}\cdot\widehat{\boldsymbol{n}} + \widehat{g}_s^n \qquad \text{on } \Sigma. \qquad (63)$$

The previous problem could be solved either monolithically or by means of a block Gauss-Seidel method that in fact introduces subiterations splitting the solution of (62) and (63). When $\boldsymbol{P} = \boldsymbol{0}$, the special choice

$$\sigma_f = \widetilde{\sigma}_f = \frac{\rho_s H_s \beta}{\alpha \Delta t} + \frac{\chi H_s \Delta t}{\alpha}, \tag{64}$$

introduced in (62c), yields to

$$(\widetilde{\sigma}_f \boldsymbol{v}^n + \boldsymbol{T}_f(\boldsymbol{v}^n, p^n)\,\boldsymbol{n}^*) \cdot \boldsymbol{n}^* = \widetilde{\sigma}_f g_{fs}^n \qquad \text{on } \Sigma^*. \tag{65}$$

At this stage, this is a Robin condition for the fluid problem without any explicit dependence on d_r^n. Thus, the monolithic problem given by (62)-(63)-(64) is equivalent to the stand-alone fluid problem (62a)-(62b)-(62d)-(65), see [413]. The solution of this fluid problem can then be used to feed the right hand side of (63) and to get the structure displacement $\widehat{d}_r^n$. In this way, the fluid and structure problems are in fact decoupled, even if the coupling conditions are treated implicitly. This provides a smart and efficient way to solve the monolithic problem (60) exactly, at the expense of a single fluid problem solve (note that the membrane problem (63) is solved very cheaply).

Starting from this result, a stable Robin-Neumann scheme based on an operator-splitting has been proposed in [233] for a general membrane law ($\boldsymbol{P} \neq \boldsymbol{0}$). The inertial vessel wall term is treated implicitly as in the previous case leading to a Robin boundary condition for the fluid with $\sigma_f = \frac{\rho_s H_s \beta}{\alpha \Delta t}$, whereas the elastic and algebraic contributions are treated explicitly. In [173], an incremental version of this scheme is proposed, where the elastic and algebraic parts of the membrane law are included in the Robin condition for the fluid problem by means of a suitable extrapolation from previous time steps. Finally, we mention [113], where the whole membrane law is treated implicitly, leading to a generalized Robin condition, which however requires an ad-hoc implementation.

Partitioned algorithms based on the Schur complement. We discuss here partitioned schemes arising from an interface equation written for the FSI problem and introduced in [137]. For the sake of exposition, we introduce the algebraic counterpart of (48) related to a Finite Element discretization for the case of linear elasticity for the vessel wall problem:

$$\left[\begin{array}{cc:cc} C^{ff} & C^{f\Sigma} & 0 & 0 \\ 0 & M^{\Sigma} & -M^{\Sigma} & 0 \\ \hdashline C^{\Sigma f} & C^{\Sigma\Sigma} & G^{\Sigma\Sigma} & G^{\Sigma s} \\ 0 & 0 & G^{s\Sigma} & G^{ss} \end{array}\right] \left[\begin{array}{c} \boldsymbol{V}^f \\ \boldsymbol{V}^{\Sigma} \\ \hdashline \boldsymbol{U}^{\Sigma} \\ \boldsymbol{D}^s \end{array}\right] = \left[\begin{array}{c} \boldsymbol{b}^f \\ \boldsymbol{0} \\ \hdashline \boldsymbol{b}^{\Sigma} \\ \boldsymbol{b}^s \end{array}\right], \tag{66}$$

where the subscript f refers to internal degrees of freedom (d.o.f.) for the fluid, s to internal d.o.f. for the vessel wall, Σ to the FS interface d.o.f.; the notation C (with subscripts) refers to fluid matrices, G to vessel wall matrices, M^{Σ} is the FS interface mass matrix; $\boldsymbol{V}$ collects the fluid d.o.f. (in this case also the pressure ones), $\boldsymbol{D}^s$ the vessel wall displacement

internal d.o.f., and $\boldsymbol{U}^\Sigma$ the vessel wall velocity interface d.o.f.; vectors $\boldsymbol{b}$ represent the right hand sides. The first row corresponds to the momentum and mass conservation for the fluid, the second and third rows to the interface kinematic and dynamic conditions, and the last row to the vessel wall problem. By eliminating $\boldsymbol{V}^f$, $\boldsymbol{V}^\Sigma$ and $\boldsymbol{D}^s$ from (66), we obtain the following interface equation

$$(\widetilde{C}^\Sigma + \widetilde{G}^\Sigma)\boldsymbol{U}^\Sigma = \widetilde{\mathbf{b}}^\Sigma, \tag{67}$$

where $\widetilde{C}^\Sigma = C^{\Sigma\Sigma} - C^{\Sigma f}(C^{ff})^{-1}C^{f\Sigma}$ and $\widetilde{G}^\Sigma = G^{\Sigma\Sigma} - G^{\Sigma s}(G^{ss})^{-1}G^{s\Sigma}$ are the fluid and vessel wall Schur complement matrices and $\widetilde{\mathbf{b}}^\Sigma = \mathbf{b}^\Sigma - C^{\Sigma f}(C^{ff})^{-1}\mathbf{b}^f - G^{\Sigma s}(G^{ss})^{-1}\mathbf{b}^s$ the corresponding right hand side.

The Robin-Robin method (58)-(59) could be obtained by applying the Richardson method to the interface equation (67) preconditioned by the matrix

$$P = \frac{1}{\sigma_f + \sigma_s}\left(\widetilde{C}^\Sigma + \sigma_f M^\Sigma\right)(M^\Sigma)^{-1}\left(\widetilde{G}^\Sigma + \sigma_s M^\Sigma\right). \tag{68}$$

This leads to a new family of partitioned schemes obtained by applying other Krylov methods to (67) with the same preconditioner. For example, GMRES preconditioned by the Dirichlet-Neumann preconditioner $P = \widetilde{G}^\Sigma$ is considered in [25], whereas GMRES preconditioned with the RR preconditioner (68) is introduced in [24]. The first of these two schemes highlighted better convergence properties with respect to the classical Dirichlet-Neumann method, whereas the second one is more robust with respect to the choice of the interface parameters σ_f, σ_s than the classical Robin-Robin method.

In some works, a non-linear interface equation is written directly for the non-linear problem (47) and a Newton method is then applied to this equation [176, 132].

Remark 2. *In the partitioned schemes introduced above, the vessel wall subproblem appearing at each iteration is still non-linear, i.e. we did not discuss how to tackle point iii) in the list of issues reported at the begin of the paragraph. The simplest way to treat the vessel wall non-linearity, very appropriate when a non-linear structural solver is available, is to introduce inner Newton subiterations at each Robin-Robin iteration. Alternatively, a scheme based on managing together the five sources of non-linearities/coupling (geometric coupling and adherence, fluid and structure constitutive non-linearities, physical coupling) in a single inexact-Newton loop is proposed in [312]. Other possible combinations will be discussed later on as specific monolithic procedures. For a detailed overview with numerical comparisons we refer to [411].*

Monolithic solvers. As an alternative to partitioned schemes, monolithic procedures have been successfully considered in hemodynamics for the solution of the FSI problem (48). These methods consist in applying an exact or inexact Newton method to the whole non-linear FSI problem. Referring to the notation introduced above, by considering a Finite Element space discretization and the inexact Newton method, we obtain from (48) (we suppress for the sake simplicity the temporal index n)

$$\widetilde{J}(\boldsymbol{x}_{(k-1)})\delta\boldsymbol{x}_{(k)} = \boldsymbol{G} - \boldsymbol{A}(\boldsymbol{x}_{(k-1)}), \tag{69}$$

where $\widetilde{J}$ is the Jacobian matrix or a suitable approximation of it, $\boldsymbol{x} = [\boldsymbol{V}^f \ \boldsymbol{V}^\Sigma \ \boldsymbol{U}^\Sigma \ \boldsymbol{D}^s]^T$, and $\boldsymbol{A}(\boldsymbol{x}) = \boldsymbol{G}$ is the non-linear system related to (48). The exact Jacobian matrix is given by

$$J(\boldsymbol{x}_{(k-1)}) = \left[\begin{array}{cc:cc} C^{ff} & C^{f\Sigma} & 0 & 0 \\ 0 & M^\Sigma & -M^\Sigma & 0 \\ \hdashline C^{\Sigma f} & C^{\Sigma\Sigma} & J_G^{\Sigma\Sigma}(\boldsymbol{U}^\Sigma_{(k-1)}) & J_G^{\Sigma s}(\boldsymbol{D}^s_{(k-1)}) \\ 0 & 0 & J_G^{s\Sigma}(\boldsymbol{U}^\Sigma_{(k-1)}) & J_G^{ss}(\boldsymbol{D}^s_{(k-1)}) \end{array}\right], \tag{70}$$

where the submatrices J_G are the exact Jacobians of $\boldsymbol{A}$ related to the structure d.o.f. For the solution of the linear systems (69) with the exact Jacobian, classical strategies used so far for hemodynamics are, e.g., GMRES preconditioned by a one-level additive Schwarz method [36] and global algebraic multigrid [203]. In [37], a two-level Newton method is used in combination with a two-level hybrid Schwarz preconditioner, where the solution on a coarse grid is used to provide a good initial guess to the Newton method. Alternatively, inexact Newton methods have been considered, e.g. by means of block approximations $\widetilde{J}$ of J splitting the fluid velocity, pressure and vessel wall unknowns [246, 125].

A particular class of inexact Newton methods is obtained by neglecting the term $-M_\Sigma$ appearing in the upper-right block of the exact Jacobian (70). This yields in fact a class of partitioned schemes of Dirichlet-Neumann type where issues iii) and v) (vessel wall non-linearity and physical coupling) are treated within the same iterations. An example is given by the preconditioner proposed in [125], where the fluid and structure blocks in (70) are approximated by the corresponding algebraic additive Schwarz preconditioners. This method is strongly scalable for hemodynamic applications. Recently, a variant of the previous preconditioner has been introduced in [138]. This new preconditioner, named FaCSI, is based on operating a static condensation of the fluid interface d.o.f. and using a SIMPLE preconditioner for the fluid block.

For the sake of exposition, we have discussed numerical strategies for the FSI problem based on Finite Elements for the space discretization and Finite Differences for the time discretization. Other strategies considered so far in hemodynamics are space-time Finite Elements, see, e.g., [544, 42], and the methods based on the iso-geometric analysis, see [40, 41].

In Figure 10 we report a couple of examples of numerical results obtained in real geometries reconstructed from radiological images (see the caption for details).

4.6.4 Numerical methods for defective boundary problems

For the numerical solution of the augmented formulation (30), one could rely either on a monolithic strategy where the full augmented matrix is built and solved, or on splitting techniques. As for the latter choice, in [184, 561] it is proposed to write the Schur complement equation with respect to the Lagrange multiplier of the linearized and discretized (in time and space) augmented formulation. This is a linear system whose dimension is

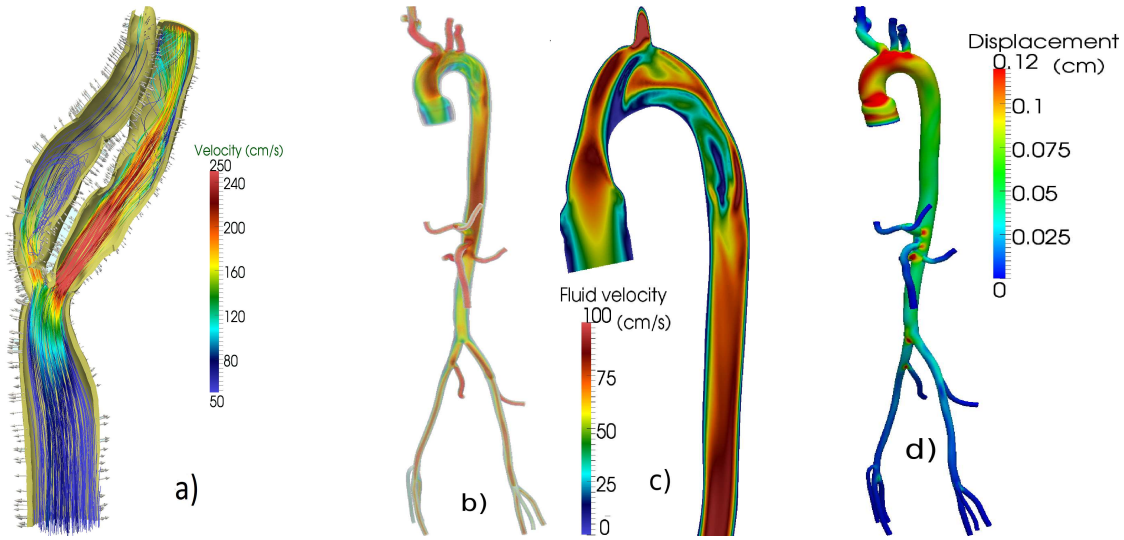

Figure 10: a) Blood velocity streamlines and vessel wall displacement vectors in a stenotic carotid artery (MRI images from the Vascular-surgery and Radiology Divisions at Ospedale Maggiore Policlinico, Milan, Italy); b-c-d) Results of a FSI simulation in the ascending and thoracic aorta (MRI images from http://www.vascularmodel.com/sandbox/doku.php?id =repository). Blood velocity magnitude in the whole domain (b) and on a selected longitudinal section (c), vessel wall displacements (d). All cases refer to the systolic peak. These numerical results are obtained using *LifeV*, $P1-Bubble/P1$ Finite Elements for the fluid problem and $P1$ Finite Elements for the vessel wall problem; the backward Euler scheme and the midpoint method have been used for the time discretization of the fluid and vessel wall problems, respectively. The implicit Robin-Robin partitioned scheme has been used in case a) and the FaCSI preconditioner in cases b-c-d)

equal to the number of flow rate conditions, say $m \geq 1$. By applying the GMRES method to iteratively solve this system, the exact solution is reached after exactly m iterations (in exact arithmetics). At each iteration, the solution of a standard fluid problem with Neumann conditions is needed (*exact splitting technique*). The solution of a further standard fluid problem is required to compute the initial residual in the GMRES algorithm. This approach is quite expensive, even in the case $m = 1$, which requires the solution of two fluid problems per time step. However, it preserves *modularity*, indeed it can be implemented using available standard fluid solvers in a *black box* mode. This is an interesting property when applications to cases of real interest are addressed, see [576, 569, 453, 226, 227].

To reduce the computational time required by the exact splitting approach, in [562] a different (inexact) splitting procedure is proposed, requiring the solution of m steady problems out of the temporal loop and of one unsteady null flow rate problem at each time step. This strategy introduces an error near the section which is smaller than the one based on conjecturing the velocity profile in the original (non-null) flow rate problem,

see Sect. 4.4.1.

As for the numerical solution of the control-based approach described in Sect. 4.4.3, classical iterative methods have been considered in [190, 191] for the solution of the resulting KKT system.

Recently, a numerical approach based on the *Nitsche method* has been considered to prescribe a flow rate condition. In particular, the original idea of prescribing Dirichlet conditions with a consistent penalization approach [408] is extended to the case of flow rate boundary conditions in [615]. This strategy does not introduce further variables, other than those of the original problem, however it requires to properly tune a penalization parameter. In addition, it deals with non-standard bilinear forms that need ad hoc implementation. However, it should be very effective if flow rate conditions are implemented in a DG code. A similar approach has been considered to fulfill the mean pressure condition (3) and the FSI case in [565], see also [459].

For a more comprehensive overview of numerical strategies for defective boundary problems, we refer the reader to [192].

4.6.5 Numerical methods for the geometric reduced models and multiscale approach

For the numerical solution of the 1D reduced model (33), in principle any convenient approximation method for non-linear hyperbolic equations can be used. The peculiar feature of this model, however, is the lack of discontinuous solutions. A common approach relies on the Finite Element version of the Lax-Wendroff scheme, thanks to its excellent dispersion properties [183]. Being this scheme explicit, a CFL-like condition is required to ensure absolute stability. In presence of a visco-elastic term, the 1D model is usually discretized by means of a splitting procedure where the solution is split into two components, one satisfying the pure elastic problem and the second one the visco-elastic correction [185, 352]. High order method are suitable to capture the (physical) reflections at bifurcations induced by the vessel tapering, see e.g. [519, 518] for a Discontinuous Galerkin discretization and [387] for a finite volume scheme.

Regarding 0D models, they are in general described by systems of DAE (differential and algebraic equations), possibly non-linear due to the presence of diodes to represent the valves [188]. Usually, for hemodynamic applications, these systems can be reduced to classical Cauchy problems and solved by classical Runge-Kutta methods.

As for the solution of the 3D-1D coupled problems described in Sect. 4.5.2, we can in principle identify three different strategies, namely *partitioned schemes*, *monolithic approaches*, and methods based on the solution of an *interface equation*. In partitioned schemes, the 3D and 1D problems are solved separately in an iterative framework. The coupling interface conditions can be enforced in many different ways: for example, we can prescribe the flow rate condition (42a) to the 3D problem and the pressure condition (45) to the 1D problem. Different algorithms are obtained by switching the role of the interface conditions in the iterative algorithm or by considering other interface conditions (e.g. (42b)). This is also the case when one of the two interface conditions is replaced by a condition expressing the continuity of the characteristic variable W_1 entering the 1D

domain [183, 431], i.e., according to (36),

$$W_1(t)|_{z=0} = \zeta_1 \left(\left| \Gamma_f^t \right|, \int_{\Gamma_f^t} \boldsymbol{v} \cdot \boldsymbol{n} \, d\gamma \right).$$

In any case, each of these approaches yields a 3D problem with a defective boundary condition, which could be dealt with one of the strategies described in Sect. 4.4. Explicit algorithms based on the solution of the 3D and 1D problems only once per time step have been successfully considered in [186, 431]. These algorithms enforce a limitation on Δt, which, however, is milder with respect to the one imposed by the numerical scheme adopted for the 1D model. Alternatively, iterative methods applied directly to the monolithic linearized system have been introduced in [57, 58]. A different approach to solve the 3D-1D coupled problem relies on writing an interface equation involving only the 3D-1D interface unknowns. We can interpret this equation as the geometric heterogeneous counterpart of the Schur complement equation. For its numerical solution, either the Broyden or the Newton method have been used in [330, 351, 55], in combination with GMRES. Methods relying on the numerical solution of the interface equation are simple to implement in the case of multiple interfaces, such as those that arise in complex arterial networks.

In Figure 11 we report a numerical result obtained by the coupling between the 3D model of an ascending aorta and a 1D model of the systemic circulation. This result highlights the suitability of the 1D model in providing absorbing conditions to the 3D model and in propagating the pressure wave along the whole network [350].

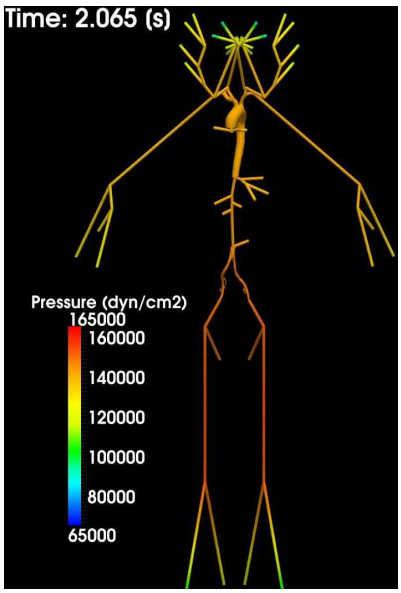

Figure 11: Pressure wave propagation in an ascending aorta (3D model) and in the 1D model of the systemic circulation. These numerical results are obtained using *LifeV*; the Newton method has been used for the interface equation. Courtesy of C. Malossi

Part II
THE HEART FUNCTION

5 Basic facts on quantitative physiology

5.1 Basic anatomy

The heart is a hollow organ that pumps the blood into the arteries of the systemic and pulmonary circulations and collects it after its return through the veins. It is formed by the left and the right heart, each of them being composed by two chambers, an *atrium* and a *ventricle*. The left and right hearts are separated by the *interatrial* and *interventricular septa*, which do not allow the transfer of blood, whereas the atria and the ventricles are connected by the *atrio-ventricular valves* (*tricuspid valve* in the right heart, *mitral valve* in the left heart) that either allow or prevent the blood transfer from the atria to the ventricles depending on the their position (open or closed, respectively), see Figure 12. In particular, they open when the atrial pressure is higher than the ventricular one and close as soon as the blood flow rate, normally going from the atrium to the ventricle, becomes negative, i.e. coming back in the atrium. The *papillary muscles*, located in the ventricles, attach to the cusps of these valves via the *chordae tendineae* preventing their inversion (prolapse) during the closure.

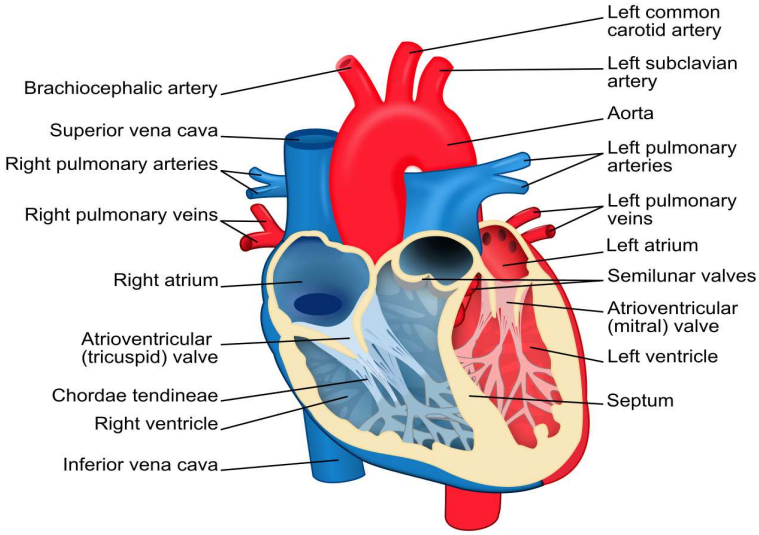

Figure 12: Schematic representation of the heart

All the four chambers are connected with the circulatory system: the left ventricle through the aorta, the right ventricle through the pulmonary artery, the left atrium through the *pulmonary veins*, and the right atrium through the *superior* and *inferior venae cavae*. The ventricles are separated by the circulatory system by two further valves,

the *aortic valve* on the left side and the *pulmonary valve* on the right side, whose opening/closure mechanism is similar to the one of the atrio-ventricular valves, i.e. they open when the pressure is higher in the ventricle with respect to the corresponding connected artery, whereas they close when the flow rate becomes negative (i.e. going from the artery to the ventricle). No valves are located between the atria and the corresponding terminal veins.

The heart wall is composed by three layers: the internal thin *endocardium*, the thick muscular *myocardium*, and the external thin *epicardium*. The myocardium of the left ventricle is almost two times thicker than the one of the right ventricle. The epicardium is surrounded by the *pericardium*, a serous membrane that isolates the heart from the closest organs, facilitating its movements.

5.2 The cardiac cycle

The main purpose of the heart is to pump the blood in the circulatory system through the aorta and the pulmonary artery. To do this, it needs to win the resistances in the arteries where blood has a non-null pressure (about $70\,mmHg$ in the aorta, $10\,mmHg$ in the pulmonary artery) due to the reaction of the elastic vessel wall to the deformation induced by blood inside. Moreover, the heart supplies to blood the energy needed to reach the microvasculature or the lungs. The total work made by the heart per heartbeat is

$$W = QP + \frac{1}{2}mv^2,$$

Q and m being the blood flow rate and mass ejected, P the arterial blood pressure, and v the blood velocity in the aorta or pulmonary artery. The kinetic component of the work is quite negligible with respect to the potential one (about 2% for the left heart and about 5% for the right heart), although it could become more relevant (up to 25%) under physical effort. The flow rate Q in normal conditions is about $5 \cdot 10^3\,cm^3/min$, so that, assuming $60 - 90$ heartbeats per minute, we have about $55.5 - 83.3\,cm^3$ of blood expelled at each heartbeat. The energetic requirements to pump blood are obtained, as it happens in all the organs, by the consumption of oxygen that is provided to the heart by blood in the coronary arteries. The efficiency of the heart, i.e. the ratio between the energy W and the total energy consumption, is in physiological cases about 25%.

The cardiac cycle comprises different phases. For its description, we consider the left heart and we start from the situation where the left atrium is filled by oxygenated blood coming from the pulmonary veins, the mitral valve is closed, and the left ventricle has reached its maximum contraction.

1. *Ventricular filling.* Due to the continuous inflation of blood, when the pressure in the atrium exceeds the ventricular one (about $10\,mmHg$) the mitral valve opens. Blood starts filling the left ventricle which relaxes. In a first stage ($\sim 0.15\,s$), there is a fast inflation of blood due to the pressure gradient between the atrium and the ventricle, where probably the ventricle exerts also a suction due to its expansion (phase 1a in Figure 13). In any case, this is a passive phase. In a second stage ($\sim 0.25\,s$,

phase 1b in Figure 13), the atrium actively contracts (*atrial systole*) producing a slow ventricular inflation of the remaining blood;

2. *Isovolumic contraction.* After the atrial systole, the ventricular active contraction starts. This produces an increase of the ventricular pressure causing retrograde flow that accordingly closes the mitral valve. However, the ventricular pressure is still lower than the aortic one, so that also the aortic valve is closed. Thus, during this phase, there is a continuous and fast increase of the ventricular pressure without any change of blood volume due to blood incompressibility ($\sim 0.05\,s$, phase 2 in Figure 13);

3. *Ventricular ejection.* As soon as the ventricular pressure reaches the aortic pressure (about $70\,mmHg$), the aortic valve opens and blood is ejected in the systemic circulation. Since the ventricular contraction carries on also after the valve opening, the ventricular pressure continues to increase. Accordingly, also the aortic pressure increases due to the elastic adaption of the vessel wall. However, at each time, there is a pressure difference between ventricle and aorta that allows blood to accelerate ($\sim 0.05\,s$, phase 3a in Figure 13). When the ventricle stops its active contraction, this pressure difference reduces and, after a short period (but not immediately due to inertial effects), becomes zero, allowing the flow rate to reach its maximum ($\sim 0.05\,s$, phase 3b in Figure 13). Then, the pressure difference starts to become negative (higher in the aorta) provoking a deceleration of blood that however continues to enter the aorta. When, due to this deceleration, the flow rate becomes negative, the aortic valve closes and the blood ejection stops ($\sim 0.15\,s$, phase 3c in Figure 13). Notice that, once the active contraction stops, the ventricle starts to relax releasing the elastic energy accumulated during the contraction. However, this energetic relaxation is not immediately followed by a mechanical relaxation which should result in an increase of the ventricular volume. Indeed, due to inertial effects, there is a "passive" mechanical contraction which allows to eject all the blood.

4. *Isovolumic relaxation.* When the aortic valve closes, the release of energy of the ventricle continues with both valves closed, so that no changes of ventricular volume are produced resulting in a fast decrease of the ventricular pressure ($\sim 0.10\,s$, phase 4 in Figure 13). After the valve closure, the aortic pressure keeps (slightly) increasing, due to the elastic recoil of the closing valve (*dicrotic wave*, see Figure 13).

All these mechanisms apply to the right heart as well, the only difference being the pressure values, smaller in this case. This justifies the thicker myocardium of the left heart since higher values of resistances need to be won.

5.3 Electric propagation

As seen in the previous paragraph, the main responsible for blood ejection in the circulatory system is the active ventricular contraction. The heart is able to produce itself the electric impulse that determines this contraction, triggered by an electric potential that propagates along all the myocardium. This is possible owing to the excitability of the heart

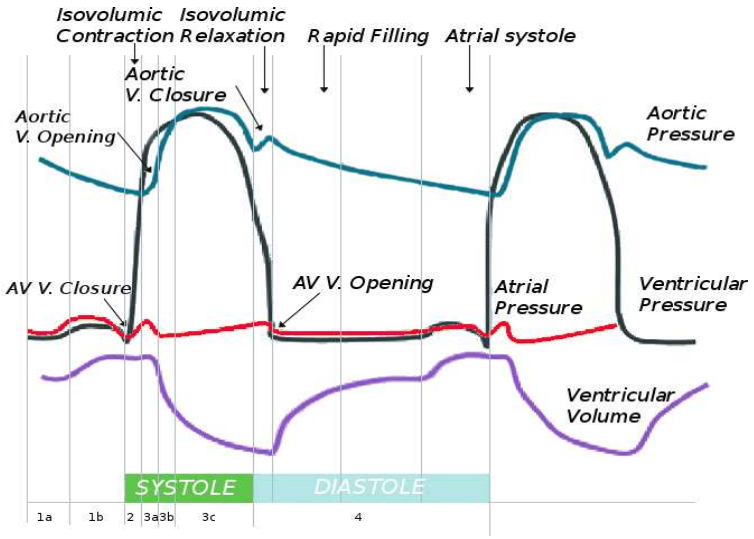

Figure 13: Aortic pressure, ventricular pressure, atrial pressure, and ventricular volume during an heartbeat

cells, the *cardiomyocites*, that, when suitably stimulated, are able to produce a variation of the membrane voltage. At rest, the membrane potential is negative ($\sim -90\,mV$), whereas when stimulated it reaches a positive value ($\sim 20\,mV$) in a very short period (about $2\,ms$). After this depolarization, a plateau around $0\,mV$ is observed that corresponds to the refractory period (see below). Then, the repolarization phase starts that brings the potential back to the rest value allowing for a new excitation (see Figure 14, left). This action potential is generated by several ion channels that open and close and by the resulting currents passing through the membrane. The most important channels are those of calcium, sodium, and potassium. In particular, a fast inward sodium current is the main responsible for the rapid depolarization, a slow inward flux of extra-cellular calcium ions is the main responsible for the characteristic plateau appearing after the depolarization, whereas the outward potassium currents are responsible for the repolarization.

Unlike other cells in the human body, the cardiomyocites obey to the "all-or-none" law, meaning that if the stimulus is above a suitable threshold, a complete action potential with peak value independent of the stimulus is generated, otherwise no response is provided by the cell. Another characteristic of the heart cells is the presence of a *refractary* period after the generation of an action potential, which inhibits any further stimulus independently of its intensity. Thus, during this period the cell is non-excitable at all (*absolute refractary period*, infinite threshold). Afterwards, the cardiomyocites recover their excitability with a value of the threshold needed to generate the action potential which decreases in time (*relative refractory period*). Finally, once the threshold value reaches its minimum, the cells returns to its complete excitable state and the threshold remains constant.

The cardiomyocites act as a syncytium, i.e. the stimulation of an individual cell produces the action potential and the corresponding current that result in the excitation

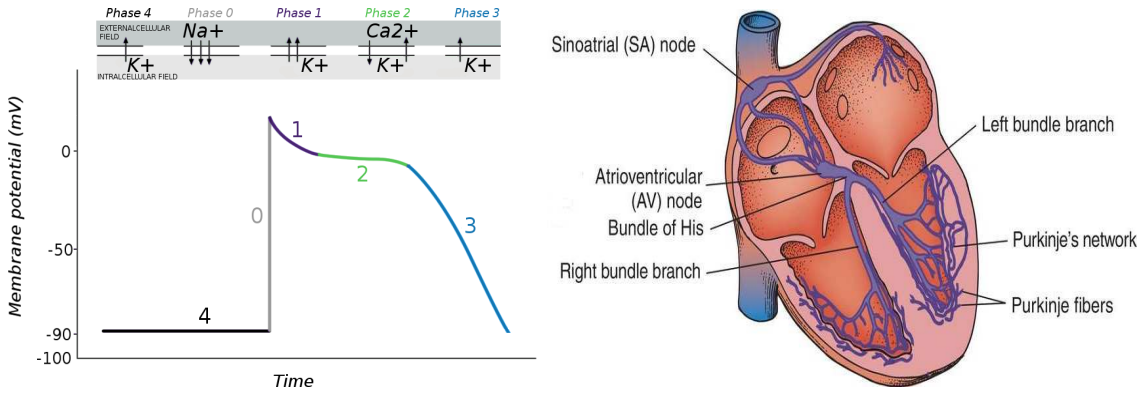

Figure 14: Characteristic action potential of cardiomyocites (left) and anatomy of the cardiac conduction system (http://medical-dictionary.thefreedictionary.com, right)

of the neighbor cells, and thus of the whole myocardium. This is allowed by the *gap junctions*, intercellular channels characterized by a low resistance and located between cardiomyocites that permit the electric potential to travel on the cellular membranes from cell to cell.

In normal conditions, the signal spontaneously originates at the *sinoatrial node*, located in the right atrium at the junction with the superior vena cava. It represents the natural pacemaker of the heart and imposes its rhythm to all the myocardium (*sinusal rhythm*, $\sim 60 - 90$ heartbeats per minute). The impulse generated by the sinoatrial node propagates through all the cardiomyocites of the atria, activating all their regions and allowing their contraction. The propagation is faster in the direction of the ventricles ($\sim 200\, cm/s$) allowing to reach the *atrioventricular node*, located between the atria and the ventricles. When the signal arrives at this node, it is subjected to a delay ($\sim 0.12\, s$) that allows the complete contraction of the atria before the propagation in the ventricles starts. Moreover, this node provides a filter to possible high frequencies of the atrial signal, induced e.g. by atrial fibrillation, protecting the ventricles. This node, when the sinoatrial node looses its automatism, becomes the leading pacemaker and takes on the role of giving the pace to all the ventricle stimulation. Then, the electric signal enters the *bundle of His*, propagating in the ventricles through the two (left and right) *bundle branches* and then through the *Purkinje fibers* (see Figure 14, right). The bundle of His, bundle branches and Purkinje fibers form the *cardiac conduction system* (CCS), a subendocardic specialized network responsible for the fast and coordinated propagation of the electric impulse in the ventricle. The propagation in the CCS is very fast ($\sim 350\, cm/s$) and its role is to reach the entire endocardium through the dense network of Purkinje fibers, activating it almost simultaneously. Notice that the cells of the CCS are specialized in the electric propagation so that they are not involved in the muscular contraction. Then, the electric signal enters the myocardium through the *Purkinje muscle junctions* (PMJ) which are the terminal points of the Purkinje network. At the PMJ, the signal is subjected to a delay ($\sim 0.01\, s$) and then propagates into the ventricular muscle towards the epicardium with a

reduced velocity ($\sim 80\, cm/s$).

To better understand how the propagation of the electric potential spreads into the ventricles, we observe that cardiomyocites are of cylindrical type. This allows us to define the *fiber direction* of the cell, resulting in a macroscopic fiber direction intended as the average cell orientation in a sufficiently small control volume. A transmural variation of the fiber direction is measured between the epicardium and the endocardium ($\sim -70^o$ and $\sim 80^o$ with respect to the normal direction to the surface, respectively). The fibers are in turn organized in *sheets* of collagen. The velocity of propagation of the electric potential is about two times faster along the fiber direction than in the directions tangential to the fibers.

5.4 Mechanisms of contraction and cardiac blood fluid-dynamics

The propagation of the electric signal through the cardiomyocites is responsible of their contraction (*electro-mechanical coupling*), resulting in the atrial and, more importantly, ventricular contractions. The characteristic connections between the cardiomyocites resulting in a syncytium allows for a coordinated contraction of the heart.

At the cellular level, as discussed in the previous paragraph, there is an inward flux of extra-cellular calcium ions just after the depolarization of the cell. Once in the intracellular space, calcium ions bind to *troponin*, which allows *myosin* to bind to *actin* and contraction of the cell to occur.

At the macroscopic level, the ventricles contraction results in a longitudinal (apex-to-base) shortening of about 15% from the diastolic configuration, in a ventricular wall thickening of about 30%, and in a torsion around the longitudinal axis of about 15^o. This is due to the particular fiber orientation of the cardiomyocites which highly influences also the mechanical response of the heart.

The heart obeys to the *Frank-Starling law*, stating that an increase (for any reason) of the end diastolic volume (i.e. the maximum ventricular expansion) results in an increase of the *stroke volume*, i.e. the volume of blood pumped by the left ventricle per heartbeat. This is due to an increase of load experienced by the cardiomyocites as a result of the increased volume of blood filling the ventricle. This extra-stretching of the cells produces a greater number of actin-myosin bridges resulting in an augmented muscle contraction power. It should be noticed however that the Frank-Starling law holds true only up to a certain level of increased stretch: for higher values, the contractility power of the heart, and thus the stroke volume, decreases.

Besides the influence of electric processes on the mechanical behavior, cardiomyocites experience also a mechano-electric feedback. This is due to the formation of *stretch-activated* ion channels and to changes of cells conductivity by means of the stretch of the cell that changes the membrane shape and distance between gap junctions. This mechanism seems to be of utmost importance to describe evolution of spiral waves and thus arrhythmias [549, 289].

Blood flow in the cardiac chambers features different characteristics with respect to the vascular one. In particular, peculiar challenges are the large-scale motion and complex deformation of the myocardium, the complex interaction with valves leading to specific

flow patterns, and the higher Reynolds number (about 4000). For some authors, all these aspects are responsible for transition to turbulence effects, especially in pathological conditions, even if not all the authors agree with the fact that also in normal conditions turbulence could occur. Another important aspect of cardiac blood flow is given by the formation of a large vortex ring in the long axis plane of the left ventricle due to the asymmetry of the mitral valve leaflets that forces the blood flow jet to impinge on the posterior wall [91]. The interaction of this ring with the wall gives rise to a complex flow pattern. Also in the left atrium, complex vortex rings ejected by the pulmonary veins can be observed [375].

5.5 A brief summary of heart diseases

The principal heart diseases (cardiopaties) are the *ischemic cardiopathy*, the *cardiomyopaties*, the *hypertensive cardiopathy*, and the *valvular pathologies*.

The ischemic cardiopathy is the most important, for frequency and clinical impact, among cardiopathies. It is caused by a reduced coronary flow rate (due to the atherosclerosis of coronaries) with consequent malnutrition of the myocardium. When, due to the coronary occlusion, the decrease of the oxygen supply is abrupt, long-lasting, and total, the *infarct of the myocardium* occurs. This is the most classical event of the ischemic cardiopathy resulting in the necrosis of cardiomyocytes and leading, at the end of the process, to the formation of a *scar*.

In the *dilated cardiomyopathy* the ventricle wall becomes thinner due to the partial substitution of cardiomyocites by fibrosis and small scars, leading to the dilation of the ventricle. In the *hyperthrophic cardiomyopathy* the ventricular wall becomes thicker, with a consequent increase of the ventricular blood pressure resulting in a decreased filling of the ventricle. As in all the cases of ventricular hyperthropy, this produces a malnutrition of the myocardium, since the amount of blood supplied by the coronaries remains unchanged. Moreover, in this specific hypertrofic cardiomiopathy, the orientation of the fibers is not coordinated as in normal conditions (this is called *electric disarray*).

In the hypertensive cardiopathy, there is an increase of blood pressure resulting in a increased work needed by the heart to pump blood, leading again to the thickening of the myocardial wall and to a malnutrition of the myocardium.

Valvular main pathologies are *stenosis* and *insufficiency*. In the aortic valve stenosis, the narrowing of the maximum opening of the aortic valve causes the heart to require an increased work to properly pump blood into the aorta, resulting again in the thickening of the myocardial wall and malnutrition. In the mitral valve stenosis, there is an increase in the pressure of the left atrium and in the pulmonary circulation, with consequences on the right heart. Aortic and mitral valve insufficiency is due to the partial reversal flow (going from the aorta to the left ventricle in case of aortic insufficiency, from the left ventricle to the left atrium in mitral insufficiency), that occurs as a consequence of the non adequate closure of the valve. In this case, the heart dilates in order to supply this retrograde flow resulting in an increase of its contraction power owing to the Frank-Starling law. However, sooner or later, the diastolic cell stretching overcomes the threshold of validity of the Frank-Starling law, resulting in a decreased contractility power.

The two main events, possibly fatal, that heart may encounter as a consequence of these cardiopaties are the *cardiac arrest*, due to *ventricular fibrillation*, and the *heart failure*.

In the ventricular fibrillation, the cardiomyocites are not excited in a coordinate way and thus do not contract homogeneously, but, continuously, groups of cells contract whereas other groups relax. This chaotic excitation, if the fibrillation perpetuates, inhibits the normal functioning of the heart pump that is no longer able to regularly pump the blood in the circulatory system, finally leading to death. All the cardiopaties described above could yield altered electric properties (i.e. velocity of conduction and refractariness) which could lead to ventricular fibrillation. For example, in the myocardial infarct, the arrhythmogenic substrate is given by the vicinity of healthy cardiomyocites, necrotic cardiomyocites, and scars, whereas in the hypertrofic cardiomiopathy it is provided by the electric disarray.

When the blood pumped by the heart at each heartbeat is below the required amount needed by the body (but not absent as in ventricular fibrillation), the heart on the one hand increases its frequency so as to guarantee that the blood ejected per minute (*cardiac output*) is almost normal, and on the other hand it increases its diastolic filling to increase the stroke volume. However, the increase of the frequency (*tachycardia*) is energetically disadvantageous for the heart, and a possible excessive diastolic cell stretching leads to the loss of validity of the Frank-Starling law. When these two compensating mechanisms become no longer effective, the cardiac output dramatically decreases leading to heart failure. In absence of other causes of death (cardiac arrest or death for non-cardiac reasons), all the cardiopaties described above, sooner or later, leads to heart failure.

6 Landscape on data

As discussed in Section 3, the use of patient-specific data is mandatory in view of numerical modeling aiming at understanding biophysical processes and supporting clinicians. This holds true also for the heart modeling. The latter accounts for three processes that are intimately coupled: the electrical propagation, the mechanical contraction and relaxation, and the blood fluid-dynamics. The first two processes occur in the cardiac tissue (here called muscle region), whereas the latter occurs in the four hollow regions (chambers) delimited by the endocardium. As done in Section 3 for the circulatory system, in what follows we briefly discuss how to obtain geometric, boundary, and biological cardiac data.

6.1 Cardiac geometric data

Referring to Figure 15, we need to build two computational domains, the muscle region Ω_{mus}, delimited by the external surface of the epicardium Σ_{epi} and by the internal surface of the endocardium Σ_{endo}, and the cavities Ω_{cav}, referred in what follows to as heart cavities or chambers, delimited by the endocardium. The cavities are easily obtained once the endocardium has been reconstructed, so that in fact the cardiac image reconstruction process relies on identifying the endocardium and the epicardium surfaces.

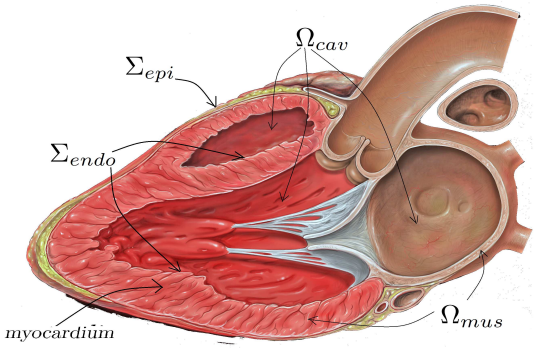

Figure 15: Longitudinal section of a complete heart domain

This problem features several challenging issues. First of all, unlike the vascular case where the external wall surface is usually obtained by extruding the internal one under the assumption of constant (or in any case known) wall thickness, for the heart it is crucial to identify and reconstruct the epicardium. This is mandatory because of the high variability of the myocardial thickness (both in terms of latitude and of patient variability) that makes the extrusion of the endocardium not meaningful. Second, the motion of the heart produces large displacements. This means that if one is interested in obtaining a reconstruction of the heart not only at the end-diastolic phase, a dynamic acquisition procedure (allowing for the acquisition of several frames per heartbeat) is required. Third, the presence of the papillary muscle and wall irregularities given by *trabeculations* makes the reconstruction of the endocardium very problematic.

As in the vascular case, the two most common radiological techniques used for acquisition of cardiac images are MRI and CT. Often, due to the heart motion, temporally resolved acquisitions are performed allowing to obtain 20-30 frames per heartbeat.

The main interest is for the left ventricle, due to its vital importance and to its pronounced thickness, ranging between 6 and 16 mm. The shape of its cavity is often approximated by an ellipsoid. Instead, the right ventricle and the atria are characterized by a thickness that usually does not reach the spatial resolution of the acquisition technologies, thus their reconstruction is hard and for this reason less studied.

The standard cardiac acquisition plane is orthogonal to the long (apex-base) axis (short axis plane). Blood appears brighter whereas the myocardium and the surrounding tissue darker, see Figure 16. Not all the slices on the short axis plane share the same degree of complexity in their reconstruction. In particular, apical and basal slices images are more difficult to segment than mid-ventricular ones.

Before the ventricle segmentation starts, a preliminary localization procedure is performed, in order to identify a region of interest and reduce the computational effort. This step is usually performed automatically, taking advantage of the movement of the heart on a fixed background, see, e.g., [110]. Another automatic heart location is based on extracting rectangular subwindows from the image and to compute for them specific features. Then, based on a priori chosen class, the subwindows satisfying specific features

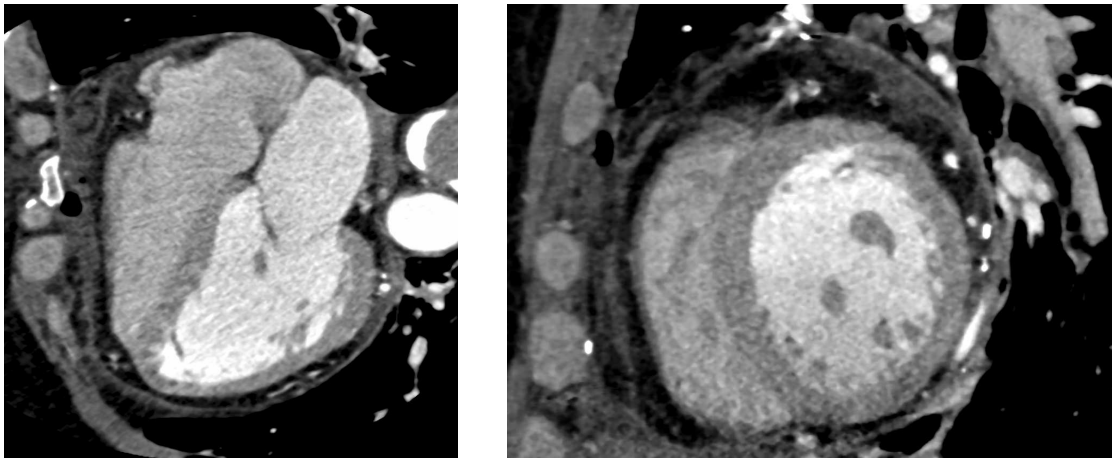

Figure 16: Left: Longitudinal CT slice of the heart. Right atrium (top left), right ventricle (bottom left), left atrium (top right), left ventricle (bottom right). Right: CT slice in the short axis plane. In both figures, on the right the thick left ventricle myocardium is detectable in darker grey. Radiological images from Ospedale Sacco, Milan, Italy

are recognized as belonging to the heart.

A first class of ventricle segmentation methods makes use of few (or even none) a priori information. Usually in these methods the endocardium is first segmented by means of thresholding (see Section 3 and refer, e.g., to [219]). Alternatively, *dynamic programming* methods have been considered, where the optimal path in a cost matrix, assigning a low cost to frontiers, is searched. Taking advantage of the circular shape of the ventricle, polar coordinates are used and one-dimensional search is performed [237]. In order to exclude papillary muscles in the segmentation, possible strategies are the computation of the convex hull of the contour [557] or a smoothing of the latter by means of the fitting of a parametric curve [582]. As for the vascular case, deformable models are used for cardiac segmentation (see Section 3). In particular, the functional to be minimized often includes a regularization term to control the smoothness of the reconstructed curves [451].

Specific automatic methods that have been developed for cardiac image segmentation are based on a strong a priori information on the shape of the ventricles that is included in the segmentation algorithm by means of statistical models. These strategies are suited for cardiac segmentation since the variability among patients of the heart shape is, unlike the arteries, very small in normal conditions. These statistical model-based segmentation strategies rely on identifying an average shape of available geometries forming a training set and on modeling the variability within the latter. This is usually done by means of the *principal component analysis* of positions and, in case, displacements, that allows to compute the eigenvalues and eigenvectors of the covariance matrix related to the training set. These strategies allow an automatic segmentation that does not need any interaction of the user, at the expense of having at disposal a training set. For example, deformable models have been extended to this framework by adding to the functional to be minimized

a term that penalizes the distance to a reference model (for example the mean shape of the training set). Another very common statistical model-based strategy is the *atlas-guided segmentation*. Given an atlas, i.e. an integrated image from multiple segmentations, a registration procedure is performed based on mapping the coordinates of the image under investigation to those of the atlas [341]. This transformation is then applied to the atlas obtaining the final segmentation. The registration process could be based on non-rigid transformations that account for elastic deformations. For a recent review of cardiac segmentation methods we refer to [449].

Finally, we observe the importance of including the fibers orientation in the reconstructed geometries in view of modeling the electrical propagation and mechanical contraction in the muscle region. Indeed, as discussed in Section 5, the conduction velocity of the action potential propagation assumes different values along the fibers than in the tangential direction. Moreover, the stretching ability of the myocardium is facilitated along the fibers direction.

Diffusion-tensor-MRI is a MRI technology able to identify the fibers orientation, however, not yet daily used in the clinical practice, and hardly applicable because of the heart movement. Since the fibers direction is unfortunately hardly detectable by the common radiological acquisition technologies, analytical representations of the fibers suitably mapped onto the geometry under investigation have been proposed so far to supply the lack of information provided by the imaging. For example, in [447] fibers are described as geodesics, whereas in [461] they are represented by means of spiral surfaces. Other strategies are based on a computational generation of the fibers orientation to provide a plausible configuration, e.g. by means of the solution of a Poisson equation [39, 496, 596], or by using the unscented Kalman filter [395].

As for the Purkinje fibers, they are not detectable from classical radiological acquisitions since their thickness falls below the spatial resolution. For this reason, in [1, 513, 276] it has been proposed to exploit the fractal nature of these fibers to generate a realistic Purkinje network, whereas in [567, 427, 428] such a fractal network has been personalized to the patient at hand by including patient-specific measures of the activation times (see Section 6.2 for a description of the latter).

For the muscle region mesh generation, the strategies described in Section 3 could be applied as well as to cardiac geometries. For ideal ellipsoid geometries, usually considered in numerical experiments to test the performance of the numerical algorithms, structured mesh of hexahedra are often used exploiting the symmetry of the ventricles around the long axis, see e.g. [436]. However, also unstructured meshes composed by tetrahedra have been considered so far [218], in particular for real geometries reconstructed by MRI or CT, see e.g. [496, 595, 566], or for the atria [575]. Hybrid unstructured meshes composed by tetrahedra and hexahedra have also been successfully considered [238]. We notice that for the solution of the mechanical problem in the muscle region, no particular requirements are needed for the mesh generation, whereas for the electrical propagation problem, due to the very steep front (about $200\,\mu m$), the required mesh resolution should be at least of the order of $100\,\mu m$ in order to spatially resolve this front [109]. For the mesh generation of the heart chambers in view of the numerical solution of the fluid-dynamic problem, often unstructured tetrahedral elements are considered, see e.g. [375]. In this case the mesh

resolution needs to be very fine, even smaller than the one of CT or MRI technologies ($\simeq 0.5\,mm$), in order to capture the complex flow structures arising in particular in the left atrium and left ventricle.

6.2 Cardiac boundary data

The acquisition of boundary data on the electrical activation in the muscle region is nowadays possible owing to specific therapeutic techniques. For example, the *NavX system*, is able to accurately locate any electrode catheter inserted in the heart chambers, providing accurate, real-time recording of the local endocardial electrical activity in a point in contact with the catheter [153, 567]. In particular, this allows one to acquire endocardial maps of the activation times, defined as the time at which the action potential in a point reaches an intermediate value between the rest and the plateau ones. However, this acquisition is performed only for specific therapeutic purposes, such as the ablation of anomalous electrical pathways.

For the mechanical problem involving the muscle region, commonly data that could be available are the stresses exerted by the blood on the endocardium of the left ventricle and the endocardial and/or epicardial vessel wall displacements. As for the first type of data, they are usually extracted from a measure of the aortic pressure (see Section 3.2). This represents a good approximation; as a matter of fact the ventricular and circulatory pressures are not the same (thus allowing the acceleration and decelaration of blood) but they are very similar, see Figure 13. As for the vessel wall displacements, they can be obtained from dynamic MRI or CT images, which allows one to have 20/30 frames per heartbeat, providing the position of the endocardium and epicardium at several instants. After suitable post-processing, these techniques can provide an estimate of the vessel wall displacement (and thus velocity) by comparing two consecutive frames. The endocardial vessel wall velocity, thanks to a continuity argument, could also be interpreted as the blood velocity at the interface with the endocardium [295, 375].

Another useful measure that could be provided quite easily by means of Doppler echocardiographic methods or PC-MRI (see Section 3.2) is the flow rate at the mitral and aortic valve orifices. With PC-MRI technology the measure of blood velocity is possible in principle in any point of the ventricles and atria chambers.

In Section 7 we will see how these data can be used to provide boundary conditions for the different cardiac models that we are about to introduce.

6.3 Cardiac biological data

The classical *monodomain* and *bidomain* models, widely used to describe the electrical propagation in the muscle region and Purkinje network (see Section 7.1), would require the following data: the membrane capacitance per unit area C, the membrane surface-to-volume ratio χ, and the conductivities σ (see next Section). Their subject-specific acquisition is in general out of reach. An acceptable range of values for the capacitance C_m in the myocardium is $(0.8-1.0)\,\mu F/cm^2$ [497, 269]; the capacitance C_p in the Purkinje network features a higher value ($\sim 1.3\,\mu F/cm^2$ [327]). The value of membrane surface-

to-volume ratio in the muscle region χ_m varies in the range $(200, 3000) cm^{-1}$ [403, 460], whereas for the Purkinje network, a measure in a porcine heart lead to $\chi_p = 1467\, cm^{-1}$ [523]. In the myocardium, we need to distinguish between the conductivities along the fibers direction (index f) and that in the direction of sheets (index s). Sometimes, also a third direction (orthogonal to sheets) is considered (if this is the case, we will use the index n). Moreover, in view of the bidomain model, we also distinguish between the intra-cellular (index i) and extra-cellular (index e) conductivities. Following [498], acceptable ranges used in the numerical experiments are: $\sigma_f^i \in (0.17, 0.34)\, (\Omega\, m)^{-1}$, $\sigma_s^i \in (0.02, 0.06)\, (\Omega\, m)^{-1}$, $\sigma_f^e \in (0.12, 0.62)\, (\Omega\, m)^{-1}$, $\sigma_s^e \in (0.08, 0.24)\, (\Omega\, m)^{-1}$.

Another classical model used so far to describe the activation of Purkinje and muscle cells is provided by the *Eikonal* equation (see Section 7.1). In this case, one needs to prescribe explicitly the conduction velocity V, unlike in the monodomain and bidomain models where this is determined by the conductivity and the membrane capacitance. Acceptable ranges of values of the conduction velocity are $V_f \in (0.6, 1.0)\, m/s$ [293], $V_s \simeq V_f/2$ [197], $V_n \simeq V_f/4$ [108], and $V_p \in (3.0 - 4.0)\, m/s$ [273], where again index f refers to the direction along the fibers in the muscle region, s to the direction along sheets, and p to the Purkinje network.

All these electrical data are hardly measurable in vivo so that no patient specific measures are usually available. Nevertheless, the use of extra data such as the activation time at the endocardium provided by the NavX system could be used to estimate some of these parameters by solving a suitable inverse problem, see e.g. [515, 567] for the case of the Purkinje network.

Regarding the parameters involved in the cardiac mechanic model, they depend on the chosen constitutive law. In general, the linearization of the stress-strain curves gives the following values for the corresponding varying-in-time Young modulus E [495]: during a traction/compression test along the fibers direction, we have $E \simeq 20\, kPa$ during traction at small deformation and during compression, and $E \simeq 1500\, kPa$ during traction for deformation of about 15%; during traction the material behaves as transversally isotropic so that the stiffness in the two tangential directions (along sheets and orthogonal to fibers and sheets) is the same, whereas during compression the stiffness in the sheets direction is higher than that in the direction orthogonal to fibers and sheets. As for the Poisson modulus, usually a value of 0.45 is considered.

Regarding the aortic valve leaflets, measures in dogs featured a low stiffness during systole ($\simeq 240\, kPa$) and an increased stiffness during diastole ($\simeq 5000\, kPa$). For the mitral valve, a different stiffness behavior is observed for the two leaflets (the anterior and the posterior ones). In particular, in [311] the following values of the Young modulus are proposed: for the anterior leaflet $E = 6200\, kPa$ and $E = 2100\, kPa$ in the directions parallel and perpendicular to the annulus, respectively, whereas for the posterior leaflet $E = 2300\, kPa$ and $E = 1900\, kPa$, respectively.

Blood in the heart features the same behavior than in the circulatory systems so that its parameters (density and viscosity) are taken in the ranges reported in Section 3.3.

7 Modeling the heart

In this section we discuss the main mathematical models introduced so far to describe the heart function and the related numerical strategies developed for their solution. In particular, Section 7.1 is devoted to the electrical propagation, Section 7.2 to the cardiac mechanics and electro-mechanical coupling, Section 7.3 to the ventricular fluid-dynamics, Section 7.4 to the valve modeling and its interaction with blood fluid-dynamics, and finally Section 7.5 to their integration.

7.1 Cardiac electric activity

7.1.1 The bidomain model

As observed in Section 5.3, the electric activation of the heart is the result of two processes: at the microscopic scales, the generation of ionic currents through the cellular membrane producing a local action potential, and at the macroscopic scales, the travelling of the action potential from cell to cell allowed by the presence of the gap junctions. The former is a discrete process, in the sense that there is a delay between the depolarization of a cardiomyocyte and its neighbours, whereas the latter can be assimilated to a smooth process [150].

At the macroscopic level, the propagation of the potentials is described by means of partial differential equations, suitably coupled with ordinary differential equations modeling the ionic currents in the cells. In particular, the single membrane cell can be modeled as a capacitor separating charges that accumulate at its *intracellular* and *extracellular* surfaces. Moreover, as observed in Section 5, ionic currents cross the membrane through suitable channels which open and close during the excitation. A suitable model can therefore be expressed by the simple electric circuit depicted in Figure 17, for which

$$I_m = \chi_m \left(C_m \frac{\partial V_m}{\partial t} + I_{ion} \right),$$

where I_m is the membrane current per unit volume, C_m the membrane capacitance, χ_m the surface area-to-volume ratio (see Section 6.3 for a quantification of the latter two), $V_m(t, \boldsymbol{x})$ the transmembrane potential, and $I_{ion}(t, \boldsymbol{x})$ the ionic currents. Due to the conservation of current and charge, this current should equal the divergence of both the intracellular and extracellular current fluxes $\boldsymbol{j}_i$ and $\boldsymbol{j}_e$

$$\nabla \cdot \boldsymbol{j}_i = -I_m, \qquad \nabla \cdot \boldsymbol{j}_e = I_m. \tag{71}$$

The Ohm's law in the intracellular and extracellular regions give

$$\boldsymbol{j}_i = -\boldsymbol{\Sigma}_i \nabla \phi_i, \qquad \boldsymbol{j}_e = -\boldsymbol{\Sigma}_e \nabla \phi_e, \tag{72}$$

$\boldsymbol{\Sigma}_i$, $\boldsymbol{\Sigma}_e$ being the conductivity tensors and $\phi_i(t, \boldsymbol{x})$, $\phi_e(t, \boldsymbol{x})$ the intracellular and extracellular potentials, so that

$$V_m = \phi_i - \phi_e. \tag{73}$$

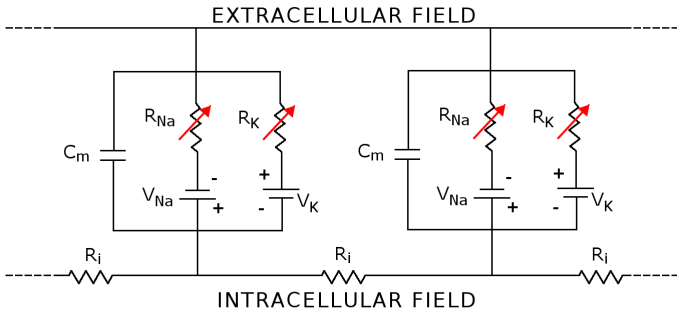

Figure 17: Electric circuit for the sequence of two cardiac cells. Each of them is composed by a capacitor and a series of resistances, one for each ionic current (here only sodium and potassium ionic channels are depicted). In the intracellular region, two adjacent cells are connected by a resistance representing a gap junction. However, the latter is not explicitly modeled at the macroscopic scales, rather its effect is hidden in the conductivity tensor, see the text

Notice that, due to the anisotropy of the cardiac tissue induced by the presence of fibers and sheets, each conductivity tensor is in general expressed in terms of three scalar quantities representing the conductivities along the fiber direction $\boldsymbol{a}_f(\boldsymbol{x})$, the direction $\boldsymbol{a}_s(\boldsymbol{x})$ orthogonal to $\boldsymbol{a}_f$ and tangential to sheets, and the direction $\boldsymbol{a}_n(\boldsymbol{x})$ orthogonal to sheets, i.e.

$$\boldsymbol{\Sigma}_\beta = \sigma_f^\beta \boldsymbol{a}_f \boldsymbol{a}_f^T + \sigma_s^\beta \boldsymbol{a}_s \boldsymbol{a}_s^T + \sigma_n^\beta \boldsymbol{a}_n \boldsymbol{a}_n^T, \quad \beta = i, e. \tag{74}$$

Putting together all the previous equations and using a homogenization procedure (see e.g. [118] for a rigorous derivation), we obtain for each $t > 0$ the following system of two partial differential equations called *parabolic-parabolic (PP) formulation of the bidomain* equations:

$$\chi_m C_m \frac{\partial V_m}{\partial t} - \nabla \cdot (\boldsymbol{\Sigma}_i \nabla \phi_i) + \chi_m I_{ion} = I_i^{ext} \qquad \text{in } \Omega_{mus}, \tag{75a}$$

$$-\chi_m C_m \frac{\partial V_m}{\partial t} - \nabla \cdot (\boldsymbol{\Sigma}_e \nabla \phi_e) - \chi_m I_{ion} = -I_e^{ext} \qquad \text{in } \Omega_{mus}, \tag{75b}$$

where $I_i^{ext}(t, \boldsymbol{x})$, $I_e^{ext}(t, \boldsymbol{x})$ are applied currents per unit volume.

Thanks to (71), $\nabla \cdot (\boldsymbol{j}_i + \boldsymbol{j}_e) = 0$; thus, using (72) and (73), we obtain the following *parabolic-elliptic (PE) formulation of the bidomain* equations:

$$\chi_m C_m \frac{\partial V_m}{\partial t} - \nabla \cdot (\boldsymbol{\Sigma}_i (\nabla \phi_e + \nabla V_m)) + \chi_m I_{ion} = I_i^{ext} \qquad \text{in } \Omega_{mus}, \tag{76a}$$

$$-\nabla \cdot (\boldsymbol{\Sigma}_i \nabla V_m) - \nabla \cdot ((\boldsymbol{\Sigma}_i + \boldsymbol{\Sigma}_e) \nabla \phi_e) = I_i^{ext} - I_e^{ext} \qquad \text{in } \Omega_{mus}. \tag{76b}$$

Due to the homogenization procedure, the effect of the gap junctions, which at the cellular level contributes in determining the current flux $\boldsymbol{j}_i$, is hidden in the conductivity

tensor $\mathbf{\Sigma}_i$. We also notice that both bidomain problems (75) and (76) hold in the whole computational domain Ω_{mus} given by the union of the myocardium with endocardium and epicardium, see Figure 15. Indeed, again because of the homogenization procedure, no

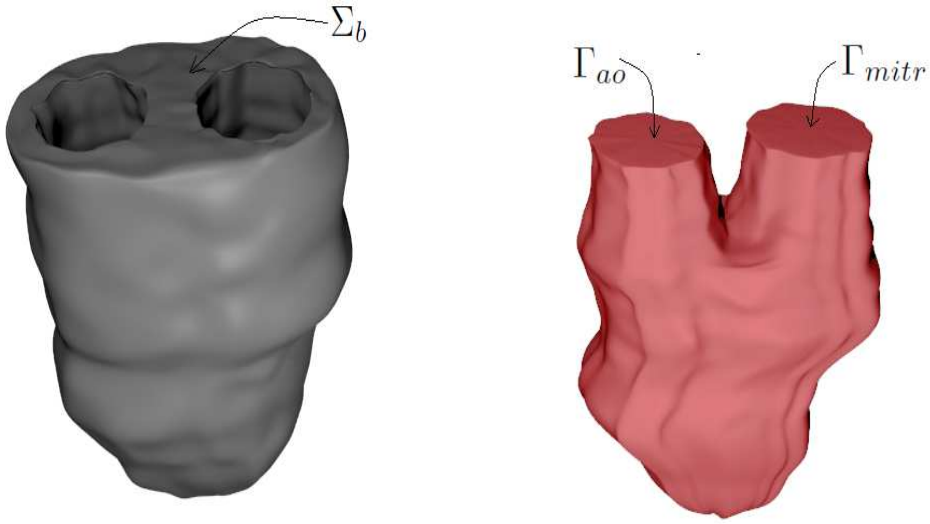

Figure 18: Left ventricular myocardial domain obtained by the cut at the basis (left), and corresponding fluid cavity domain (right)

geometrical distinction is made between the intracellular and extracellular regions, even if their different functionality is maintained in the bidomain models.

7.1.2 Cardiac cell models

In order to close equations (75) and (76) we need to provide a model for the ionic current I_{ion}. In what follows we briefly describe three families of models, featuring different levels of complexity and accuracy.

The first family, the so-called *reduced ionic models* only provide a description of the action potential and disregard sub-cellular processes:

$$I_{ion} = f(V_m, \boldsymbol{w}), \tag{77a}$$

$$\frac{\partial \boldsymbol{w}}{\partial t} = \boldsymbol{g}_w(V_m, \boldsymbol{w}), \tag{77b}$$

where $f, \boldsymbol{g}_w$ are suitable functions, while $\boldsymbol{w} : [0,T] \times \Omega_{mus} \to \mathbb{R}^M$ collects the so-called *gating variables* which represent the percentage of open channels per unit area of the membrane. The most celebrated reduced model for ventricular cells is *FitzHugh-Nagumo*'s [182] where $f(V_m, w) = -kV_m(V_m - a)(V_m - 1) - w$ and $g_w(V_m, w) = \epsilon(V_m - \gamma w)$, for suitable constant parameters k, a, γ. In this case the gating variable w plays in fact the role of a *recovery* function that allows to model the refractariness of cells. Other, more sophisticated ventricular cell models of this family are, e.g., the *Roger-McCulloch* [494], the *Aliev-Panfilov* [5], the *Fenton-Karma* [172], and the *Bueno-Orovio* [78] models.

Like FitzHugh-Nagumo's, the first two models are characterized by the dynamics of one gating variable and by a cubic non-linear expression of the ionic current. Instead, the Fenton-Karma model and its Bueno-Orovio variant specifically addressed for the human ventricular cells, feature two and three gating variables, respectively, and a more complex non-linearity in the ionic current expression. These simple models are very appealing, especially because their parameters have a direct physical interpretation, such as the action potential duration, allowing for an easy setting of the model properties. For example, the Aliev-Panfilov model has been used successfully in the first simulations of ventricular fibrillation in a real geometry [429]. However, they are not able to describe any process occurring at the level of the ionic channels and of the cell, so that they are recommended when one is only interested in the heart electric activity.

The second family of ventricular cell models we consider is that of the so-called *first-generation* models. Unlike reduced models that surrogate the ionic current by means of the sole function f, they allow for an explicit description of the kinetics of different ionic currents by using several gating variables. They read

$$I_{ion} = \sum_{k=1}^{N} I_k(V_m, \boldsymbol{w}), \quad I_k = G_k \left(\prod_{j=1}^{M} w_j^{p_{j_k}} \right) (V_m - V_k), \quad \frac{\partial \boldsymbol{w}}{\partial t} = \boldsymbol{g}_w(V_m, \boldsymbol{w}),$$

where N is the total number of ionic currents and M the total number of gating variables, V_k is the Nernst potential of the $k-th$ ion (a constant value corresponding to the thermodynamical equilibrium of the ion at hand), I_k is the current related to the $k-th$ ion, p_{j_k} accounts for the influence of the $j-th$ gating variable on the $k-th$ ionic current (possibly vanishing), G_k is the maximal conductance of the $k-th$ ion. The M components of $\boldsymbol{g}$ usually have the expression $g_{w,j} = (w_j^\infty(V_m) - w_j)/\tau_j(V_m)$, where w_j^∞ is the equilibrium state and τ_j the characteristic time constant. The most famous model of this family, *Hodgkin-Hukley*'s (HH) [254], depends on three ionic currents, namely the sodium, potassium and leakage ones, and three gating variables

$$I_{Na} = G_{Na} w_1^3 w_2 (V_m - V_{Na}), \quad I_K = G_K w_3^4 (V_m - V_K), \quad I_L = G_L(V_M - V_L).$$

Although introduced to describe the action potentials in nerves, the HH model inspired all the following models introduced specifically for the ventricle. Among these, we cite the *Beeler-Reuter* [43], the *Luo-Rudy I* [343], and the *TenTusscher-Panfilov* [554] models. These models were widely used to study specific features of the ventricular electric activation, such as re-entry and fibrillation [598].

Finally, we mention the family of the *second-generation* ventricular cell models, like the *Luo-Rudy dynamic* model [344, 345], where, unlike in first-generation models, a detailed description of some ion concentration variables $\boldsymbol{c}$ is provided. They provide a detailed description of many processes allowing for the study, e.g., of channelopathies and of drug action. However, due to their increased complexity, the required computational time is very huge for a complete heart model and often the tuning of the parameters is very demanding. We refer to [109] for a discussion of second-generation models and to [501] for a general review of cardiac cell models.

Although most of research studies focused on ventricular cell models as those mentioned above, specific models have been introduced also for the atrial cells, see e.g. [249], and for the sinoatrial node cells, see e.g. [605].

All the cardiac cell models belonging to the three families described above, used in combination with the bidomain problem (75) or (76), leads to a system of two PDEs coupled with two systems of ODEs, i.e. the equations for the gating variables and ion concentrations written for each point $\boldsymbol{x}$ (the latter, in case, vanishing). The general expression of such coupled problem reads (we only detail the PP case): Find at each time $t > 0$ the potentials V_M, ϕ_i and ϕ_e, the gating variable $\boldsymbol{w}$ and the ion concentrations $\boldsymbol{c}$ such that

$$\chi_m C_m \frac{\partial V_m}{\partial t} - \nabla \cdot (\boldsymbol{\Sigma}_i \nabla \phi_i) + \chi_m I_{ion}(V_m, \boldsymbol{w}, \boldsymbol{c}) = I_i^{ext} \qquad \text{in } \Omega_{mus}, \tag{79a}$$

$$-\chi_m C_m \frac{\partial V_m}{\partial t} - \nabla \cdot (\boldsymbol{\Sigma}_e \nabla \phi_e) - \chi_m I_{ion}(V_m, \boldsymbol{w}, \boldsymbol{c}) = -I_e^{ext} \qquad \text{in } \Omega_{mus}, \tag{79b}$$

$$I_{ion} = \sum_{k=1}^{N} I_k(V_m, \boldsymbol{w}, \boldsymbol{c}) \qquad \text{in } \Omega_{mus}, \tag{79c}$$

$$I_k = G_k \left(\prod_{j=1}^{M} w_j^{p_{j_k}} \right) (V_m - V_k(\boldsymbol{c})) \qquad \text{in } \Omega_{mus}, \tag{79d}$$

$$\frac{\partial \boldsymbol{w}}{\partial t} = \boldsymbol{g}_w(V_m, \boldsymbol{w}) \qquad \text{in } \Omega_{mus}, \tag{79e}$$

$$\frac{\partial \boldsymbol{c}}{\partial t} = \boldsymbol{g}_c(V_m, \boldsymbol{w}, \boldsymbol{c}) \qquad \text{in } \Omega_{mus}, \tag{79f}$$

where, together with the notation introduced above for the reduced and first-generation models, $\boldsymbol{c} : [0, T] \times \Omega_{mus} \to \mathbb{R}^S$ collects the S ionic concentration variables and $\boldsymbol{g}_c$ is a suitable function, see e.g. [118]. We observe, in general, the dependence of the Nernst potential V_k on the variable $\boldsymbol{c}$. Well-posedness results of the previous coupled problem are provided, e.g., in [121], where the existence and uniqueness of the solution of the PP formulation coupled with the FitzHugh-Nagumo model is proved, and in [76], where a Faedo-Galerkin technique is applied to the PE formulation coupled with a general first-generation cell model.

The ODE systems modeling the gating variables and the ionic concentrations variables are in general stiff since the Jacobians $\partial \boldsymbol{g}_w / \partial \boldsymbol{w}$ and $\partial \boldsymbol{g}_c / \partial \boldsymbol{c}$ feature a wide range of eigenvalues.

For each $t > 0$, the weak formulation of the bidomain model (79) together with homogeneous Neumann conditions and initial conditions (see Section 7.1.4) reads: Given $I_i^{ext}(t)$, $I_e^{ext}(t) \in L^2(\Omega_{mus})$, find $V_m(t), \phi_e(t), \phi_i(t) \in H^1(\Omega_{mus})$, $\boldsymbol{w} \in [L^2(\Omega_{mus})]^M$ and

$\boldsymbol{c} \in [L^2(\Omega_{mus})]^S$ such that

$$\chi_m C_m \int_{\Omega_{mus}} \frac{\partial V_m}{\partial t} z \, d\omega + \int_{\Omega_{mus}} \boldsymbol{\Sigma}_i \nabla \phi_i \cdot \nabla z \, d\omega + \chi_m \int_{\Omega_{mus}} I_{ion}(V_m, \boldsymbol{w}, \boldsymbol{c}) z \, d\omega = \int_{\Omega_{mus}} I_i^{ext} z \, d\omega, \tag{80a}$$

$$-\chi_m C_m \int_{\Omega_{mus}} \frac{\partial V_m}{\partial t} z \, d\omega + \int_{\Omega_{mus}} \boldsymbol{\Sigma}_e \nabla \phi_e \cdot \nabla z \, d\omega - \chi_m \int_{\Omega_{mus}} I_{ion}(V_m, \boldsymbol{w}, \boldsymbol{c}) z d\omega = -\int_{\Omega_{mus}} I_e^{ext} z d\omega, \tag{80b}$$

$$\int_{\Omega_{mus}} \frac{\partial \boldsymbol{w}}{\partial t} \cdot \boldsymbol{y} \, d\omega = \int_{\Omega_{mus}} \boldsymbol{g}(V_m, \boldsymbol{w}) \cdot \boldsymbol{y} \, d\omega, \tag{80c}$$

$$\int_{\Omega_{mus}} \frac{\partial \boldsymbol{c}}{\partial t} \cdot \boldsymbol{\zeta} \, d\omega = \int_{\Omega_{mus}} \boldsymbol{g}_c(V_m, \boldsymbol{w}, \boldsymbol{c}) \cdot \boldsymbol{\zeta} \, d\omega, \tag{80d}$$

for all $z \in H^1(\Omega_{mus})$, $\boldsymbol{y} \in [L^2(\Omega_{mus})]^M$ and $\boldsymbol{\zeta} \in [L^2(\Omega_{mus})]^S$, together with (79c)-(79d).

7.1.3 Reduced continuous models: the monodomain and Eikonal equations

To reduce the complexity of the bidomain models (75) and (76), an assumption of proportionality between the intracellular and extracellular conductivities, i.e. $\boldsymbol{\Sigma}_e = \lambda \boldsymbol{\Sigma}_i$ for a suitable constant λ, is introduced. Substituting this relation in (76b), eliminating $\boldsymbol{\Sigma}_e$ and substituting the corresponding relation for $\boldsymbol{\Sigma}_i$ in (76a), we obtain the *monodomain* equation: Find for each $t > 0$ the transmembrane potential V_m such that

$$\chi_m C_m \frac{\partial V_m}{\partial t} - \nabla \cdot (\boldsymbol{\Sigma} \nabla V_m) + \chi_m I_{ion} = I^{ext} \quad \text{in } \Omega_{mus}, \tag{81}$$

where

$$\boldsymbol{\Sigma} = \frac{\lambda}{1+\lambda} \boldsymbol{\Sigma}_i \tag{82}$$

is the effective conductivity and $I^{ext} = \frac{\lambda I_i^{ext} + I_e^{ext}}{1+\lambda}$. Again, a ventricular cell model is needed to provide the ionic current I_{ion}. The same models discussed above for the coupling with the bidomian problem are used in combination with the monodomain problem as well. Once the transmembrane potential V_m has been computed, the extracellular potential ϕ_e could be computed as a post-processing by solving the elliptic problem (76b).

For each $t > 0$, the weak formulation of the monodomain problem (81) together with homogeneous Neumann conditions and initial conditions (see Section 7.1.4) reads: Given $I^{ext}(t) \in L^2(\Omega_{mus})$, find $V_m(t) \in H^1(\Omega_{mus})$, $\boldsymbol{w} \in [L^2(\Omega_{mus})]^M$ and $\boldsymbol{c} \in [L^2(\Omega_{mus})]^S$ such

that

$$\chi_m C_m \int_{\Omega_{mus}} \frac{\partial V_m}{\partial t} z \, d\omega + \int_{\Omega_{mus}} \boldsymbol{\Sigma} \nabla V_m \cdot \nabla z \, d\omega + \chi_m \int_{\Omega_{mus}} I_{ion}(V_m, \boldsymbol{w}, \boldsymbol{c}) z \, d\omega = \int_{\Omega_{mus}} I^{ext} z \, d\omega, \tag{83a}$$

$$\int_{\Omega_{mus}} \frac{\partial \boldsymbol{w}}{\partial t} \cdot \boldsymbol{y} \, d\omega = \int_{\Omega_{mus}} \boldsymbol{g}(V_m, \boldsymbol{w}) \cdot \boldsymbol{y} \, d\omega, \tag{83b}$$

$$\int_{\Omega_{mus}} \frac{\partial \boldsymbol{c}}{\partial t} \cdot \boldsymbol{\zeta} \, d\omega = \int_{\Omega_{mus}} \boldsymbol{g}_c(V_m, \boldsymbol{w}, \boldsymbol{c}) \cdot \boldsymbol{\zeta} \, d\omega, \tag{83c}$$

for all $z \in H^1(\Omega_{mus})$, $\boldsymbol{y} \in [L^2(\Omega_{mus})]^M$ and $\boldsymbol{\zeta} \in [L^2(\Omega_{mus})]^S$, together with (79c)-(79d).

Although the hypothesis underlying the monodomain model, i.e. the proportionality between the internal and external conductivities, is not physiological as shown by some experiments, in some cases this model provides a very accurate solution in comparison with the bidomain one. In particular, this is true when there is no injection of current in the extracellular region [120, 460]. On the contrary, when an external current is injected such as in defibrillation, the monodomain solution is not anymore accurate and the bidomain model is mandatory since the unequal anisotropy is fundamental to successfully describe these scenarios [548].

A further simplification is provided by the *eikonal* equation. Starting from the bidomain model coupled with a simplified representation of the ionic current which does not consider any gating variable and allows for the description only of the depolarization phase, in [115] the following *eikonal-diffusion* equation is derived:

$$c_o \sqrt{\nabla \psi \cdot \boldsymbol{M} \nabla \psi} - \nabla \cdot (\boldsymbol{M} \nabla \psi) = 1, \tag{84}$$

where $\psi(\boldsymbol{x})$ is the unknown *activation time* (see Section 6.2), c_o represents the velocity of the depolarization wave along the fiber direction for a planar wavefront and $\boldsymbol{M} = \boldsymbol{\Sigma}/(\chi C_m)$. A different derivation has been provided in [286], leading to the following *eikonal-curvature* equation

$$c_o \sqrt{\nabla \psi \cdot \boldsymbol{M} \nabla \psi} - \sqrt{\nabla \psi \cdot \boldsymbol{M} \nabla \psi} \nabla \cdot \left(\frac{\boldsymbol{M} \nabla \psi}{\sqrt{\nabla \psi \cdot \boldsymbol{M} \nabla \psi}} \right) = 1. \tag{85}$$

They are both steady equations providing an information on the activation of each cell. The contours of $\psi(\boldsymbol{x})$ give the position of the wavefront at time $t = \psi$. The eikonal-diffusive model (84) is an elliptic equation, where the propagation speed is influenced by the tissue surrounding the wavefront. Once the activation time ψ has been computed, it is possible to obtain an approximate value of the extracellular potential ϕ_e by solving at each time step a suitable elliptic problem, see [114].

Instead, the eikonal-curvature model (85) is of parabolic type since the "diffusive" term lacks the second drivative in the direction of propagation. This term is also proportional to an anisotropic generalization of the mean curvature [546]. This implies that the propagation is faster when the wavefront is concave. This is in accordance with the diffusion

of charge which allows for a faster depolarization in regions close to already depolarized tissues.

The eikonal equations are unsuitable for recovering the action potential and the ionic currents. However, they provide accurate results about the activation of cells even in complex scenarios such as front-front collision, see e.g. [114] for the eikonal-diffusive model.

The eikonal models are however very appealing from the computational point of view. First of all, they consist in a single steady PDE. Although being non-linear, it does not require to manage the coupling with the ODE systems. More importantly, the activation time, unlike the transmembrane potential, does not feature any internal or boundary layer, so that no special restriction on the mesh is needed in this case (see Section 6.1).

7.1.4 Boundary conditions and Purkinje network models

We discuss here the initial and boundary conditions of the problems introduced above. The bidomain and monodomain equations and the ODE systems for the gating variables and ionic concentrations need to be equipped with suitable initial conditions, i.e.

$$V_m|_{t=0} = V_{m,0}, \qquad \boldsymbol{w}|_{t=0} = \boldsymbol{w}_0, \qquad \boldsymbol{c}|_{t=0} = \boldsymbol{c}_0 \qquad \text{in } \Omega_{mus},$$

for given functions $V_{m,0}(\boldsymbol{x}), \boldsymbol{w}_0(\boldsymbol{x}), \boldsymbol{c}_0(\boldsymbol{x})$.

Regarding boundary conditions for the bidomain, monodomain and eikonal-diffusion problems, a homogeneous Neumann condition is commonly prescribed at the external surface Σ_{epi} of the epicardium and, in case of a ventricular domain solely, at the basis Σ_b (see Figures 15 and 18, left) to prescribe null outgoing current fluxes. In particular, the following conditions have to be prescribed on $\Sigma_{epi} \cup \Sigma_b$:

$$\begin{aligned}
&(\boldsymbol{\Sigma}_\beta \nabla \phi_\beta) \cdot \boldsymbol{n} = 0 \quad \beta = i, e && \text{for the PP formulation (75),}\\
&\left.\begin{aligned}&(\boldsymbol{\Sigma}_i \nabla (V_m + \phi_e)) \cdot \boldsymbol{n} = 0\\ &((\boldsymbol{\Sigma}_i + \boldsymbol{\Sigma}_e)\nabla \phi_e) \cdot \boldsymbol{n} + (\boldsymbol{\Sigma}_i \nabla V_m) \cdot \boldsymbol{n} = 0\end{aligned}\right\} && \text{for the PE formulation (76),}\\
&(\boldsymbol{\Sigma} \nabla V_m) \cdot \boldsymbol{n} = 0 && \text{for the monodomain problem (81),}\\
&(\boldsymbol{M} \nabla \psi) \cdot \boldsymbol{n} = 0 && \text{for the eikonal-diffusion problem (84).}
\end{aligned}$$

Moreover, for the bidomain problems (75) and (76), they force the following compatibility conditions on the applied external currents:

$$\int_{\Omega_{mus}} I_i^{ext} = \int_{\Omega_{mus}} I_e^{ext}.$$

On the internal surface Σ_{endo} of the endocardium, again Neumann conditions are prescribed. In this case, however, they could be non-homogeneous at specific stimulation points (e.g. the atrio-ventricular node and the points of the His bundle). For the eikonal problem, Dirichlet data on the activation time could be prescribed at some specific locations in case they are available thanks to e.g. the NavX system (see Section 6.2) [515]. When redundant (e.g. in presence of the Purkinje network, see below) these data have

been used to solve inverse problems, for example to estimate the conduction velocity in the myocardium [515] or to obtain personalized Purkinje networks [567, 427, 428].

If the mathematical model accounts for the presence of the Purkinje network, interface conditions on Σ_{endo} describing the continuity of the current and of the potential at the PMJ are implicitly provided for the bidomain and monodomain problems by the solution of the coupled muscle region/Purkinje network problem [572, 566]. For the sake of exposition, we do not detail here the bidomain and monodomain models for the Purkinje network, referring the interested readers to [572, 72, 566]. We only notice that, unlike the muscular case, in the network the gap junctions connecting two consecutive Purkinje cells are often explicitly modeled by means of resistances. Specific Purkinje cell models, with the same structure of those developed for the muscular cells, have also been developed, see e.g. [140]. However, we describe here the mechanisms of coupling, in particular, we refer to the coupled problem obtained by considering the monodomain problem both in the muscle region and in the Purkinje network [566]. We consider N PMJ located at $\boldsymbol{x} = \boldsymbol{s}_j$ and we assume that each of them could be modeled by means of a resistance R_{PMJ}. Then, the *monodomain/monodomain coupled problem* reads: Find for each $t > 0$, V_p, V_m, $\boldsymbol{w}_p$, $\boldsymbol{w}$ and γ_j, $j = 1, \ldots, N$, such that:

$$P_m\left(V_m, \boldsymbol{w}, \sum_{j=1}^{N} \frac{1}{A_r} \mathcal{I}_{\mathcal{B}_r(\boldsymbol{s}_j)} \gamma_j + I^{ext}\right) = 0, \tag{86a}$$

$$P_p\left(V_p, \boldsymbol{w}_p, \boldsymbol{\gamma}\right) = 0, \tag{86b}$$

$$\gamma_j = \frac{V_p(\boldsymbol{s}_j) - \frac{1}{A_r}\int_{\mathcal{B}_r(\boldsymbol{s}_j)} V_m \, d\boldsymbol{x}}{R_{PMJ}} \quad j = 1, \ldots, N, \tag{86c}$$

where $P_m\left(V_m, \boldsymbol{w}, F\right) = 0$ represents the monodomain problem in the myocardium with source term F, $P_p\left(V_p, \boldsymbol{w}_p, \boldsymbol{\eta}\right) = 0$ the monodomain problem in the Purkinje network with Neumann conditions with data η_j at the PMJ, V_p and $\boldsymbol{w}_p$ are the transmembrane potential and the gating variables in the Purkinje network, γ_j are the PMJ currents which are determined by the Ohm's laws (86c), $\mathcal{I}_Y$ is the characteristic function related to the region $Y \subset \Omega_{mus}$, $\mathcal{B}_r(\boldsymbol{s}_j)$ is the ball of radius r centered at the point $\boldsymbol{s}_j$ and A_r the volume of this ball. We observe that the two monodomain problems are coupled by means of the PMJ currents γ_j: for the 3D problem the latter act as source terms distributed in balls of radius r, whereas for the network they act as Neumann conditions [72]. A similar approach could be considered for the bidomain problems as well.

The coupling between eikonal muscular and Purkinje network problems has been addressed in [567] for normal propagation and in [427] for pathological propagations.

7.1.5 Computing the surface electrocardiogram signals

The computation of the potentials related to the electric propagation in the heart could be used to numerically compute the surface electrocardiogram (ECG) signals, i.e. the electric potential on the surface of the body, thus simulating what happens in the common clinical practice. This could be obtained by coupling the bidomain or monodomain problem with

the propagation in the torso, modeled by a simple diffusion problem for the extracellular potential at each $t > 0$:

$$\nabla \cdot (\boldsymbol{\Sigma}_T \nabla \phi_T) = 0 \qquad \text{in } \Omega_T,$$

where Ω_T is the torso domain that surrounds the heart domain Ω_{mus} (i.e. all the heart boundary surface $\Sigma_{epi} \cup \Sigma_b$ represents the interface with the torso), $\Omega_T \cap \Omega_{mus} = \emptyset$, with ϕ_T representing the extracellular potential in the torso. Homogeneous Neumann conditions have to be applied on the external torso surface Σ_T, whereas the following interface conditions, that replace the boundary conditions for the heart problem, need to be prescribed at the torso/heart interface:

$$\begin{aligned}
&\phi_e = \phi_T && \text{on } \Sigma_{epi} \cup \Sigma_b, \\
&(\boldsymbol{\Sigma}_e \nabla \phi_e) \cdot \boldsymbol{n} = (\boldsymbol{\Sigma}_T \nabla \phi_T) \cdot \boldsymbol{n} && \text{on } \Sigma_{epi} \cup \Sigma_b, \\
&(\boldsymbol{\Sigma}_i \nabla (V_m + \phi_e)) \cdot \boldsymbol{n} = 0 && \text{on } \Sigma_{epi} \cup \Sigma_b.
\end{aligned}$$

7.1.6 Numerical discretization

The numerical solution of the bidomain and monodomain problems is very demanding. Together with the strict constraint on the spatial mesh size due to the propagation of a very steep front (see Section 6.1), a time step of the order of dozens or even hundredths of milliseconds has to be used in order to capture the fast dynamics characterizing the propagation, with time constants of the order of $0.1\,ms$. Moreover, as discussed below, the algebraic solution of the linear systems arising at each time step using e.g. Finite Elements requires a careful treatment due to the coupled nature of the problem, to the singularity of some of the matrices involved, and to the presence of the non-linear term due to the ionic currents.

Several time discretizations strategies have been considered so far. We can gather them into four main categories, i.e. *explicit*, *semi-implicit*, *implicit* and *operator splitting-based* methods, which are now briefly presented. We start by introducing the Finite Element matrices and vectors:

$$\begin{aligned}
(M)_{jk} &= \int_{\Omega_{mus}} \psi_k \psi_j \, d\omega, \\
(A_\beta)_{jk} &= \int_{\Omega_{mus}} \boldsymbol{\Sigma}_\beta \nabla \psi_k \cdot \nabla \psi_j \, d\omega, \ \beta = i, e \\
(\boldsymbol{I}_{ion}(\boldsymbol{V}_m^n, \boldsymbol{W}^r, \boldsymbol{C}^s))_j &= \int_{\Omega_{mus}} I_{ion}(V_m^n, \boldsymbol{w}^r, \boldsymbol{c}^s) \psi_j \, d\omega, \\
(\boldsymbol{G}(\boldsymbol{V}_m^n, \boldsymbol{W}^r))_j &= \int_{\Omega_{mus}} \boldsymbol{g}(V_m^n, \boldsymbol{w}^r) \cdot \boldsymbol{y}_j \, d\omega, \\
(\boldsymbol{S}(\boldsymbol{V}_m^n, \boldsymbol{W}^r, \boldsymbol{C}^s))_j &= \int_{\Omega_{mus}} \boldsymbol{g}_c(V_m^n, \boldsymbol{w}^r, \boldsymbol{c}^s) \cdot \boldsymbol{\zeta}_j \, d\omega,
\end{aligned}$$

with ψ_i, $\boldsymbol{y}_j$ and $\boldsymbol{\zeta}_j$ denoting the basis functions of the Finite Element spaces, and n, r, s integers representing the time discrete instants. Vectors $\boldsymbol{V}_m$, $\boldsymbol{\Phi}_e$, $\boldsymbol{\Phi}_i$, $\boldsymbol{W}$ and $\boldsymbol{C}$ denote the unknown coefficients of the Finite Elements solutions associated to the unknowns V_m, ϕ_e, ϕ_i, $\boldsymbol{w}$, $\boldsymbol{c}$. Notice that the dimension of $\boldsymbol{W}$ and $\boldsymbol{C}$ is MK and SK, respectively,

where K is the number of degrees of freedom associated with the mesh and the choice of Finite Elements (e.g. the number of vertices for linear FE). In all the cases, in order to simplify the notation, we will set $I_e^{ext} = I_i^{ext} = 0$ and we assume that the running temporal index $^{n+1}$ is understood.

Explicit methods. In explicit methods, all the problems in (80) are discretized by means of an explicit scheme, e.g. forward Euler both for the PDEs and for the ODE systems, [466, 161]. This choice allows to decouple the 4 blocks of the bidomain system (the two PDEs and the two ODEs system), involving in the PP formulation only the mass matrix, thus in principle avoiding the need to solve any linear system provided that the mass-lumping is performed. Instead, for the PE formulation, the absence of time derivative in the second PDE implies that a linear system in the unknown $\boldsymbol{\Phi}_e$ needs in any case to be solved (we detail the forward Euler method):

$$
\begin{aligned}
&\chi_m C_m M \frac{\boldsymbol{V}_m - \boldsymbol{V}_m^n}{\Delta t} = -A_i(\boldsymbol{V}_m^n + \boldsymbol{\Phi}_e^n) - \chi_m \boldsymbol{I}_{ion}(\boldsymbol{V}_m^n, \boldsymbol{W}^n, \boldsymbol{C}^n),\\
&A_i \boldsymbol{V}_m + (A_i + A_e)\boldsymbol{\Phi}_e = \boldsymbol{0},\\
&M\frac{\boldsymbol{W} - \boldsymbol{W}^n}{\Delta t} = \boldsymbol{G}(\boldsymbol{V}_m^n, \boldsymbol{W}^n), \qquad M\frac{\boldsymbol{C} - \boldsymbol{C}^n}{\Delta t} = \boldsymbol{S}(\boldsymbol{V}_m^n, \boldsymbol{W}^n, \boldsymbol{C}^n).
\end{aligned}
$$

Explicit methods lead to a severe constraint on the time discretization of the type $\Delta t < h^2/\Sigma$, Σ being a representative value of the conductivity [466]. In [507], it has been shown for a model problem that an explicit method is not absolutely stable for a value of Δt much smaller than the one required to capture the front propagation. For this reason and due to the increased CPU availability, nowadays explicit methods are not so much used.

Semi-implicit methods. ODE systems are usually solved at each time step by means of explicit or semi-implicit methods (in the latter case the dependence on V_m is treated explicitly). This suggests to use semi-implicit methods [287, 440, 117] for the whole coupled PDEs/ODEs problem. These methods are the most used together with operator splitting-based ones (see below). They are based on treating implicitly the diffusive term and explicitly the non-linear term. A possible semi-implicit (first order) scheme for the PP formulation (80) reads as follows (see e.g. [117]):

$$
\begin{aligned}
&M\frac{\boldsymbol{W} - \boldsymbol{W}^n}{\Delta t} - \boldsymbol{G}(\boldsymbol{V}_m^n, \boldsymbol{W}) = \boldsymbol{0}, \qquad M\frac{\boldsymbol{C} - \boldsymbol{C}^n}{\Delta t} - \boldsymbol{S}(\boldsymbol{V}_m^n, \boldsymbol{W}, \boldsymbol{C}) = \boldsymbol{0},\\
&\chi_m C_m M \frac{\boldsymbol{V}_m - \boldsymbol{V}_m^n}{\Delta t} + A_i \boldsymbol{\Phi}_i + \chi_m \boldsymbol{I}_{ion}(\boldsymbol{V}_m^n, \boldsymbol{W}, \boldsymbol{C}) = \boldsymbol{0},\\
&-\chi_m C_m M \frac{\boldsymbol{V}_m - \boldsymbol{V}_m^n}{\Delta t} + A_e \boldsymbol{\Phi}_e - \chi_m \boldsymbol{I}_{ion}(\boldsymbol{V}_m^n, \boldsymbol{W}, \boldsymbol{C}) = \boldsymbol{0}.
\end{aligned}
$$

A semi-implicit method like the one reported here features two nice properties. First of all, the two PDEs are decoupled by the ODE systems, highly simplifying the numerical solution of the entire problem. This decoupling strategy is justified by noticing that the Jacobian entries of a fully implicit discretization feature dominant values on the diagonal

suggesting a weak coupling between potentials and gating/ionic concentrations variables [388]. Secondly, it allows for a linearization of the non-linear reaction term given by the ionic currents, thus requiring the solution of a (2×2 block) linear system.

A special attention has been paid to the evaluation of the ionic current in a Finite Element context. In particular, two strategies have been mainly considered, i.e. *ionic current interpolation* (ICI) and *state variable interpolation* (SVI). In the first case, only the nodal values are used to build an interpolation of the ionic current, whereas in the second case the transmembrane potential and the gating/ionic concentration variables are interpolated within each element and the ionic current is then evaluated by using these interpolated variables [434]. The ICI approach is of course more efficient from the computational point of view and allows one to express the reaction term by means of a mass matrix. However, it features a lower accuracy with respect to SVI, in particular, the computed conduction velocity is generally larger than the true one, see [434].

From the algebraic point of view, the solution of a semi-implicit discretized problem is very demanding, since the matrix of the linear system associated to the PDEs written in terms of the unknowns $\mathbf{\Phi}_i$ and $\mathbf{\Phi}_e$ is given by

$$B = \frac{\chi_m C_m}{\Delta t} \begin{bmatrix} M & -M \\ -M & M \end{bmatrix} + \begin{bmatrix} A_i & 0 \\ 0 & A_e \end{bmatrix}.$$

Both terms of this matrix are singular, the first one due to the degenerate parabolic nature of the PP bidomain formulation, the second one being each block A_β related to a pure Neumann diffusive problem. However, matrix B is positive semidefinite, hence the preconditioned conjugate gradient method is often used for its numerical solution [440, 117]. Preconditioning is mandatory since matrix B is highly ill-conditioned due to the block 2×2 mass matrix that, unlike usually happens for the classical mass matrix, worsen the spectrum of the stiffness matrix. Efficient preconditioners are, e.g., block Jacobi and Gauss-Seidel [361], block SSOR [440], multilevel additive Schwarz [435], multigrid [456, 573], and a functional block preconditioner obtained by the monodomain solver [206].

Semi-implicit methods have been proposed also for the PE formulation, see, e.g., [177]. For example, with respect to the unknowns $\boldsymbol{V}_m$ and $\mathbf{\Phi}_e$, we have

$$B = \frac{\chi_m C_m}{\Delta t} \begin{bmatrix} M & 0 \\ 0 & 0 \end{bmatrix} + \begin{bmatrix} A_i & A_i \\ A_i & A_i + A_e \end{bmatrix}.$$

Again the matrix is singular, ill-conditioned, and semidefinite positive. In this context, we cite [454] for an incomplete block LU factorization precontitioner and [571] where the two PDEs are decoupled by treating explicitly V_m in (76a) and ϕ_e in (76b).

In any case, semi-implicit methods are conditionally stable with a bound on Δt which is however independent of the mesh size [177, 118].

A variant of the semi-implicit method reported above arises from treating implicitly the reaction term I_{ion}. In this case, Newton-Krylov-Schwarz methods are very efficient [388]. Second order semi-implicit schemes have been successfully considered as well, see e.g. [161].

Operator splitting-based methods. These methods separate the reaction operator from the diffusive operator, in a way similar to what is done in fractional step methods for fluid problems. They were first introduced for the monodomain problem in [467]. We present here an operator splitting-based method for the PP formulation of the bidomain problem [534, 118]:

Step 1. Given the quantities at time step t^n, solve the reaction problem and the ODE systems in $(t^n, t^n + \theta\Delta t]$:

$$\chi_m C_m M \frac{\widetilde{\boldsymbol{V}}_m^{n+\theta} - \boldsymbol{V}_m^n}{\Delta t} + \chi_m \boldsymbol{I}_{ion}(\boldsymbol{V}_m^*, \boldsymbol{W}^*, \boldsymbol{C}^*) = \boldsymbol{0},$$
$$M \frac{\widetilde{\boldsymbol{W}}^{n+\theta} - \boldsymbol{W}^n}{\Delta t} - \boldsymbol{G}(\boldsymbol{V}_m^*, \boldsymbol{W}^*) = \boldsymbol{0}, \qquad M \frac{\widetilde{\boldsymbol{C}}^{n+\theta} - \boldsymbol{C}^n}{\Delta t} - \boldsymbol{S}(\boldsymbol{V}_m^*, \boldsymbol{W}^*, \boldsymbol{C}^*) = \boldsymbol{0};$$

Step 2. Given $\widetilde{\boldsymbol{V}}_m^{n+\theta}$, solve the diffusion problems in $(t^n, t^{n+1}]$:

$$\chi_m C_m M \frac{\widehat{\boldsymbol{V}}_m^{n+1} - \widetilde{\boldsymbol{V}}_m^{n+\theta}}{\Delta t} + A_i \boldsymbol{\Phi}_i^* = \boldsymbol{0},$$
$$-\chi_m C_m M \frac{\widehat{\boldsymbol{V}}_m^{n+1} - \widetilde{\boldsymbol{V}}_m^{n+\theta}}{\Delta t} + A_e \boldsymbol{\Phi}_e^* = \boldsymbol{0};$$

Step 3. Given $\widehat{\boldsymbol{V}}_m^{n+1}$, $\widetilde{\boldsymbol{W}}^{n+\theta}$, $\widetilde{\boldsymbol{C}}^{n+\theta}$, solve the reaction problem and the ODE systems in $(t^n + \theta\Delta t, t^{n+1}]$:

$$\chi_m C_m M \frac{\boldsymbol{V}_m^{n+1} - \widehat{\boldsymbol{V}}_m^{n+1}}{\Delta t} + \chi_m \boldsymbol{I}_{ion}(\boldsymbol{V}_m^*, \boldsymbol{W}^*, \boldsymbol{C}^*) = \boldsymbol{0},$$
$$M \frac{\boldsymbol{W}^{n+1} - \widetilde{\boldsymbol{W}}^{n+\theta}}{\Delta t} - \boldsymbol{G}(\boldsymbol{V}_m^*, \boldsymbol{W}^*) = \boldsymbol{0}, \qquad M \frac{\boldsymbol{C}^{n+1} - \widetilde{\boldsymbol{C}}^{n+\theta}}{\Delta t} - \boldsymbol{S}(\boldsymbol{V}_m^*, \boldsymbol{W}^*, \boldsymbol{C}^*) = \boldsymbol{0}.$$

The superscript * means that the quantity at hand could be treated either explicitly or implicitly. The variable θ could assume value $1/2$ or 1. In the latter case, step 3 is unnecessary, we set $\boldsymbol{V}_m^{n+1} = \widehat{\boldsymbol{V}}_m^{n+1}$, $\boldsymbol{W}^{n+1} = \widetilde{\boldsymbol{W}}^{n+1}$, $\boldsymbol{C}^{n+1} = \widetilde{\boldsymbol{C}}^{n+1}$, and a first order method is obtained (*Godunov splitting*). For $\theta = 1/2$, we have a second order method provided that all the subproblems are solved with a second order strategy (*Strang splitting*). Notice that if step 2 is solved implicitly, then the same preconditioners introduced below for the semi-implicit schemes could be applied as well since it applies to the same operator.

Implicit methods. Some authors considered a fully implicit discretization of the full bidomain problem (75) or (76), see e.g. [77, 389]. In this case the whole Jacobian is built and the Newton method is applied. Due to the small time step required in bidomain simulations to capture the propagating front and due to the excellent stability properties of semi-implicit and operator splitting-based methods, fully implicit method are nowadays

not so much considered.

In Figures 19 and 20 we report some examples of numerical results related to the solution of the electrical propagation in the myocardium.

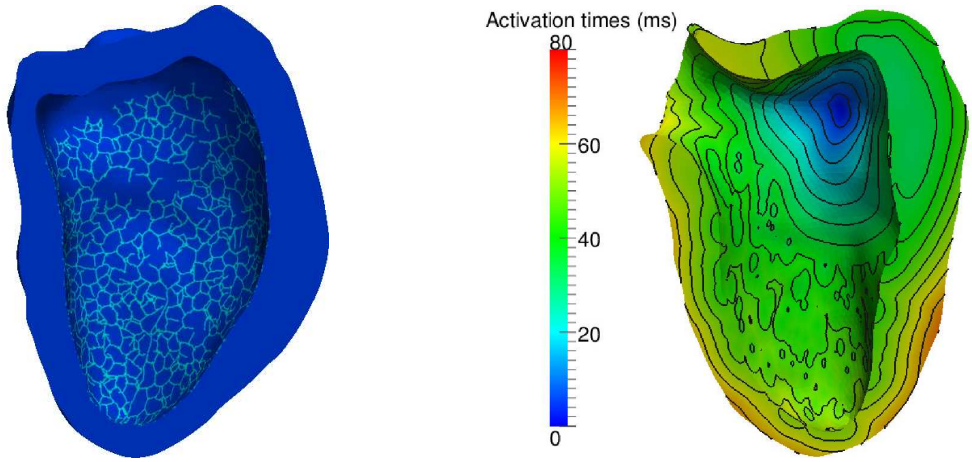

Figure 19: Left: Purkinje network generated by the algorithm proposed in [428] in the case of a real left ventricle. Right: Map of the activation times computed by means of the Eikonal equation. The time marching scheme and P1 finite elements have been used. The source term (dark blue) is located within the myocardium as typically happens in the Wolff-Parkinson-White syndrome. Results obtained by means of a code implemented in the *VMTK* envoirment (www.vmtk.org). CT images from the Cardiology Division at Ospedale S. Maria del Carmine, Rovereto (TN), Italy, and from the Radiology Division of Borgo-Trento (TN), Italy

7.2 Cardiac mechanics and electro-mechanics coupling

7.2.1 The continuous mechanics problems

During a physiological contraction, the cardiac cells change their length up to 20%-30%, so that finite elasticity models are mandatory to describe heart contraction and relaxation. In particular, the first Piola-Kirchhoff tensor is written as the sum of two terms [396, 405], a *passive component*, $\widehat{\boldsymbol{T}}_s^P$, describing the stress required to obtain a given deformation of the passive myocardium (similarly to arteries), and an *active component*, $\widehat{\boldsymbol{T}}_s^A$, representing the tension generated by the depolarization of the propagating electric signal that provides the internal active forces responsible of the contraction (see Section 5.4):

$$\widehat{\boldsymbol{T}}_s = \widehat{\boldsymbol{T}}_s^P + \widehat{\boldsymbol{T}}_s^A, \tag{93}$$

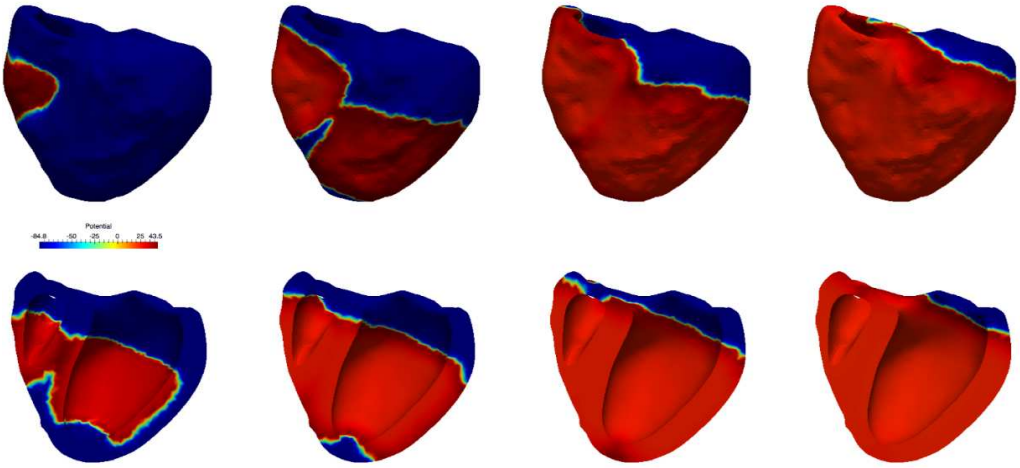

Figure 20: Propagation of the transmembrane potential in the two ventricles at eight different instants during an heartbeat. Monodomain simulation, semi-implicit method, P1 Finite Elements. These results have been obtained using *LifeV*; the computational mesh has been obtained by an open source biventricular geometry segmented from CT images, see [499]

where according to the notation of Part 1, $\widehat{\ }$ refers to quantities computed in the reference domain.

The passive component of the stress is obtained as the derivative of a suitable strain energy function, see (11). The heart mechanics response (just like the electric propagation, see Section 7.1) highly depends on the presence of fibers and sheets. For this reason, the passive myocardium is modeled as an *orthotropic* material, characterized by two principal directions and with different material responses on three mutually orthogonal planes, identified by these directions. This is in accordance with the shear tests performed on pig hearts, that highlighted an elevated resistance to shear deformations producing an extension along the fiber direction, an intermediate resistance in the direction orthogonal to fibers and tangential to sheets, and the least resistance in the third orthogonal direction [146]. By denoting with $\widehat{\boldsymbol{a}}_f$, $\widehat{\boldsymbol{a}}_s$, $\widehat{\boldsymbol{a}}_n$ the unit vectors along these directions (see Section 7.1) in the reference configuration, the following strain energy function has been proposed in [258]:

$$\Theta(I_1, I_{4,f}, I_{4,s}, I_{8,fs}) = \frac{a}{2b} e^{b(I_1-3)} + \sum_{i=f,s} \frac{a_i}{2b_i} \left[e^{b_i (I_{4,i}-1)^2} - 1 \right] + \frac{a_{fs}}{2b_{fs}} \left[e^{b_{fs} I_{8,fs}^2} - 1 \right], \quad (94)$$

where, referring to the notation introduced in Section 4.2, $I_1 = tr\, \boldsymbol{C}$, $I_{4,i} = \widehat{\boldsymbol{a}}_i \cdot (\boldsymbol{C}\widehat{\boldsymbol{a}}_i)$, $i = f, s$, $I_{8,fs} = \widehat{\boldsymbol{a}}_f \cdot (\boldsymbol{C}\widehat{\boldsymbol{a}}_s)$ are invariants of $\boldsymbol{C}$, and a, b, a_f, b_f, a_s, b_s, a_{fs}, b_{fs} are material parameters. I_1 is the first isotropic invariant and the related term in Θ accounts for the isotropic response of the myocardium at small deformations; $I_{4,f}$ and $I_{4,s}$ are the squares of the stretch of $\widehat{\boldsymbol{a}}_f$ and $\widehat{\boldsymbol{a}}_s$ in the deformed configuration and the related terms in the

energy are associated with the increased stiffness of the material along the two principal directions $\boldsymbol{a}_f$ and $\boldsymbol{a}_s$ for large deformations; finally, $I_{8,fs}$ represents the angle spanned by the two principal directions in the deformed configuration and the related term in the energy describes the coupling between the two principal directions. Convexity of this energy is guaranteed for positive parameter values [258]. Other orthotropic models have been proposed, e.g., in [272, 124], whereas *transversally isotropic* models with only one principal direction (that along the fibers) had been previously introduced, e.g., in [271, 225]. Some authors model the myocardium as incompressible [258], in accordance with the experiments reported in [579]. In this case the term $p_s(J-1)$ is added to the strain energy functions, as done in (16).

On the basis of experimental evidences, reported e.g. in [146], highlighting hysteresis under shear deformations, viscoelastic orthotropic models have recently been proposed for the passive myocardium, see [234]. The viscoelastic behavior is probably due to the extracellular fluid that filtrates through the solid part.

Regarding the active contribution of the cardiac cells to the contraction, this is regulated by the opening of calcium channels as a response to the depolarization, with a consequent entry of calcium ions in the cells. As detailed in Section 5.4, this process is responsible for the cardiac contraction. Since the latter occurs along the axial direction of the cardiac cells, i.e. along the fiber direction, the active part of the stress tensor has usually the following form [396]

$$\widehat{\boldsymbol{T}}_s^A = P^A \boldsymbol{a}_f \otimes \widehat{\boldsymbol{a}}_f, \tag{95}$$

where the scalar function of time and space P^A represents the pointwise active stress and should be properly modeled.

In the classical model for the active stress function proposed in [396], P^A depends on the transmembrane potential V_m solely. In particular, for each spatial point, the following ODE equation is introduced

$$\frac{dP^A(t)}{dt} = \varepsilon(V_m(t)) \left[k_P(V_m(t) - V_r) - P^A(t) \right], \tag{96}$$

where V_r is the resting potential, k_P is a suitable parameter controlling the amplitude of P^A, and ε controls the delay of the contraction with respect to the action potential. For example, in [218] the following expression has been proposed

$$\varepsilon(V_m) = \varepsilon_0 + (\varepsilon_\infty - \varepsilon_0) e^{-e^{-\xi(V_m - \bar{V}_m)}},$$

where ε_0, ε_∞, ξ, $\bar{V}_m$ are suitable parameters.

Since the cardiac cell contraction is regulated by the calcium ions concentrations, the active stress function P^A can be assumed to directly depend on this specific concentration, say c_{ca}, rather than on the more general variable V_m. For example, in [595] a system of ODEs of the same structure of (96) has been proposed, however using c_{ca} instead of V_m on the right hand side.

In more sophisticated models, the active stress function also depends on the stretch in the fiber direction $\lambda = \sqrt{\widehat{\boldsymbol{a}}_f^T C \widehat{\boldsymbol{a}}_f}$ and on the fiber stretch rate $\dfrac{d\lambda}{dt}$ [402, 317]. In compact form, these models are written as follows:

$$\begin{aligned} \frac{d\boldsymbol{y}}{dt} &= \boldsymbol{g}_y \left(P^A, \lambda, \frac{d\lambda}{dt}, \boldsymbol{c}, \boldsymbol{y} \right), \\ P^A &= g_{P^A}(\lambda, \boldsymbol{y}), \end{aligned} \tag{97}$$

for suitable functions $\boldsymbol{g}_y$ and g_{P^A} and where $\boldsymbol{c}$, as in Section 7.1, is the ionic concentration variables (in particular the calcium one), whereas $\boldsymbol{y}$ collects other myofilament and electrophysiology state variables.

Alternatively to the decomposition (93) where the stress tensor is split into a passive and an active component (*active stress* approach), a different strategy based on an *active strain* approach has been proposed in [98, 7]. In this case, the following multiplicative decomposition of the deformation tensor is introduced

$$\boldsymbol{F} = \boldsymbol{F}^P \boldsymbol{F}^A,$$

where $\boldsymbol{F}^A$ is the active factor acting at the microscales and representing a distortion of the fibers not preserving in general the compatibility of the body, whereas $\boldsymbol{F}^P$ is the factor describing the passive deformation at the macroscales and the deformation needed to restore compatibility. With this choice, quite common when analyzing plasticity and the remodeling of living tissues, the microscale information related to the fiber contraction is directly incorporated in the body kinematics, allowing for the inclusion of fiber contraction driven by the depolarization as a prescribed active deformation rather than a further contribution to stress. In this case, the first Piola-Kirchhoff stress tensor is given by

$$\widehat{\boldsymbol{T}}_s = J^A \frac{D\Theta}{D\boldsymbol{F}^P} (\boldsymbol{F}^A)^{-T},$$

and, in analogy with (95), a possible expression for $\boldsymbol{F}^A$ is

$$\boldsymbol{F}^A = \boldsymbol{I} - \beta V_m \widehat{\boldsymbol{a}}_f \otimes \widehat{\boldsymbol{a}}_f,$$

for a suitable parameter β [7]. The active strain approach is probably more satisfactory from the modeling point of view, since, unlike active stress, it should provide the expected fiber contraction without any tuning. However, from the numerical point of view it is more problematic since standard Finite Element finite elasticity solvers cannot be directly used and should be properly adapted. From now on we refer only to the active stress approach. For a comparison between the two approaches we refer to [7, 8], and to [450, 496] for related computational results.

7.2.2 The coupled electro-mechanics problem

The values of the transmembrane potential V_m or calcium ion concentration c_{ca} to be used in (96) or (97) to compute the active stress function P^A are sometimes prescribed

as given data to the mechanics problem, see e.g. [157]. However, in most of the cases, they are obtained from the bidomain or monodomain equations. This leads to a *coupled electro-mechanical* problem.

The electric propagation problem needs to be solved in a domain that changes in time, because of the cardiac contraction and relaxation. Under suitable assumptions [119], in an Eulerian framework, these problems assume the form (75), (76), or (81), provided that the conductivity tensors (74) or (82) are computed by using the deformed unit directions $\boldsymbol{a}_f$, $\boldsymbol{a}_s$, $\boldsymbol{a}_n$, see e.g. [289]. However, for computational simplicity, most often the bidomain and monodomain equations are set in a Lagrangian framework and written in the reference undeformed configuration. We report in what follows the corresponding monodomain equation (according to the notation of Part 1, we set $\Omega_{mus} = \Omega^0_{mus}$):

$$\begin{aligned} J\chi_m C_m \left(\frac{\partial \widehat{V}_m}{\partial t} - \boldsymbol{F}^{-T} \nabla \widehat{V}_m \cdot \frac{\partial \boldsymbol{\psi}}{\partial t} \right) - \nabla \cdot \left(J \boldsymbol{F}^{-1} \boldsymbol{\Sigma} \boldsymbol{F}^{-T} \nabla \widehat{V}_m \right) + \\ J\chi_m \widetilde{I}_{ion} \left(\widehat{V}_m, \widehat{\boldsymbol{w}}, \widehat{\boldsymbol{c}}, \lambda \right) = J \widehat{I}^{ext} \quad \text{in } \Omega_{mus}, \end{aligned} \tag{98}$$

coupled with the ODE systems (79e)-(79f) (similar arguments hold true for the bidomain equations as well). The spatial derivatives have to be intended with respect to the undeformed domain, $\boldsymbol{\psi}$ is the deformation map between Ω^0_{mus} and Ω^t_{mus} and λ is the stretch in the fiber direction introduced above.

From the previous equation, we observe that there are three sources of *mechano-electric feedbacks*, i.e. three ways through which the mechanics problem influences the electric one:

i) the effective conductivity tensor $\widehat{\boldsymbol{\Sigma}} = J \boldsymbol{F}^{-1} \boldsymbol{\Sigma} \boldsymbol{F}^{-T}$ depends on the deformation gradient $\boldsymbol{F}$;

ii) the ionic current term I_{ion} depends on the stretch in the fiber direction λ;

iii) the relation between the spatial and material time derivatives introduces the advection term $-\boldsymbol{F}^{-T} \nabla \widehat{V}_m \cdot \frac{\partial \boldsymbol{\psi}}{\partial t}$ which depends on the solution of the mechanics problem [119].

The first and the third terms are due to the pulling back of the monodomain equation in the undeformed domain (geometrical feedback). The second one is instead due to a well-known physical process consisting in the opening of ion channels under the action of deformation (stretch-activated channels, see Sect. 5.4) [299, 300]. Accordingly, the ionic current term is written as the sum of two contributions,

$$\widetilde{I}_{ion} = I_{ion} \left(\widehat{V}_m, \widehat{\boldsymbol{w}}, \widehat{\boldsymbol{c}} \right) + I^{SAC} \left(\widehat{V}_m, \lambda \right), \tag{99}$$

where I_{ion} represents one of the classical independent-stretch models described in Section 7.1.2, and I^{SAC} is the current activated by the deformation. A quite general expression for the latter term is given by

$$I^{SAC} = \sum_i K_i(\widehat{V}_m)(\lambda - 1)(\widehat{V}_m - V_i) H(\lambda - 1), \tag{100}$$

where the $i-th$ term of the sum represents the stretch-activated currents related to the $i-th$ ion (usually sodium and potassium), K_i is a suitable function, V_i the Nerst potential introduced in Section 7.1.2. The Heaviside function $H(\cdot)$ guarantees that the stretch-activated ion channels open only under fiber tension ($\lambda > 1$) [404]. In [119], it was shown (computationally) that these terms do not significantly alter the morphology of the action potential, however they strongly influence the action potential duration.

Stretch-activated ionic currents together with the active stress component of the stress tensor (or equivalently, to the active strain component of the deformation gradient) make the electro-mechanics problem a highly coupled system, that can be summarized as follows: Find the muscle displacement $\boldsymbol{d}$, the transmembrane potential V_m, the gating variables $\boldsymbol{w}$, and the ionic concentration variables $\boldsymbol{c}$, such that

$$\nabla \cdot \left(\widehat{\boldsymbol{T}}_s^P(\widehat{\boldsymbol{d}}) + \widehat{\boldsymbol{T}}_s^A \left(\widehat{\boldsymbol{c}}, \widehat{\boldsymbol{d}}, \frac{d\widehat{\boldsymbol{d}}}{dt} \right) \right) = \boldsymbol{0} \qquad \text{in } \Omega_{mus}, \tag{101a}$$

$$\widehat{\boldsymbol{T}}_s^A = P^A \boldsymbol{a}_f \otimes \widehat{\boldsymbol{a}}_f, \qquad P^A = \mathcal{A}\left(\widehat{\boldsymbol{c}}, \widehat{\boldsymbol{d}}, \frac{d\widehat{\boldsymbol{d}}}{dt} \right) \qquad \text{in } \Omega_{mus}, \tag{101b}$$

$$\widehat{V}_m = \mathcal{M}\left(\widehat{V}_m; \widehat{\boldsymbol{d}}, \widehat{\boldsymbol{w}}, \widehat{\boldsymbol{c}} \right) \qquad \text{in } \Omega_{mus}, \tag{101c}$$

$$(\widehat{\boldsymbol{w}}, \widehat{\boldsymbol{c}}) = \mathcal{G}(\widehat{\boldsymbol{w}}, \widehat{\boldsymbol{c}}; \widehat{V}_m) \qquad \text{in } \Omega_{mus}. \tag{101d}$$

In the previous system, equation (101a) stands for the mechanical problem. Notice that, unlike for the vessel case, see (10), the time dependent inertial term has been neglected, as commonly done for the heart mechanics. Moreover, $\widehat{\boldsymbol{T}}_s^P = \dfrac{\partial \Theta}{\partial \boldsymbol{F}}$, where Θ is given for example by the orthotropic law (94), and P^A is given by either (96) or (97). Equation (101c) represents in compact form the monodoman problem (98) together with the ionic current expression given by (99)-(79c)-(79d)-(100). Finally, (101d) is a shorthand notation for the ODE systems (79e)-(79f) for the gating and ionic concentration variables characterizing the cardiac cell model. Notice also that in writing system (101), we have exploited the fact that λ and $\boldsymbol{F}$ could be written in terms of $\boldsymbol{d}$, allowing us to indicate the dependences of the monodomain problem on λ and $\boldsymbol{F}$ and of $\widehat{\boldsymbol{T}}_s^A$ on λ in compact form through $\boldsymbol{d}$.

Regarding the well-posedness of the electro-mechanics coupled problem (101), very few results have been obtained so far. We mention [433], where it has been noticed that for the general active stress model (97), the equilibrium equation (101a) is not even elliptic when there is an explicit dependence on the rate of stretch $\frac{d\lambda}{dt}$, and [9], where the existence of a weak solution is proved for the case of a linearized elasticity equation in the active strain formulation coupled with the bidomain equations including the geometrical feedback affecting the conductivity tensors.

7.2.3 The issue of boundary conditions for the mechanics problem

As for the mechanical contraction problem (101a), proper boundary conditions should be prescribed at both the external epicardium and internal endocardium surfaces. For the former, the presence of both the pericardium and the surrounding tissue has to be

accounted for, because of their effect on the heart movement. A sophisticated model of interaction with the pericardium accounting for a frictionless contact has been proposed in [198]. More commonly, similarly to the vascular case, a Robin condition like (1) is prescribed at Σ_{epi}.

At the endocardium internal surface Σ_{endo}, in presence of a fluid model in the atrial and ventricular cavities, the usual dynamic and kinematic conditions (22c)-(22d), arising from the fluid-structure interaction model, implicitly provides both the endocardial displacement and normal stresses (see Section 7.5). When the fluid in the ventricular cavity is not modeled, suitable strategies to prescribe boundary conditions at Σ_{endo} are mandatory. A common strategy relies on prescribing a Neumann condition of type

$$\widehat{\boldsymbol{T}}_s\widehat{\boldsymbol{n}} = P\widehat{\boldsymbol{n}}, \tag{102}$$

where P is a suitable estimate of the blood pressure distribution at the endocardium.

During the ventricular filling, condition (102) is prescribed both for atria and ventricles by means of selected values of blood pressures taken from literature (see Figure 13).

During the isovolumic contraction, the ventricular volume is kept constant by means, e.g., of fixed point iterations, where the value of the endocardial pressure to be prescribed in (102) at each time step is updated until satisfaction of the constraint given by the unchanged volume [556, 157]:

$$P_{(k+1)} = P_{(k)} + (V - V^n)/C_k,$$

where V is the cavity volume, k the subiteration index, C_k a penalty parameter, and where the current temporal index $^{n+1}$ is as usual understood. Alternatively, a Lagrange multiplier approach could be employed as well [238]. During this phase the atrial pressure is kept constant to the values reached when the mitral and tricuspid valves close.

For the ventricular ejection, a reduced 0D model (based on the analogy with electric circuits, see Section 4.5.1) for the systemic (and in case pulmonary) circulation is usually coupled with the cardiac mechanics problem, assuming that the ventricular pressure equals the pressure in the aorta (or in the pulmonary artery) [556, 157]. This is a good approximation since, although the ventricular and circulatory pressures are different (thus allowing for the acceleration and deceleration of blood, see Figure 13), they are very similar. In this case we have a coupled problem between the cardiac mechanics and the lumped parameters model where the two subproblems exchange suitable interface conditions (e.g. in an iterative framework). For example, the 0D model could provide the pressure to be prescribed to the mechanics problem by means of (102), whereas the flow rate $Q = \rho_f \frac{dV}{dt}$ is prescribed to the 0D model. During the ejection phase the atrial pressure is determined by the venous pressure that could be obtained again by a 0D model or by literature values.

Finally, during the isovolumic relaxation, the endocardial pressure is decreased according to literature values until it reaches the pressure atrial value. Also during this phase the atrial pressure is determined by the venous pressure.

When only the ventricular mechanics is modeled (no atria), a truncated computational domain like the one depicted in Figure 18, left, is considered. In this case we have to provide suitable boundary conditions at the ventricular basis Σ_b. Often, this surface is kept fixed by

enforcing homogeneous Dirichlet conditions. In other cases, the tangential displacement is allowed by prescribing a homogeneous Neumann condition along the tangential directions.

7.2.4 Numerical approximation

The coupled electro-mechanics problem (101) is composed by four differential blocks, namely the two PDEs (101a) and (101c) describing the heart mechanics and electric propagation, respectively, the ODE system (101b) providing the active stress function, and the ODE systems (101d) modeling gating and ionic concentration variables. Moreover, the algebraic source of coupling (99)-(100) need to be accounted for to determine the stretch-activated ion currents. Their influence on the electric problem has been included directly in the right hand side of (101c).

A common numerical solution strategy for problem (101) addresses two PDEs separately by relying (when possible) on pre-existing mechanics and electric codes: for instance the mechanics subproblem is solved in [436] using efficient Newton-Krylov iterations, while the electric subproblem (monodomain+cell ODE model) is solved by means of one of the strategies described in Section 7.1.6 (see also [535] for an operator splitting method).

In this context, at each time step the electric subproblem is solved first and the mechanics problem later [396, 238, 535]. In particular, after time discretization, the following scheme is employed (as usual the current temporal index $^{n+1}$ is understood and * means that the related term could be treated either implicitly or explicitly, depending on the temporal scheme used):

EM1 Algorithm:
At each time step

1. solve the monodomain problem together with the cell model:

$$\widehat{V}_m = \mathcal{M}\left(\widehat{V}_m^*; \widehat{\boldsymbol{d}}^n, \widehat{\boldsymbol{w}}^*, \widehat{\boldsymbol{c}}^*\right) \qquad \text{in } \Omega_{mus}, \tag{103a}$$

$$(\widehat{\boldsymbol{w}}, \widehat{\boldsymbol{c}}) = \mathcal{G}(\widehat{\boldsymbol{w}}^*, \widehat{\boldsymbol{c}}^*; \widehat{V}_m^*) \qquad \text{in } \Omega_{mus}; \tag{103b}$$

2. then, solve the mechanics problem:

   2a. update the active stress contribution

$$\widehat{\boldsymbol{T}}_s^A = P^A \boldsymbol{a}_f \otimes \widehat{\boldsymbol{a}}_f, \qquad P^A = \mathcal{A}\left(\widehat{\boldsymbol{c}}, \widehat{\boldsymbol{d}}^n, \frac{\widehat{\boldsymbol{d}}^n - \widehat{\boldsymbol{d}}^{n-1}}{\Delta t}\right) \quad \text{in } \Omega_{mus};$$

   2b. solve the equilibrium equation by means of the following Newton iterations: at each iteration k solve

$$\nabla\cdot\left(D_F \widehat{\boldsymbol{T}}_s^P\left(\widehat{\boldsymbol{d}}_{(k-1)}\right)\right)\delta\widehat{\boldsymbol{d}}_{(k)} = -\nabla\cdot\left(\widehat{\boldsymbol{T}}_s^P(\widehat{\boldsymbol{d}}_{(k-1)}) + \widehat{\boldsymbol{T}}_s^A\left(\widehat{\boldsymbol{c}}, \widehat{\boldsymbol{d}}^n, \frac{\widehat{\boldsymbol{d}}^n - \widehat{\boldsymbol{d}}^{n-1}}{\Delta t}\right)\right) \text{ in } \Omega_{mus}.$$

According to the notation introduced in Section 4.6.2, D_F is the Gâteaux derivative with respect to $\boldsymbol{F}$, $\delta\widehat{\boldsymbol{d}}_{(k)} = \widehat{\boldsymbol{d}}_{(k)} - \widehat{\boldsymbol{d}}_{(k-1)}$, and, for simplicity, we have considered a Forward Euler approximation of $\frac{dw}{dt}\big|_{t^n}$. The active stress contribution is treated explicitly, i.e. it is updated once per time step. This choice may lead to numerical instabilities, as computationally reported in [405]. In [433] it has been speculated that such instability could be ascribed to the (necessarily) explicit time discretization of the explicit stretch rate term $\frac{d\lambda}{dt}\big|_{t^n}$ (instead of $\frac{d\lambda}{dt}\big|_{t^{n+1}}$) in the active stress function solution.

To overcome these instabilities, in [405] it has been proposed to update the active stress function at each Newton step, i.e. to substite step 2 in the previous scheme with the following one:

EM1/bis Algorithm:

2bis. solve the mechanics problem by the following Newton iterations: at each iteration k

2bis/a. update the active stress contribution

$$\widehat{\boldsymbol{T}}_s^A = P^A \boldsymbol{a}_f \otimes \widehat{\boldsymbol{a}}_f, \qquad P^A = \mathcal{A}\left(\widehat{\boldsymbol{c}}, \widehat{\boldsymbol{d}}_{(k-1)}, \frac{\widehat{\boldsymbol{d}}_{(k-1)} - \widehat{\boldsymbol{d}}^n}{\Delta t}\right) \quad \text{in } \Omega_{mus};$$

2bis/b. solve the equilibrium equation

$$\nabla\cdot\left(D_F\widehat{\boldsymbol{T}}_s^P\left(\widehat{\boldsymbol{d}}_{k-1}\right)\right)\delta\widehat{\boldsymbol{d}}_k = -\nabla\cdot\left(\widehat{\boldsymbol{T}}_s^P(\widehat{\boldsymbol{d}}_{k-1}) + \widehat{\boldsymbol{T}}_s^A\left(\widehat{\boldsymbol{c}}, \widehat{\boldsymbol{d}}_{(k-1)}, \frac{\widehat{\boldsymbol{d}}_{(k-1)} - \widehat{\boldsymbol{d}}^n}{\Delta t}\right)\right) \text{ in } \Omega_{mus}.$$

Notice that step 2bis does not coincide with a fully Newton iterations on (101a)-(101b). Although at the expence of a higher number of iterations, this scheme provides stable solutions and allows the use of a standard solver for the mechanics part.

A fully Newton method for the solution of the mechanics problem (101a)-(101b) used in combination with a different explicit decoupled scheme has been successfully proposed in [436], where the electric problem (101c)-(101d) is split into the cellular and macroscopic problems (semi-implicit treatment) and the mechanics problem is solved in between, as follows:

EM2 Algorithm:
At each time step

1. solve the ODE system for the gating and ionic concentration variables

$$(\widehat{\boldsymbol{w}}, \widehat{\boldsymbol{c}}) = \mathcal{G}(\widehat{\boldsymbol{w}}^*, \widehat{\boldsymbol{c}}^*; \widehat{V}_m^*) \quad \text{in } \Omega_{mus};$$

2. then, solve the mechanics problem by the following fully Newton method: at each iteration k solve

2a. update the active stress contribution

$$\widehat{\boldsymbol{T}}_s^A = P^A \boldsymbol{a}_f \otimes \widehat{\boldsymbol{a}}_f, \qquad P^A = \mathcal{A}\left(\widehat{\boldsymbol{c}}, \widehat{\boldsymbol{d}}_{(k-1)}, \frac{\widehat{\boldsymbol{d}}_{(k-1)} - \widehat{\boldsymbol{d}}^n}{\Delta t}\right) \quad \text{in } \Omega_{mus},$$

2b. solve the equilibrium equation

$$\nabla \cdot \left(D_F \widehat{\boldsymbol{T}}_s^P \left(\widehat{\boldsymbol{d}}_{(k-1)}\right) + D_F \widehat{\boldsymbol{T}}_s^A \left(\widehat{\boldsymbol{c}}, \widehat{\boldsymbol{d}}_{(k-1)}, \frac{\widehat{\boldsymbol{d}}_{(k-1)} - \widehat{\boldsymbol{d}}^n}{\Delta t}\right)\right) \delta\widehat{\boldsymbol{d}}_{(k)}$$

$$= -\nabla \cdot \left(\widehat{\boldsymbol{T}}_s^P (\widehat{\boldsymbol{d}}_{(k-1)}) + \widehat{\boldsymbol{T}}_s^A \left(\widehat{\boldsymbol{c}}, \widehat{\boldsymbol{d}}_{(k-1)}, \frac{\widehat{\boldsymbol{d}}_{(k-1)} - \widehat{\boldsymbol{d}}^n}{\Delta t}\right)\right) \quad \text{in } \Omega_{mus};$$

3. solve the monodomain problem

$$\widehat{V}_m = \mathcal{M}\left(\widehat{V}_m^*; \widehat{\boldsymbol{d}}, \widehat{\boldsymbol{w}}, \widehat{\boldsymbol{c}}\right) \quad \text{in } \Omega_{mus}.$$

A simplified variant of the previous decoupled algorithms has been proposed in [9] for the active strain formulation. We report here, for coherence with the previous algorithms, a variant of this scheme for the active stress formulation, where however in the second equation of (101b) we have $P^A = \mathcal{A}(\widehat{\boldsymbol{c}})$, i.e. the active stress function does not depend on the stretch and stretch rate:

EM3 Algorithm:
At each time step

1. update the active stress contribution

$$\widehat{\boldsymbol{T}}_s^A = P^A \boldsymbol{a}_f \otimes \widehat{\boldsymbol{a}}_f, \qquad P^A = \mathcal{A}\left(\widehat{\boldsymbol{c}}^{n-1}\right) \qquad \text{in } \Omega_{mus};$$

2. solve the equilibrium mechanics problem by the following Newton method : at each iteration k solve

$$\nabla \cdot \left(D_F \widehat{\boldsymbol{T}}_s^P \left(\widehat{\boldsymbol{d}}_{k-1}\right)\right) \delta\widehat{\boldsymbol{d}}_k = -\nabla \cdot \left(\widehat{\boldsymbol{T}}_s^P (\widehat{\boldsymbol{d}}_{k-1}) + \widehat{\boldsymbol{T}}_s^A \left(\widehat{\boldsymbol{c}}^{n-1}\right)\right) \qquad \text{in } \Omega_{mus};$$

3. then, solve the electric problem

$$\begin{aligned} &\widehat{V}_m = \mathcal{M}\left(\widehat{V}_m^*; \widehat{\boldsymbol{d}}^{n-1}, \widehat{\boldsymbol{w}}^*, \widehat{\boldsymbol{c}}^*\right) && \text{in } \Omega_{mus}, \\ &(\widehat{\boldsymbol{w}}, \widehat{\boldsymbol{c}}) = \mathcal{G}(\widehat{\boldsymbol{w}}^*, \widehat{\boldsymbol{c}}^*; \widehat{V}_m^*) && \text{in } \Omega_{mus}. \end{aligned}$$

In [9] the convergence of the finite element solution of Algorithm EM3 towards the continuous solution of (101) is proven.

Although segregated algorithms as those reported above are the most widely used to numerically solve the coupled electro-mechanics problem (101), a monolithic approach has

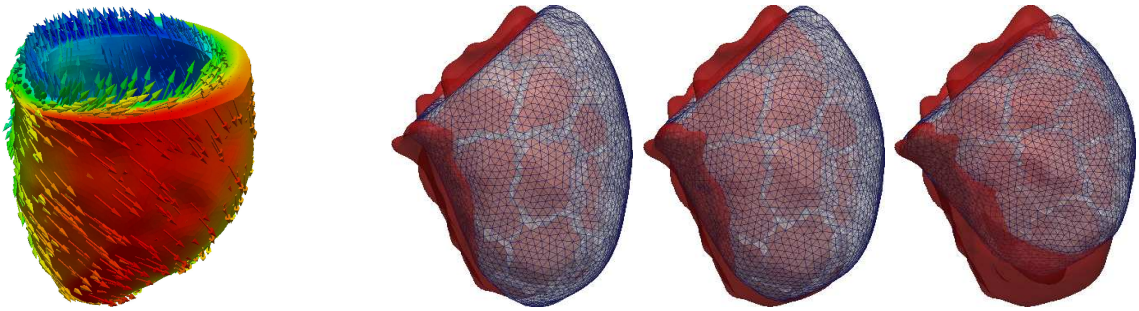

Figure 21: Left: Fiber orientation in a real left ventricle obtained with the method proposed in [496]. CT images from the Cardiology Division of Ospedale S. Maria del Carmine, Rovereto (TN), Italy, and from the Radiology Division of Borgo-Trento (TN), Italy. Right: Displacement configuration of a real left ventricle during the contraction phase at three different instants. Orthotropic model of activation, see [35]. These numerical results are obtained using *LifeV* and taken from [35]. CT images from the Cardio-surgery and Radiology Divisions at Ospedale Sacco, Milan, Italy

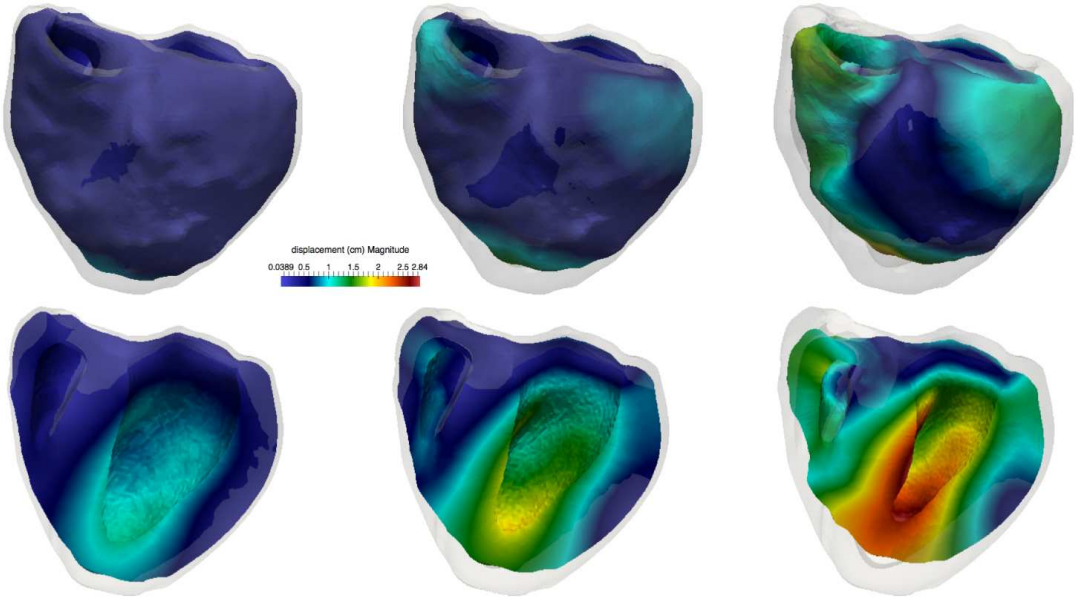

Figure 22: Displacements of the two ventricles at six different instants during the systolic contraction. Electro-mechanic coupled simulation, P1 Finite Elements. These numerical results are obtained using *LifeV*; the computational mesh has been obtained by an open source biventricular geometry segmented from CT images, see [499]

been used in [218], where a Newton method has been successfully applied to the whole

coupled problem with a FitzHugh-Nagumo cardiac cell model (i.e. without the ODE systems (101d)).

In Figure 21 we report an example of fiber configuration in the left ventricle, whereas in the same figure and in Figure 22, the results of an electro-mechanical simulation.

7.3 The ventricular fluid-dynamics

Blood flow in heart cavities Ω_{cav}, reported in Figure 15, can be regarded as homogeneous, Newtonian and incompressible [570, 589]. The displacements induced by the interaction with the myocardium can be larger than 30%, hence the solution of fluid-structure interaction problems is mandatory. Despite the large displacements, the ALE technique introduced in Section 4.6.3 is suitable in this context, as shown by several authors, see e.g. [97, 416]. Alternatively, the Immersed Boundary method [446], that does not require remeshing neither induces mesh deformation, has been often used since the celebrated paper by C. Peskin [375, 103] ; see Section 7.4 for its mathematical description.

One of the main features of the intraventricular fluid-dynamics is represented by the formation of a vortex ring during diastole (i.e. the filling phase) just downstream the mitral valve. This ring is generated during the peak flow due to pressure gradient between left atrium and ventricle, and it is highly distorted due to the asymmetry of the mitral valve leaflets [514]. At the end of this phase, the vortex ring is broken up into small-scale structures that propagate towards the posterior wall and the apex. After the second mitral peak flow due to the atrium contraction, additional vortex rings pop up. However, due to the small duration of this phase, they do not propagate far into the chamber [322]. Similar vortex rings are generated in the left atrium from the flow ejected by the pulmonary vein [375]. This complex and disturbed fluid-dynamics, in presence of a quite high Reynolds number ($\simeq 4000$), leads to transitional effect to turbulence even in the healthy case [483]. For this reason, inclusion of turbulence model in heart simulations is common practice; see e.g. [102] for LES models and [537] for the Variational Multiscale (VMS) formulation, that includes in a unified framework some stable schemes controlling the numerical instabilities arising in the convective regimes (e.g. SUPG) and LES turbulence models [268].

Regarding boundary conditions, at the endocardium Σ_{endo} (see Figure 15) the kinematic and dynamic conditions are implicitly determined by the coupling with the structural problem holding in the myocardium, leading to a fluid-structure interaction problem (see Section 7.5). The solution of a coupled fluid-structure interaction (FSI) problem can be avoided in those cases where the wall velocity can be derived from dynamic MRI or CT images. This requires however having at disposal several (20-30) wall displacement fields at different instants of an heartbeat. The wall myocardium velocity (that provides the Dirichlet boundary condition for the fluid equations in the ventricle) can be generated by numerically differentiating the displacement field [295, 375]. Alternatively, the wall myocardium velocity could be provided by the solution of the electromechanics model in case the latter is segregated from the fluid model [103].

The heart has also four artificial sections that delimit it from the circulatory system, namely the aortic and pulmonary valve orifices (outlets) and the interfaces with the venae

cavae and the pulmonary vein (inlets). In these cases, suitable conditions could be obtained by coupling the heart fluid-dynamics with the aorta, the pulmonary artery, and the above-mentioned veins. These can be modeled by means of 3D, 1D or 0D models.

In the case of simulation in the left ventricle solely (see Figure 18, right) we have to prescribe suitable boundary conditions also at the mitral valve orifice Γ_{mitr}. For example, in [295] it has been proposed to prescribe the flow rates at Γ_{mitr} and at the aortic valve outlet Γ_{ao} obtained by measuring from MRI images the volume changes of the left ventricle chamber, noticing that the two valves are never simultaneously open. Alternatively, flow rates curves taken from literature could be applied as well, see e.g. [416].

7.4 Valves modeling

Heart valves are made of thin leaflets. They do not cause any resistance to the blood during systole and sustain large pressure gradients during diastole. Moreover, unlike vascular vessel wall, they are subjected to very large displacements. These features make the mathematical and numerical modeling of the valves mechanics and of their interaction with the blood flow very demanding, requiring ad hoc techniques for their description. Our main focus will be on the aortic and mitral valves of the left ventricle, the most studied from the mathematical point of view. For recent reviews on valve modeling see, e.g., [363, 580].

7.4.1 Mechanical models of the leaflets

Due to fibers alignment, which occurs mostly in the circumferential direction $\boldsymbol{a}$, and to the presence of collagen, most of the valve mechanical models proposed so far are of non-linear transversally isotropic type. In particular, they depend on the two invariants $I_1 = tr\,\boldsymbol{C}$ and $I_4 = \widehat{\boldsymbol{a}} \cdot (\boldsymbol{C}\widehat{\boldsymbol{a}})$. For example, in [369, 463] the following strain energy function has been used

$$\Theta(I_1, I_4) = c\left[e^{b_1(I_1-3)^2+b_4(I_4-1)^2} - 1\right],$$

for suitable constants c, b_1, b_4. Variants of the previous energy have been considered e.g. in [271, 370, 592]. For a comparison of numerical results obtained with these constitutive laws, see [18]. More sophisticated energy functions include also the microstructure of the leaflets tissue, see e.g. [152].

Due to their small thickness, heart valves are often modeled as membrane shells by neglecting the shear bending forces that are one order of magnitude smaller than the in plane stresses [371, 296, 262].

Some works on the mitral valve consider also the presence of the chordae tendinae (see Sect. 5.1). They comprise independent rings models, where the chordae are modeled as non-linear springs with zero elasticity during compression and exponential-like stiffness during traction [310, 353], and one-dimensional models characterized by a non-linear energy function [152, 581, 424].

Another difficulty arises when modeling the contact among the leaflets during the closure. A common strategy to handle this process is given by a penalty method [262, 363,

353]. This is based on measuring the distance between each vertex and the closest leaflet and on locating a spring between the vertex and the collision point when the distance is below a critical value. In [14] a more sophisticated algorithm has been proposed, based on the introduction of subiterations that guarantee the satisfaction of the contact constraint by the introduction of Lagrange multipliers that act as a force of repulsion among the leaflets.

The numerical simulation of valves mechanics has been usually obtained by prescribing a pressure difference between the two sides of the leaflets, mimicking the effect of the fluid [217, 580]. However, more realistic models are obtained by considering the FSI problem arising between the blood flow and the leaflets. This is the topic of the next two subsections.

7.4.2 Reduced models for fluid-valve interaction

As noticed, the simulation of the fluid-structure interaction between blood and valve leaflets is computationally demanding. However, if one is interested only in the fluid-dynamic quantities and not in the internal leaflet stresses, reduced models could be considered.

The first family does not explicitly represent the leaflets, rather, only the opening/closure mechanism of the valve is modeled through the description of the valve orifice. The simplest strategy consists in a priori operating the opening and closing of the valve on the basis of a flow rate or pressure profile obtained from literature or from clinical data, see e.g. [166]. For an example, see [41, 569, 398] for the flow simulation in the aorta and [295] for that in the left ventricle. A more realistic situation is obtained by simulating the opening/closure mechanism of the aortic valve orifice by means of the following conditions prescribed to the fluid problem:

$$\begin{array}{l} \text{if } P_u > P_d \quad \text{then the valve opens;} \\ \text{if } Q_d < 0 \quad \text{then the valve closes,} \end{array} \tag{104}$$

where P_u is the upstream pressure, P_d and Q_d the downstream pressure and flow rate [187]. The quantities P_u, P_d, Q_d could be prescribed as data, or else being the results of the numerical computation of the flow field. For example, in a fluid-dynamic simulation in the aorta, P_u is the prescribed left ventricular pressure, whereas P_d and Q_d are the unknown aortic pressure and flow rate. For a left ventricular flow simulation, the situation is more involved as we have to distinguish between the mitral and the aortic valve: for the former, P_u is the prescribed atrial pressure, whereas P_d and Q_d are the unknown left ventricular pressure and flow rate; for the latter, P_u is the unknown left ventricular pressure, whereas P_d and Q_d the prescribed aortic pressure and flow rate. Many works considered a zero-dimensional model of the systemic circulation to provide the latter quantities [593]. In any case, the opening/closure mechanism is not prescribed a priori. This leads to a non-linear boundary condition for the fluid problem at the valve orifice which, in the electrical circuit analogy of zero-dimensional models (see Section 4.5.1), is represented by an ideal diode. Similar models have been proposed in [303, 56], to account for diseased valves, by introducing a suitable non-ideal law for the diode. More refined reduced models consider

the opening/closure mechanism not simply in an on-off mode, rather the open part of the orifice dynamically changes continuously by projecting the supposed leaflet position on the orifice plane. For example, in [533] the dynamics of the valve orifice opening/closure is given by a prescribed law, whereas in [302] it is given by

$$A_V = \frac{(1-\cos\theta)^2}{(1-\cos\theta_{max})^2},$$

where $A_V \in [0,1]$ is the percentage of open orifice area, θ the opening leaflet angle ($\theta = 0$ means closed valve) and θ_{max} the maximum opening angle. The value of θ is determined by the following ODE

$$\frac{d^2\theta}{dt^2} + k_1\frac{d\theta}{dt} + k_2(P_d - P_u)\cos\theta = 0, \tag{105}$$

for suitable parameters k_1 and k_2.

For all these models, that do not explicitly include the leaflets, there could be the need to switch between Dirichlet to Neumann (and vice versa) boundary conditions along a single heartbeat in a fluid problem. Indeed, a Dirichlet condition is usually prescribed when the valve is closed (e.g. homogeneous in the physiological case), whereas a Neumann or a resistance condition could be preferred when the valve is open. This could be problematic at the numerical level, in particular in view of the implementation. In [537], a new way to overcome this problem has been proposed, based on a Robin-like condition implemented by means of the extended Nitsche's method proposed in [282]. We detail here for the sake of simplicity the case of a Neumann-like condition for the open valve and we refer the reader to [537] for the more physiological case of a resistance condition. Let Γ be the valve orifice at hand and suppose that one wants to prescribe at each time the following conditions:

$$\boldsymbol{u} = \boldsymbol{g} \qquad \text{if the valve is closed;} \tag{106a}$$

$$\boldsymbol{T}_f\boldsymbol{n} = \boldsymbol{h} \qquad \text{if the valve is open.} \tag{106b}$$

For example, $\boldsymbol{g}$ could be obtained by a prescribed flow rate (null in the physiological case) by assuming a priori the shape of the velocity profile (e.g. flat), whereas usually $\boldsymbol{h} = P\boldsymbol{n}$, with P a prescribed mean pressure. Thus, the following term is added to the weak formulation (9) of the fluid problem:

$$-\int_\Gamma \frac{\gamma h}{\xi+\gamma h}\boldsymbol{T}_f(\boldsymbol{v},p)\boldsymbol{n}\cdot\boldsymbol{w}\,d\omega - \int_\Gamma \frac{\gamma h}{\xi+\gamma h}(\boldsymbol{v}-\boldsymbol{g})\cdot(\boldsymbol{T}_f(\boldsymbol{w},q)\boldsymbol{n})\,d\omega + \int_\Gamma \frac{1}{\xi+\gamma h}(\boldsymbol{v}-\boldsymbol{g})\cdot\boldsymbol{w}\,d\omega$$
$$-\int_\Gamma \frac{\xi\gamma h}{\xi+\gamma h}(\boldsymbol{T}_f(\boldsymbol{v},p)\boldsymbol{n}-\boldsymbol{h})\cdot(\boldsymbol{T}_f(\boldsymbol{w},q)\boldsymbol{n})\,d\omega + \int_\Gamma \frac{\xi}{\xi+\gamma h}\boldsymbol{h}\cdot\boldsymbol{w}\,d\omega,$$

where $\xi \in [0,+\infty)$ and $\gamma > 0$ are two parameters and h is the mesh size (possibly not constant). This discrete problem preserves the usual Finite Elements accuracy. We notice that for $\xi = 0$ we recover the classical Nitsche method to prescribe the Dirichlet condition (106a), whereas for $\xi \to +\infty$ the formulation is consistent with the Neumann condition (106b). Thus, the idea is to change the value of ξ (0 or $+\infty$) allowing for the switch

between Dirichlet and Neumann conditions. Alternatively, the switch between a flow rate and mean pressure condition could be prescribed by means of the defective version of the extended Nitsche method proposed in [565].

A second family of reduced strategies includes a reduced model of the leaflets without solving the full 3D mechanical problem. These methods are very useful when one wants to determine with a good accuracy the influence of the leaflets on the direction of the fluid jet. A first simple model is based on including the position of the open leaflets obtained by a preliminary mechanic simulation and considering an on-off opening/closure mode, see e.g. [70]. A similar model has been proposed in [16], where however an immersed resistive approach has been considered to switch between the open and closed configuration. In particular, the following term is added to the variational formulation of the fluid problem

$$\int_{\Gamma_o} R_o \boldsymbol{v} \cdot \boldsymbol{w} \, d\gamma + \int_{\Gamma_c} R_c \boldsymbol{v} \cdot \boldsymbol{w} \, d\gamma,$$

where Γ_o and Γ_c are the surfaces representing the open and closed leaflets configurations, respectively, and R_o and R_c the corresponding resistance, which act as penalization terms to enforce the no-slip condition $\boldsymbol{v} = \boldsymbol{0}$ at the leaflet. Thus, when the value of the resistance is high, the corresponding surface configuration is physically included in the model, the velocity is zero at the leaflet and, accordingly, a pressure drop is generated across the leaflet; on the contrary, when the value of the resistance is zero, the leaflet is invisible to the model, no constraint is prescribed on the velocity and no pressure drop is generated. The switch between large and vanishing values of the resistances is determined by (104).

More sophisticated models account not only for the open and closed configurations of the leaflets, but also provide a simplified dynamics of the whole valve opening/closure mechanism. For example, in [314, 171] a leaflet Γ is represented as a surface described by two embedded level-set functions which depend on a single scalar function of time, i.e. the opening angle θ. The latter is determined by a relation very similar to (105). At each time step, the term

$$\int_{\Gamma} R(\boldsymbol{v} - \boldsymbol{v}_{leaf}) \cdot \boldsymbol{w} \, d\gamma,$$

is added to the weak formulation of the fluid problem, in order to guarantee a no-slip condition at the leaflet ($\boldsymbol{v} = \boldsymbol{v}_{leaf}$, where $\boldsymbol{v}_{leaf}$ is the leaflet velocity determined from θ) by selecting the resistance R large enough. A similar approach has been recently adopted also in [19], where however the leaflet is represented in a more simplified way by means of the opening angle solely (no level set functions involved).

In Figure 23, we report an example of fluid-dynamics across the aortic valve obtained by means of the method proposed in [171].

7.4.3 Interaction between blood and leaflets

To accurately model the interaction between blood and valve leaflets, aimed, for example to a detailed computation of the internal leaflet stresses, the solution of a fully FSI problem is mandatory.

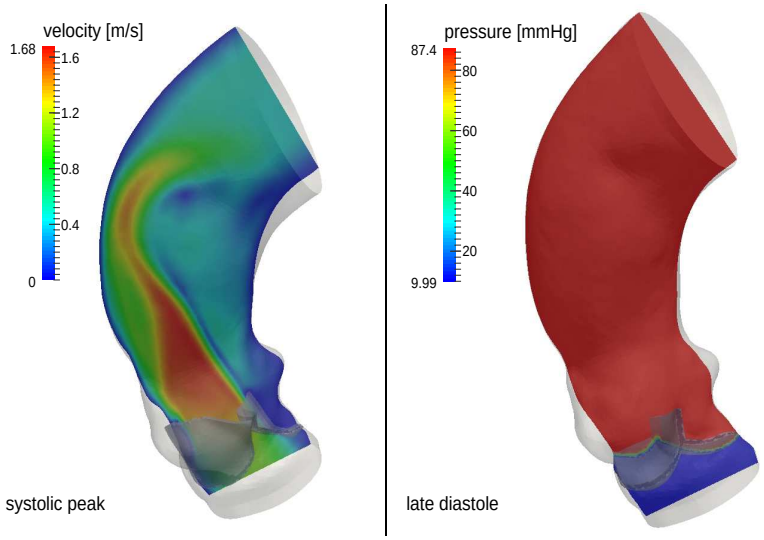

Figure 23: Fluid-dynamics in the ascending aorta with patient-specific aortic valve. These numerical results are obtained using *LifeV*. See [171] for a complete overview of the results

Unlike for the blood vessel and ventricular simulations, the Arbitrary Lagrangian-Eulerian (ALE) formulation, described in Section 4.6, is not suited to handle the FSI problem arising between blood and heart valve leaflets. Indeed, due to the large displacements of the leaflets, the fluid mesh becomes highly distorted, producing severely stretched mesh elements and thus requiring a frequent remeshing of the grid. For this reason, specific FSI techniques have been developed specifically for the numerical solution of this problem. The most successful are the *Immersed Boundary* method, the *Fictitious Domain* approach, and the *Cut-FEM*, together with their numerous variants. All these methods are characterized by a fixed fluid mesh and allow to treat non-conforming interface meshes.

Immersed Boundary method. The celebrated Immersed Boundary (IB) method has been specifically developed for the fluid-dynamics in the heart in [446]. The leaflets are represented by membranes in a Lagrangian framework thought as a part of the fluid, represented in an Eularian framework, and exerting to the latter internal localized forces. This is achieved by introducing a Dirac *delta* distribution, δ, on the membrane.

The IB method has been originally developed for finite differences spatial discretization, see e.g. [446, 374, 448]. In this case, in order to avoid leaks, the Lagrangian grid should be fine enough so that the distance between two adjacent points is less than the Eulerian mesh size. Then, the structural forces are interpolated into the fixed nodes of the fluid mesh. The major issue when finite differences are used is the approximation of δ. Usually, this is obtained by a function δ_h which is non-singular for each h and tends to δ for $h \to 0$ [448].

Here, we report the variational formulation of the IB method proposed in [65] which is useful for a Finite Element approximation and does not require any specific approx-

imation of the delta distribution. Given a two dimensional fluid domain Ω_f, let Γ_s be the immersed (one-dimensional) structure, whose material points are located at each t in $\boldsymbol{X}(s,t)$, where $s \in [0,L]$ is the Lagrangian coordinate. We consider as an example the case of a massless linear elastic structure with elasticity constant κ. Thus, referring to the notation introduced in Section 4.1 and assuming homogeneous boundary conditions, the weak formulation of the IB methods reads for each $t > 0$ [66]: Find $\boldsymbol{v} \in \boldsymbol{V}$, $\boldsymbol{v} = \boldsymbol{v}_0$ for $t = 0$, $p \in L^2(\Omega_f)$, and $\boldsymbol{X} = \boldsymbol{X}(t)$, $\boldsymbol{X} = \boldsymbol{X}_0$ for $t = 0$, such that

$$\rho_f \int_{\Omega_f} \frac{\partial \boldsymbol{v}}{\partial t} \cdot \boldsymbol{w}\, d\omega + \mathcal{A}_f(\boldsymbol{v},\boldsymbol{v},\boldsymbol{w}) + \mathcal{B}(p,\boldsymbol{w}) = \int_0^L \kappa \frac{\partial^2 \boldsymbol{X}(s,t)}{\partial s^2} \boldsymbol{w}(\boldsymbol{X}(s,t)) ds, \tag{107a}$$

$$\mathcal{B}(q,\boldsymbol{v}) = 0, \tag{107b}$$

$$\frac{\partial \boldsymbol{X}}{\partial t}(s,t) = \boldsymbol{v}(\boldsymbol{X}(s,t),t), \tag{107c}$$

for all $\boldsymbol{w} \in \boldsymbol{V}$ and $q \in L^2(\Omega_f)$. In fact, the right hand side of (107a) guarantees the satisfaction of the normal stress continuity at the membrane, whereas (107c) is the velocity continuity.

For the Finite Element approximation of the previous problem, usually the forcing term is integrated by parts. For example, in the case of linear Finite Elements for the structure, it becomes for each $t > 0$ [66]

$$\sum_{i=0}^{M-1} \kappa \left(\frac{\partial \boldsymbol{X}_h^{i+1}}{\partial s} - \frac{\partial \boldsymbol{X}_h^{i}}{\partial s} \right) \boldsymbol{w}(\boldsymbol{X}_h^i),$$

where $\boldsymbol{X}_h^i = \boldsymbol{X}_h(s_i)$, $i = 0, \ldots, M$, is the Finite Element approximation of $\boldsymbol{X}$ and s_i are the nodes of the one-dimensional mesh.

Regarding the time discretization, a first approach consists in considering a fully implicit scheme. For the backward Euler approximation, unconditional stability is guaranteed [552]. However, this scheme requires the introduction of subiteratons to handle the coupling between fluid and structure in (107). A more useful approach relies on treating the right hand side of (107a) explicitly and the remaining of the equation implicitly. The position occupied by the structure is then updated in a second step by means of a suitable implicit approximation of (107c). This scheme has been proved to be stable under a CFL-like condition [66].

Several extensions and applications of the IB method have been provided. Among them, we mention: the variational formulation for the case of a thick immersed structure proposed in [67], where the right hand side of (107a) becomes $\int_{\Omega_s} \widehat{\boldsymbol{T}}_s(\widehat{\boldsymbol{d}}(\boldsymbol{s},t)) : \nabla \boldsymbol{w}(\boldsymbol{X}(\boldsymbol{s},t)) d\boldsymbol{s}$, $\boldsymbol{s}$ being in this case a vectorial Lagrangian coordinate; a mesh adaptive approach used in combination with a second order scheme, see [221]; the use of a curvilinear fixed fluid mesh to improve flexibility and efficiency (*CURVIB* approach, see [71]); the application to realistic three-dimensional mitral and aortic valves successfully addressed in [222, 608].

Fictitious Domain approach. The Fictitious Domain (FD) approach was first introduced in [216, 52] and then applied to the contest of heart valve in [243, 129]. FD can be

regarded as the dual of the IB method, in the sense that in the latter a weak enforcement of the normal stresses continuity at the FS interface is added to the weak formulation of fluid problem, whereas in the FD approach the velocity continuity is weakly enforced at the FS interface. This is achieved by means of Lagrange multipliers, as detailed in what follows (we refer to Sections 4.1, 4.2 and 4.3 for the notation, in particular variables with $\widehat{\ }$ are referred to the reference domain, and we assume homogeneous boundary conditions): Find $\boldsymbol{v}(t) \in \boldsymbol{V}^t$, $\widehat{\boldsymbol{d}}(t) \in \boldsymbol{D}$, $\boldsymbol{\lambda}(t) \in \boldsymbol{H}^{-1/2}(\Sigma^t)$ and $p(t) \in L^2(\Omega_f^t)$, such that

$$
\begin{aligned}
&\rho_f \int_{\Omega_f^t} \frac{\partial \boldsymbol{v}}{\partial t} \cdot \boldsymbol{w}\, d\omega + \mathcal{A}_f(\boldsymbol{v}, \boldsymbol{v}, \boldsymbol{w}) + \mathcal{B}(p, \boldsymbol{w}) + \rho_s \int_{\Omega_s} \frac{\partial^2 \widehat{\boldsymbol{d}}}{\partial t^2} \cdot \widehat{\boldsymbol{e}}\, d\omega + \int_{\Omega_s} \widehat{\boldsymbol{T}}_s \left(\widehat{\boldsymbol{d}}\right) : \nabla \widehat{\boldsymbol{e}}\, d\omega \\
&\qquad = \int_{\Sigma^t} \boldsymbol{\lambda} \cdot (\boldsymbol{w} - \boldsymbol{e}) d\sigma, \\
&\mathcal{B}(q, \boldsymbol{v}) = 0, \\
&\int_{\Sigma^t} \boldsymbol{\mu} \cdot \left(\boldsymbol{v} - \frac{\partial \boldsymbol{d}}{\partial t}\right) d\sigma = 0, \\
&\boldsymbol{d}_f = \boldsymbol{d} \qquad \text{at } \Sigma^t,
\end{aligned}
\tag{108}
$$

for all $\boldsymbol{w} \in \boldsymbol{V}, \widehat{\boldsymbol{e}} \in \boldsymbol{D}$, $\boldsymbol{\mu} \in \boldsymbol{H}^{-1/2}(\Sigma^t)$ and $q \in L^2(\Omega_f)$. For the well-posedness of the discretized-in-time version of problem (108) we refer to [191]. We notice that the use of the same Lagrange multiplier $\boldsymbol{\lambda}$ from both the fluid and structure sides guarantees also the continuity of normal stresses [191].

A validation with experimental measures has been successfully reported in [528], whereas an application of the FD approach for three-dimensional problems in combination with a contact model for the leaflets has been reported in [14].

Cut-FEM approach. A natural strategy to handle an internal interface cutting in an arbitrary way the mesh consists in writing two weak formulations of the problem at hand, one for each of the two subdomains generated by the presence of the interface, and then to sum them up. In this case, the meshes of the two subdomains are fixed (background meshes). Since some of the mesh elements are cut by the interface, their contribution in the matrices assembling is split into two parts, see Figure 24, left. This method is known as Cut-FEM [240, 241]. Here, the jump between the normal stresses at the interface is determined by the physical interaction with the interface, as happens for the blood/valve interaction.

A common strategy used to guarantee the satisfaction of the interface continuity conditions is the *Discontinuous Galerkin* (DG) mortaring (often referred to as *Nitsche* mortaring). This is a very effective choice since DG method prescribes interface conditions in a weak sense, thus allowing a great degree of flexibility of the solution at the interface [240, 241].

Finally, we notice that the implementation of the Cut-FEM method is not standard since in the cut elements we may have polygonal elements, see for example Figure 24, left, where the original triangle is split into a triangle and a trapezoid. A solution is offered by the *Extended Finite Elements* method (X-FEM), where the FE space is suitably enriched in order to make easy the tratment of the cut elements. In particular, the basic idea is to

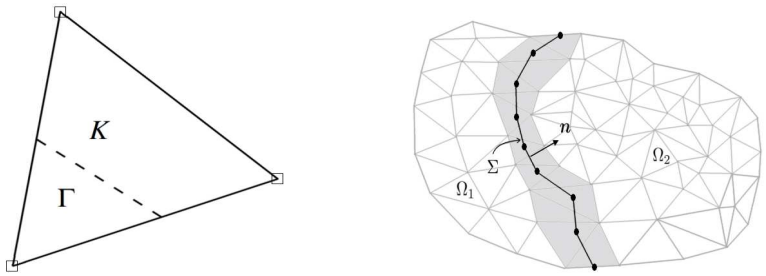

Figure 24: Element mesh K cut by the interface Γ (left) and FS domain (right). For the latter, we notice that Ω_f^1 and Ω_f^2 are two non-overlapping subdomains, whereas the related computational meshes feature an overlap (in grey) in view of the X-FEM approach

duplicate the degrees of freedom in the cut elements and to use in both the subdomains the basis functions of the original triangle either to represent the FE solution and to compute the integrals [240].

To provide a concrete example of the Cut-FEM method, we report in what follows the weak formulation introduced and analyzed in [4], related to the case of a valve embedded in blood and represented by the membrane of equation

$$\rho_s H_s \frac{\partial \boldsymbol{d}}{\partial t} + \boldsymbol{L}\boldsymbol{d} = -[\![\boldsymbol{T}_f \boldsymbol{n}]\!] \qquad \text{in } \Sigma,$$

where Σ is the embedded membrane, $\boldsymbol{L}$ is an elliptic operator, and $[\![.]\!]$ denoted the jump across the membrane. In particular, referring to Figure 24, right, let Ω_f^1 and Ω_f^2 be two non-overlapping subdomains separated by Σ, and $\Omega_{f,h}^1$ and $\Omega_{f,h}^2$ two meshes containing Ω_f^1 and Ω_f^2, respectively, with an overlap region (in gray in the figure) containing the membrane. Moreover, let $\boldsymbol{V}_h^i$ and Q_h^i be velocity and pressure Finite Elements spaces related to $\Omega_{f,h}^i$ and $\mathcal{C}^i$ one of the bilinear o trilinear forms $\mathcal{C}$ introduced in Section 2 restricted to $\Omega_{f,h}^i$. Thus we have

$$\sum_{i=1}^{2} \left[\rho_f \int_{\Omega_f^i} \frac{\partial \boldsymbol{v}_h^i}{\partial t} \cdot \boldsymbol{w}\, d\omega + \mathcal{A}_f^i(\boldsymbol{v}_h^i, \boldsymbol{v}_h^i, \boldsymbol{w}) + \mathcal{B}^i(p_h^i, \boldsymbol{w}) - \mathcal{B}^i(q, \boldsymbol{v}_h^i) \right]$$

$$+ s_h(\boldsymbol{v}_h, \boldsymbol{w}) + \rho_s H_s \int_\Sigma \frac{\partial \boldsymbol{d}_h}{\partial t} \cdot \boldsymbol{e}\, d\sigma + \int_\Sigma \boldsymbol{L}\boldsymbol{d}_h \cdot \boldsymbol{e}\, d\sigma$$

$$+ \sum_{i=1}^{2} \Bigg[- \int_\Sigma \boldsymbol{T}_f(\boldsymbol{v}_h^i, p_h^i)\boldsymbol{n}^i \cdot (\boldsymbol{w} - \boldsymbol{e}) d\sigma -$$

$$\int_\Sigma \boldsymbol{T}_f(\boldsymbol{w}, q)\boldsymbol{n}^i \cdot \left(\boldsymbol{v}_h^i - \frac{\partial \boldsymbol{d}_h}{\partial t} \right) d\sigma + \frac{\gamma}{h} \int_\Sigma \left(\boldsymbol{v}_h^i - \frac{\partial \boldsymbol{d}_h}{\partial t} \right) \cdot (\boldsymbol{w} - \boldsymbol{e}) d\sigma \Bigg] = 0.$$

The terms in the third and fourth rows of the previous formulation are nothing but the usual DG terms guaranteeing consistency, symmetry and stability of the method, whereas $s_h(\cdot,\cdot)$ accounts for the *ghost nodes stabilization* [79] that guarantees an optimal convergence order. This formulation has been introduced for infinitesimal displacements. However, the authors treat also the case of a moving interface, for details see [4].

Finally, we notice that the Cut-FEM approach has been also considered for the case of a thick structure, see [81, 614].

7.5 The total heart integration modeling

We conclude this section by providing some hints on the modeling of the complete heart function, a challenging endeavor. The latter is very complex and requires the merge of all the mathematical, numerical and computational issues highlighted previously in this section, see [325, 88, 417, 470].

Basically, an heart integrated model involves the coupling of the electro-mechanical problem (101), the blood fluid-dynamics (see Sect. 7.3), and the valve functioning (see Sect. 7.4). The coupling between the first two subproblems occurs at the endocardium Σ_{endo}, see Figure 15. In particular, this is determined by the classical fluid-structure interaction coupling conditions, i.e. the kinematic condition (22c) and the dynamic condition (22d). In particular, referring to the notation of Sect. 4.1-7.2 and to Figure 15, we have the following problem: Find the blood velocity $\boldsymbol{v}$ and pressure p, the muscle displacement $\boldsymbol{d}$, the transmembrane potential V_m, the gating variables $\boldsymbol{w}$, and the ionic concentration variables $\boldsymbol{c}$, such that

$$\rho_f \left(\frac{\partial \boldsymbol{v}}{\partial t} + \rho_f (\boldsymbol{v} \cdot \nabla)\boldsymbol{v} \right) - \nabla \cdot \boldsymbol{T}_f(\boldsymbol{v}, p) = \boldsymbol{0} \qquad \text{in } \Omega^t_{cav}, \tag{109a}$$

$$\nabla \cdot \boldsymbol{v} = 0 \qquad \text{in } \Omega^t_{cav}, \tag{109b}$$

$$\boldsymbol{v} = \frac{\partial \boldsymbol{d}}{\partial t} \qquad \text{at } \Sigma^t_{endo}, \tag{109c}$$

$$\left(\boldsymbol{T}^P_s(\boldsymbol{d}) + \boldsymbol{T}^A_s\left(\boldsymbol{c}, \boldsymbol{d}, \frac{d\boldsymbol{d}}{dt}\right) \right) \boldsymbol{n} = \boldsymbol{T}_f(\boldsymbol{v}, p)\, \boldsymbol{n} \qquad \text{at } \Sigma^t_{endo}, \tag{109d}$$

$$\nabla \cdot \left(\widehat{\boldsymbol{T}}^P_s(\widehat{\boldsymbol{d}}) + \widehat{\boldsymbol{T}}^A_s\left(\widehat{\boldsymbol{c}}, \widehat{\boldsymbol{d}}, \frac{d\widehat{\boldsymbol{d}}}{dt}\right) \right) = \boldsymbol{0} \qquad \text{in } \Omega_{mus}, \tag{109e}$$

$$\widehat{\boldsymbol{T}}^A_s = P^A \boldsymbol{a}_f \otimes \widehat{\boldsymbol{a}}_f, \qquad P^A = \mathcal{A}\left(\widehat{\boldsymbol{c}}, \widehat{\boldsymbol{d}}, \frac{d\widehat{\boldsymbol{d}}}{dt}\right) \qquad \text{in } \Omega_{mus}, \tag{109f}$$

$$\widehat{V}_m = \mathcal{M}\left(\widehat{V}_m; \widehat{\boldsymbol{d}}, \widehat{\boldsymbol{w}}, \widehat{\boldsymbol{c}}\right) \qquad \text{in } \Omega_{mus}, \tag{109g}$$

$$(\widehat{\boldsymbol{w}}, \widehat{\boldsymbol{c}}) = \mathcal{G}(\widehat{\boldsymbol{w}}, \widehat{\boldsymbol{c}}; \widehat{V}_m) \qquad \text{in } \Omega_{mus}. \tag{109h}$$

After numerical discretization in time and space, the corresponding nonlinear algebraic system is tremendously stiff and can feature a very high numerical dimension. Devising efficient numerical strategies for its solution is a very active research area.

An effective strategy to numerically solve the entire heart coupled problem is given by the iterative solution at each time step of the electro-mechanical and fluid subproblems and based on the exchange of the interface conditions (109c)-(109d). In particular, one of the partitioned strategies described in Sect. 4.6.3 can be adapted and used for problem (109) as well. Of course, at each iteration of the partitioned algorithm, the electro-mechanical problem could be solved by means of one of the strategies reported in Sect. 7.2.

Another partitioned algorithm for the solution of problem (109) is obtained by considering the solution at each time step of the electrical problem first and the FSI problem later [417]. This is nothing but an extension of Algorithms EM1 and EM1/bis reported in Sect. 7.2, where steps 2b and 2bis/b are replaced by a Newton iteration over the FSI problem.

A different approach is based on the monolithic solution of the integrated heart problem (109) by means of a full Newton method. In particular, in [470] fully implicit and semi-implicit methods are described. The latter is based on updating only a part of the Jacobian as a consequence of an operator splitting technique. The authors highlighted by means of numerical experiments that particular choices of the splitting and of the temporal scheme could lead to numerical instabilities. Whatever strategy is adopted, the tangent problem at each Newton iteration is solved by means of a preconditioned iterative method, which is in this case particularly suited due to the block structure of the Jacobian, see [470].

Stability and convergence analysis of the different approaches is a field of current investigation.

Part III
OPTIMIZING, CONTROLLING, ADDRESSING UNCERTAINTY, REDUCING COMPLEXITY

8 Going beyond direct simulation

In all problems considered so far, for given set of inputs (geometry, source terms, boundary and initial conditions, etc.) the goal was to solve numerically a forward PDE problem and, possibly, evaluate some physical indices of clinical interest, such as a flow rate across a vessel section, the wall shear stress over a portion of the lumen boundary, the oscillatory shear index, etc. On the other hand, efficient numerical algorithms and computational resources nowadays available allow to tackle several additional kind of problems.

When simulating blood flows one has to face the variability of input data, like geometrical features of the vessel, boundary conditions, physical coefficients (e.g. the Reynolds number, the Womersley number, the structural model or material parameters related to

the vessel wall). Very often, these data vary within a broad range and are almost impossible to be characterized exactly. All these inputs affect the solution of the problem under investigation, as well as the outcomes of clinical interest. Being able to efficiently characterize input/output relationships is thus important in the clinical context, in order to investigate both *intra-patients* and *inter-patients* variability. In the former case we include all those effects due to variations affecting a single patient, e.g., over time, or before/after clinical intervention. Regarding the latter case, we mention for instance the morphological variability among vessel shapes due to age, size or pathological factors (see, e.g., [599] in the case of distal coronary anastomoses). Developing mathematical techniques capable to detect the most relevant parameters, and then address the impact of their variation on the outputs of interest, is thus of paramount importance. This requires the solution of *many queries* to the *forward* problem. In this context, three classical situations we may face are those of: *(i)* optimal control and optimal design, *(ii)* parameter identification and data assimilation, and *(iii)* uncertainty quantification.

1. *Optimal control and optimal design problems.* When we pursue a suitable objective through an optimal strategy to be determined, we act on some *inputs* of the given partial differential equation, the *state* problem, such as boundary data, physical coefficients, or the shape of the domain itself, the *control* variables, so that the solution of the corresponding state problem could meet the prescribed goal. This yields a PDE-constrained optimization problem; its numerical solution usually poses severe computational challenges, as the state problem needs to be solved several times while searching the optimal control in an iterative way. Exploiting numerical optimization procedures for blood flow simulations is meant to *(i)* improving the design of prosthetic devices (such as stents, grafts, ventricular assist devices) with the aim of fulfilling a specific target, or *(ii)* customizing treatments or surgical procedures provided patient-specific information can be acquired. Examples include the optimal placement of electrodes in a defibrillation stage to damp the electrical activity in the myocardium in a desired way when dealing with the therapeutic treatment of cardiac arrythmias [393], the optimization of the shape of a cannula in order to maximize the flow-rate through a ventricular assist device [364], the improvement of the shape of a coronary bypass graft in order to possibly avoid vessel reocclusion [329, 149], to mention a few. The first example mentioned above represents an optimal control problem, where the control variable is a current source for the monodomain (or bidomain) equation (see Sect. 7.1) – i.e. one of its data. The two other examples address a *shape optimization* or *optimal design* problem to be solved, the control variable being the *shape* of the domain where the state problem is set.

2. *Parameter identification and data assimilation.* In principle, cardiovascular models necessitate a huge amount of data, such as patient's radiological images and measurements. In general, however, some of them may be missing – remember for instance the issue of missing or defective boundary conditions discussed in Section 4.4, or the lack of biological parameters characterizing the tissue properties. For instance, it is very hard to estimate electrical conductivity of the myocardium for electrophysiology

models, whereas (pointwise) measures of the electrical potential – whose mathematical modeling can be characterized by a PDE model requiring electrical conductivities as inputs – can be more easy to acquire. By solving *inverse/identification problems* in cardiovascular modeling, we aim at identifying those inputs which are unknown or affected by uncertainty. For that, we rely on suitable quantities which are *(i)* acquired from measurements, such as displacements, pressures, flow rates, etc., and *(ii)* obtained as outcome of a numerical simulation, and match these two sets of values. In other words, identifying those input values yielding the acquired measurements requires to drive the PDE outcome as near as possible to the measured quantity. In general, vastly different inputs may have produced the observed outcome: this is why, instead of finding the most likely input configuration resulting in the performed observation, we rather rely on statistical inversion theory, in order to incorporate all possible information about the unknown inputs we may have prior to the measurement. This requires to reformulate inverse problems as problems of statistical inference, e.g. by means of Bayesian statistics. A second issue is *data assimilation*: this rather generic term encompasses a wide range of techniques exploited to merge measures/images into the mathematical model in order to improve numerical simulations. Not only, a filtering effect induced by the numerical simulation can also be exploited in view of noise reduction in images/measures acquisition as well.

3. *Uncertainty quantification and propagation.* The confidence in the outcome of a cardiovascular simulation directly depends on the level of accuracy and certainty at which inputs can be determined. In fact, although outcomes are computed from inputs through a deterministic process, often input data are polluted by some experimental noise, or cannot be fully ascertained. Common sources of uncertainty in cardiovascular simulations include *(i)* boundary conditions, *(ii)* anatomical models, where each geometrical model is polluted by image noise, *(iii)* flow-split, since very often there is a lack of clinical data to determine flow distribution to multiple distal branches, and *(iv)* material properties, related to vessel walls or blood [505]. Due to uncertainty, computational simulations have to be performed for a set of different parameter configurations and then merged in order to determine how robust simulation outcomes are with respect to variations of uncertain inputs [506]. This is indeed strictly related with the task of parametric studies and sensitivity analyses, and can be seen as a *forward uncertainty quantification (UQ) problem.* Evaluating the propagation of input uncertainties through computed outputs means to evaluate suitable statistics of the outputs (such as expected values, moments, confidence bands) that are functions of the parameters affected by uncertainty. On the other hand, also the solution of optimal control and inverse identification problems depends on those experimental noises affecting observations and measures exploited during the identification process or the setup of a desired target. Evaluating the effect of uncertainties in this case, providing suitable *confidence* bands about the estimated quantities – and not only point estimates – and characterizing the statistical distribution of the unknown parameters by taking into account a set of measured data represent instances of *inverse UQ problems.* In this second case, quantifying uncertainties is

even more important because an inverse problem is intrinsically ill-posed.

In the following sections we sharpen our discussion about these three classes of problems, showing relevant examples in cardiovascular modeling.

9 Control and Optimization

Solving a PDE-constrained optimization problem consists of reaching a target by acting on a system governed by PDEs. The goal is to act on a *state problem* $\mathcal{E}(y,u) = 0$ given by a PDE system modeling the behavior of a state variable y, through a control variable u in order to reach a desirable target. This is usually done by minimizing (or maximizing) a cost functional $J = J(y,u)$ expressing some physical index of interest encoding the desired objective – for instance, the squared distance from a target state. For a comprehensive presentation of the functional setting and well-posedness analysis of PDE-constrained optimization see the monographs [252, 235]. Other classes of problems of interest in cardiovascular applications, such as those related with *parameter estimation*, can also be casted into a PDE-constrained optimization framework; see, e.g., Sect. 10.1 for further insights.

Generally speaking, a PDE-constrained optimization problem reads

$$\min_{y,u} J(y,u) \qquad \text{subject to} \quad \mathcal{E}(y,u) = 0, \quad y \in V, \quad u \in \mathcal{U}_{ad} \subseteq \mathcal{U}. \tag{110}$$

Here V and $\mathcal{U}$ denote the state and the control space, whereas $\mathcal{E} : V \times \mathcal{U} \to V^*$ and $J : V \times \mathcal{U} \to \mathbb{R}$ denote the state equation and the cost functional, respectively; V^* is the dual space of V, and $\langle \cdot\ ,\ \cdot \rangle_{V^*,V}$ denotes the duality between two elements in V^* and V; in the same way, $\langle \cdot\ ,\ \cdot \rangle_{\mathcal{U}^*,\mathcal{U}}$ indicates the duality between two elements in $\mathcal{U}^*$ and $\mathcal{U}$. Additional constraints, depending on the problem at hand, can also be imposed, e.g. under the form of inequalities – we express this fact by saying that we seek the optimal control in a closed subset $\mathcal{U}_{ad} \subseteq \mathcal{U}$ of admissible controls.

We assume that the state equation $\mathcal{E}(y,u) = 0$ has a unique solution $y = y(u) \in V$, and that the Fréchet derivative (with respect to y) $\mathcal{E}_y(y(u),u)$ has a bounded inverse for each $u \in \mathcal{U}$. Under these assumptions, the solution operator of the state equation is continuously differentiable – we denote by $y'(u)$ its derivative – and the following *reduced formulation*

$$\min_{u} \tilde{J}(u) = J(y(u),u), \quad u \in \mathcal{U}_{ad} \tag{111}$$

is equivalent to (110). Note that this is a convenient framework to embrace – upon defining suitable functional spaces and operators – both stationary and time-dependent state problems; in the following we will make clear whether or not the proposed methods can be used to tackle both classes of problems.

9.1 Optimality conditions

The solution $(\hat{y}, \hat{u})$ of a PDE-constrained optimization problem like (110) requires a system of optimality conditions to be fulfilled, including the state equation and an optimality condition which involves the gradient of the cost functional. Indeed, if $\hat{u} \in U_{ad}$ is a local minimum of $\tilde{J}$, then it satisfies the variational inequality (also referred to as *optimality condition* or *minimum principle*)

$$\langle \tilde{J}'(\hat{u}), v - \hat{u} \rangle_{\mathcal{U}^*,\mathcal{U}} \geq 0 \qquad \forall v \in \mathcal{U}_{ad}. \tag{112}$$

The quantity appearing at the left-hand side is the so-called Gâteaux derivative of $\tilde{J}$, evaluated at $\hat{u}$, in the generic, admissible direction $v - \hat{u}$; see, e.g., [551]; $\tilde{J}'(\hat{u})$ denotes the gradient of $\tilde{J}$ at $\hat{u}$. To express this latter quantity in terms of the state solution y, we can use either *(i)* the sensitivity approach, or *(ii)* the adjoint approach. As we will see below, in both cases at least a second PDE problem has to be solved in order to evaluate $\tilde{J}'(u)$.

9.1.1 Sensitivity approach

Computing *sensitivities* requires the evaluation of directional derivatives of both the cost functional and the state solution. For any $u, v \in \mathcal{U}$, we can write

$$\langle \tilde{J}'(u), v \rangle_{\mathcal{U}^*,\mathcal{U}} = \langle J_y(y(u), u), y'(u)v \rangle_{V^*,V} + \langle J_u(y(u), u), v \rangle_{\mathcal{U}^*,\mathcal{U}}. \tag{113}$$

The quantity $\delta_v y = y'(u)v$ represents the sensitivity of the state with respect to the control, evaluated at u, for a given variation v, and can be obtained by solving a further PDE: indeed, differentiating the state equation $\mathcal{E}(y(u), u) = 0$ along the direction v we obtain

$$\mathcal{E}_y(y(u), u)y'(u)v + \mathcal{E}_u(y(u), u)v = 0, \tag{114}$$

being $\mathcal{E}_y(y, u)$, $\mathcal{E}_u(y, u)$ the Fréchet derivatives of the state operator with respect to y and u, respectively; see, e.g., [551]. Then, $\delta_v y = y'(u)v$ is given by the solution of the linearized state equation

$$\mathcal{E}_y(y(u), u)\delta_v y = -\mathcal{E}_u(y(u), u)v. \tag{115}$$

Note that $y'(u) : \mathcal{U} \to V$ is a linear operator so that, for any admissible $v \in \mathcal{U}$, a new problem has to be solved to evaluate $\delta_v y$. Numerically, this approach is very demanding if the whole gradient $\tilde{J}'(u)$ is required: in this case, the number of linearized state equations (115) to be solved is equal to the dimension of the control space $\mathcal{U}$, a task that becomes out of reach as soon as the control has dimension larger than $\mathcal{O}(10)$.

9.1.2 Adjoint approach and Lagrange multipliers

A convenient alternative is based on the so-called *adjoint approach*. By rewriting (113) as

$$\langle \tilde{J}'(u), v \rangle_{\mathcal{U}^*,\mathcal{U}} = \langle (y'(u))^* J_y(y(u), u) + J_u(y(u), u), v \rangle_{\mathcal{U}^*,\mathcal{U}} \tag{116}$$

and exploiting problem (114), we can express the first term at the right-hand side of (116) as

$$(y'(u))^* J_y(y(u), u) = -\mathcal{E}_u^*(y(u), u)((\mathcal{E}^*{}_y(y(u), u)))^{-1} J_y(y(u), u),$$

where $\mathcal{E}_u^*(y(u),u)$ is the adjoint operator[2] of $\mathcal{E}_u(y(u),u)$. Let us introduce an additional variable $\lambda = \lambda(u) \in V$, called *adjoint state*, the solution of

$$\mathcal{E}_y(y(u),u))^*\lambda = -J_y(y(u),u). \tag{117}$$

Then $(y'(u))^* J_y(y(u),u) = \mathcal{E}_u^*(y(u),u)\lambda$; moreover, owing to (116), the evaluation of

$$\tilde{J}'(u) = \mathcal{E}_u^*(y(u),u)\lambda(u) + J_u(y(u),u), \tag{118}$$

simply requires solving the state problem and a further PDE problem, no matter which the dimension of the control space $\mathcal{U}$ is. Note that the adjoint problem is always a linear PDE.

The adjoint-based expression of the gradient of the cost functional (and, more in general, a system of first-order optimality conditions) can also be obtained, in a more straightforward way, relying on the Lagrange multipliers' method [252]. Let us define the Lagrangian functional $\mathcal{L} : V \times \mathcal{U} \times V \to \mathbb{R}$,

$$\mathcal{L}(y,u,\lambda) = J(y,u) + \langle \lambda, \mathcal{E}(y,u)\rangle_{V,V^*},$$

where $\lambda \in V$ denotes a Lagrange multiplier enforcing the PDE constraint (playing the role of adjoint variable); note that in this case the three variables are independent.

By deriving $\mathcal{L}$ with respect to λ and imposing that the derivative is equal to zero, we recover the state problem,

$$\langle \mathcal{L}_\lambda(y,u,p), \varphi\rangle_{V^*,V} = 0 \quad \forall \varphi \in V \qquad \Leftrightarrow \qquad \mathcal{E}(y,u) = 0.$$

Similarly, by deriving $\mathcal{L}$ with respect to y, we obtain the expression of the adjoint problem (117),

$$\langle \mathcal{L}_y(y,u,p), \psi\rangle_{V^*,V} = 0 \quad \forall \psi \in V \qquad \Leftrightarrow \qquad J_y(y,u) + \mathcal{E}_y^*(y,u) = 0. \tag{119}$$

Finally, we impose that at the optimum,

$$\langle \mathcal{L}_u(y,u,\lambda), v-u\rangle_{\mathcal{U}^*,\mathcal{U}} = 0 \ \ \forall v \in \mathcal{U}_{ad} \quad \Leftrightarrow \quad \langle J_u(y,u)+\mathcal{E}_u(y,u)^*\lambda, v-u\rangle_{\mathcal{U}^*,\mathcal{U}} \geq 0 \quad \forall v \in \mathcal{U}_{ad}.$$

In this way, a system of first-order necessary optimality conditions to be fulfilled by the optimal solution (y,u) and the corresponding adjoint state λ is given by the following Karush-Kuhn-Tucker (KKT) system:

$$\begin{cases} \mathcal{E}(y,u) = 0, \\ \mathcal{E}_y(y,u)^*\hat{\lambda} = -J_y(y,u), \\ \langle J_u(y,u) + \mathcal{E}_u(y,u)^*\lambda, v-u\rangle_{\mathcal{U}^*,\mathcal{U}} \geq 0 \quad \forall v \in \mathcal{U}_{ad}. \end{cases} \tag{120}$$

[2]The adjoint operator of $\mathcal{E}$, denoted by $\mathcal{E}^*$, is given by the relation $(\mathcal{E}^*\varphi,\psi)_{L^2(\Omega)} = (\varphi,\mathcal{E}\psi)_{L^2(\Omega)}$ for any $\varphi,\psi \in C_0^\infty(\Omega)$; note that no boundary condition is involved in its definition. For this reason, $\mathcal{E}^*$ is also referred to as the *formal* adjoint operator.

In the unconstrained case $\mathcal{U}_{ad} \equiv \mathcal{U}$, the variational inequality reduces to an equation,

$$\langle J_u(y,u) + \mathcal{E}_u(y,u)^* \lambda, v \rangle_{\mathcal{U}^*,\mathcal{U}} = 0 \qquad \forall v \in \mathcal{U},$$

so that (120) can be viewed as the Euler-Lagrange system for the Lagrangian functional, that is, the solutions of (120) are the stationary points of $\mathcal{L}(\cdot,\cdot,\cdot)$, i.e.

$$\nabla \mathcal{L}(y,u,\lambda)[w,v,\eta] = 0 \qquad \forall (\phi, v, \psi) \in Y \times \mathcal{U} \times V.$$

The third inequality of system (120) allows to recover the expression of the gradient $\tilde{J}'(u)$. Indeed, since $\mathcal{E}(y(u),u) = 0$, it holds $\mathcal{L}(y(u),u,\lambda) = \tilde{J}(u)$ for any arbitrary $\lambda \in V$, so that, by differentiating this latter equality with respect to u, we obtain

$$\langle \tilde{J}'(u), v \rangle_{\mathcal{U}^*,\mathcal{U}} = \langle \mathcal{L}_y(y(u),u,\lambda), y'(u)v \rangle_{V^*,V} + \langle \mathcal{L}_u(y(u),u,\lambda), v \rangle_{\mathcal{U}^*,\mathcal{U}} = \langle \mathcal{L}_u(y(u),u,\lambda), v \rangle_{\mathcal{U}^*,\mathcal{U}}.$$

Hence, $\tilde{J}'(u) = \mathcal{L}_u(y(u),u,\lambda(u))$, since $\langle \mathcal{L}_y(y(u),u,\lambda), \psi \rangle_{V^*,V} = 0$ for any $\psi \in V$, thanks to (119).

For the sake of illustration, we discuss a specific example, by considering the problem of minimizing the energy

$$J(\boldsymbol{v},\boldsymbol{u}) = \frac{1}{2}\int_{\Omega_{obs}} |\boldsymbol{v} - \boldsymbol{v}_d|^2 d\Omega + \frac{\alpha}{2}\int_{\Gamma_{con}} |\nabla \boldsymbol{u}|^2 d\Gamma,$$

of a fluid flow in a tract of blood vessel where a device (e.g. a bypass or a cannula) is implanted. The function of the device is represented by a velocity control $\boldsymbol{u}$ acting on the boundary $\Gamma_{con} \subset \partial\Omega_f$ that represents the crossing section between the device and the vessel, see Fig. 25. The goal is to regularize the velocity pattern in a suitable observation region $\Omega_{obs} \subseteq \Omega_f$ by requiring $\boldsymbol{v}$ to be as close as possible to a desired distribution $\boldsymbol{v}_d$; see the related discussion in the next section. Referring to the notation in Section 4, for the sake of simplicity, we consider a steady version of the Navier-Stokes equations (4a)–(4b), for which the velocity-pressure couple $y = (\boldsymbol{v}, p) \in V = (H^1_{0,\Gamma_D}(\Omega_f))^d$ solves the state problem

$$\begin{aligned}
-\nabla \cdot \mathbf{T}_f(\boldsymbol{v},p) + \rho_f(\boldsymbol{v}\cdot\nabla)\boldsymbol{v} &= \mathbf{0} && \text{in } \Omega_f \\
\nabla \cdot \boldsymbol{v} &= 0 && \text{in } \Omega_f \\
\boldsymbol{v} &= \boldsymbol{v}_{in} && \text{on } \Gamma_{in} \\
\boldsymbol{v} &= \mathbf{0} && \text{on } \Gamma_w \\
\boldsymbol{v} &= \boldsymbol{u} && \text{on } \Gamma_{con} \\
\boldsymbol{T}_f(\boldsymbol{v},p)\boldsymbol{n} &= \mathbf{0} && \text{on } \Gamma_{out}
\end{aligned}$$

where the control variable is the velocity $\boldsymbol{u} \in \mathcal{U} = (H^1_0(\Gamma_{con}))^d$ imposed on the boundary Γ_{con}. $\alpha > 0$ is a parameter penalizing the control magnitude (or cost); this can also be seen as a regularization term, ensuring the convexity of the cost functional. The fluid Cauchy stress tensor $\mathbf{T}_f(\boldsymbol{v},p)$ has been defined in (5).

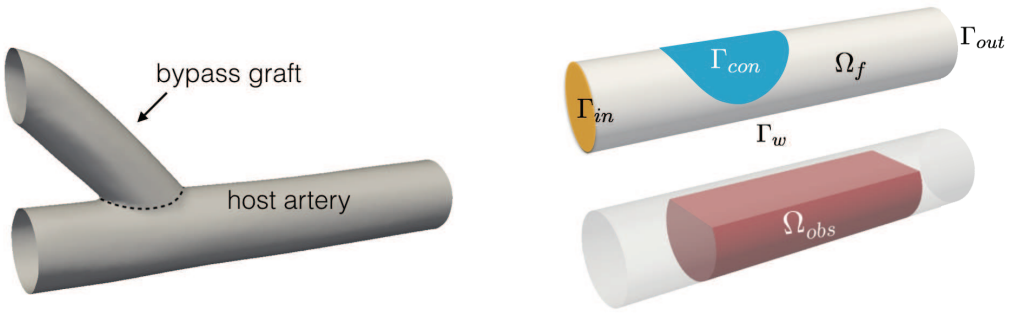

Figure 25: Left: schematic representation of a bypass graft. Right: domain, boundary portion and observation region for the bypass model problem

Following the Lagrangian approach, we can derive a system of first-order optimality conditions, where the adjoint problem for the adjoint variables $\lambda = (\boldsymbol{z}, q) \in V$ reads

$$\begin{aligned} -\nabla \cdot \mathbf{T}_f(\boldsymbol{z}, q) + \rho_f(\nabla^T \boldsymbol{v})\boldsymbol{z} - \rho_f(\boldsymbol{v} \cdot \nabla)\boldsymbol{z} = (\boldsymbol{v} - \boldsymbol{v}_d)\mathcal{I}_{\Omega_{obs}} \qquad & \text{in } \Omega_f \\ \nabla \cdot \boldsymbol{z} = 0 \qquad & \text{in } \Omega_f \\ \boldsymbol{z} = \mathbf{0} \qquad & \text{on } \Gamma_{in} \cup \Gamma_w \cup \Gamma_{con} \\ \boldsymbol{T}_f(\boldsymbol{z}, q)\boldsymbol{n} = \mathbf{0} \qquad & \text{on } \Gamma_{out} \end{aligned}$$

being $\mathcal{I}_{\Omega_{obs}} = \mathcal{I}_{\Omega_{obs}}(\mathbf{x})$ the characteristic function of the region Ω_{obs}. Note that the adjoint problem is linear in $(\boldsymbol{z}, q)$, and comes from the linearization of the Navier-Stokes equations around the state solution; the optimality condition reads instead

$$\alpha \boldsymbol{u} + \boldsymbol{z} = \mathbf{0} \qquad \text{on } \Gamma_{con}.$$

Remark 3. *In the case of time-dependent state problems, the adjoint problem is a backward in time time-dependent problem. Depending on the observation appearing in the cost functional – which can be either on the whole time interval $(0, T)$, or at the final time T only – the dependency of the adjoint problem on the state is only at $t = T$ (thus, as initial condition) or on the whole interval $(0, T)$. The approach followed so far can still be employed to derive a system of optimality conditions, see, e.g., Sect. 9.3.2 for further details on a case of interest.*

9.2 Numerical approximation

Solving a PDE-constrained optimization problem entails a computational effort bigger than the one required for the solution of a forward (state) problem. The two formulations (110) and (111) yield two different paradigms for the approximation of such a problem. In the former case, both state and control variables are optimization variables and PDE constraints are explicitly specified; in the latter, only the control variable u is an optimization variable, whereas the state variable y is considered to be an implicit function of

u through the PDE constraint[3]. In this latter case, the solution of the state problem is *nested* in the evaluation of the gradient $\tilde{J}'(u)$ of the reduced cost functional.

Algorithms for solving PDE-constrained optimization problems can be sorted following several criteria. a first classification criterion is between *iterative methods*, rooted on iterative minimization algorithms for the reduced cost functional, and *all-at-once methods*, where the PDE constraint is kept explicitly and the three equations forming (120) are solved simultaneously. Another criterion is concerned with the highest order of derivatives exploited by the algorithm, yielding derivative-free methods, gradient-based methods and Hessian-based methods.

A different perspective is taken when addressing the interplay between *optimization* and *discretization*: numerical discretization can be performed prior or after the derivation of a system of optimality conditions. More precisely, in the so-called *optimize, then discretize* approach optimization is carried out at the continuous level (e.g. to find system (120)) and then the discretization is operated on the resulting optimality system; alternatively, using the *discretize, then optimize* approach we first approximate the state equation (and the cost functional) and then carry out the optimization at the discrete level. Here we address the former approach; further details are given at the end of this section. For the sake of brevity, we recall the main features of iterative and all-at-once methods in the case of *unconstrained* problems, that is, problems without further equality/inequality constraints or, equivalently, for which $\mathcal{U}_{ad} \equiv \mathcal{U}$. In particular, $\boldsymbol{Y} \in \mathbb{R}^{n_y}$, $\boldsymbol{U} \in \mathbb{R}^{n_u}$ denote the discrete representation of the state and the control variable, respectively, whereas $\boldsymbol{\lambda} \in \mathbb{R}^{n_\lambda}$ is the discrete adjoint variable.

9.2.1 Iterative methods

Iterative (also referred to as *black-box*) methods treat the reduced problem

$$\min_{\boldsymbol{U}} \tilde{J}(\boldsymbol{U}) = J(\boldsymbol{Y}(\boldsymbol{U}), \boldsymbol{U}),$$

once $\boldsymbol{U}$ is known; $\boldsymbol{Y}(\boldsymbol{U})$ is obtained as the solution of the state equation. An existing algorithm for the solution of the state equation has therefore to be embedded into an optimization loop, and any available PDE and optimization routines can be freely combined. In particular, iterative methods represent a popular choice when dealing with OCPs by extending an existing code for the state problem. Within this class, a notable difference exists between gradient and non-gradient based algorithms.

Non-gradient based (or *derivative-free*) algorithms – such as the popular *Nelder & Mead algorithm* – exploit either the comparison among functional evaluations in different directions at each step, or low-order local approximants of $\tilde{J}$ in order to assess its local behavior and localize the minimizer; see for instance [365]. Employing a finite difference approximation of the gradient is an attractive alternative due to its ease of implementation, but it may suffer from limited accuracy and large costs in the presence of many design variables.

[3]From the numerical standpoint, the former approach is often given the name of *Simultaneous Analysis and Design* (SAND), whereas the latter is referred to as *Nested Analysis and Design* (NAND).

Hence, these methods are feasible only in the case where the control space has very small dimension – e.g., if the control is expressed in terms of a vector of $n_u = \mathcal{O}(10)$ design variables.

Gradient-based algorithms exploit the gradient $\tilde{J}'$ to iteratively update the control until a suitable convergence criterion is fulfilled. Remarkable instances are descent methods, such as the gradient, (nonlinear) conjugate gradient, quasi-Newton or Newton methods. In the simplest case of a gradient method, starting from an initial guess $\boldsymbol{U}^{(0)}$ we iteratively generate a sequence

$$\boldsymbol{U}^{(k+1)} = \boldsymbol{U}^{(k)} - \tau_k \tilde{J}'(\boldsymbol{U}^{(k)}), \qquad k = 0, 1, \dots$$

being $\tau_k > 0$ a step size, possibly varying at each step, until e.g. $\|\tilde{J}'(\boldsymbol{U}^{(k)})\| < \varepsilon$, for a given tolerance $\varepsilon > 0$. Further details can be found, e.g. in [415, 290]. The solver for the state equation has to be augmented with a routine which provides the gradient of the state with respect to the optimization variables, and hence the solution of the adjoint problem. Relying on optimization procedures showing a faster convergence rate is mandatory to speedup the execution of the whole algorithm. Although straightforward to implement, the gradient method suffers from a poor rate of convergence when dealing with the numerical solutions of PDE-constrained optimization problems; more efficient methods, such as quasi-Newton methods, are more typically employed; see e.g. [73] for further details.

9.2.2 All-at-once methods

By treating both the control and the state variables as independent optimization variables, coupled through the PDE constraint, we deal with an equality constrained nonlinear optimization problem, the state equation playing now the role of equality constraint. The goal of all-at-once (also referred to as *one-shot*) methods is to tackle the (possibly) nonlinear optimality system (120) as a whole problem to be solved. After numerical discretization, in the unconstrained case we land on the algebraic system

$$\begin{cases} J_{\boldsymbol{Y}}(\boldsymbol{Y}, \boldsymbol{U}) + \mathbf{e}_{\boldsymbol{Y}}^T(\boldsymbol{Y}, \boldsymbol{U})\boldsymbol{\lambda} &= \mathbf{0} \\ J_{\boldsymbol{U}}(\boldsymbol{Y}, \boldsymbol{U}) + \mathbf{e}_{\boldsymbol{U}}^T(\boldsymbol{Y}, \boldsymbol{U})\boldsymbol{\lambda} &= \mathbf{0} \\ \mathbf{e}(\boldsymbol{Y}, \boldsymbol{U}) &= \mathbf{0}. \end{cases} \tag{121}$$

Here $\mathbf{e}(\boldsymbol{Y}, \boldsymbol{U})$ denotes the discrete state operator, $J_{\boldsymbol{Y}}$ and $J_{\boldsymbol{U}}$ are the gradients of J with respect to state and control variables, respectively, whereas $\mathbf{e}_{\boldsymbol{Y}}$ and $\mathbf{e}_{\boldsymbol{U}}$ are the Jacobians of the state equations with respect to state and control variables, respectively. The three equations of system (121) can also be seen as the conditions obtained by requiring that the gradient of the discrete Lagrangian $\mathcal{L}(\boldsymbol{Y}, \boldsymbol{U}, \boldsymbol{\lambda}) = J(\boldsymbol{Y}, \boldsymbol{U}) - \boldsymbol{\lambda}^T \mathbf{e}(\boldsymbol{Y}, \boldsymbol{U})$ vanishes.

The strategy above is well-suited for PDE-constrained optimization problems involving stationary state systems, however it is more computationally involved in the time-dependent case. If $J(\boldsymbol{Y}, \boldsymbol{U})$ is quadratic and $\mathbf{e}(\boldsymbol{Y}, \boldsymbol{U})$ is linear in $\boldsymbol{Y}$ and $\boldsymbol{U}$, (121) is a

linear system of equations in saddle-point form, as those arising from quadratic programming. In this case, preconditioned iterative methods for linear systems such as those based on Krylov subspaces could be employed; in this respect, several preconditioners have been proposed in the last decade, in which multigrid schemes are exploited as inner solvers (or preconditioners) for some blocks of the KKT matrix within an outer iterative solver; see, e.g., [47, 488]. More recent extensions to constrained problems have been addressed, e.g., in [73] and the references therein.

If the state problem is nonlinear, the optimality system has to be solved through appropriate linearization procedures (like sequential quadratic programming methods) or modern penalty methods (like augmented Lagrangian methods). Indeed, the equations of system (121) are still linear in $\boldsymbol{\lambda}$ but are nonlinear in $(\boldsymbol{Y}, \boldsymbol{U})$. When a Newton-type method is applied to (121), each iteration on the KKT system entails the solution of the following linear system

$$\begin{pmatrix} \mathcal{L}_{\boldsymbol{YY}} & \mathcal{L}_{\boldsymbol{YU}} & \mathbf{e}_{\boldsymbol{Y}}^T \\ \mathcal{L}_{\boldsymbol{UY}} & \mathcal{L}_{\boldsymbol{UU}} & \mathbf{e}_{\boldsymbol{U}}^T \\ \mathbf{e}_{\boldsymbol{Y}} & \mathbf{e}_{\boldsymbol{U}} & 0 \end{pmatrix} \begin{pmatrix} \delta \boldsymbol{Y} \\ \delta \boldsymbol{U} \\ \boldsymbol{\lambda}^{(k+1)} \end{pmatrix} = - \begin{pmatrix} J_{\boldsymbol{Y}} \\ J_{\boldsymbol{U}} \\ \mathbf{e} \end{pmatrix} \tag{122}$$

for the update $\delta \boldsymbol{X}^T = (\delta \boldsymbol{Y}, \delta \boldsymbol{U})^T$ of the optimization variable and the new value $\boldsymbol{\lambda}^{(k+1)}$ of the adjoint variable; then, we set $(\boldsymbol{Y}^{(k+1)}, \boldsymbol{U}^{(k+1)})^T = (\boldsymbol{Y}^{(k)}, \boldsymbol{U}^{(k)})^T + (\delta \boldsymbol{Y}, \delta \boldsymbol{U})^T$. Here

$$\mathcal{H} = \begin{pmatrix} \mathcal{L}_{\boldsymbol{YY}} & \mathcal{L}_{\boldsymbol{YU}} \\ \mathcal{L}_{\boldsymbol{UY}} & \mathcal{L}_{\boldsymbol{UU}} \end{pmatrix}$$

denotes the Hessian of the Lagrangian functional, to be evaluated at $(\boldsymbol{Y}^{(k)}, \boldsymbol{U}^{(k)}, \boldsymbol{\lambda}^{(k)})^T$. Note the saddle-point structure of system (122), where the adjoint variable indeed plays the role of multiplier for the constraint expressed by the (linearized) state equation. The system (122) can be equivalently obtained as the KKT system for the following linear-quadratic optimization problem, see, e.g., [252, 73],

$$\min_{\delta \boldsymbol{X}} \left[\frac{1}{2} \delta \boldsymbol{X}^T \mathcal{H} \delta \boldsymbol{X} + \begin{pmatrix} J_{\boldsymbol{Y}} \\ J_{\boldsymbol{U}} \end{pmatrix}^T \delta \boldsymbol{X} \right] \qquad \text{subject to} \quad \begin{pmatrix} \mathbf{e}_{\boldsymbol{Y}} \\ \mathbf{e}_{\boldsymbol{U}} \end{pmatrix} \delta \boldsymbol{X} + \mathbf{e} = 0,$$

whence the name of *sequential quadratic programming* method which is commonly used to refer to the Newton iterations on system (122). Indeed, a quadratic programming problem has to be solved at each step, e.g. by means of a preconditioned Krylov mehod like MINRES, until a suitable convergence criterion is fulfilled. Suitable approximation of the Hessian, based e.g. on quasi-Newton methods, are required to make this algorithm more computationally attractive, see, e.g., [73].

Remark 4. *Constraints on the control and/or state variables add nonlinearity to the optimization problem. A first option is to treat inequality constraints in an outer loop, through* penalty methods *which allow to convert them into additional terms in the cost functional. For instance, if $u \leq b$ is a pointwise control constraint, the term $\frac{c}{2} \| \max\{0, u - b\} \|_{\mathcal{U}}^2$ can be added, being $c > 0$ a penalty parameter to be properly selected, and then an*

iterative method can be used in the inner loop. Another option in iterative methods is to perform a projection over the space of admissible controls at each step. More efficient strategies to tackle constrained problems are usually obtained when dealing with constraints in the main optimization loop, such as in the case of primal-dual active set *strategies, see, e.g., the monographs [73, 252].*

We finally point out that in this section we have opted for the optimize, then discretize approach; that is, we have shown how to recover a system of optimality conditions and then proceed to its numerical discretization. The opposite strategy (discretize, then optimize) would have led to substantially similar numerical methods, by setting either an iterative or an all-at-once method on the system of optimality conditions derived once the original state system had been discretized. The two approaches do not yield identical solutions in general; see, e.g., [252] for a discussion.

9.3 Examples of applications in cardiovascular modeling

9.3.1 Optimal design of bypass grafts

PDE-constrained optimization problems are obtained when looking for the optimal design of prosthetic devices, such as ventricular assist devices or bypass grafts. For instance, coronary artery bypass grafting (CABG) is a standard surgical procedure to restore blood perfusion to the cardiac muscle by redirecting blood from the aorta through a graft vessel to the downstream of a coronary artery affected by stenosis or occlusion. Being able to design the graft-vessel connection (the so-called anastomosis, which we refer to as the domain Ω) in an efficient way is a critical factor to prevent post-operative recurrence of restenosis.

It is nowadays accepted that intimal wall thickening, caused by the accelerated growth of smooth muscle cells and surrounding matrix, represents one of the leading causes of long-term failure of end-to-side vascular grafts [244]. Low and/or highly oscillatory patterns of WSS, as well as strong vorticity and recirculations, cause intimal wall thickening [160, 294] at sites where curvatures, bifurcations, tortuosity and branching occur, and, more in general, where flow departs from unidirectional patterns [213, 342]. In mathematical terms, an *optimal* graft is one that minimizes suitable cost functionals involving the area of low WSS, spatial WSS gradient [329] or the vorticity [473, 358], see e.g. [298] for a detailed review. Taking as state variables blood velocity $\mathbf{v}$ and pressure p, and as control variable $u = \Omega$, i.e. the shape of the domain itself, the goal is thus to find the optimal shape $\hat{\Omega}$ of the graft by minimizing, e.g.

$$J(\boldsymbol{v}, \Omega) = \int_0^T \int_{\Omega_{obs}} |\nabla \times \boldsymbol{v}|^2 \, d\Omega \, dt,$$

where $\Omega_{obs} \subset \Omega$ is a given observation region, in the artery portion right after the anastomosis. Indeed, high downstream vorticity may lead to strong flow recirculation, yielding similar effects in terms of intimal thickening.

Other cost functionals that can be employed are, for instance:

- a tracking-type functional, in order to drive the blood velocity (and pressure, if $\delta > 0$) towards a specified velocity (and pressure) target state $\boldsymbol{v}_d$, p_d, featuring a regular pattern

$$J(\boldsymbol{v}, \Omega) = \frac{1}{2} \int_0^T \int_{\Omega_{obs}} |\boldsymbol{v} - \boldsymbol{v}_d|^2 d\Omega dt + \frac{\delta}{2} \int_0^T \int_{\Omega_{obs}} |p - p_d|^2 \, d\Omega \, dt;$$

  a typical choice of $(\boldsymbol{v}_d, p_d)$ is provided by the Stokes (or a low-Reynolds Navier-Stokes) flow in the same domain;

- in dimension two, a *Galilean invariant* vortex measure identifies a region to be a vortex if $\nabla \boldsymbol{v}$ has complex eigenvalues, that is, if $\det(\nabla \boldsymbol{v}) > 0$; following [251, 309, 318], the functional

$$J(\boldsymbol{v}, \Omega) = \int_0^T \int_{\Omega_{obs}} \max(0, \det(\nabla \boldsymbol{v})) \, d\Omega \, dt$$

  can be used as a cost functional when dealing with vortex suppression;

- a WSS gradient-based functional is given by

$$J(\boldsymbol{v}, \Omega) = \int_0^T \int_{\Gamma_{\text{obs}}} WSSG(t) \, d\Gamma \, dt, \qquad WSSG(t) = \left(\left(\frac{\partial \boldsymbol{w}_p}{\partial \boldsymbol{\tau}_p} \right)^2 + \left(\frac{\partial \boldsymbol{w}_n}{\partial \boldsymbol{\tau}_n} \right)^2 \right)$$

  that is, by a time-average of the WSS gradient, measured over the portion $\Gamma_{\text{obs}} \subset \partial\Omega$ of the boundary in the anastomosis region. Here we refer to WSSG as to the WSS gradient, being $\boldsymbol{w} = \boldsymbol{w}(t, \boldsymbol{x})$ the WSS vector of components $\boldsymbol{w}^{(j)} = \nabla \boldsymbol{v} \boldsymbol{n}(t, \boldsymbol{x}) \cdot \boldsymbol{\tau}^{(j)}$, $\boldsymbol{\tau}_p$ and $\boldsymbol{\tau}_n$ the unit vectors parallel and normal to the direction of the time-averaged WSS vector $\boldsymbol{w}$, respectively. Only a linear combination of the *normal* components $\partial \boldsymbol{x}_j / \partial \boldsymbol{\tau}_j$, $j = p, n$ is considered as index to quantify the tension yielding to intimal thickening. Moreover, the time-averaged WSS is relatively insensitive to changes in the anastomosis configuration, while the time-averaged WSS gradient is highly sensitive, and has been linked to localized mechanobiological responses in tissues (see [329] and discussion therein). Using WSSG rather than WSS can be understood as filtering the WSS by removing its component induced by the steady mean flow and considering only the spatially fluctuating term as part of the indicator. For the sake of numerical efficiency of the whole optimization process, a steady flow simulation (e.g., corresponding to the systolic peak) can be considered, and the WSS gradient of the steady flow can be taken as an approximation of the time-averaged WSS gradient. The interested reader can refer, e.g., to [298] for further details.

Many works have focused in the last decades on the optimal shape design of end-to-side anastomoses, typically by acting on the wall shape near the anastomosis by local shape variations. If a simpler parametric optimization approach is considered, the three most significant design variables are [342]: the anastomosis angle, the graft-to-host diameter ratio [294, 144], and the toe shape, that is, the profile of the bypass junction. Optimizing

a complex configuration in terms of few design variables is more advantageous since it is known that grafts usually feature an extended patch or cuff that effectively provides a hood to ease the flow transition from the graft to the artery. Not only, improved anastomosis design must comply with the constraints set by surgical realization. For a more comprehensive review of bypass graft design results, we refer to [373, 342, 423, 364].

Concerning the objective to be minimized, each cost functional involves suitable observations, obtained as functions of the state variables over the entire domain or some boundary portions, and over a given time interval and, possibly, data acquired from measurements, like in the case of a tracking-type functional. There are of course other parameters affecting the distribution of physical indices like the WSS or the vorticity: this is e.g. the case of the Reynolds number, or of the flow split between the proximal host artery and the graft [213]. All these parameters should be considered as uncertainties within a robust optimization framework, in order to characterize the optimal shape of the graft in a range of possible operating conditions. First examples of optimal design in presence of uncertainty in cardiovascular applications have been considered e.g. in [505].

As a concluding remark, we point out that the coupling of optimization algorithms to blood flow simulations is computationally challenging, since each evaluation of the cost functional requires the solution of an unsteady, three-dimensional Navier-Stokes problem. If relying on the adjoint approach to characterize the gradient of the cost functional, a further linearized Navier-Stokes (Oseen) problem has to be solved at every iteration. For this reason, the most part of works related to applications in surgery and device optimization have focused, so far, on small-scale and/or two-dimensional problems, or on steady-flow problems, usually relying on gradient-free methods.

For the sake of illustration, we report some numerical results for the optimal design of a femoro-popliteal bypass graft. This surgery is used to bypass diseased blood vessels above or below the knee, and represents one of the most common surgical treatments of chronic lower-extremity ischemia. We model the blood flow across a bypass graft by a steady Navier-Stokes model and consider a vorticity cost functional

$$J(\boldsymbol{v}, \Omega) = \int_{\Omega_{obs}} |\nabla \times \boldsymbol{v}|^2 \, d\Omega$$

where $\Omega_{obs} \subset \Omega$ is the observation region. Initial and optimal shapes are shown in Fig. 26 for the case of a stenosed host artery; its occlusion, either total or partial, is expressed through a Dirichlet boundary condition on the incoming velocity field on Γ_{res}, homogeneous for the completely occluded case, non-homogeneous otherwise; see Fig. 26 (b) for the definition of Ω_{obs} and Γ_{ref}. A shape parametrization technique based on Free-Form Deformations (FFD) is very suitable to describe admissible shapes through a deformation of a reference configuration by acting on a small set of control points; see, e.g., [354, 358].

9.3.2 Optimal control of electrical defibrillation

While in healthy conditions the electrical activation of the heart is an extremely organized (and efficient) process, some disturbances in the formation and/or propagation of electri-

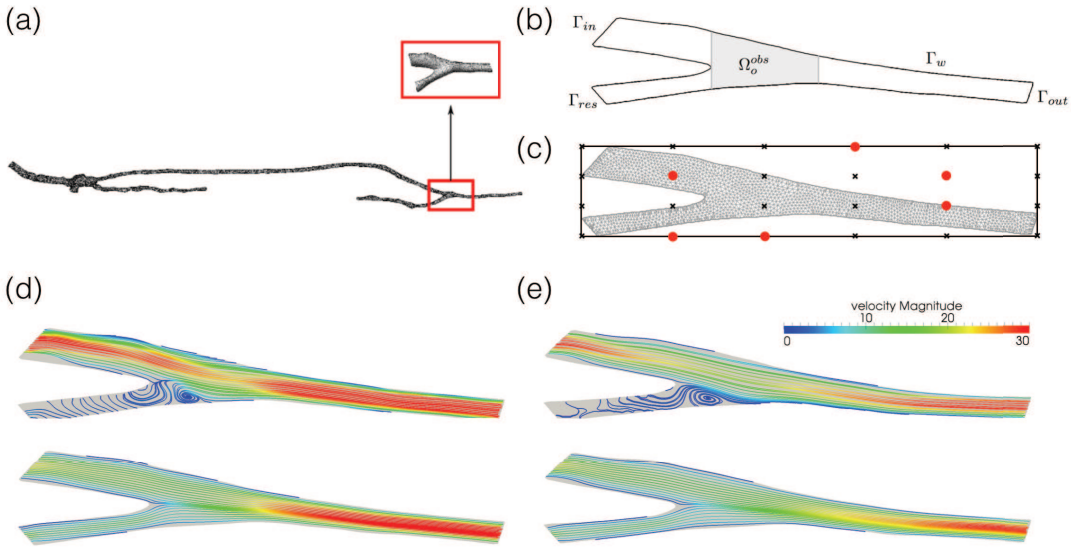

Figure 26: Optimal design of bypass grafts. (a) A tract of femoral artery with the bypass graft; (b) computational domain, boundaries and observation region; (c) FFD shape parametrization used to generate admissible shapes. Global shape deformations are induced by the displacement of few, selected control points (shown in red) in the 6×4 FFD lattice. These control points are selected by a preliminary screening procedure based on sensitivity analysis; (d) initial and (e) optimal bypass configurations in the case of total (above) or partial (below) occlusion. These numerical results are obtained using the Matlab Finite Element library `MLife`

cal signals may induce reentrant activation patterns which lead to tachycardia, that is, a noticeable increase in the hearts activation rate. In the worst cases, this may turn to an even less organized activation pattern, called fibrillation. A common therapy to terminate a fibrillation and restore a regular cardiac rhythm is electrical defibrillation, consisting in the delivery of a strong electrical shock by injecting external currents through a set of electrodes. This restores a spatially uniform activation pattern, recovering an extracellular potential distribution showing damped voltage gradients. Electrical defibrillation is nowadays operated by implanting some devices (the so-called cardioverters defibrillators) able to monitor the heart rhythm and then to deliver electrical discharges when needed.

This process can be modeled e.g. by considering as state system the monodomain equation (81), for which the extracellular stimulation current $I_e = I_e(t)$ to be applied plays the role of distributed control function, and has to be determined in order to minimize e.g. the cost functional

$$J(V_m, I_e) = \frac{1}{2}\int_0^T \int_{\Omega_{obs}} |V_m - v_d|^2 d\Omega dt + \frac{\alpha}{2}\int_0^T \int_{\Omega_{con}} |I_e|^2 d\Omega dt. \tag{123}$$

Here V_m is the transmembrane potential, $\Omega_{obs} \subseteq \Omega_{mus}$ is the observation domain, $\Omega_{con} \subseteq$

Ω_{mus} is the control domain, whereas v_d is the target potential distribution. For instance, if $v_d = 0$, the minimum of $J(V_m, I_e)$ corresponds to the case of an excitation wave which is suppressed in the region Ω_{obs}, see e.g. [391]. The transmembrane potential V_m can be obtained by solving the following monodomain equations (see Sect. 7.1.3)

$$\begin{aligned} \chi_m C_m \frac{\partial V_m}{\partial t} - \nabla \cdot (\boldsymbol{\Sigma} \nabla V_m) + \chi_m I_{ion} = I_e \quad & \text{in } \Omega_{mus} \times (0,T) \\ \frac{\partial w}{\partial t} = g(V_m, w) \quad & \text{in } \Omega_{mus} \times (0,T) \\ V_m|_{t=0} = V_{m,0} \quad & \text{in } \Omega_{mus} \\ w|_{t=0} = w_0 \quad & \text{in } \Omega_{mus} \\ \boldsymbol{\Sigma} \nabla V_m \cdot \mathbf{n} = 0 \quad & \text{on } \Sigma_{epi} \cup \Sigma_{endo} \end{aligned} \tag{124}$$

with I_{ion} provided e.g. by the Fitzhugh-Nagumo model (see Sect. 7.1.2),

$$I_{ion} = f(V_m, w) = -kV_m(V_m - a)(V_m - 1) - w, \qquad g(V_m, w) = \epsilon(V_m - \gamma w).$$

An analysis of this OC problem can be found, e.g., in [391]. We can exploit the Lagrangian approach to derive a system of first-order optimality conditions, by introducing the Lagrangian

$$\begin{aligned} \mathcal{L}(V_m, w, I_e, z, q) &= J(V_m, I_e) + \langle \mathcal{E}(V_m, w, I_e), (z,q) \rangle_{V,V^*} \\ &= J(V_m, I_e) \\ &+ \int_0^T \int_{\Omega_{mus}} \left(\chi_m C_m \frac{\partial V_m}{\partial t} - \nabla \cdot (\boldsymbol{\Sigma} \nabla V_m) + \chi_m I_{ion} - I_e \right) z \, d\Omega dt \\ &+ \int_0^T \int_{\Omega_{mus}} \left(\frac{\partial w}{\partial t} - g(V_m, w) \right) q \, d\Omega dt \end{aligned}$$

where (z, q) denote the dual variables of V_m, w, respectively; here $(V_m, w) \in V = L^2(0,T;\mathcal{V}) \times W^{1,2}(0,T;\mathcal{H})$, being $\mathcal{V} = H^1(\Omega_{mus})$ and $\mathcal{H} = L^2(\Omega_{mus})$; the control space can be chosen as $U = L^2(0,T;L^2(\Omega))$, and the initial conditions can be kept as explicit constraints. By setting the partial derivatives of $\mathcal{L}$ equal to zero, we find the following expression for the adjoint problem:

$$\begin{aligned} -\chi_m C_m \frac{\partial z}{\partial t} - \nabla \cdot (\boldsymbol{\Sigma} \nabla z) + \chi_m \frac{\partial I_{ion}}{\partial V_m} z - \frac{\partial g}{\partial V_m} q = v_d - V_m \quad & \text{in } \Omega_{mus} \times (0,T) \\ -\frac{\partial q}{\partial t} - \frac{\partial g}{\partial w} q + \frac{\partial I_{ion}}{\partial w} z = 0 \quad & \text{in } \Omega_{mus} \times (0,T) \\ z|_{t=T} = 0 \quad & \text{in } \Omega_{mus} \\ q|_{t=T} = 0 \quad & \text{in } \Omega_{mus} \\ \boldsymbol{\Sigma} \nabla z \cdot \mathbf{n} = 0 \quad & \text{on } \Sigma_{epi} \cup \Sigma_{endo} \end{aligned} \tag{125}$$

and the following optimality condition

$$z + \alpha I_e = 0 \qquad \text{on } \Omega_{con}. \tag{126}$$

The OC problem (123)–(124) can be solved by an *optimize-then-discretize* strategy, where both spatial and temporal discretizations are required because of the time-dependent nature of the problem. After discretization, we can employ an iterative method, by computing at each step the solution of the (coupled) state problem (124) over $(0,T)$, and

the solution of the adjoint problem (125), which is a linear problem, backward in time, where the adjoint variables are coupled similarly to (V_m, w) in the state problem. Note that the data of the adjoint problem are related with the Fréchet derivative of the cost functional with respect to the state variables, and that the adjoint problem depends on the control function only through the state variable. Moreover, the adjoint operator calls into play the linearization of the state operator around the computed state solution – that is, the derivatives $\partial I_{ion}/\partial V_m$, $\partial g/\partial V_m$, $\partial I_{ion}/\partial w$, $\partial g/\partial w$ have to be evaluated, at each step, around the computed solution of the state system. The optimality condition (126) then allows to determine the gradient $\tilde{J}'(I_e)$ of the cost functional $\tilde{J}(I_e) = J(V_m(I_e), I_e)$, required to update the control function at each step.

To simplify the OC problem, we can for instance look for control functions under the form

$$I_e(t, \mathbf{x}) = \sum_{k=1}^{N_{el}} u_k(t) \mathcal{I}_{\Omega_{con,k}}(\mathbf{x}) \mathcal{I}_{(0,T_{def})}(t)$$

where the location of N_{el} electrodes through which the current is delivered is prescribed, and only its time intensity has to be controlled over time; here $\mathcal{I}_{\Omega_{con,k}}(\mathbf{x})$ denotes the indicator function of the region $\Omega_{con,k}$ where the k-th electrode is located. Additional inequality constraints under the form $u_{min} \leq u_k(t) \leq u_{max}$ can also be taken into account in order to limit currents amplitude.

Further extensions of this framework consider e.g. the bidomain model [393], the case of boundary controls [392] and a different Mitchell-Schaeffer model to describe ionic currents, together with the presence of a conductive bath medium outside the heart effects and experimentally-based fiber and sheet orientations [394]. Moreover, the case where the shock duration itself is also optimized has been considered in [308]. The reason to consider this further effect is that after applying a defibrillation shock, the muscle tissue needs a suitable amount of time to reach a non-fibrillatory state, so that a successful defibrillation can only be assessed at a time $T \gg T_{def}$, being T_{def} the end time of the defibrillation shock and T the final observation time, at which the tissue should have reached a non-excited state. In this context, the following cost functional

$$J(V_m, u, T_{def}) = T_{def} + \frac{\mu}{2} \int_{\Omega_{obs}} |V_m(\cdot, T)|^2 d\Omega + \frac{\alpha}{2} \sum_{k=1}^{N_{el}} \int_0^T |u_k|^2 dt$$

can be minimized, accounting for *(i)* a minimum time term, for *(ii)* a final time observation at $t = T$ and *(iii)* for the amplitude of the applied currents, subject to the state system (124) to be solved over $(0, T)$. Indeed, the shock duration and its energy have to be minimized to avoid negative side effects of the applied shock, while the final time observation term is taken into account to quantify defibrillation, thus requiring that the tissue reaches a non-excited state at $T \gg T_{def}$.

For the sake of illustration, we consider the case of an axially symmetric domain $\Omega_{mus} = (0, 2) \times (0, 0.8)$ where a constant pulse of intensity u is delivered in the control domain $\Omega_{con} = (0, 0.25) \times (0.3, 0.55) \cup (1.75, 2) \times (0.3, 0.55)$, until time T_{def}; here $\boldsymbol{U} =$

$(u, T_{def})^T$ is the control variable, with $1 \leq u \leq 100$ mV and $0.1 \leq T_{def} \leq 4$ ms; the final time is $T = 64$ ms. The initial condition $(V_{m,0}, w_0)^T$ describe a reentry wave of the "figure of eight" type, obtained following the procedure described in [308], where more general optimal control problems are also taken into account. For the case at hand, a planar wave front travelling from the bottom to the top can be damped by acting an optimal control of intensity $u \approx 95$ mV until $T_{def} \approx 1.2$ ms on the control region. The successful defibrillation – resulting from a trade-off between a large intensity and a short duration of the pulse – is clearly visible in Fig. 27, where in the controlled case at the final time the tissue is almost completely unexcited. Indeed, the pulse acts on the excitable region of the tissue adjacent to the wave front, bringing it to a non-excitable state.

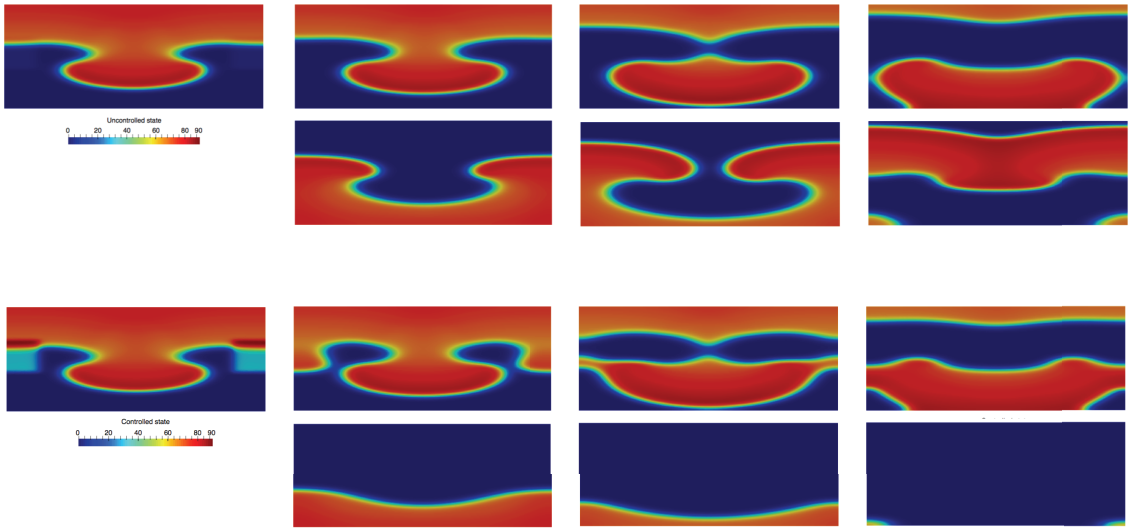

Figure 27: Electrical potential at times $t = 0, 4, 12, 20, 40, 52, 64$ ms in the uncontrolled case (top) and in the controlled case (bottom). The reentry wave appearing in the uncontrolled case is damped by the control acting on Ω_{con}

Remark 5. *We point out that choosing the cost functional and, if needed, imposing suitable constraints on the control and/or the state variable, are two extremely hard, problem-dependent tasks. Moreover, very often control functions are described in terms of (possibly few) relevant parameters, which play the role of design variables; their automatic selection however, in the case e.g. of complex, patient-dependent geometries, can result in a quite involved procedure. Last, but not least, in the case where a target state to be reached depends on acquired data, the effect of uncertainty has to be considered in the formulation (and then, solution) of the problem. This feature may be accommodated by using, e.g., robust optimization problems, or PDE-constrained optimization problems under uncertainty. This is indeed an active research field, where very few applications to cardiovascular modeling have been considered so far.*

10 Parameter estimation from clinical data

When dealing with the mathematical and numerical modeling of the circulatory system, initial conditions, boundary conditions or physical coefficients, e.g., tissue properties, might be (partially) unwknown [563], see Sects. 3 and 6. Hereon we refer to any of these quantities as input parameters, independently of their mathematical nature – they could be scalar or vectors, or even parametric fields varying in space – and to the issue of making inferences about unknown parameters from data as to *parameter estimation* (or *identification*). To perform parameter estimation for a system of PDEs we need to combine state observations and additional data which are not strictly required for solving the PDE problem, and have to be acquired from measurements.

Parameter estimation for PDEs can be done according to several techniques, which can be coarsely classified depending on their outcome [539, 143]. *Point estimates* rely on either *variational* or *sequential* methods [274]. Both methods provide optimal least-squares estimates by minimizing a cost functional accounting for the misfit between measured data and state observations. A second class of techniques yields instead *confidence regions* or, more generally speaking, the possibility to characterize the probability distribution of the unknown parameters provided they are described in terms of random variables; this is the goal, e.g., of statistical inversion theory relying on *Bayesian inference*, which Sect. 11.2 is largely devoted to.

In the context of cardiovascular modeling, parameter estimation is necessary for the sake of *model calibration/personalization*, e.g. in view of diagnosis or treatment purposes; indeed, parameters that are not directly measurable – this is e.g. the case of tissue conductivity or vessel compliance – are tuned so that the outcome of the numerical model is able to reproduce patient-specific data [305]. Difficulties arise because of data sparsity [301]: indeed, spatial resolution and temporal frequency are typically undersampled; on the other hand, experimental data are always polluted by measurement noise.

Remark 6. *Data assimilation (DA) is the process by which a numerical model of a given system, usually affected by noise or model uncertainties, is improved by incorporating*

system observations. Although DA relies on the same variational or filtering approaches addressed in this section, in the case of, e.g., geophysical fluids, its main goal often goes beyond parameter estimation; indeed, it is more often related to state estimation*, namely, to improving the outcome of the numerical model and of its initial state to correctly initialize forecasts, by assimilating available measurements into the numerical model itself. DA is intrinsically related to time-varying phenomena and deals with highly nonlinear dynamical systems, very often far from being periodical (such as in the case of meteorological models) and ill-posed; see, e.g., [61, 577, 143] for a detailed discussion. In the last decade several works dealing with cardiovascular applications have focused on* data assimilation *[516, 135, 49, 315] which has been considered, in many cases, as synonymous of* parameter estimation*.*

In this section we provide an overview of both variational and sequential approaches for parameter estimation in time-dependent systems. Parameter estimation problems dealing with stationary systems in cardiovascular applications have also been solved – see, e.g., [133, 49, 347, 406, 319, 355] for the sake of space and relevance here we focus on time-dependent problems.

10.1 Variational approach: PDE-constrained optimization

The variational approach recasts parameter estimation in the framework of PDE-constrained optimization, by considering the equations governing the problem at hand as state system and the discrepancy between the observation of the state and the measured data as cost functional to be minimized [33, 92]. The parameters to be estimated (often involving the initial condition) play the role of optimization variables, just like control variables in the case of optimal control (OC) problems; however, differently than the OC case, parameters to be estimated are quantities which no one can actually control. Often, they are coefficients of the operator appearing in the PDE problem.

Here we provide an abstract formulation of the variational approach, following [51, 61]; for more see, e.g., [400, 89, 516]. We assume that the state problem has already been discretized in space. We denote by $\boldsymbol{X}(t) \in \mathbb{R}^{n_x}$ the semi-discrete state, by $\boldsymbol{\theta} \in \mathbb{R}^p$ the parameters of the model to be estimated, and by $\boldsymbol{A}(t, \boldsymbol{X}(t), \boldsymbol{\theta})$ the (semi-discretized in space) state operator; note that usually $p \ll n_x$. The state variable then solves the dynamical system

$$\begin{cases} \dot{\boldsymbol{X}}(t) &= \boldsymbol{A}(t, \boldsymbol{X}(t), \boldsymbol{\theta}), \quad t \in (0, T), \\ \boldsymbol{X}(0) &= \boldsymbol{G}. \end{cases} \tag{127}$$

For instance, in the case of the FSI system (22), $\boldsymbol{X} = (\boldsymbol{v}, p, \boldsymbol{d})$ contains fluid velocity and pressure, and structure displacement, $\boldsymbol{\theta}$ may contain, e.g., the value of the Young modulus (here assumed to be piecewise constant) in different patches of the arterial wall.

We consider the case where the parameter vector $\boldsymbol{\theta}$ is unknown, and for which the estimation problem consists in finding $\widehat{\boldsymbol{\theta}}$ such that the discrepancy between the observation and a set of measurements $\boldsymbol{Z}(t) \in \mathbb{R}^{n_z}$, $t \in (0, T)$, is minimized, e.g. in a least-squares sense. The case of unknown initial data $\boldsymbol{G}$ to be estimated can be treated essentially in the same way. Usually, we assume that measurements $\boldsymbol{Z}(t)$ are related to observations of

the true state through an *additive noise* model, that is,

$$\boldsymbol{Z}(t) = H(t)\boldsymbol{X}(t) + \boldsymbol{\varepsilon}(t), \qquad t \in (0,T),$$

where $H = H(t) \in R^{n_z \times n_x}$ is an observation operator which maps the state space into the observation space R^{n_z}, and $\boldsymbol{\varepsilon} = \boldsymbol{\varepsilon}(t)$ is a *noise* term accounting for measurement errors. The following minimization problem is then solved

$$J(\boldsymbol{X}, \boldsymbol{\theta}) = \frac{1}{2}\int_0^T \|\boldsymbol{Z}(t) - H(t)\boldsymbol{X}(t)\|_M^2 \, dt + \frac{\alpha_\theta}{2}\|\boldsymbol{\theta} - \boldsymbol{\theta}_0\|_{P_\theta^{-1}}^2 \ \rightarrow \min_{\boldsymbol{\theta}\in\mathcal{P}} \tag{128}$$

being $\boldsymbol{X} = \boldsymbol{X}(t)$ the solution of (127). Here $\mathcal{P} \subset R^p \times R^{n_x}$ denotes the set of admissible parameters. Additional information is usually added to the least-squares objective expressed by the first term in (128), through a background estimate $\boldsymbol{\theta}_0$ of $\boldsymbol{\theta}$; M and P_θ^{-1} are suitable symmetric positive definite matrices (the reason why we consider an inverse matrix to define this latter norm will be clarified in the following). This procedure goes under the name of *Levenberg-Marquardt-Tykhonov regularization*; see, e.g., [283] for a discussion on classical regularization methods for inverse problems; note that usual penalization coefficients are embedded in the definition of the matrix P_θ^{-1}.

The minimization problem (128) can be solved by an optimization algorithm based e.g. on the evaluation of the gradient of J with respect to $\boldsymbol{\theta}$; as shown in Sect. 9.1, this latter can be computed by relying on the solution of a suitable *adjoint problem*. This is a *four-dimensional variational* (4D-Var) assimilation (a three-dimensional variational (3D-Var) assimilation would arise in the case of steady state systems). See Sect. 10.3.1 for further details on a relevant example in cardiovascular modeling and, e.g., [61, 89] for more on 4D-Var assimilation problems.

Since measurements $\boldsymbol{Z}$ are only available at a discrete number of time instants $\tau^1, \ldots, \tau^K$, we formulate the identification problem by replacing the dynamical system (127) with its discretized-in-time version:

$$\begin{cases} \boldsymbol{X}^{k+1} &= \boldsymbol{A}_{k|k+1}(\boldsymbol{X}^k, \boldsymbol{\theta}), \qquad k = 0, \ldots, K-1 \\ \boldsymbol{X}^0 &= \boldsymbol{G} \end{cases} \tag{129}$$

where $\boldsymbol{A}_{k|k+1}$ is a nonlinear function describing the evolution of the state from time τ^k to time τ^{k+1} and $\boldsymbol{X}^k \approx \boldsymbol{X}(k\Delta\tau)$ denotes the state vector at time τ^k. Note that the length $\Delta\tau = \tau^{k+1} - \tau^k$ of the time windows between two subsequent measurements is usually larger than the time step Δt used for the sake of time discretization, and that $\boldsymbol{\theta}$ does not depend on k. We notice that hereon k will denote the temporal index of the system evolution, thus using a different notation from the one introduced in Parts 1 and 2 (the temporal index was denoted by n therein).

We then formulate an optimal discrete time minimization criterion and, finally, determine the corresponding adjoint problem, rather than discretizing in time the adjoint problem. This yields the minimization problem

$$J_K(\boldsymbol{X}, \boldsymbol{\theta}) = \frac{1}{2}\sum_{k=1}^{K} \|\boldsymbol{Z}^k - H\boldsymbol{X}^k\|_{M_k}^2 + \frac{1}{2}\|\boldsymbol{\theta} - \boldsymbol{\theta}_0\|_{P_\theta^{-1}}^2 \ \rightarrow \min_{\boldsymbol{\theta}\in\mathcal{P}} \tag{130}$$

where $\boldsymbol{X} = (\boldsymbol{X}^1, \ldots, \boldsymbol{X}^k)$ and we set

$$\boldsymbol{Z}^k = H_k \boldsymbol{X}^k + \boldsymbol{\varepsilon}^k. \tag{131}$$

Here $\boldsymbol{\varepsilon}^k$ denotes the noise of the measurement device at $\tau^k = k\Delta\tau$; a possible choice for M_k is $M_k = \Delta\tau M$, whereas $H_k \approx H(k\Delta\tau)$. Also in this case a gradient-based optimization procedure can be used to solve the constrained optimization problem (129)–(130) with gradients evaluated by introducing a suitable adjoint problem.

10.2 Sequential approach: Kalman filter and extensions

A drawback of the variational approach is the need to wait until the whole set of measurements has been acquired in order to perform an optimization step. A sequential approach, instead, performs the assimilation of acquired measurements *on the fly* and updates the estimate of the unknown quantities accordingly.

A numerical milestone for the solution of sequential estimation problems, the Kalman Filter (KF) [284], has been introduced as a recursive filter for the estimation of the state of a noisy dynamical system from a set of measurements, that is, to improve the prediction of the state dynamics by taking into account additional data; an augmented form of the KF can be easily adapted, as we will see, also to the problem of estimating unknown parameters. Originally designed for linear dynamical systems, the KF has severe memory requirements. To mitigate these two limitations, several improvements and extensions have been proposed in the past decades, most notably the Extended KF (EKF), the Unscented KF (UKF) and the Ensemble KF (EnKF); detailed reviews can be found, e.g., in [283, 520, 270]. In this section we recall the formulation of the basic KF and provide some hints about its extensions, with special focus on the field of cardiovascular modeling where these techniques have been applied.

The literature offers many possible derivations of the KF; following [270, 89], here we exploit the analogy with the solution of a recursive least-squares problem yielding the best linear unbiased estimator for a linear model; alternative derivations can be obtained, e.g., relying on the so-called push-forward and subsequent conditioning of Gaussian measures [531] or a sequential Bayesian estimation framework [321].

10.2.1 The Kalman filter algorithm

The KF algorithm sequentially generates an estimate of the unknown quantity through a linear combination of the current estimate and the acquired measurement. Let us first consider the case where there is no dynamics and data are generated by the linear model

$$\boldsymbol{Z} = H\boldsymbol{X} + \boldsymbol{\varepsilon} \tag{132}$$

where H is a given $n_z \times n_x$ matrix of rank n_x, $\boldsymbol{\varepsilon}$ is an n_z-dimensional random variable with zero mean and known positive-definite covariance $Q = \mathbb{E}[\boldsymbol{\varepsilon}\boldsymbol{\varepsilon}^T] > 0$ and $\boldsymbol{Z}$ represents known, but inexact, measurements with errors given by $\boldsymbol{\varepsilon}$. The vector $\boldsymbol{X} \in R^{n_x}$ is the quantity to be estimated from the observation $\boldsymbol{Z}$; $\mathbb{E}[\cdot]$ denotes the expected value.

Among all linear estimators of $\boldsymbol{X}$, that is estimators of the form $\widehat{\boldsymbol{X}} = K\boldsymbol{Z}$ for some matrix $K \in R^{n_x \times n_z}$, which are unbiased (i.e. $\mathbb{E}[\widehat{\boldsymbol{X}}] = \boldsymbol{X}$), the best choice is the one which minimizes the mean-squared error $\mathbb{E}[(\widehat{\boldsymbol{X}} - \boldsymbol{X})^T(\widehat{\boldsymbol{X}} - \boldsymbol{X})]$; by the Gauss-Markov theorem (see, e.g., [531, Chap. 7]), the best or minimum variance linear unbiased estimator for (132) is given by

$$\widehat{\boldsymbol{X}} = (H^T Q^{-1} H)^{-1} H^T Q^{-1} \boldsymbol{Z}. \tag{133}$$

In that case, $E[(\widehat{\boldsymbol{X}} - \boldsymbol{X})(\widehat{\boldsymbol{X}} - \boldsymbol{X})^T] = (H^T Q^{-1} H)^{-1}$. Equivalently, (133) can also be obtained by solving the weighted least-squares problem

$$\widehat{\boldsymbol{X}} = \frac{1}{2}\|H\boldsymbol{X} - \boldsymbol{Z}\|^2_{Q^{-1}} \to \min_{\boldsymbol{X}} \tag{134}$$

again resorting to a variational argument. In the slightly different case where we want to combine the observation and a background estimate $\boldsymbol{X}_0$ of $\boldsymbol{X}$ with covariance P^-, (134) becomes

$$\widehat{\boldsymbol{X}} = \frac{1}{2}\|H\boldsymbol{X} - \boldsymbol{Z}\|^2_{Q^{-1}} + \frac{1}{2}\|\boldsymbol{X} - \boldsymbol{X}_0\|^2_{(P^-)^{-1}} \to \min_{\boldsymbol{X}}$$

and, instead of (133) we find

$$\widehat{\boldsymbol{X}} = \boldsymbol{X}_0 + K(\boldsymbol{Z} - H\boldsymbol{X}_0), \qquad K = P^+ H^T Q^{-1}, \tag{135}$$

upon defining the matrix playing the role of *updated* covariance as

$$P^+ = ((P^-)^{-1} + H^T Q^{-1} H)^{-1}. \tag{136}$$

Note that this estimate is given by a linear combination of the background estimate $\boldsymbol{X}_0$ and the so-called *innovation* $\boldsymbol{Z} - H\boldsymbol{X}_0$. K is usually referred to as *Kalman gain matrix*; it can also be evaluated exploiting the prior covariance P^- instead than the updated covariance P^+, according to the equivalence

$$P^+ H^T Q^{-1} = P^- H^T (H P^- H^T + Q)^{-1}. \tag{137}$$

We consider now the case of a discrete-time linear system, with data acquired over a time interval. Then, the model (132) is replaced by

$$\begin{aligned} \boldsymbol{X}^k &= A_{k-1|k}\boldsymbol{X}^{k-1} + \boldsymbol{v}^k, \quad k = 1, \ldots, K, \qquad \boldsymbol{X}^0 = \boldsymbol{G}, \\ \boldsymbol{Z}^k &= H_k \boldsymbol{X}^k + \boldsymbol{w}^k \end{aligned} \tag{138}$$

where $\boldsymbol{X}^k \in \mathbb{R}^{n_x}$ denotes the state and $\boldsymbol{Z}^k \in \mathbb{R}^{n_z}$ are the measurements; $\boldsymbol{v}_k$ and $\boldsymbol{w}_k$ are uncorrelated zero-mean random noise processes with positive-definite covariances Q_k and R_k, modeling the uncertainty of the model and the additive noise in the observation, respectively. The state estimation problem is the problem to find the state $\boldsymbol{X}^k$ given k known observations $\boldsymbol{Z}^1, \ldots, \boldsymbol{Z}^k$.

The Kalman filter is a recursive algorithm that provides the best linear unbiased estimate $\boldsymbol{X}^k_a$ of $\boldsymbol{X}^k$ in terms of both the previous estimate $\boldsymbol{X}^{k-1}_a$ and the latest data $\boldsymbol{Z}^k$ up to that point in time. It is based on a *predictor-corrector* strategy, made of:

1. a *prediction* step (called forecast, or time update) consists in letting the system dynamics evolve from $\boldsymbol{X}_a^{k-1}$ without taking into account the observations, yielding the *forecast* state $\boldsymbol{X}_f^k$;

2. a *correction* step (called analysis, or measurement update) updates the forecast state $\boldsymbol{X}_f^k$ by *assimilating* the measurements into the model, yielding the *assimilated* state $\boldsymbol{X}_a^k$.

To derive the expression of the correction step, let us suppose that the current prediction based on observations $\boldsymbol{Z}^1, \ldots, \boldsymbol{Z}^{k-1}$ is $\boldsymbol{X}_f^k$, with covariance matrix P_k^f. If the true state is $\boldsymbol{X}_k$, model (132) becomes

$$\begin{bmatrix} \boldsymbol{X}_f^k \\ \boldsymbol{Z}^k \end{bmatrix} = \begin{bmatrix} I \\ H_k \end{bmatrix} \boldsymbol{X}^k + \boldsymbol{\varepsilon}$$

being $\boldsymbol{\varepsilon}$ an $(n_x + n_z)$-dimensional random variable with zero mean and covariance $Q_k = diag(P_k^f, R_k)$. The best linear unbiased estimator of this system (see (133)) is given by

$$\boldsymbol{X}_a^k = P_k^a \begin{bmatrix} I & H_k^T \end{bmatrix} \begin{bmatrix} (P_k^f)^{-1} & 0 \\ 0 & R_k^{-1} \end{bmatrix} \begin{bmatrix} \boldsymbol{X}_f^k \\ \boldsymbol{Z}^k \end{bmatrix} = P_k^a \left((P_k^f)^{-1} \boldsymbol{X}_f^k + H_k^T R_k^{-1} \boldsymbol{Z}^k \right) \tag{139}$$

and results from the linear combination of the current estimate and the *last* observation $\boldsymbol{Z}^k$, where

$$P_k^a = \left(\begin{bmatrix} I & H_k^T \end{bmatrix} \begin{bmatrix} (P_k^f)^{-1} & 0 \\ 0 & R_k^{-1} \end{bmatrix} \begin{bmatrix} I \\ H_k \end{bmatrix} \right)^{-1} = ((P_k^f)^{-1} + H_k^T R_k^{-1} H_k)^{-1};$$

note the formal analogy with (136), where now P_k^f and P_k^a play the role of P^- and P^+ , respectively. (139) can be written in the more convenient form

$$\begin{aligned} \boldsymbol{X}_a^k &= P_k^a [(P_k^a)^{-1} - H_k^T R_k^{-1} H_k)) \boldsymbol{X}_f^k + H_k^T R_k^{-1} \boldsymbol{Z}^k] = \boldsymbol{X}_f^k + P_k^a H_k^T R_k^{-1} (\boldsymbol{Z}^k - H_k \boldsymbol{X}_f^k) \\ &= \boldsymbol{X}_f^k + K_k (\boldsymbol{Z}^k - H_k \boldsymbol{X}_f^k) \end{aligned}$$

as a function of the innovation $\boldsymbol{Z}^k - H_k \boldsymbol{X}_f^k$. Similarly to (137), the following relation holds

$$K_k = P_k^a H_k^T R_k^{-1} = P_k^f H_k^T (H_k P_k^f H^T + R_k)^{-1}, \tag{140}$$

so that it is possible to evaluate the Kalman gain matrix K_k as a function of P_k^f, and then correct the covariance,

$$P_k^a = ((P_k^f)^{-1} + H_k^T R_k^{-1} H_k)^{-1} = (I - K_k H_k) P_k^f (I - K_k H_k)^T + K_k R_k K_k^T = (I - K_k H_k) P_k^f.$$

The prediction step instead exploits the dynamical system to propagate the state, yielding

$$\boldsymbol{X}_f^{k+1} = A_{k|k+1} \boldsymbol{X}_a^k$$

for the time update of the state, and

$$\begin{aligned} P_{k+1}^f &= \mathbb{E}[(\boldsymbol{X}_f^{k+1} - \boldsymbol{X}^{k+1})(\boldsymbol{X}_f^{k+1} - \boldsymbol{X}^{k+1})^T] \\ &= \mathbb{E}[(A_{k|k+1}\boldsymbol{X}_a^k - A_{k|k+1}\boldsymbol{X}_k - \boldsymbol{w}_k)(A_{k|k+1}\widehat{\boldsymbol{X}}_a^k - A_{k|k+1}\boldsymbol{X}_k - \boldsymbol{w}_k)^T] \\ &= A_{k|k+1}P_k^a A_{k|k+1}^T + Q_{k+1} \end{aligned}$$

for the time update of the covariance. Grouping together the prediction and the correction steps, we finally obtain the k-th step of the KF algorithm:

$$\boldsymbol{X}_f^k = A_{k-1|k}\boldsymbol{X}_a^{k-1} \qquad \text{state prediction} \tag{141a}$$

$$P_k^f = A_{k-1|k}P_{k-1}^a A_{k-1|k}^T + Q_k \qquad \text{error covariance prediction} \tag{141b}$$

$$K_k = P_f^k H_k^T (H_k P_k^f H_k^T + R_k)^{-1} \qquad \text{Kalman gain evaluation} \tag{141c}$$

$$\boldsymbol{X}_a^k = \boldsymbol{X}_f^k + K_k(\boldsymbol{Z}^k - H_k\boldsymbol{X}_f^k) \qquad \text{state correction} \tag{141d}$$

$$P_k^a = (I - K_k H_k)P_k^f \qquad \text{error covariance correction.} \tag{141e}$$

Note that from (141d) only the estimated state from the previous step and the current measurement are needed to compute the estimate of the current state. The two prediction and correction steps alternate: the prediction advances the state until the next measurement is acquired, then the correction incorporates this latter.

Remark 7. *The Kalman gain K_k defined in* (140) *can also be expressed as $K_k = P_k^{X_f Z}(P_k^Z)^{-1}$; here $P_k^{X_f Z} = \mathbb{E}[\boldsymbol{X}_f^k(\boldsymbol{Z}^k - H_k\boldsymbol{X}_f^k)^T] = P_k^f H_k^T$ is the the cross-covariance between $\boldsymbol{X}_f^k$ and the innovation $\boldsymbol{Z}^k - H_k\boldsymbol{X}_f^k$, whereas $P_k^Z = \mathbb{E}[(\boldsymbol{Z}^k - H_k\boldsymbol{X}_f^k)(\boldsymbol{Z}^k - H_k\boldsymbol{X}_f^k)^T] = H_k P_k^f H_k + R_k$ is the innovation covariance. Similarly,* (141e) *can be rewritten as $P_k^a = P_k^f - K_k P_k^Z K_k^T$. This interpretation is useful when dealing with the unscented Kalman filter (see Sect. 10.2.3).*

Remark 8. *In the linear case, the variational and the sequential approaches yield the same result at the end of a time window, provided the following assumptions are made: the same background estimation and the same covariance matrices are used, the same measurements are acquired – that is, both algorithms are optimal in a least-squares or minimum variance standpoint.*

Let us now return to our problem of estimating the parameter $\boldsymbol{\theta}$. For that, we apply the KF algorithm to the system:

$$\begin{aligned} \boldsymbol{X}^k &= A_{k-1|k}\boldsymbol{X}^{k-1} + B_k\boldsymbol{\theta}^k + \boldsymbol{v}^k, \quad k = 1, \ldots, K, \qquad \boldsymbol{X}^0 = \boldsymbol{G}, \\ \boldsymbol{\theta}^k &= \boldsymbol{\theta}^{k-1} \end{aligned}$$

with observations

$$\boldsymbol{Z}^k = H_k\boldsymbol{X}^k + \boldsymbol{w}^k, \qquad k = 1, \ldots, K;$$

here $\boldsymbol{\theta}_k \in R^p$ denotes the parameter vector and (under the linearity assumption), $B_k \in \mathbb{R}^{n_x \times p}$ and we assume that no random error is associated with model parameters. This

is the so-called *state augmentation* technique. In order to exploit the KF algorithm, we consider as state vector $\widetilde{\boldsymbol{X}}^k = (\boldsymbol{X}^k, \boldsymbol{\theta}^k)^T$ instead of $\boldsymbol{X}^k$, thus yielding the following *augmented* KF algorithm:

$$\begin{aligned}
\widetilde{\boldsymbol{X}}_f^k &= \widetilde{A}_{k-1|k}\widetilde{\boldsymbol{X}}_a^{k-1} && \text{state prediction} && (142a)\\
\widetilde{P}_k^f &= \widetilde{A}_{k-1|k}\widetilde{P}_{k-1}^a\widetilde{A}_{k-1|k}^T + \widetilde{Q}_k && \text{error covariance prediction} && (142b)\\
K_k &= \widetilde{P}_f^k\widetilde{H}_k^T(\widetilde{H}_k\widetilde{P}_k^f H_k^T + \widetilde{R}_k)^{-1} && \text{Kalman gain evaluation} && (142c)\\
\widetilde{\boldsymbol{X}}_a^k &= \widetilde{\boldsymbol{X}}_f^k + K_k(\widetilde{\boldsymbol{Z}}^k - \widetilde{H}_k\widetilde{\boldsymbol{X}}_f^k) && \text{state correction} && (142d)\\
\widetilde{P}_k^a &= (I - K_k\widetilde{H}_k)\widetilde{P}_k^f && \text{error covariance correction} && (142e)
\end{aligned}$$

where

$$\widetilde{A}_{k-1|k} = \begin{bmatrix} A_{k-1|k} & B_k \\ 0 & I \end{bmatrix}, \quad \widetilde{\boldsymbol{Z}}^k = \begin{bmatrix} \boldsymbol{Z}^k \\ 0 \end{bmatrix}, \quad \widetilde{H}_k = \begin{bmatrix} H_k & 0 \\ 0 & 0 \end{bmatrix}, \quad \widetilde{Q}_k = \begin{bmatrix} Q_k \\ 0 \end{bmatrix}, \quad \widetilde{R}_k = \begin{bmatrix} R_k & 0 \\ 0 & 0 \end{bmatrix}.$$

We point out that, by construction of the filtering procedure, the estimated parameter values evolve along the simulation period and the actual estimation is achieved with the final values, that is, the estimated parameter vector is $\widehat{\boldsymbol{\theta}} = \boldsymbol{\theta}_a^K$. Hence, we expect these estimation *trajectories* to become less and less fluctuating more during the simulation (see, e.g., Fig. 32 in Sect. 11.3.2); non-converging case would therefore denote the presence of persistent modeling errors.

We close this section by pointing out that when a sequential approach like the Kalman filter is used for the sake of parameter estimation, the dynamical system has to be solved only once, by updating the parameter value after each assimilation of new measurements. On the other hand, a variational approach would require to solve the dynamical system on the whole time interval several times, assuming that an iterative approach is used for performing the optimization; see the sketch in Fig. 28.

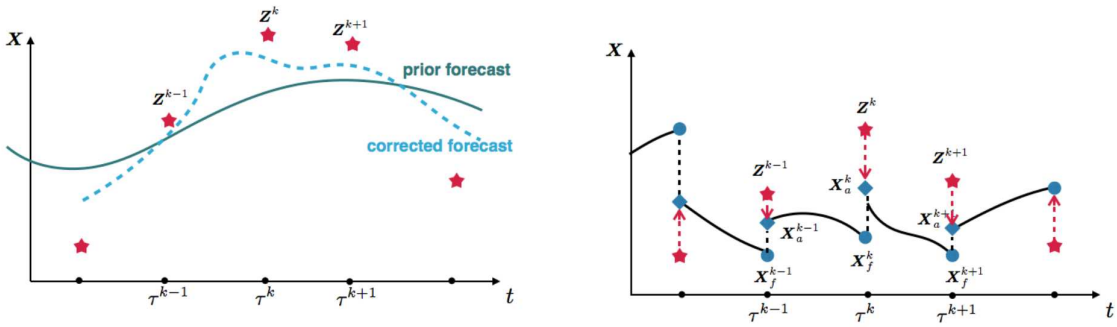

Figure 28: Variational approach (left) versus KF (right) approach: in the former, at each optimization stage the whole state dynamics has to be computed, whereas in the latter each measurement is sequentially used for the state (and parameter) correction

10.2.2 Extended Kalman Filter

The classical KF formulation is well-suited for low-dimensional, linear dynamical systems, although in real applications these assumptions are seldom verified. The extended Kalman filter (EKF) has been introduced for nonlinear dynamical systems, where (138) is replaced by

$$\boldsymbol{X}^k = \mathbf{f}(\boldsymbol{X}^{k-1}, \tau^k) + \boldsymbol{\varepsilon}^k, \qquad \boldsymbol{Z}^k = \mathbf{h}(\boldsymbol{X}^k, \tau^k) + \boldsymbol{\eta}^k, \tag{143}$$

being $\mathbf{f}$ and $\mathbf{h}$ two nonlinear functions. Nonlinearity here involves both the system dynamics and the observation model. The EKF consists in applying the KF algorithm (141a)–(141e) to a linearized version of (143) around the previous state, so that at each step we set

$$A_{k-1|k} = \left.\frac{\partial \mathbf{f}}{\partial \boldsymbol{X}}\right|_{\boldsymbol{X}_a^{k-1}, \boldsymbol{\theta}^k}, \qquad H_k = \left.\frac{\partial \mathbf{h}}{\partial \boldsymbol{X}}\right|_{\boldsymbol{X}_f^k}.$$

At each step two Jacobian matrices have to be evaluated at the current predicted state/parameters. A similar extension of the algorithm (142a)–(142e) provides the EKF for parameter estimation. Although feasible in principle, EKF suffers from several drawbacks: for instance, it entails prohibitive computational costs to invert large matrices and to propagate the covariance matrix in time. Even more importantly, the EKF may lack of stability, meaning that as the estimated state deviates from the true state, the linearized model becomes inaccurate, which may lead to an even larger error in state estimation. To mitigate these shortcomings, several strategies have been put in place: low rank approximation of the covariance matrices have been considered, and other extensions of the original Kalman filter like UKF and EnKF have been introduced.

10.2.3 Unscented Kalman filter

While the EKF exploits the differentiation of nonlinear operators modeling both the state dynamics and the observation process to evaluate the propagation of means and covariances, the unscented Kalman Filter (UKF), introduced in [281], relies on a set of well-chosen deterministic points (or *sigma points*) whose propagation through the nonlinear operators yields the empirical means and covariances required in the Kalman prediction/correction formulas. The rationale behind goes under the name of *unscented transformation*, whose goal is to map a set of points so that their sample distribution approximates the true distribution [280].

Supposing that we know the mean $\mathbb{E}[\boldsymbol{X}]$ and the covariance Σ of a random vector $\boldsymbol{X} \in \mathbb{R}^{n_x}$, the simplest choice is to select $2n_x$ (symmetric) sigma points $x_{(i)}$ as

$$x_{(i)} = \mathbb{E}[\boldsymbol{X}] + \left(\sqrt{n_x \Sigma}\right)_i, \quad x_{(n_x+i)} = \mathbb{E}[\boldsymbol{X}] - \left(\sqrt{n_x \Sigma}\right)_i, \qquad i = 1, \dots, n_x$$

being $\left(\sqrt{n_x \Sigma}\right)_i$ the $i-th$ column of the Cholesky factor of $n_x \Sigma$; different options for the sigma points selection are however possible, see, e.g., [279].

The prediction-correction strategy of the KF is then performed. Referring to the same notation used in Sect. 10.2.1 and supposing that the current forecast based on $\boldsymbol{Z}^1, \dots, \boldsymbol{Z}^{k-1}$ is $\widehat{\boldsymbol{X}}_f^k$, with covariance matrix P_k^f, the following *correction step* is performed:

- from the estimated mean $\widehat{\boldsymbol{X}}_f^k$ and covariance P_k^f at time τ^k, select a set of $2n_x$ sigma points

$$x_{f,(i)}^k = \widehat{\boldsymbol{X}}_f^k + \left(\sqrt{n_x P_k^f}\right)_i, \quad x_{f,(n_x+i)}^k = \widehat{\boldsymbol{X}}_f^k - \left(\sqrt{n_x P_k^f}\right)_i, \qquad i = 1, \dots, n_x$$

centered around $\widehat{\boldsymbol{X}}_f^k$ at a distance given by the standard deviation extracted from the covariance matrix and obtain the predicted measurement

$$\widehat{\boldsymbol{Z}}^k = \frac{1}{2n_x} \sum_{i=1}^{2n_x} \widehat{\boldsymbol{Z}}_{(i)}^k, \qquad \text{being} \quad \widehat{\boldsymbol{Z}}_{(i)}^k = \mathbf{h}(x_{f,(i)}^k, \tau^k), \quad i = 1, \dots, 2n_x;$$

- estimate the covariance of the predicted measurement

$$P_k^Z = \frac{1}{2n_x} \sum_{i=1}^{2n_x} \left(\widehat{\boldsymbol{Z}}_{(i)}^k - \widehat{\boldsymbol{Z}}^k\right) \left(\widehat{\boldsymbol{Z}}_{(i)}^k - \widehat{\boldsymbol{Z}}^k\right)^T + R_k$$

and the cross-covariance between $\boldsymbol{X}_f^k$ and $\widehat{\boldsymbol{Z}}^k$

$$P_k^{X_f Z} = \frac{1}{2n_x} \sum_{i=1}^{2n_x} \left(\widehat{\boldsymbol{X}}_f^k - x_{f,(i)}^k\right) \left(\widehat{\boldsymbol{Z}}^k - \widehat{\boldsymbol{Z}}_{(i)}^k\right)^T;$$

- perform the Kalman gain evaluation, state correction and the error covariance correction similarly to (142c)–(142e) (recall Remark 7),

$$\begin{aligned} K_k &= P_k^{X_f Z} (P_k^Z)^{-1} \\ \widehat{\boldsymbol{X}}_a^k &= \widehat{\boldsymbol{X}}_f^k + K_k(\boldsymbol{Z}^k - \widehat{\boldsymbol{Z}}^k) \\ P_k^a &= P_k^f - K_k P_k^Z K_k^T. \end{aligned}$$

In the *prediction step*, a set of sigma points is selected as

$$x_{a,(i)}^k = \widehat{\boldsymbol{X}}_a^k + \left(\sqrt{n_x P_k^a}\right)_i, \quad x_{a,(n_x+i)}^k = \widehat{\boldsymbol{X}}_a^k - \left(\sqrt{n_x P_k^a}\right)_i, \qquad i = 1, \dots, n_x$$

and a forward computation of one time window is performed to get the state prediction at step $k+1$

$$\widehat{\boldsymbol{X}}_f^{k+1} = \frac{1}{2n_x} \sum_{i=1}^{2n_x} x_{f,(i)}^{k+1}, \qquad \text{being} \quad x_{f,(i)}^{k+1} = \mathbf{f}(x_{a,(i)}^k, \tau^{k+1})$$

(note that each sigma point is treated independently); finally, the covariance is updated as

$$P_{k+1}^f = \frac{1}{2n_x} \sum_{i=1}^{2n_x} \left(\widehat{\boldsymbol{X}}_f^{k+1} - x_{f,(i+1)}^k\right) \left(\widehat{\boldsymbol{X}}_f^{k+1} - x_{f,(i+1)}^k\right)^T + Q_{k+1}.$$

Provided the analysis step is performed in parallel, the cost of the whole estimation procedure is comparable to that of a simple forward simulation; by contrast, a variational estimation would require a significant number of successive iterations (typically, order of hundreds) of both forward and adjoint simulations.

An augmented formulation of the UKF can be easily obtained, similarly to (142), in order to treat the case where the system depends on a set of p parameters affected by uncertainty, which need to be estimated; nevertheless, the very large dimension of the state vector (depending on the spatial discretization of the state variable) makes this filter intractable in practice. In those cases where uncertainty only affects the parameters, and $p \ll n_x$, a much more feasible version yielding a reduced-order UKF limits the computations of the filter operator to a subspace of small dimension and is much more efficient. The reduction to the parametric space as regarding the choice of the sigma-points for the sake of parameter estimation was originally introduced in [452, 261]; a first application to the estimation of electrophysiology parameters can be found instead in [588] and in [587]. A detailed analysis of the reduced-order UKF can be found, e.g., in [377]. A possible alternative, recently explored in [426, 425], is to perform instead a *state reduction* relying on a reduced-order model, and then consider the problem of simultaneous state-parameter estimation.

10.3 Examples of applications in cardiovascular modeling

In the past decade, parameter identification problems have been considered in several applications to cardiovascular modeling. In this section we report a list of relevant contributions; two meaningful examples will be more specifically discussed in Sects. 10.3.1–10.3.2.

The problem of identifying a set of parameters of one-dimensional models for the arterial circulation has been first considered in [366], where a nonlinear least squares approach based on the optimization of a cost function and the introduction of a suitable adjoint problem has been considered. A relevant application in this context is the estimation of the elastic coefficient of a subject-specific vessel based on measurements of its displacement recovered from medical images. A *variational approach* based on the minimization of suitable functionals has been proposed in [442] and, more recently, in [50]; we present this technique in Sect. 10.3.1. A different approach based on an unscented Kalman filter has been proposed in [51] and further explored in [376] for estimating modeling parameters pertaining to vessel wall boundary conditions. Similar strategies based on the unscented Kalman filter have been considered e.g. in [340] to solve inverse problems in large one-dymensional arterial networks, and in [430] for the sake of estimation of lumped (e.g., windkessel) model parameters by using the pressure curve in ascending aorta.

Other approaches have been considered e.g. in [59] to characterize the terminal peripheral resistances in a network describing one-dimensional arterial blood flow, or in [522] to adjust the parameters of a windkessel outflow boundary conditions of three-dimensional blood flow models, in order to match some desired features of pressure and flow waveforms.

Several works have been recently focused on parameter identification and, more generally speaking, on the solution of inverse problems in heart modeling. The classical *inverse problem in electrocardiology* has been considered by many authors in the last decades; it consists in recovering the electrical potential at the epicardial surface by using a number of remote, non-invasive or minimally-invasive potential recordings, e.g. acquired along the body surface [500, 464, 96] which are usually referred to as *body surface-potential data*.

In its original formulation, this problem involves the pure (linear) diffusion model for the torso as direct problem [122, 116, 604], see Sect. 7.1.5. Such inverse problem is mathematically ill-posed, and several regularization strategies have been proposed; see, e.g., the reviews [465, 118]. Another method to solve the inverse electrocardiology problem relies on measurements of the electrical potential within one of the heart chambers (ventricles and atria) by means of non-contact multi electrode catether arrays, and tries to estimate the endocardial surface potential from them. Since the measurements are recorded closer to the endocardial surface than the ones acquired on the body surface, this problem is less ill-conditioned than the former. If the problem is recast under the form of a parameter estimation problem, i.e. where the epicardial potential distribution is described in terms of a set of parameters, the inverse problem can be more easily tackled.

More generally speaking, inverse and parameter estimation problems have been considered in several works in order to reconstruct, e.g., the cardiac electrical activity in the myocardium, or to locate ischemic or infarcted zones by estimating conductibility parameters. Concerning *variational approaches*, we can mention a level set framework for identifying heart infarctions [346] by relying on a least-squares formulation and an adjoint problem to determine the gradient of the cost functional. In this case, the infarcted region in a simplified two-dimensional domain has been described in terms of a discrete level-set function, involving a set of parameters to be identified from synthetic ECG boundary measurements, and a Tikhonov regularization procedure. The solution of a parameter identification problem to locate (in terms of size and position) ischemic regions, where a simplified state elliptic system modeling the electrical potential in both the heart and the torso in the resting phase is considered also in [347, 406]. In all these papers, the PDE-constrained optimization problem has been solved using an iterative method, following an *optimize, then discretize* approach. An all-at-once approach has been instead considered in [407] for a similar problem, taking also into account anisotropic cardiac conductivities and fiber orientation. A more involved version of this problem, still focusing on the inverse electrocardiographic source localization of ischemias, has been more recently considered in [585], taking into account physically-based constraints (in both equality and inequality forms), a total variation regularization and a primal-dual interior point method.

The personalization of a cardiac electrophysiology model involving e.g. the identification of conductivities, local conduction velocities and parameters related to action potential duration restitution curve has been addressed in [100, 489] – although relying on a simplified Eikonal model – and applied to a clinical dataset derived from a hybrid X-ray/magnetic resonance imaging and non-contact mapping procedure on patients with heart failure. More recently, a variational approach for the estimation of cardiac conductivities entering in a bidomain model, from measures of the transmembrane and extracellular potentials available at some sites of the tissue, has been proposed in [606]. It relies on a derivative-based optimization method where the gradient of the functional to minimize is computed by resorting to the adjoint equations of the bidomain model. Parameter estimation in a problem where the bidomain model for the heart is coupled with the Laplace equation for the passive conduction in the torso has been considered in [74] for the sake of estimating the torso conductivity parameters.

The unscented Kalman filter has been exploited in [587] and more recently in [360, 538] for the identification of scar locations and their size from body surface-potential and MRI data, using a monodomain two-variables Allev-Panfilov model. A reduced-order UKF has been recently exploited in [123] for the estimation of electrical parameters within an electromechanical model, by taking advantage of observations from both electrocardiograms and myocardium displacements.

Another inverse problem in electro-physiology has been studied in [567, 428]. The measures of the electrical activation time on the endocardium, acquired by the NavX system (see Sect. 6.2), were used to find the optimal Purkinje network configuration. For this problem, the parameters to be estimated are the coordinates of the network. In particular, starting from an initial network with fractal shape, a functional accounting for the discrepancy between measured and computed activation times is minimized in order to find the patient specific location of the PMJ (see Sect. 5.3). This methodology has been successfully applied to real pathological scenarios, see [427].

Regarding instead cardiac biomechanics, the estimation of contractility parameters has been addressed in [379, 377] using the unscented Kalman filter, where the degree of damage in cardiac tissues caused by an infarct is estimated using velocity measurements coming e.g. from tagged MRI; see also [378]. A reduced-order UKF has been applied in [597] for the sake of identification of material parameters in a transversally isotropic mechanical model; further details concerning this applications will be provided in Sect. 10.3.2. Later on, the same technique has been exploited in [87] for estimating contractility values in a more complex cardiac model, where the tissue is described by combining an active constitutive law in the muscle fiber direction and a visco-hyperelastic material, using actual clinical data consisting of in-vivo Cine-MR image sequences and pressure measurements.

Finally, concerning the coupled electromechanical problem, very few numerical results are nowadays available. The personalization of a 3D electromechanical model has been tackled by variational approaches e.g. in [516], where local ventricular myocardium contractility has been estimated using MRI in an electromechanical model. Similarly, in [135] both the parameters of a Mitchell-Schaeffer model and cardiac contractilities are estimated from catheterized electrophysiology data and cine-MRI images, respectively. The calibration of mechanical parameters of a complete electro-mechanical model of the heart involving the Eikonal model for electrophysiology and an isotropic Mooney-Rivlin material for cardiac mechanics has been performed e.g. by relying on the unscented Kalman filter in [359].

Although several works have made a big step ahead, the solution of parameter estimation problems remains an open computational challenge if complex, coupled models and patient-specific data are taken into account. Also in the case where UKF and EnKF techniques are exploited – which features natural parallelism to a high degree – the need to evaluate the state dynamics for several different scenarios (given e.g. by the elements of the ensemble) makes the computational effort exorbitant. For this reason, simplified physical models have been considered in many contexts so far; on the other hand, reduced-order strategies, like the reduced-order unscented Kalman filter, have been recently proposed

as a possible way to overcome the computational complexity arising from these problems. Dramatic progress is expected in the following years in this field.

10.3.1 A variational approach for estimating the tissue compliance

In this section we illustrate a variational approach introduced in [442] for estimating the Young modulus E of a cardiovascular tissue from displacement data. Indeed, this parameter – and, more generally speaking, the deformability of a soft tissue – is an important index for detecting diseases: low compliance may indicate atherosclerosis or hypertension in the case of an artery, or a marker of diastolic dysfunction in the case of the left ventricle wall. The basic steps consist in *(i)* retrieving the vessel displacement $\boldsymbol{d}_{meas}$ by image registration procedures on time frames of the vessel of interest, and then *(ii)* minimizing the difference between $\boldsymbol{d}_{meas}$ and the displacement computed by solving the coupled 3D blood-vessel problem, in order to estimate the Young modulus. Here the structure is assumed to be linearly elastic and the only parameter to be estimated is E, which is in general a function of space (e.g. an atherosclerotic plaque has different modulus than healthy tissue) but not of time.

The former step consists of data acquisition, image segmentation and reconstruction, and finally registration, see [442] for further details. The latter, which we focus on, is an example of an *inverse fluid-structure interaction* (IFSI) problem, and results in a constrained optimization problem, where the constraint is the FSI problem, and the functional to be minimized is a measure of the mismatch between the data and the computed solution.

A first formulation of the IFSI problem is obtained by assuming that the displacement data $\boldsymbol{d}_{meas}(\boldsymbol{x}, \tau_k)$ for $\boldsymbol{x} \in \Sigma^{\tau_k}$ retrieved from the image registration process are available within the interval $[0, T]$ in some instants denoted by τ^k, $k = 1, \ldots, K$. K is the number of instants when image registration is performed, $\Delta\tau$ the time step between two measurements, driven by the sampling frequency of the image devices, Σ^{τ_k} denotes the interface between the fluid and the structure domain. Following the formulation of problem (130), we consider the functional

$$\mathcal{J}_K(\boldsymbol{d}, E) = \frac{1}{2}\sum_{k=1}^{N} \int\limits_{\Sigma^{\tau_k}} \Big(\boldsymbol{d}_{meas}(\boldsymbol{x}, \tau^k) - \boldsymbol{d}(\boldsymbol{x}, \tau^k)\Big)^2 d\sigma + \frac{\alpha_E}{2}\sum_{k=1}^{N} \int\limits_{\Omega_s} \Big(E(\boldsymbol{x}, \tau^k) - E_{ref}\Big)^2 d\boldsymbol{x}, \tag{144}$$

where $\boldsymbol{d}(\boldsymbol{x}, \tau^k)$ denotes the solution of the FSI system (47) in the ALE formulation, at $t = \tau^k$ and the second term is a non-negative *Tikonov* regularization term. Here E_{ref} is a prior estimate (available e.g. from *ex vivo* specimens), so that the regularization forces E to be close to its reference value. Given an admissible set $\mathcal{E}_{ad}$ where we seek the parameter E, a possible formulation of the IFSI problem reads: for $t > 0, \boldsymbol{x} \in \Omega_s$, find $E = E(\boldsymbol{x}, t) \in \mathcal{P}$ that minimizes (144) under the constraint (47). A possible choice for $\mathcal{P}$ is

$$\mathcal{P} = \{E : E \in L^\infty(\Omega_s),\, 0 < E_{min} \leq E \leq E_{max}, \text{with } E_{min}, E_{max} \in \mathbb{R}\}. \tag{145}$$

Such a problem entails the solution of a time-dependent minimization problem, for which a classical KKT system can be obtained using the Lagrange multipliers method. In this

setting the parameter E plays the role of control variable. However, this approach is rather involved, since the adjoint problem results in a final value problem which would involve differentiation with respect to the deformable domain, too – the so-called *shape derivative*. Moreover, it requires a massive memory occupancy as the solution at all the time steps needs to be stored due to the back-in-time nature of the adjoint problem.

A more convenient alternative numerical approach proposed in [442] considers first the time-discretization of the forward problem, and formulates a minimization problem at each time step. For the sake of simplicity a constant time step $\Delta t = \frac{\Delta \tau}{s}$ is assumed, for a suitable $s \in \mathbb{N}$, $s \geq 1$, that is, the instants τ^k in which measurements are acquired are a subset of the time discretization of (47); for the sake of simplicity, hereon we consider $s = 1$. For the time discretization of (47) implicit methods with a semi-implicit treatment of the convective term and of the fluid domain are considered, whereas the fluid viscous term is treated implicitly. Exploiting the notation already introduced in Sect. 4.6.1; we denote by $\Omega_f^\star$, $\boldsymbol{u}^\star$ and $\boldsymbol{w}^\star$ appropriate extrapolations of the fluid domain, fluid velocity and fluid domain velocity, respectively, and introduce the following spaces:

$$\boldsymbol{V}^\star = \{\boldsymbol{v} \in \boldsymbol{H}^1(\Omega_f^\star) : \boldsymbol{v}|_{\Gamma_{D,f}^\star} = \boldsymbol{0}\},\ Q^\star = L^2(\Omega_f^\star),\ \boldsymbol{W} = \{\boldsymbol{\psi} \in \boldsymbol{H}^1(\Omega_s) : \boldsymbol{\psi}_{\Gamma_{D,s}} = \boldsymbol{0}\},$$

where $\Gamma_{D,f}^\star$ and $\Gamma_{D,s}$ are the portions of the boundary where a Dirichlet condition is prescribed. We denote moreover $\boldsymbol{Z}^\star = \{(\boldsymbol{v}, \boldsymbol{\psi}) \in \boldsymbol{V}^\star \times \boldsymbol{W} : \boldsymbol{v}|_{\Sigma^\star} - \widehat{\boldsymbol{\psi}}|_{\Sigma^\star}/\Delta t = \boldsymbol{0}\}$ and introduce the following bilinear forms:

$$\begin{aligned} a(\boldsymbol{v}, \boldsymbol{d}; \boldsymbol{w}, \boldsymbol{\psi})^\star &= \frac{\rho_f}{\Delta t}(\boldsymbol{v}, \boldsymbol{w})_f^\star + (\boldsymbol{T}_f(\boldsymbol{v}, p), \nabla \boldsymbol{w})_f^\star + \rho_f(((\boldsymbol{v}^\star - \boldsymbol{v}_f^\star)\cdot\nabla)\boldsymbol{v}, \boldsymbol{w})_f^\star + \rho_s\left(\frac{\boldsymbol{d}}{\Delta t^2}, \frac{\boldsymbol{\psi}}{\Delta t}\right)_s, \\ b(q; \boldsymbol{w})^\star &= -(q, \nabla\cdot\boldsymbol{w})_f^\star, \end{aligned}$$

where $(\boldsymbol{v}, \boldsymbol{w})_f^\star = \int_{\Omega_f^\star} \boldsymbol{v}\cdot\boldsymbol{w}\, d\boldsymbol{x}$ and $(\boldsymbol{\psi}, \boldsymbol{\chi})_s = \int_{\Omega_s} \boldsymbol{\psi}\cdot\boldsymbol{\chi}\, d\boldsymbol{x}$. Then, for any given $E \in \mathcal{E}_{ad}$, at each time t^{n+1}, the time discrete forward FSI problem consists of the following steps:

1. compute extrapolations $\Omega_f^\star$, $\boldsymbol{v}^\star$ and $\boldsymbol{v}_f^\star$ for approximating Ω_f^{n+1}, $\boldsymbol{v}^{n+1}$ and $\boldsymbol{v}_f^{n+1}$;
2. given $\boldsymbol{f}_f^{n+1} \in \boldsymbol{L}^2(\Omega_f^\star)$ and $\boldsymbol{f}_s^{n+1} \in \boldsymbol{L}^2(\Omega_s)$, find $(\boldsymbol{v}^{n+1}, \boldsymbol{d}^{n+1}) \in \boldsymbol{Z}^\star$ and $p^{n+1} \in Q^\star$ such that

$$\begin{aligned} &a(\boldsymbol{v}^{n+1}, \boldsymbol{d}^{n+1}; \boldsymbol{w}, \boldsymbol{\psi})^\star + \left(E\,\boldsymbol{S}_s(\boldsymbol{d}^{n+1}), \tfrac{1}{\Delta t}\nabla\boldsymbol{\psi}\right)_s + b(p^{n+1}; \boldsymbol{v})^\star \\ &\qquad = F_f^{n+1}(\boldsymbol{w}) + F_s^{n+1}\left(\tfrac{\boldsymbol{\psi}}{\Delta t}\right) - a(\boldsymbol{R}_f^{n+1}, \boldsymbol{0}; \boldsymbol{w}, \boldsymbol{\psi})^\star \qquad \forall (\boldsymbol{w}, \boldsymbol{\psi}) \in \boldsymbol{Z}^\star \\ &b(q; \boldsymbol{v}^{n+1})^\star = 0 \qquad \forall q \in Q^\star; \end{aligned} \tag{146}$$

3. update the fluid domain to obtain Ω_f^{n+1}.

For the sake of notation, here we have set

$$\boldsymbol{S}_s(\boldsymbol{d}) = \frac{1}{2(1+\nu)}(\nabla\boldsymbol{d} + (\nabla\boldsymbol{d})^T) + \frac{\nu}{(1+\nu)(1-2\nu)}(\nabla\cdot\boldsymbol{d})\boldsymbol{I}$$

so that we can write $\boldsymbol{T}_s = E\,\boldsymbol{S}_s$; moreover, given $\boldsymbol{g} \in \boldsymbol{H}^{1/2}(\Sigma^\star)$, we have denoted by $\boldsymbol{R}_f(\boldsymbol{g}) \in \boldsymbol{H}^{div}(\Omega_f^\star) = \{\boldsymbol{v} \in \boldsymbol{H}^1(\Omega_f^\star) : \nabla \cdot \boldsymbol{v} = 0\}$ and $\boldsymbol{R}_s(\boldsymbol{g}) \in \boldsymbol{H}^1(\Omega_s)$ two lifting functions for the fluid-structure interface continuity, defined as

$$\boldsymbol{R}_f(\boldsymbol{g}) - \boldsymbol{R}_s(\boldsymbol{g}) = -\boldsymbol{g}/\Delta t \quad \text{on } \Sigma^\star.$$

Due to the arbitrariness of one of these functions, in what follows we set $\boldsymbol{R}_s(\boldsymbol{g}) = \boldsymbol{0}$; moreover, when applied to function $\boldsymbol{d}^{m-1}$, it is possible to set $\boldsymbol{R}_f^m = \boldsymbol{R}_f(\boldsymbol{d}^{m-1})$. Finally, the functionals F_f^{n+1} and F_s^{n+1} in (146) account for forcing terms, boundary data on $\partial\Omega_f^\star \setminus \Sigma^\star$ and $\partial\Omega_s \setminus \Sigma$ and terms coming from the time discretization at previous time steps.

Regarding the parameter estimation problem, once the problem has been discretized in time, the minimization of the following cost functional

$$\widetilde{\mathcal{J}}_k(\boldsymbol{d}, E) = \int_\Sigma \Big(\boldsymbol{d}_{meas}(\boldsymbol{x}, \tau^k) - \boldsymbol{d}(\boldsymbol{x}, \tau^k)\Big)^2 d\sigma + \frac{\alpha_E}{2} \int_{\Omega_s} \Big(E(\boldsymbol{x}, \tau^k) - E_{ref}\Big)^2 d\boldsymbol{x}$$

for each $k = 1, 2, \ldots, K$ is considered in [442], under the constraint (146). Hence, a system of KKT conditions can be derived relying on the standard Lagrange multiplier approach (see Sect. 9.1.2), by introducing the Lagrangian functional at time τ^k

$$\begin{aligned}\mathcal{L}(\boldsymbol{v}, p, \boldsymbol{d}; \boldsymbol{\lambda}_v, \lambda_p, \boldsymbol{\lambda}_d; E) = \quad & \widetilde{\mathcal{J}}_k(\boldsymbol{d}, E) + a(\boldsymbol{v}, \boldsymbol{d}; \boldsymbol{\lambda}_v, \boldsymbol{\lambda}_d)^\star + \left(E\,\boldsymbol{S}_s(\boldsymbol{d}), \frac{1}{\Delta t}\nabla\boldsymbol{\lambda}_d\right)_s \\ & + b(p; \boldsymbol{\lambda}_v)^\star + b(\lambda_p; \boldsymbol{v})^\star - F_f(\boldsymbol{\lambda}_v) - F_s\left(\frac{\boldsymbol{\lambda}_d}{\Delta t}\right) + a(\boldsymbol{R}_f, \boldsymbol{0}; \boldsymbol{\lambda}_v, \boldsymbol{\lambda}_d)^\star.\end{aligned}$$

By imposing that the gradient of $\mathcal{L}$ vanishes, we obtain:

- the *adjoint problem*, by forcing to zero the (Gâteaux) derivatives of the Lagrangian functional with respect to $(\boldsymbol{v}, p, \boldsymbol{d})$, which in fact is a discretized-in-time FSI problem (see below for the interface condition): find $(\boldsymbol{\lambda}_u, \boldsymbol{\lambda}_d) \in \boldsymbol{Z}^\star$, $\lambda_p \in Q^\star$ such that

$$\begin{aligned}& a(\boldsymbol{v}, \boldsymbol{\psi}; \boldsymbol{\lambda}_u, \boldsymbol{\lambda}_d)^\star + \left(E\,\boldsymbol{S}_s(\frac{\boldsymbol{\psi}}{\Delta t}), \nabla\boldsymbol{\lambda}_d\right)_s + b(\lambda_p; \boldsymbol{v})^\star \\ & \qquad\qquad + \int_\Sigma (\boldsymbol{d} - \boldsymbol{d}_{meas}) \cdot \boldsymbol{\psi}\, d\sigma = 0 \\ & b(q; \boldsymbol{\lambda}_u)^\star = 0 \qquad\qquad \forall (\boldsymbol{v}, \boldsymbol{\psi}) \in \boldsymbol{Z}^\star, q \in Q^\star;\end{aligned} \tag{147}$$

- the *optimality condition*

$$(\varphi\,\boldsymbol{S}_s(\boldsymbol{d}), \nabla\boldsymbol{\lambda}_\eta)_s = 0 \qquad \forall \varphi \in L^\infty(\Omega_s),$$

  by forcing to zero the derivative with respect to E.

These two problems, together with the state problem: find $(\boldsymbol{u}, \boldsymbol{d}) \in \boldsymbol{Z}^\star$, $p \in Q^*$ such that

$$\begin{aligned}& a(\boldsymbol{u}, \boldsymbol{d}; \boldsymbol{v}, \boldsymbol{\psi})^\star + \left(E\,\boldsymbol{S}_s(\boldsymbol{d}), \frac{1}{\Delta t}\nabla\boldsymbol{\psi}\right)_s + b(p; \boldsymbol{v})^\star = \quad F_f(\boldsymbol{v}) + F_s\left(\frac{\boldsymbol{\psi}}{\Delta t}\right) - a(\boldsymbol{R}_f, \boldsymbol{0}; \boldsymbol{v}, \boldsymbol{\psi})^\star \\ & b(q; \boldsymbol{u})^\star = 0 \qquad\qquad \forall (\boldsymbol{v}, \boldsymbol{\psi}) \in \boldsymbol{Z}^\star, q \in Q^\star,\end{aligned}$$

formally obtained by deriving the Lagrangian with respect to $(\lambda_v, \lambda_p, \lambda_d)$, yield at each τ^k the system of KKT conditions, which couples two linearized FSI problems and a scalar equation.
In particular, for the adjoint problem the interface velocity condition reads

$$\boldsymbol{\lambda}_u = \frac{\boldsymbol{\lambda}_d}{\Delta t} \quad \text{on } \Sigma^\star,$$

whereas the interface stress condition is

$$\boldsymbol{T}_s(\boldsymbol{\lambda}_d)\,\boldsymbol{n} - \boldsymbol{T}_f(\boldsymbol{\lambda}_u, \lambda_p)\,\boldsymbol{n} = -\left(\boldsymbol{d} - \boldsymbol{d}_{meas}\right) \qquad \text{on } \Sigma^\star, \tag{148}$$

taking into account the mismatch between the data and the solution, and modifying the homogeneous interface stress condition (22d) accordingly.

The same strategies described in Sect. 9.2 (e.g., gradient-based methods) can be exploited to solve numerically the KKT system. To take into account the constraint $E > 0$ in the case at hand, it is possible to transform the parameter as $\psi = \log(E)$, so that $E = \exp(\psi) > 0$ for every $\psi \in L^\infty(\Omega_s)$ and then optimize with respect to ψ. Finally, a finite element discretization in space is required to solve numerically the state and the adjoint problem.

By construction, this approach provides an estimate for E at each time; a possible option is then to average them in order to obtain a unique estimate, although this may suffer of instabilities in presence of highly noisy data. A more robust approach consists of solving the minimization problem over time. In this case, however, the complexity of the problem would increase due to the inclusion of the shape derivatives into the minimization problem. In Fig. 29, we report the number of iterations and the convergence history for the algorithm described above for the estimation of the Young modulus.

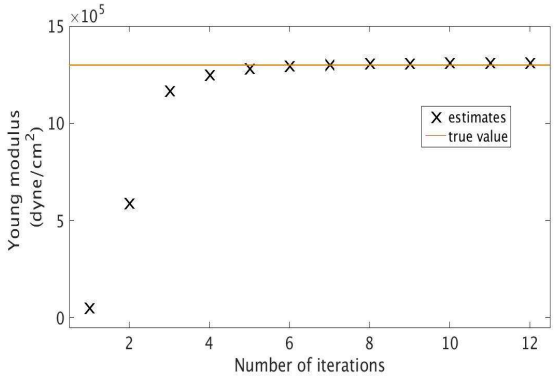

Figure 29: Convergence history for the estimation of the Young modulus by means of the algorithm proposed in [442]. Rectangular fluid and structure domains are used, with synthetic measures generated by means of forward FSI simulations. These numerical results are obtained using the Matlab Finite Element library `MLife`

10.3.2 A Kalman filter approach for estimating material parameters in cardiac mechanics

In this section we illustrate a Kalman filter approach introduced in [597] for estimating material parameters entering in the mechanical model describing myocardial contractility. Only passive mechanics is modeled making a quasi-static assumption, and without taking into account the electro-mechanical coupling. A transversely isotropic Guccione's constitutive law [225] is used and four parameters are estimated *in-silico* from noisy displacement measurements of material points located on the myocardial surface. A similar approach can be in principle applied, e.g., also to identify the material parameters affecting the orthotropic model (94).

The transversely isotropic strain energy function in the Guccione law can be expressed as

$$\Theta(\boldsymbol{E}) = \frac{1}{2}\theta_1(e^Q - 1)$$

where

$$Q = \theta_2 E_{ff}^2 + \theta_3(E_{ss}^2 + E_{nn}^2 + 2E_{sn}^2) + \theta_4(2E_{fs}^2 + 2E_{fn}^2);$$

here $\boldsymbol{\theta} = (\theta_1, \ldots, \theta_4) \in \mathbb{R}^p$ denotes a vector of $p = 4$ material parameters, whereas E_{ij} is the (i,j)-th component of the Green-Lagrange strain tensor $\boldsymbol{E} = \frac{1}{2}(\boldsymbol{F}^T\boldsymbol{F} - I) = \frac{1}{2}(\boldsymbol{C} - I)$, with $i,j \in \{f,s,n\}$ denoting fiber, sheet and sheet-normal directions, respectively. After performing spatial discretization, at each time step the augmented state $\widetilde{\boldsymbol{X}}^k = (\boldsymbol{X}^k, \boldsymbol{\theta}^k)^T \in \mathbb{R}^{n_x+p}$ made by the deformed configuration $\boldsymbol{X}^k$ and the material parameter vector $\boldsymbol{\theta}^k$ has to be determined by solving a nonlinear problem of the form

$$\widetilde{\boldsymbol{X}}^k = \mathbf{f}(\widetilde{\boldsymbol{X}}^{k-1}, \boldsymbol{u}^{k-1}) + \boldsymbol{\varepsilon}^k, \qquad \mathbf{f}(\widetilde{\boldsymbol{X}}^{k-1}, \boldsymbol{u}^{k-1}) = \begin{bmatrix} G(\boldsymbol{\theta}^{k-1}, \boldsymbol{u}^{k-1}) \\ \boldsymbol{\theta}^{k-1} \end{bmatrix},$$

being the input vector $\boldsymbol{u}^{k-1}$ at time $k-1$ given by the external forces, with observations

$$\boldsymbol{Z}^k = \boldsymbol{h}(\widetilde{\boldsymbol{X}}^k) + \boldsymbol{w}^k, \qquad k = 1, \ldots, K.$$

In [597] $\boldsymbol{h} : \mathbb{R}^{n_x+p} \to \mathbb{R}^{n_z}$ is taken as a linear (interpolation) matrix $H \in \mathbb{R}^{(n_x+p)\times n_z}$ mapping the augmented state vector to the coordinates of the points where measured are acquired; those measurements are assumed to be corrupted by a noise term $\boldsymbol{w}^k$ with zero mean and covariance R_k; note that the material parameter has no time dependence itself. Nevertheless, as already pointed out, the filter will provide recursively updated estimates of $\boldsymbol{\theta}^k$; the goal is thus to compute the estimate $\boldsymbol{\theta}^K$ at the final time $t = t^K$.

Moreover, since the augmented state vector $\widetilde{\boldsymbol{X}}^k$ does not depend on the deformed configuration $\widetilde{\boldsymbol{X}}^{k-1}$, the rank of the error covariance matrix $\widetilde{P}_k$ at each step will be equal to p; this is a crucial point in order to devise a reduced-order UKF, making possible to *(i)* store a covariance matrix of dimension $(n_x + p) \times p$, *(ii)* perform inversion of $p \times p$ matrices and, even more importantly, *(iii)* decrease from $\mathcal{O}(n_x + p)$ to $\mathcal{O}(p)$ the number of model evaluations required by the filter at each time step.

Slight differences arise with respect to the UKF formulation addressed in Sect. 10.2.3, due to the reduction of the estimation process to the subset of $\widetilde{\boldsymbol{X}}^k$ corresponding to the p parameter components. The filtering algorithm consists of three steps:

- *inizialization*: a singular value decomposition $P_0^a = L_0^a \Lambda_0^a (L_0^a)^T$ of the initial error covariance $P_0^a \in \mathbb{R}^{(n_x+p)\times(n_x+p)}$ is performed; for instance, P_0^a can be given by a diagonal matrix with p non-zero entries representing the variances of the initial (or background) parameter estimates. Denoting by $L_{0,p}^a$ the matrix whose columns are the first p singular vectors of L_0^a and $\Lambda_{0,p}^a$ the $p \times p$ diagonal matrix of the singular values, the reduced-rank square-root approximation $S_0^a \in \mathbb{R}^{(n_x+p)\times p}$ can be obtained as

$$S_0^a = L_{0,p}^a \sqrt{\Lambda_{0,p}^a};$$

- *prediction (or time update)*: at each step $k = 1, \ldots$, starting from the assimilated state $\widehat{\widetilde{\boldsymbol{X}}}_a^{k-1}$ at step $k-1$, a set of sigma points is selected as

$$\widetilde{x}_{a,(i)}^{k-1} = \widehat{\widetilde{\boldsymbol{X}}}_a^{k-1} + \left(S_{k-1}^a\right)_i, \quad \widetilde{x}_{a,(p+i)}^{k-1} = \widehat{\widetilde{\boldsymbol{X}}}_a^{k-1} - \left(S_{k-1}^a\right)_i, \quad i = 1, \ldots, p.$$

  Then, the sigma points are transformed through the state dynamics to obtain

$$\widetilde{x}_{f,(i)}^k = \mathbf{f}\left(\widetilde{x}_{a,(i)}^{k-1}, \boldsymbol{u}^{k-1}\right), \quad i = 1, \ldots, 2p,$$

  the mean $\widehat{\widetilde{\boldsymbol{X}}}_f^k$ and the error covariance P_k^f are estimated as

$$\widehat{\widetilde{\boldsymbol{X}}}_f^k = \sum_{i=1}^{2p} \widetilde{x}_{f,(i)}^k, \quad P_k^f = \sum_{i=1}^{2p} (\widehat{\widetilde{\boldsymbol{X}}}_f^k - \widetilde{x}_{f,(i)}^k)(\widehat{\widetilde{\boldsymbol{X}}}_f^k - \widetilde{x}_{f,(i)}^k)^T;$$

  to preserve the low-rank structure of the correlation matrix P_k^f, a singular value decomposition $P_k^f = L_k^f \Lambda_0^f (L_k^f)^T$ is performed, thus yielding

$$P_k^f = S_k^f (S_k^f)^T, \qquad S_k^f = L_{k,p}^f \sqrt{\Lambda_{k,p}^f};$$

- *correction (or measurement update)*: at each step $k = 1, \ldots$, the observation $\boldsymbol{Z}^k$ is assimilated into the forecast $\hat{\widetilde{X}}_f^k$ yielding the corrected state

$$\hat{\widetilde{\boldsymbol{X}}}_a^k = \hat{\widetilde{\boldsymbol{X}}}_f^k + K_k(\boldsymbol{Z}^k - H\hat{\widetilde{\boldsymbol{X}}}_f^k).$$

  In this case the Kalman gain can be obtained as

$$K_k = S_k^f (I + (HS_k^f)^T R_k^{-1} HS_k^f)^{-1} (HS_k^f)^T R_k^{-1}$$

along with the square-root of the error covariance, given by

$$S_k^a = S_k^f (I + (HS_k^f)^T R_k^{-1} HS_k^f)^{-1/2}.$$

Note that here, compared to the UKF formulation derived in Sect. 10.2.3, update formulas for the Kalman gain and the error covariance are directly obtained for the square-root of the covariance matrix; see, e.g., [520, 597] for further details.

In [597] such a reduced-order UKF is shown to be able to estimate $p = 4$ (and, subsequently, $p = 12$) material parameters starting from a set of synthetic measurements generated by adding a Gaussian noise to a set of noise-free measurements obtained through model simulation for a chosen, ground-truth, parameter vector. Myocardial dilation is considered by loading the structure with a given ventricular pressure on the endocardium, and $n_z = 600$ material points located on the epicardium and endocardium.

We have chosen to report this example to illustrate how to take advantage of a KF strategy in a *relatively* simple cardiovascular application; further details and more involved cases can be found, e.g., in [377, 51, 87, 376, 123]. Numerical results related to parameter identification in electrophysiology by means of an Ensemble Kalman Filter – a technique which shares several similarities with the UKF, indeed – will be shown in Sect. 11.2.2.

11 Including uncertainty

Moving towards model personalization – that is, the adaptation of model inputs to subject-specific conditions – the question on the sensitivity of model predictions to errors and uncertainties in the model inputs dramatically arises. The inputs to be personalized may include the computational domain (e.g., vascular networks), physical parameters (such as vascular material properties), and boundary conditions. Because of noise in input measurements, as well as of their large biological variability, model inputs are unavoidably hampered by uncertainty. Furthermore, as already seen in Sect. 10, not all model inputs are directly measurable, as in the case of the local mechanical properties of the arterial wall, thus calling into play the need of solving parameter estimation problems. The uncertainties carried by patient-specific features should then be incorporated into the computational model, to quantify their impact on the computed results and to obtain more reliable predictions or best/worst-case scenarios [151]. These are the main reasons behind the very rapid growth of applications of sensitivity analysis and uncertainty quantification (UQ) to cardiovascular problems in the last decade. Being UQ a very active (and less mature than PDE-constrained optimization or parameter estimation) field from both a mathematical and a computational viewpoint, in this section we only touch some basic, yet relevant, issues related to UQ techniques; see, e.g., [531, 283, 323] for a more in-depth overview of numerical aspects of UQ.

Typically, UQ problems involve a mathematical model for a process of interest, subject to some uncertainty about the correct form of this model or, more frequently, about some

of its parameters. Although featuring substantial overlap with the field of parameter estimation and data assimilation, UQ problems additionally involve the propagation of uncertainty on output of interest, reliability or certification problems, prediction problems and, very often, consist of several of these aspects coupled together. For instance, after estimating some model parameters, we may use them to forward propagate some other uncertainties. Often, though not always, uncertainties are treated probabilistically, thus calling into play probabilistic and statistical methods. Here we focus on basic aspects related with *forward propagation* and *backward propagation* of uncertainty, focusing for the latter case on statistical inversion methods within a Bayesian framework.

11.1 Forward Uncertainty Quantification

The goal of forward UQ is to derive information about the uncertainties in system outputs of interest, given information about the uncertainties in the system inputs. The goal is to obtain the probability density function (PDF) of some output of interest $\boldsymbol{Z} = \boldsymbol{f}(\boldsymbol{\theta}) \in \mathbb{R}^{n_z}$ given the probability distribution of the input $\boldsymbol{\theta} \in \mathbb{R}^p$, or evaluate moments (such as the expected value and the variance), correlation functions, confidence regions, quantiles, etc[4]. Here $\boldsymbol{f} : \mathbb{R}^p \to \mathbb{R}^{n_z}$ denotes an input-output map; for instance, in [506] the radius of an abdominal aortic aneurysm, the radii and the inflow velocity of the carotid artery bifurcation, and the flow split of the left and right pulmonary arteries are taken as random variables to account for the uncertainty impact on blood flows modeled by three-dimensional Navier–Stokes equations with rigid arterial walls, by considering as outputs blood velocity and wall shear stresses.

Once a probabilistic description of the random inputs has been provided, a suitable strategy to propagate uncertainties through the model is needed. Regarding the former aspect, the simplest case is the one where the PDE system depends on a set of random inputs that are constant with respect to space and time. In this case, they can be described by means of a finite-dimensional random vector, with a given probability distribution. A more involved case is the one where input data may vary randomly from one point of the physical domain to another (and, possibly, from one time instant to another); in this case, they are described in terms of random fields. Two popular strategies to describe correlated random fields include Karhunen-Loève expansions and expansions in terms of global orthogonal polynomials [210, 602]. Made by infinitely many terms, these expansions are usually truncated to approximate random fields: the milder the variations in space and time of the random field realizations, the fewer the terms retained in the expansion.

Several approaches to solve PDE problems with random input data are available. Monte Carlo (MC) methods are the most popular; they are based on independent realizations $\boldsymbol{\theta}_1, \ldots, \boldsymbol{\theta}_M$ of the random variable $\boldsymbol{\theta}$ (whose probability distribution is denoted by μ) yielding approximations of the expectation by averaging over the corresponding realizations of that quantity, that is,

[4]Sensitivity analysis (see, e.g., [502] for a detailed review) may be seen as a precursor of forward UQ, sharing the need of providing a quantitative description of the dependence of the solution of a model on input parameters. See, e.g., [147] for the application of SA to a pulse wave propagation model of arterial flows.

$$\mathbb{E}[\boldsymbol{f}(\boldsymbol{\theta})] = \int_{\mathbb{R}^p} f(\boldsymbol{\theta})\mu(d\boldsymbol{\theta}) \approx \frac{1}{M}\sum_{i=1}^{M} \boldsymbol{f}(\boldsymbol{\theta}_i) \tag{149}$$

where the sample $\boldsymbol{\theta}_1, \ldots, \boldsymbol{\theta}_M$ is generated randomly from the probability distribution of $\boldsymbol{\theta}$. Such a method requires a deterministic PDE query for each realization, and a very large number of queries to achieve a small error, this latter being proportional to $1/\sqrt{M}$. This entails an excessive computational burden especially for systems which are already computationally expensive in their deterministic setting. See, e.g., [181, 491, 578] for more on MC methods, [141] and [212] for quasi Monte Carlo and multilevel Monte Carlo methods, respectively.

When the solution depends analytically on the random input parameters, other approaches feature much faster convergence rates. These include spectral (global) stochastic Galerkin (SG) methods [210, 601, 22] and stochastic collocation (SC) methods [21, 600, 412]; see, e.g., the detailed review [236] and the recent books [323, 531] for a mathematical and numerical discussion. These methods are based on the discretization of a PDE system not only with respect to spatial variables, but also with respect to the random inputs. SG methods are intrusive approaches since the physical and the probabilistic degrees of freedom are coupled; stochastic sampling (SS) and interpolatory-type SC methods are instead non-intrusive. SG methods require the solution of discrete systems that couple all spatial and probabilistic degrees of freedom, whereas SC methods can combine standard approximations in physical space with globally defined polynomial approximation in the probability domain, either by full polynomial spaces, tensor product polynomial spaces, or sparse tensor product polynomials. The stochastic space can then be queried at any point in order to construct the PDF of the output, the interpolation in the stochastic space being built on top, and independently, of the PDE solver.

For the sake of illustration, we report in Fig. 30 the activation times obtained using the monodomain model coupled with the Aliev-Panfilov cell model. This computation is carried out on a patient-specific left ventricle geometry, obtained by considering different levels of tissue damage (or ischemia), caused by an insufficient blood perfusion of the myocardium. In this case, each component of the conductivity $\boldsymbol{\Sigma}$ is multiplied by a spatial field $\sigma(\boldsymbol{x};\boldsymbol{\theta})$ ranging from 0 (lack of conductivity, damaged tissue) to 1 (regular conductivity, healthy tissue), which we refer to as relative conductivity; as soon as the position and the size of the ischemia are unknown, σ is a random field, depending on (a finite number p of) random inputs $\theta_1, \ldots, \theta_p$. We highlight that in this case input uncertainty yields significant variability in the output, thus making uncertainty propagation a problem of interest in this context.

11.2 Inverse Uncertainty Quantification

Inverse UQ (or backward uncertainty propagation) problems refer to those situations in which input quantities are inferred starting from observed system outputs. Variational or sequential methods described in Sect. 10.1–10.2 provide point estimates of the quantities of interest, given a set of observations. The *statistical inversion* approach provides a well-

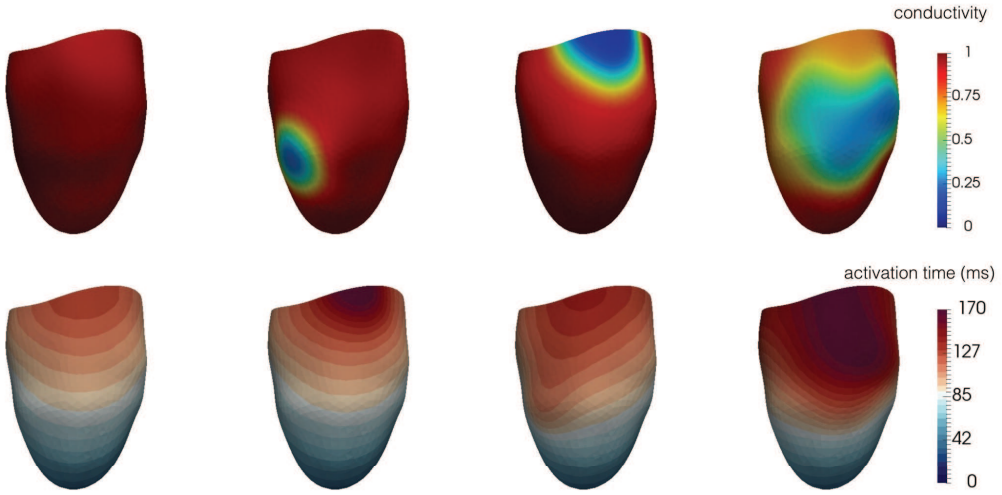

Figure 30: Different degrees of tissue damage in terms of relative conductivity (top) and activation times in milliseconds (bottom) for an healthy case (left) and different ischemic regions on the myocardium. The patient-specific geometry of the left ventricle has been reconstructed using the semi-automatic segmentation method proposed in [170]. These numerical results are obtained using the Finite Element library *redbKIT v2.1* (github.com/redbKIT/redbKIT/releases)

established framework to better characterize the uncertainty in the data, and the resulting uncertainty in the computed estimates, adopting a Bayesian formulation. In this setting, all the model inputs included in the model are described by random variables, where randomness accounts for the available degree of information concerning their realizations, and is expressed in terms of probability distributions; as a result, the solution of the inverse UQ problem is the *posterior* PDF of the unknown inputs. Compared to variational methods of Sect. 10.1, where classical regularization methods yield point estimates by curing the ill-posedness of the problem, statistical inversion aims at removing ill-posedness by recasting the inverse problem in a larger space of probability distributions [283]. This strategy also allows to better characterize the prior information brought, e.g., by the regularization terms in (128), under the form of a *prior* PDF of the unknown inputs. The task of Bayesian inversion is to improve the knowledge on the unknown system features starting from the prior belief and exploiting information from a set of model realizations. For more on this topic, see also, e.g., [530, 531].

11.2.1 Static problems

Assume that we are measuring an output $\boldsymbol{z} = \boldsymbol{f}(\boldsymbol{\theta}, \boldsymbol{\varepsilon}) \in \mathbb{R}^{n_z}$ in order to get information on the unknown input $\boldsymbol{\theta} \in \mathbb{R}^p$, and that the measured quantity is polluted by noise $\boldsymbol{\varepsilon}$. By treating input and output as random quantities, let us denote by $\boldsymbol{Z} \in \mathbb{R}^{n_z}$ and $\boldsymbol{\Theta} \in \mathbb{R}^p$ two random variables, of which $\boldsymbol{z}$ an $\boldsymbol{\theta}$ represent the corresponding realizations. Very often,

the noise is modeled as additive and mutually independent of $\boldsymbol{\Theta}$, so that the input-output map takes the form

$$\boldsymbol{Z} = \boldsymbol{f}(\boldsymbol{\Theta}) + \boldsymbol{\varepsilon}$$

where $\boldsymbol{Z}, \boldsymbol{\varepsilon} \in \mathbb{R}^{n_z}$, $\boldsymbol{\Theta} \in \mathbb{R}^p$ are random variables. Here $\boldsymbol{Z}$ is called *measurement*, and its realization $\boldsymbol{Z} = \boldsymbol{z}$ in the actual measurement process the *data*; moreover, let us denote by $\pi_{noise}(\boldsymbol{\varepsilon})$ the PDF of the noise $\boldsymbol{\varepsilon}$, usually encoding experimental errors. Before performing output measurements, all the information (structure, regularity, etc.) about the distribution of the input $\boldsymbol{\Theta}$ are encapsulated in the *prior* PDF $\pi_{prior}(\boldsymbol{\theta})$, to be selected according to problem-specific considerations.

The conditional probability $\pi(\boldsymbol{z} \,|\, \boldsymbol{\theta})$ of $\boldsymbol{Z} \,|\, \boldsymbol{\Theta} = \boldsymbol{\theta}$ (that is, of $\boldsymbol{Z}$ conditioned on $\boldsymbol{\Theta} = \boldsymbol{\theta}$) is the so-called *(conditional) likelihood function*, and expresses the likelihood of different measurement outcomes $\boldsymbol{z}$ being $\boldsymbol{\Theta} = \boldsymbol{\theta}$ given. In our case the input/output map $\boldsymbol{f} : \mathbb{R}^p \to \mathbb{R}^{n_z}$ the solution of a PDE problem, and the evaluation of the output $\boldsymbol{f}(\boldsymbol{\theta})$. Thanks to the assumption of mutual independence of $\boldsymbol{\Theta}$ and $\boldsymbol{\varepsilon}$, $\boldsymbol{Z} \,|\, \boldsymbol{\Theta} = \boldsymbol{\theta}$ is distributed like $\boldsymbol{\varepsilon}$, that is, the likelihood function is

$$\pi(\boldsymbol{z} \,|\, \boldsymbol{\theta}) = \pi_{noise}(\boldsymbol{z} - \boldsymbol{f}(\boldsymbol{\theta})).$$

Assuming that the measurement data $\boldsymbol{Z} = \boldsymbol{z}$ is given, in the Bayesian framework the inverse problem is to find the conditional PDF $\pi(\boldsymbol{\theta} \,|\, \boldsymbol{z})$ of $\boldsymbol{\Theta}$; this latter is the *posterior* PDF of $\boldsymbol{\Theta}$ given the data $\boldsymbol{Z} = \boldsymbol{z}$ and can be expressed through the Bayes theorem as

$$\pi(\boldsymbol{\theta} \,|\, \boldsymbol{z}) = \frac{\pi_{prior}(\boldsymbol{\theta})\pi(\boldsymbol{z} \,|\, \boldsymbol{\theta})}{\pi(\boldsymbol{z})};$$

$\pi(\boldsymbol{z}) = \int_{\mathbb{R}^{n_z}} \pi(\boldsymbol{z} \,|\, \boldsymbol{\theta})\pi_{prior}(\boldsymbol{\theta}) d\boldsymbol{\theta}$ plays the role of a normalization constant, and has often little importance from a computational standpoint.

Solving an inverse UQ problem in the static case – alternatively, in literature such a problem is referred to as *stationary inverse problem* – thus consists in finding a prior PDF $\pi_{prior}(\boldsymbol{\theta})$, expressing the likelihood function $\pi(\boldsymbol{z} \,|\, \boldsymbol{\theta})$ using the interplay between the observation and the unknown and finally developing suitable numerical techniques to explore the posterior PDF. Each of these tasks is a challenging problem from a computational standpoint; here we provide some hints on how to cast in this framework a wide range of applications related with backward uncertainty quantification in cardiovascular modeling.

In the case where the unknown is a random variable with few components, the posterior PDF can also be visualized under the form of a nonnegative function of these variables; most applications however yield larger scale inverse UQ problems, and resulting PDFs in high-dimensional spaces, for which it is much more effective to evaluate suitable *point estimators*, like the *maximum a posteriori* estimator

$$\boldsymbol{\theta}_{MAP} = \arg\max_{\boldsymbol{\theta} \in \mathbb{R}^p} \pi(\boldsymbol{\theta} \,|\, \boldsymbol{z})$$

or the *conditional mean*

$$\boldsymbol{\theta}_{CM} = \mathbb{E}[\boldsymbol{\theta} \,|\, \boldsymbol{z}] = \int_{\mathbb{R}^p} \boldsymbol{\theta}\ \pi(\boldsymbol{\theta} \,|\, \boldsymbol{z})\ d\theta.$$

Evaluating the former requires the solution of an optimization problem, using e.g. iterative, gradient-based methods; computing the latter involves a numerical quadrature problem in high-dimensional spaces. The evaluation of variability estimators like the *conditional covariance*

$$Cov(\boldsymbol{\theta} \,|\, \boldsymbol{z}) = \int_{\mathbb{R}^p} (\boldsymbol{\theta} - \boldsymbol{\theta}_{CM})(\boldsymbol{\theta} - \boldsymbol{\theta}_{CM})^T \, \pi(\boldsymbol{\theta} \,|\, \boldsymbol{z}) \, d\theta \in \mathbb{R}^{p \times p}$$

or *confidence regions*, also provides further indicators for the sake of uncertainty quantification.

The simplest probabilistic model that can be used to describe experimental uncertainties is the Gaussian model, for which the noise $\boldsymbol{\varepsilon} \sim \mathcal{N}(\mathbf{0}, \Sigma_\varepsilon)$ is normally distributed, with mean $\mathbf{0}$ and covariance matrix Σ_ε. In this case, the likelihood function is

$$\pi(\boldsymbol{z} \,|\, \boldsymbol{\theta}) \propto \exp\left(-\frac{1}{2}\|\boldsymbol{z} - \boldsymbol{f}(\boldsymbol{\theta})\|^2_{\Sigma_\varepsilon^{-1}}\right).$$

If we can assume a Gaussian model also on the *prior* knowledge of the parameters distributions, i.e. $\pi_{prior} \sim \mathcal{N}(\boldsymbol{\theta}_p, \Sigma_p)$, then the posterior PDF will be normally distributed as well,

$$\pi(\boldsymbol{\theta} \,|\, \boldsymbol{z}) \propto \exp\left(-\frac{1}{2}\|\boldsymbol{z} - \boldsymbol{f}(\boldsymbol{\theta})\|^2_{\Sigma_\varepsilon^{-1}} - \frac{1}{2}\|\boldsymbol{\theta} - \boldsymbol{\theta}_p\|^2_{\Sigma_p^{-1}}\right). \tag{150}$$

In this case, the maximum a posteriori estimator is

$$\boldsymbol{\theta}_{MAP} = \arg\min_{\boldsymbol{\theta} \in \mathbb{R}^p} \left(\frac{1}{2}\|\boldsymbol{z} - \boldsymbol{f}(\boldsymbol{\theta})\|^2_{\Sigma_\varepsilon^{-1}} + \frac{1}{2}\|\boldsymbol{\theta} - \boldsymbol{\theta}_p\|^2_{\Sigma_p^{-1}}\right),$$

that is, it coincides with the estimator obtained by solving the (static version, with $K = 1$ of the) regularized least-squares problem (130), as long as we choose $\boldsymbol{\theta}_0 = \boldsymbol{\theta}_p$, $P_\theta = \Sigma_p$ and $M = \Sigma_\varepsilon^{-1}$. If we assume instead that no information is available about the parameter distribution except that it resides in a subset $\mathcal{D}$ of the parameter space $\mathbb{R}^p$, $\pi_{prior}(\boldsymbol{\theta}) \sim \mathcal{U}(\mathcal{D})$ is a uniform distribution over $\mathcal{D}$.

Remark 9. *Note that parameter estimation techniques of Sect. 10.1 can be seen as strategies yielding point estimates without any reference to underlying statistical models; however, when in the Bayesian framework a Gaussian assumption is made, the regularization term and the norms $\|\cdot\|_{\Sigma_\varepsilon^{-1}}$, $\|\cdot\|_{\Sigma_p^{-1}}$ and the value $\boldsymbol{\theta}_p$ have a clear interpretation in terms of measurement noise and prior probability distribution; hence, a prior that carries sufficient information about the true underlying structure of the parameters often provides more meaningful estimates and regularizes the inverse problem in a more natural way than relying on abstract regularization terms, as in (130), that might not have any interpretation. The benefit of casting parameter estimation problems under the form of inverse UQ problems is that one is also able to characterize the variance of the prediction due to measurement and model errors more precisely than from the single-point estimates.*

Exploring the posterior distribution in the case where the input space $\mathcal{D}$ has a larger dimension than $p = 2$ or 3 calls into play suitable *sampling methods*, among which the Markov chain Monte Carlo (MCMC) techinques represent the most relevant example. Instead than evaluating the posterior PDF at a single point, an MCMC technique is a systematic way to generate a sample which can be used to *explore* the distribution, as well as to perform MC integration like in (149) in order, e.g., to compute the conditional mean or the conditional covariance. In the former case, the posterior $\pi(\boldsymbol{\theta} \mid \boldsymbol{z})$ plays the role of target probability distribution that we want to explore, and is obtained as a realization of a Markov chain by relying, e.g., on the following *Metropolis-Hastings algorithm*:

1. Pick an initial $\boldsymbol{\theta}_1$.
2. For $m = 1, \dots, M$:
   (a) compute $\pi(\boldsymbol{\theta}^m \mid \boldsymbol{z})$;
   (b) draw $\boldsymbol{w} \sim \mathcal{N}(\mathbf{0}, \Sigma_\varepsilon)$ and take a random step to find the next candidate $\widehat{\boldsymbol{\theta}} = \boldsymbol{\theta}_k + \boldsymbol{w}$;
   (c) compute $\pi(\widehat{\boldsymbol{\theta}} \mid \boldsymbol{z})$;
   (d) define the acceptance ratio $\alpha_m = \min\left\{1, \dfrac{\pi(\widehat{\boldsymbol{\theta}} \mid \boldsymbol{z})}{\pi(\boldsymbol{\theta}_m \mid \boldsymbol{z})}\right\}$;
   (e) let $u \sim \mathcal{U}([0,1])$; if $u \leq \alpha_m$, accept, set $\boldsymbol{\theta}_{m+1} = \widehat{\boldsymbol{\theta}}$, and add to the set of samples Ξ; otherwise reject, and keep $\boldsymbol{\theta}_{m+1} = \boldsymbol{\theta}_m$.

After M steps of the algorithm, the set Ξ of samples contains realizations of the probability distribution $\pi(\boldsymbol{\theta} \mid \boldsymbol{z})$. The random step in point (b) from the current sample to the next candidate is distributed as white noise; its covariance should be chosen as large as possible while still maintaining a reasonable acceptance rate; moreover, the initial points of the generated set usually poorly represent the distribution to be explored and are then removed from the sample; to learn more on MCMC algorithms we refer, e.g., to [283, 491, 578] and references therein.

11.2.2 Dynamical problems

Backward UQ problems whose forward system is stationary, or with observations that are not acquired sequentially in time, can be cast under the form of a Bayesian inverse problem as shown in the previous section. In these cases, backward UQ can be formulated in the Bayesian framework by means of *Bayesian filtering methods*, among which the Kalman filter can be seen as a particular instance. These problems are also referred to as *nonstationary inverse problems*. As in Sect. 10.2, depending on the quantities that have to be estimated, the problem can be formulated as a state estimation or a joint state-parameter estimation problem. We will treat both these cases, but we will limit our discussion to finite-dimensional models (that usually arise from space and time discretization of unsteady PDEs) and using discrete time evolution models. Further details can be found, e.g., in [283, 508, 531].

Let us denote by $\{\boldsymbol{X}^k\}_{k=0}^K$ and $\{\boldsymbol{Z}^k\}_{k=1}^K$ two stochastic processes; the former is related with the quantity we are interested in, whereas the latter represents the measurement. In particular, the random vector $\boldsymbol{X}^k \in \mathbb{R}^{n_x}$ is referred to as the *state vector*, whereas the random vector $\boldsymbol{Z}^k \in \mathbb{R}^{n_z}$ is referred to as the *observation*, both considered at the k-th time instant τ^k. From a Bayesian standpoint, the goal is to use the observations until time k to get information about the state $\boldsymbol{X}^k$ and quantify the uncertainty related to this estimate. To frame this problem in the Bayesian setting, we assume that $\{\boldsymbol{X}^k\}_{k=0}^K$ and $\{\boldsymbol{Z}^k\}_{k=1}^K$ are an *evolution-observation model*, that is:

1. $\{\boldsymbol{X}^k\}_{k=0}^K$ and $\{\boldsymbol{Z}^k\}_{k=1}^K$ are Markov processes, that is
$$\pi(\boldsymbol{x}^{k+1} \,|\, \boldsymbol{x}^0, \boldsymbol{x}^1, \dots, \boldsymbol{x}^k) = \pi(\boldsymbol{x}^{k+1} \,|\, \boldsymbol{x}^k), \qquad k = 0, 1, \dots$$
$$\pi(\boldsymbol{z}^k \,|\, \boldsymbol{x}^0, \boldsymbol{x}^1, \dots, \boldsymbol{x}^k) = \pi(\boldsymbol{z}^k \,|\, \boldsymbol{x}^k), \qquad k = 1, 2, \dots;$$
2. $\{\boldsymbol{X}^k\}_{k=0}^K$ depends on the past observations only through its own history, that is
$$\pi(\boldsymbol{x}^{k+1} \,|\, \boldsymbol{x}^k, \boldsymbol{z}^1, \dots, \boldsymbol{z}^k) = \pi(\boldsymbol{x}^{k+1} \,|\, \boldsymbol{z}^k), \qquad k = 0, 1, \dots.$$

Here $\boldsymbol{x}^k$, $\boldsymbol{z}^k$ denote the realizations of the processes $\{\boldsymbol{X}^k\}_{k=0}^K$ and $\{\boldsymbol{Z}^k\}_{k=1}^K$, respectively. In order to characterize such a model, we need to specify the PDF of the initial state $\boldsymbol{X}^0$, $\pi_{prior}(\boldsymbol{x}^0)$, the so-called *transition kernel* $\pi(\boldsymbol{x}^{k+1} \,|\, \boldsymbol{x}^k)$, $k = 0, 1, \dots$ and the conditional probability $\pi(\boldsymbol{z}^k \,|\, \boldsymbol{x}^k)$, $k = 1, 2, \dots$, the so-called (conditional) likelihood function. We assume to deal with a *state evolution equation* under the form

$$\boldsymbol{X}^{k+1} = \boldsymbol{f}^{k+1}(\boldsymbol{X}^k, \boldsymbol{V}^{k+1}), \qquad k = 0, 1, \dots \tag{151}$$

and an *observation equation* under the form

$$\boldsymbol{Z}^k = \boldsymbol{h}^k(\boldsymbol{X}^k, \boldsymbol{W}^k), \qquad k = 1, 2, \dots; \tag{152}$$

$\boldsymbol{f}^{k+1}$ and $\boldsymbol{h}^k$ are known functions, whereas $\boldsymbol{V}^{k+1} \in \mathbb{R}^{n_x}$ and $\boldsymbol{W}^k \in \mathbb{R}^{n_z}$ represent the *state noise* and the *observation noise*, respectively. We want to determine the conditional PDF $\pi(\boldsymbol{x}^k \,|\, \boldsymbol{D}^k)$ of the state at the k-th time instant given the observations $\boldsymbol{D}^k = (\boldsymbol{z}^1, \dots, \boldsymbol{z}^k)$ up to the same time instant; this procedure is usually referred to as *filtering problem*. By recursive application of the Bayes theorem, we have that

- the *time evolution updating*, that is, the problem of determining $\pi(\boldsymbol{x}^{k+1} \,|\, \boldsymbol{D}^k)$ given $\pi(\boldsymbol{x}^k \,|\, \boldsymbol{D}^k)$ and the transition kernel $\pi(\boldsymbol{x}^{k+1} \,|\, \boldsymbol{x}^k)$, provides
$$\pi(\boldsymbol{x}^{k+1} \,|\, \boldsymbol{D}^k) = \int_{\mathbb{R}^{n_x}} \pi(\boldsymbol{x}^{k+1} \,|\, \boldsymbol{x}^k) \pi(\boldsymbol{x}^k \,|\, \boldsymbol{D}^k) d\boldsymbol{x}^k; \tag{153}$$
- the *observation updating*, that is, the problem of determining the posterior distribution $\pi(\boldsymbol{x}^{k+1} \,|\, \boldsymbol{D}^{k+1})$ of $\boldsymbol{X}^k \,|\, \boldsymbol{D}^k$ based on the new observation $\boldsymbol{Z}^{k+1}$ given $\pi(\boldsymbol{x}^{k+1} \,|\, \boldsymbol{D}^k)$ and the likelihood function $\pi(\boldsymbol{z}^{k+1} \,|\, \boldsymbol{x}^{k+1})$, provides
$$\pi(\boldsymbol{x}^{k+1} \,|\, \boldsymbol{D}^{k+1}) = \frac{\pi(\boldsymbol{z}^{k+1} \,|\, \boldsymbol{x}^{k+1}) \pi(\boldsymbol{x}^{k+1} \,|\, \boldsymbol{D}^k)}{\pi(\boldsymbol{z}^{k+1} \,|\, \boldsymbol{D}^k)} \tag{154}$$

where

$$\pi(\boldsymbol{z}^{k+1} \,|\, \boldsymbol{D}^k) = \int_{\mathbb{R}^{n_x}} \pi(\boldsymbol{z}^{k+1} \,|\, \boldsymbol{x}^{k+1}) \pi(\boldsymbol{x}^{k+1} \,|\, \boldsymbol{D}^k) d\boldsymbol{x}^{k+1}.$$

Formula (154) is the Bayes formula where $\pi(\boldsymbol{x}^{k+1} \,|\, \boldsymbol{D}^k)$ is considered as prior distribution for $\boldsymbol{x}^{k+1}$.

The Kalman filter introduced in Sect. 10.2.1 is a remarkable instance of Bayesian filter method. Indeed, let us assume that the state and the observation equations are linear with additive noise processes, that is

$$\boldsymbol{f}^{k+1}(\boldsymbol{x}^k, \boldsymbol{v}^k) = A_{k|k+1}\boldsymbol{x}^k + \boldsymbol{v}^k, \qquad \boldsymbol{h}^k = H_k \boldsymbol{x}^k + \boldsymbol{w}^k,$$

for given matrices $A_{k|k+1}$, H_k, that the noise vectors $\boldsymbol{V}^{k+1}$ and $\boldsymbol{W}^k$ are mutually independent, Gaussian, with zero mean and known covariances Q_{k+1} and R_k, respectively, and that the prior PDF of $\boldsymbol{X}^0$ is Gaussian with mean $\boldsymbol{m}^0$ and covariance P^0. Under these assumptions, the time evolution and the observation updating formulas (151)–(152) involve Gaussian distributions, whose means and covariances can be updated at each step according to prediction (141a)–(141b) and correction (141d)–(141e) formulas, respectively. In particular, we have that

$$\begin{aligned} \pi(\boldsymbol{x}^{k+1} \,|\, \boldsymbol{x}^k) \sim &\quad N(A_{k|k+1}\boldsymbol{x}^k, Q^k) \\ \pi(\boldsymbol{z}^k \,|\, \boldsymbol{x}^k) \sim &\quad N(H_k \boldsymbol{x}^k, R_k). \end{aligned}$$

The Bayesian filtering equations can be evaluated in closed form, yielding the following Gaussian distributions:

$$\begin{aligned} \pi(\boldsymbol{x}^k \,|\, \boldsymbol{D}^{k-1}) \sim &\quad \mathcal{N}(\boldsymbol{m}_f^k, P_k^f) \\ \pi(\boldsymbol{x}^k \,|\, \boldsymbol{D}^k) \sim &\quad \mathcal{N}(\boldsymbol{m}_a^k, P_k^a) \\ \pi(\boldsymbol{z}^k \,|\, \boldsymbol{D}^{k-1}) \sim &\quad \mathcal{N}(H_k \boldsymbol{m}_f^k, H_k P_k^f H_k^T + R_k) \end{aligned}$$

where the means and the variances can be computed with the following KF prediction step:

$$\begin{aligned} \boldsymbol{m}_f^k = &\quad A_{k-1|k}\boldsymbol{m}^{k-1} \\ P_k^f = &\quad A_{k-1|k} P_{k-1}^a A_{k-1|k}^T + Q_{k-1} \end{aligned} \tag{155}$$

and the consequent correction step:

$$\begin{aligned} K_k = &\quad P_k^f H_k^T (H_k P_k^f H_k^T + R_k)^{-1} \\ \boldsymbol{m}_a^k = &\quad \boldsymbol{m}_f^k + F_k(\boldsymbol{z}^k - H_k \boldsymbol{m}_f^k) \\ P_k^a = &\quad (I - K_k H_k) P_k^f. \end{aligned} \tag{156}$$

In other words, under the Gaussian assumption, the density is updated only through the mean and the covariance. A similar interpretation also holds for the EKF, as soon as a Gaussian approximation of the densities is considered, and the evolution of these densities is taken into account. In this respect, Bayesian filtering can be seen as a generalization of deterministic filters, like the KF, the EKF and the UKF introduced in Sect. 10.2. See,

e.g., [283, 508, 531].

As already remarked in Sect. 10.2.2, when the evolution model is fully nonlinear, the EKF, which can be seen as a particular instance of approximate Gaussian filter, may perform badly: this can be explained by considering that the push-forward of the previous state estimate (which has a Gaussian distribution) by a nonlinear map is poorly approximated by a Gaussian distribution. To avoid the linearization of the evolution and the observation models, one can rely on Monte Carlo methods to simulate the distributions by random samples, similarly to what has been done in the static case. This strategy yields the so-called *particle filters* (also referred to as *sequential Monte Carlo methods*), nowadays very popular for complex backward UQ problems.

The goal of a particle filter is to sequentially produce an ensemble $\{\boldsymbol{x}_1^{k|k}, \dots, \boldsymbol{x}_{N_e}^{k|k}\}$ of N_e *particles*, that is, a random sample distributed according to the conditional probability distribution $\pi(\boldsymbol{x}^k \mid \boldsymbol{D}^k)$. The Ensemble Kalman Filter (EnKF), introduced by Evensen [163, 164], is a particle filter exploiting the idea of approximating the means and the covariances of the current estimate involved in the Kalman filter prediction-correction strategy by a set of particles sampled from the distribution. Unlike the KF, we evaluate the error covariance predictions and corrections by the ensemble covariance matrices around the corresponding ensemble mean, instead of classical covariance equations (141b)–(141e) given in the KF algorithm. The covariance matrices of the state vector $\boldsymbol{X}$ need not be evolved, thus eliminating the costs associated with storing, multiplying and inverting the matrices appearing in the equations (141b)–(141e).

The ensemble is initialized by drawing N_e independent particles from, say, a Gaussian distribution with mean $\boldsymbol{m}^0$ and covariance P_0. Then:

- at each *prediction step*, each particle is evolved using the KF prediction step,

  $$\boldsymbol{x}_e^{k|k-1} = A_{k-1|k}\boldsymbol{x}_e^{k-1|k-1} + \boldsymbol{v}^{k-1}$$

  if the system is linear, or

  $$\boldsymbol{x}_e^{k|k-1} = \boldsymbol{f}^k(\boldsymbol{x}_e^{k-1|k-1}, \boldsymbol{v}^{k-1})$$

  if the system is nonlinear;

- at each *correction step*, the observation $\boldsymbol{z}^k$ is replicated N_e times, obtaining

  $$\boldsymbol{d}_e^k = \boldsymbol{z}^k + \boldsymbol{\eta}_e^k, \qquad \boldsymbol{\eta}_e^k \sim N(\boldsymbol{0}, R_k).$$

  Then, the empirical mean

  $$\bar{\boldsymbol{x}}_e^{k|k-1} = \frac{1}{N_e}\sum_{e=1}^{N_e} \boldsymbol{x}_e^{k|k-1}$$

and the empirical covariance

$$C^E_{k|k-1} = \frac{1}{N_e - 1} \sum_{e=1}^{N_e} \left(\boldsymbol{x}_e^{k|k-1} - \bar{\boldsymbol{x}}_e^{k|k-1} \right) \left(\boldsymbol{x}_e^{k|k-1} - \bar{\boldsymbol{x}}_e^{k|k-1} \right)^T$$

of the particles set $\{\boldsymbol{x}_e^{k|k-1}\}_{e=1}^{N_e}$ are computed. The exact Kalman gain is then approximated by

$$K_k^E = C^E_{k|k-1} H_k^T (H_k C^E_{k|k-1} H_k^T + R_k)^{-1}$$

and, finally, the state correction is obtained by applying the formula (141d) to each particle, that is,

$$\boldsymbol{x}_e^{k|k} = \boldsymbol{x}_e^{k|k-1} + K_k^E (\boldsymbol{d}_e^k - H_k \boldsymbol{x}_e^{k|k-1}).$$

Several alternative implementations can be found , e.g., in [163, 165]; see, e.g., also [275, 291, 158] for more on the Ensemble Kalman Filter.

If the backward UQ problem also involves random inputs (as in the case of model parameters $\boldsymbol{\theta}$, which can also be time-varying), the problem of state estimation and parameter estimation simultaneously arises. Generally speaking, there is no unique optimal solution for this problem. Similarly to the *state augmentation* technique presented in Sect. 10.2, a possible way to face this problem is to treat the unknown parameters $\boldsymbol{\theta}$ as part of the state, and use conventional filtering technique to infer the parameter and state simultaneously; this strategy goes under the name of joint estimation; see, e.g. [382, 101, 165] for more details on this aspect. An example related to cardiovascular modeling where an EnKF can be exploited to deal with state and parameter estimation is addressed in Sect. 11.3.2.

11.3 Applications to Cardiovascular Modeling

Until recently, UQ has not represented a priority for cardiovascular modeling. Today, a growing number of works focus on both forward and inverse UQ problems, taking into account uncertainties related to *(i)* measurement errors in experimental data (also referred to as observational uncertainty); *(ii)* model parameters, which may result from observational uncertainty as well as from variability, or lack of information; *(iii)* boundary and/or initial conditions and, possibly, *(iv)* the computational model itself, because of model limitations (model uncertainty) or systematic approximation errors (which can be seen as a form of *epistemic uncertainty*) introduced, e.g., when the original high-fidelity model is replaced by a cheaper surrogate model or a reduced-order model. The list of contributions we mention is unavoidably incomplete.

The effect of uncertain parameters in one dimensional models of the arterial network has first been considered in [603]; a high-order stochastic collocation method based on the generalized polynomial chaos expansion, combined with a discontinuous Galerkin spectral/hp element discretization in physical space, has been exploited to analyze the effects

of parametric uncertainties related with material properties and the initial cross-sectional area of the arterial vessel in pulse wave propagation in a network up to 37 vessels connected via 16 bifurcations. A more general setting taking into account a wider network and many more sources of parametric uncertainties, including parameter-dependent boundary conditions in each distal boundary site and geometrical parameters describing the cross section area) in each arterial segment, has been considered in [94]. Similar problems, involving both sensitivity analysis and uncertainty propagation for networks built over subject-specific datasets, can also be found in [328, 264, 263].

The use of an adaptive stochastic collocation framework to deal with UQ in haemodynamical simulations has been considered in [506], where relevant hemodynamic features are extracted – and their uncertainty is quantified – on two idealized problems, namely an abdominal aortic aneurysm and a carotid artery bifurcation, and on a first case of subject-specific problem, a Fontan procedure for congenital heart defects. In the former case, for instance, the radius of the abdominal aortic aneurysm, the radius and inflow velocity of the carotid artery bifurcation, and the flow split of the left and right pulmonary arteries are treated as random variables, following either Gaussian or uniform distributions, to account for the uncertainty impact on blood flows described by three-dimensional Navier-Stokes equations with rigid walls in small arterial portions. More detailed versions of this methodology have been recently exploited in [503, 504] to analyze the impact of geometric uncertainties (that is, anatomic uncertainties resulting in error of the reconstructed geometry) and physiological uncertainties (yielding to errors in boundary conditions or blood viscosity) on the blood flow and pressures in the coronary artery.

The problem of calibrating outflow boundary conditions of blood flow simulations in truncated arterial domains is cast in a Bayesian framework in [134, 441], with the goal of quantifying the uncertainty affecting velocity and flow related variables of interest, all treated as random variables.

A complete uncertainty propagation pipeline from clinical data to computational results has been considered in [511] focusing on single ventricle palliation surgery example. After determining the probability density functions of right pulmonary artery flow split ratio and average pulmonary pressures from clinical measurements, Bayesian parameter estimation is carried out in order to characterize the distributions of boundary conditions yielding the observed flow splits and average pressure distributions. Then, uncertainties in the boundary conditions are propagated to simulation predictions by employing sparse grid stochastic collocation to statistically characterize model predictions of post-operative hemodynamics in models with and without pulmonary artery stenosis, in order to quantify the statistical variability in virtual surgery predictions. Finally, the impact of uncertainty on the optimal design of idealized bypass graft models has been considered, e.g., in [505, 318, 319].

Regarding cardiac electrophysiology, a systematic application of UQ techniques to the forward problem of electrocardiography (namely, the characterization of the torso potential given the electrical conductivity inside the heart and the torso) has been considered in [205], focusing on a simplified two-dimensional configuration representing a geometric

model of a slice through the human thorax. The forward UQ propagation problem yielding the standard deviation of the resulting stochastic torso potentials depending on several uncertainties affecting, e.g., the electrical conductivities of the organs and the representation of cardiac sources, has been faced by a SG method based on the generalized polynomial chaos expansion. Model personalization in cardiac electrophysiology has been considered in [301], where an efficient Bayesian method exploiting polynomial chaos and compressed sensing has been applied to an eikonal-diffusion model involving a large (> 10) number of parameters, by integrating uncertainty on data and parameters.

In [278] a UQ framework for cardiac action potential models has been addressed, focusing on *(i)* the inverse UQ problem of inferring the maximal conductance of ionic channels from noisy experimental recordings, and *(ii)* the forward UQ problem of propagating the uncertainty in maximal ion channel conductances to suitable outputs of interest, such as the action potential duration. To solve the inverse UQ problem a Bayesian framework, such as the one described in Sect. 11.2, has been successfully employed, whereas the UQ propagation problem has been tackled by means of a MC approach exploiting suitable surrogate models, such as Gaussian Process emulators, to speed up the evaluation of the system model under analysis. A detailed analysis of the mechanisms underlying physiological variability in cardiac electrophysiology and pro-arrytmic risks under a variety of conditions can be found, e.g., in [390].

Concerning heart electromechanics, the quantification of the effect of uncertainties in the fiber orientation and the elasticity parameters included in the strain energy function on global output quantities such as the increase in cavity volume, the elongation of the ventricle, the increase in inner radius, the decrease in wall thickness, and the rotation at apex during the passive filling phase, has been addressed in [422]. In [584], cardiac tissue properties have been estimated by integrating structural information with electrophysiological data from, e.g., electroanatomical mapping systems. By means of Bayesian inference tools, a simultaneous description of clinically-relevant electrophysiological conduction properties and their associated uncertainty for various levels of noise have been obtained, together with suitable design strategies to optimize the location and number of measurements required to maximize information and reduce uncertainty. A relevant application of UQ techniques to nonlinear biomechanics has been considered in [54], where parametric uncertainties related with the constitutive law for the artery wall of an AAA are modeled as random fields. In particular, a lognormal three-dimensional random field is used to describe the inter- and intra-patient variations of one constitutive parameter of a hyperelastic constitutive model, and sampling-based approaches like MC are used to solve the resulting stochastic mechanical problem. A multi-fidelity Bayesian framework incorporating information from different low-fidelity models has been developed to speed up the intensive approximation of the resulting problem, following some general ideas reported in [292, 304]. Employing surrogate models or more reliable reduced-order models (for more on this subject, see Sect. 12) to speed up the numerical solution of direct and inverse UQ problems represents indeed a powerful alternative to SC and SG methods, which has only been partially touched in the case of simple problems, like in [126, 95, 142, 356, 426].

11.3.1 Backward uncertainty propagation in a simplified blood flow model

We want to compare the solution of a parameter estimation problem in a variational framework and in a Bayesian setting, on a simplified blood flow problem. We consider a two-dimensional section of a carotid bifurcation where the diameters d_c, d_b of the common carotid artery (CCA) at the bifurcation and of the mid-sinus level of the internal carotid artery (ICA) are the input parameters, assumed to be uncertain. In this idealized setting, our goal is to identify $\boldsymbol{\theta} = (d_c, d_b)^T$ from the observation of the mean pressure drop

$$\boldsymbol{z} = \int_{\Gamma_{in}} p \, d\Gamma - \int_{\Gamma_{ICA}} p \, d\Gamma$$

between the internal carotid outflow Γ_{ICA} and the inflow Γ_{in}, see Fig. 31 (a). For the sake of simplicity a steady incompressible Navier-Stokes model is employed to model the blood flow, although the same approach concerning the solution of the inverse UQ problem can be applied to the case of an unsteady fluid model, as soon as a peak (or time average) pressure drop is evaluated. Although presented here in a very simplified way for the sake of illustration, the problem of recovering information about vessel features by evaluating physical indices related to flow variables is of general interest also for diagnostic purposes; for instance, the fractional flow reserve is a procedure exploited in coronary catheterization to measure pressure differences across a coronary artery stenosis in order to determine the stenosis degree.

The parameter estimation problem is first solved by minimizing a least-squares functional for different observations of the pressure drop, $z = -1400$ and $z = -2200$, by assuming 5% relative additive noise in the measurements. The results of the inverse identification problem are represented in Fig. 31(b) for 100 realizations of random noise in both cases. The recovered diameter values are shown to be quite sensitive to small noise variations; this is due to the fact that several geometrical configurations – in terms of diameters (d_c, d_b) – may correspond to the same output observation. The backward UQ propagation problem is then solved in a Bayesian setting, characterizing the posterior PDF of $\boldsymbol{\theta} = (d_c, d_b)$ starting from a Gaussian prior and assuming a Gaussian model to describe experimental noise; in particular, we can assume that the two diameters are either *a priori* independent (case (c), left), or correlated (case (c), right)). The two corresponding posterior distributions, obtained for the observations $z = -1400$ and $z = -2200$ of the pressure drop, are reported in Fig. 31 (d-e).

11.3.2 Backward uncertainty propagation in cardiac electrophysiology

We finally consider the problem of identifying the size and the position of an ischemic region in the myocardial tissue, as a remarkable instance of backward UQ problem dealing with cardiovascular applications. Such a problem case can be cast under the form of a joint state/parameter estimation problem, and can be efficiently faced by an EnKF technique.

The state evolution equation is given by the (space and time discretization of the) monodomain equation for the transmembrane potential V_m, coupled with an Alliev-Panfilov cellular model involving a single gating variable w; the state variable is thus $\boldsymbol{u} = (V_m, w)^T$.

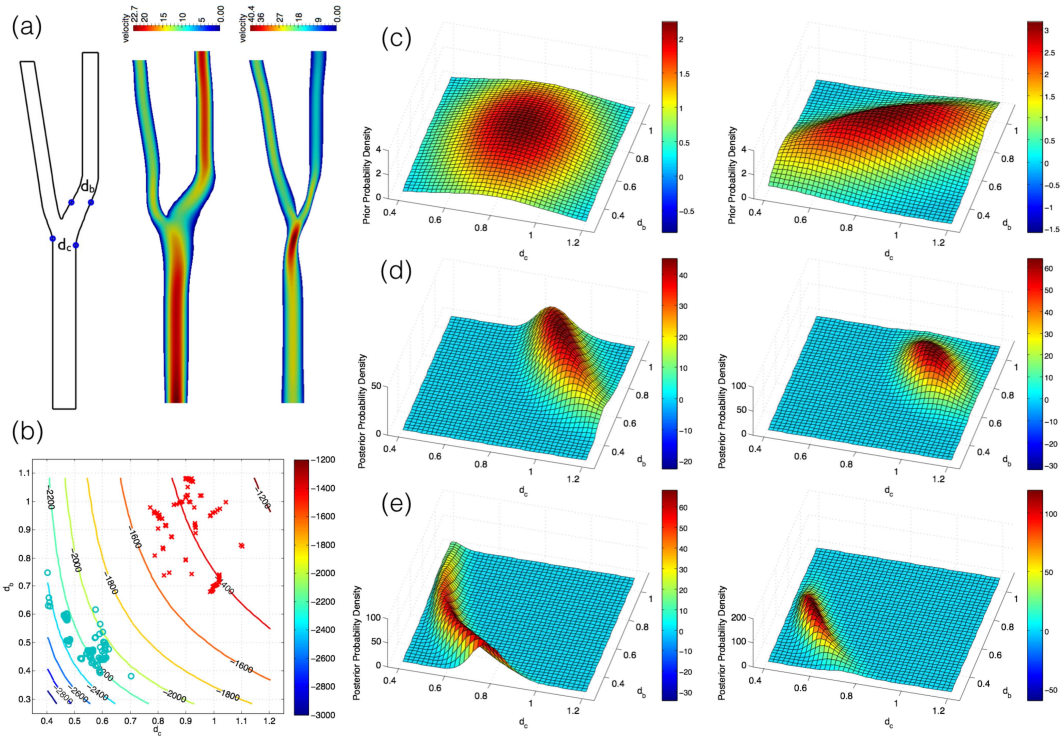

Figure 31: (a) Velocity profiles $[cm/s]$ for different carotid bifurcations parametrized with respect to the diameters d_c, d_b; (b) variational parameter estimation and isolines of the pressure drop; (c) two different choices of the prior distribution on diameters $\boldsymbol{\theta} = (d_c, d_b)^T$; (d)-(e): results of the backward UQ problem obtained with the priors in (c) with observed pressure drop $\boldsymbol{z}_{obs} = -1400$ and $\boldsymbol{z}_{obs} = -2200$ $[dyn/cm^2]$, respectively. These numerical results are obtained using the Matlab Finite Element library `MLife`

Similarly to the example in Sect. 11.1, to represent lacks of conductivity in the tissue we introduce the relative conductivity $\sigma = \sigma(\boldsymbol{x}; \boldsymbol{\theta}) \in [0, 1]$; $\sigma = 1$ and $\sigma = 0$ correspond to proper electrical conduction or total lack of conductivity, respectively.

Since the position and the extension of the ischemic region is unknown, $\sigma(\boldsymbol{x}; \boldsymbol{\theta})$ is a random field. To make its representation low-dimensional, we parametrize the field $\sigma(\boldsymbol{x}; \boldsymbol{\theta})$ in terms of $p = 20$ random inputs $\boldsymbol{\theta} = (\theta_1, \ldots, \theta_{20})^T$ entering into a linear combination of $p = 20$ radial basis functions (RBFs), around p given centers $\{\boldsymbol{x}_i\}_{i=1}^{20}$,

$$\sigma(\boldsymbol{x}; \boldsymbol{\theta}) = \frac{1}{\nu(\boldsymbol{x})} \sum_{i=1}^{p} \theta_i \exp\left(-\frac{\|\boldsymbol{x} - \boldsymbol{x}_i\|^2}{\lambda^2}\right), \qquad \nu(\boldsymbol{x}) = \sum_{i=1}^{p} \exp\left(-\frac{\|\boldsymbol{x} - \boldsymbol{x}_i\|^2}{\lambda^2}\right);$$

$\nu(\boldsymbol{x})$ is a normalization factor so that $\sigma(\boldsymbol{x}; \boldsymbol{\theta}) \in [0, 1]$. We consider a subject-specific left-ventricle geometry, and assume that a set of data $\boldsymbol{z}^1, \ldots, \boldsymbol{z}^K$ is acquired sequentially over a time interval; in particular, at each time instant τ^k, $k = 1, \ldots, K$ data are given by the

transmembrane potential values computed at a set of 9 points located on the endocardium, polluted by Gaussian noise with zero mean and known covariance, to simulate the effect of experimental noise while evaluating the so-called *simultaneous endocardial mapping* in the human left ventricle; these invasive measurements are usually obtained using a non-contact catheter (see, e.g., [512, 6]). For the sake of the computational experiment, we assume that the data $\boldsymbol{z}^k$, $k = 1, \dots, K$, are generated by the monodomain model with relative conductivity $\sigma^* = \sigma^*(\boldsymbol{x}; \boldsymbol{\theta}^*)$ for a particular choice $\boldsymbol{\theta} = \boldsymbol{\theta}^*$ of the input vector, that is,

$$\boldsymbol{z}^k = \boldsymbol{h}(\boldsymbol{u}(\boldsymbol{\theta}^*)) + \boldsymbol{\eta}^k, \qquad \boldsymbol{\eta}^k \sim N(\boldsymbol{0}, R_k).$$

The goal is thus to recover the (posterior) PDF of $\boldsymbol{\theta}^K \mid \boldsymbol{D}^k$ given the observations $\boldsymbol{D}^k = (\boldsymbol{z}^1, \dots, \boldsymbol{z}^k)$, evaluate the conditional mean $\boldsymbol{\theta}^K_{CM} = \mathbb{E}[\boldsymbol{\theta}^K \mid \boldsymbol{D}^k]$, and finally estimate the conductivity field as $\sigma(\boldsymbol{x}; \boldsymbol{\theta}^K_{CM})$.

Starting from a prior distribution for the input vector $\boldsymbol{\theta}^0 \sim \mathcal{U}([0,1]^{20})$, reflecting the lack of information about the possible presence and position of the ischemic region, we rely on the EnKF to produce sequentially an ensemble $\{\boldsymbol{\theta}^k_e\}_{e=1}^{N_e}$ of N_e particles distributed according to the conditional distribution $\pi(\boldsymbol{\theta}^k \mid \boldsymbol{D}^k)$, and the associated ensemble of N_e states $\{\boldsymbol{u}^{k|k}(\boldsymbol{\theta}^k_e)\}_{e=1}^{N_e}$. Hence, starting from the initial ensemble $\{\mathcal{P}^{(0)}, \mathcal{U}^{(0)}\}$ sampled from the prior distribution, the *prediction-analysis* procedure of the EnKF is given by the following two stages recursion:

1. at each *prediction step*, compute the solution $\boldsymbol{u}^{k|k-1}(\boldsymbol{\theta}^{k-1}_e)$ of the state system over $[\tau^{k-1}, \tau^k)$ with initial datum $\boldsymbol{u}^{k|k-1}(\boldsymbol{\theta}^{k-1}_e)$;

2. at each *correction step*, the observation $\boldsymbol{z}^k$ is replicated N_e times, obtaining

   $$\boldsymbol{d}^k_e = \boldsymbol{z}^k + \boldsymbol{\eta}^k_e, \qquad \boldsymbol{\eta}^k_e \sim N(\boldsymbol{0}, R_k).$$

   Then, the sample means

   $$\overline{\boldsymbol{u}}^{k|k-1} = \frac{1}{N_e}\sum_{e=1}^{N_e} \boldsymbol{u}^{k|k-1}(\boldsymbol{\theta}^{k-1}_e), \quad \overline{\boldsymbol{s}}^{k|k-1}_e = \frac{1}{N_e}\sum_{e=1}^{N_e} \boldsymbol{h}(\boldsymbol{u}^{k|k-1}(\boldsymbol{\theta}^{k-1}_e)), \quad \overline{\boldsymbol{\theta}}^{k-1}_e = \frac{1}{N_e}\sum_{e=1}^{N_e} \boldsymbol{\theta}^{k-1}_e, \tag{157}$$

   and the sample covariances

   $$\mathbf{C}^k_{ss} = \frac{1}{N_e - 1}\sum_{e=1}^{N_e} (\boldsymbol{h}(\boldsymbol{u}^{k|k-1}(\boldsymbol{\theta}^{k-1}_e)) - \overline{\boldsymbol{s}}^{k|k-1}_e)(\boldsymbol{h}(\boldsymbol{u}^{k|k-1}(\boldsymbol{\theta}^{k-1}_e)) - \overline{\boldsymbol{s}}^{k|k-1}_e)^T \in \mathbb{R}^{n_z \times n_z}, \tag{158}$$

   $$\mathbf{C}^k_{\theta s} = \frac{1}{N_e - 1}\sum_{e=1}^{N_e} (\boldsymbol{\theta}^{k-1}_e - \overline{\boldsymbol{\theta}}^{k-1}_e)(\boldsymbol{h}(\boldsymbol{u}^{k|k-1}(\boldsymbol{\theta}^{k-1}_e)) - \overline{\boldsymbol{s}}^{k|k-1}_e)^T \in \mathbb{R}^{p \times n_z}, \tag{159}$$

   $$\mathbf{C}^k_{us} = \frac{1}{N_e - 1}\sum_{e=1}^{N_e} (\boldsymbol{u}^{k|k-1}(\boldsymbol{\theta}^{k-1}_e) - \overline{\boldsymbol{u}}^{k|k-1})(\boldsymbol{h}(\boldsymbol{u}^{k|k-1}(\boldsymbol{\theta}^{k-1}_e)) - \overline{\boldsymbol{s}}^{k|k-1}_e)^T \in \mathbb{R}^{n_x \times n_z}; \tag{160}$$

are computed. Finally, the state/parameters ensembles are updated through the following *Kalman formula*

$$\begin{bmatrix} \boldsymbol{\theta}_e^k \\ \boldsymbol{u}^{k|k}(\boldsymbol{\theta}_e^k) \end{bmatrix} = \begin{bmatrix} \boldsymbol{\theta}_e^{k-1} \\ \boldsymbol{u}^k(\boldsymbol{\theta}_e^{k-1}) \end{bmatrix} + \begin{bmatrix} \mathbf{C}_{\theta z}^k \\ \mathbf{C}_{uz}^k \end{bmatrix} (R_k + \mathbf{C}_{zz}^k)^{-1} (\boldsymbol{d}_e^k - \boldsymbol{h}(\boldsymbol{u}^{k|k-1}(\boldsymbol{\theta}_e^{k-1}))), \quad (161)$$

for each $e = 1, \ldots, N_e$.

The numerical results obtained by this procedure are reported in Fig. 32. The data have been generated by the monodomain model with the relative conductivity field $\sigma^* = \sigma^*(\boldsymbol{x}; \boldsymbol{\theta}^*)$ reported on Fig. 32, left; a uniform prior distribution $\boldsymbol{\theta}^0 \sim \mathcal{U}([0,1]^{20})$ is assumed. After executing the EnKF algorithm, we obtain the posterior distribution whose mean and 5%, 95% quantiles are reported on Fig. 32, bottom. The uncertainty on the input parameters is greatly reduced, while the conditional mean of the posterior distribution correctly approximates the realization of the random field reported on the left, by which data exploited for the sake of parameter estimation have been generated.

12 Reduced order modeling

As seen in Sects. 9–11, several numerical strategies used to face PDE-constrained optimization, parameter estimation, and uncertainty quantification problems arising in cardiovascular modeling involve the approximation of PDE systems for several input parameter values. On the other hand, the repeated evaluation of input/output maps to characterize different scenarios requires many queries to numerical models, too. Not only, if quantitative outputs are meant to support clinicians and medical doctors in their decisions, each new numerical simulation should be carried out very rapidly (say, order of minutes) on deployed platforms rather than on huge parallel hardware architectures, possibly requiring limited data storage and memory capacity. Meeting all these requirements is a challenging task, that makes traditional *high-fidelity*, or *full-order*, techniques (such as the FE method) ill-suited, despite the constant growth of computer resources available.

Reduced-order models (ROMs) represent emerging methodologies aimed at reducing the computational complexity and costs entailed by the repeated solution of PDE problems [12, 45, 474]. In the case of parametrized PDEs (that is, PDEs depending on a vector of parameters $\boldsymbol{\mu} \in \mathcal{P} \subset \mathbb{R}^p$) PDEs, the *reduced basis* (RB) method is a remarkable example of ROM that allows to dramatically reduce the dimension of the discrete problems arising from numerical approximation – from millions to hundreds, or thousands at most, degrees of freedom.

Here, $\mathbf{y}(t; \boldsymbol{\mu})$ represent the solution of a time-dependent nonlinear problem (here $\boldsymbol{\mu} \in \mathcal{P} \subset \mathbb{R}^p$ denotes a set of input parameters) under the form:

$$\begin{aligned} M(\boldsymbol{\mu}) \frac{d\mathbf{y}(t;\boldsymbol{\mu})}{dt} + A(\boldsymbol{\mu})\mathbf{y}(t;\boldsymbol{\mu}) + F(\mathbf{y}(t;\boldsymbol{\mu})) &= \mathbf{f}(t;\boldsymbol{\mu}), \qquad t \in (0,T] \\ \mathbf{y}(0;\boldsymbol{\mu}) &= \mathbf{y}_0(\boldsymbol{\mu}) \end{aligned} \quad (162)$$

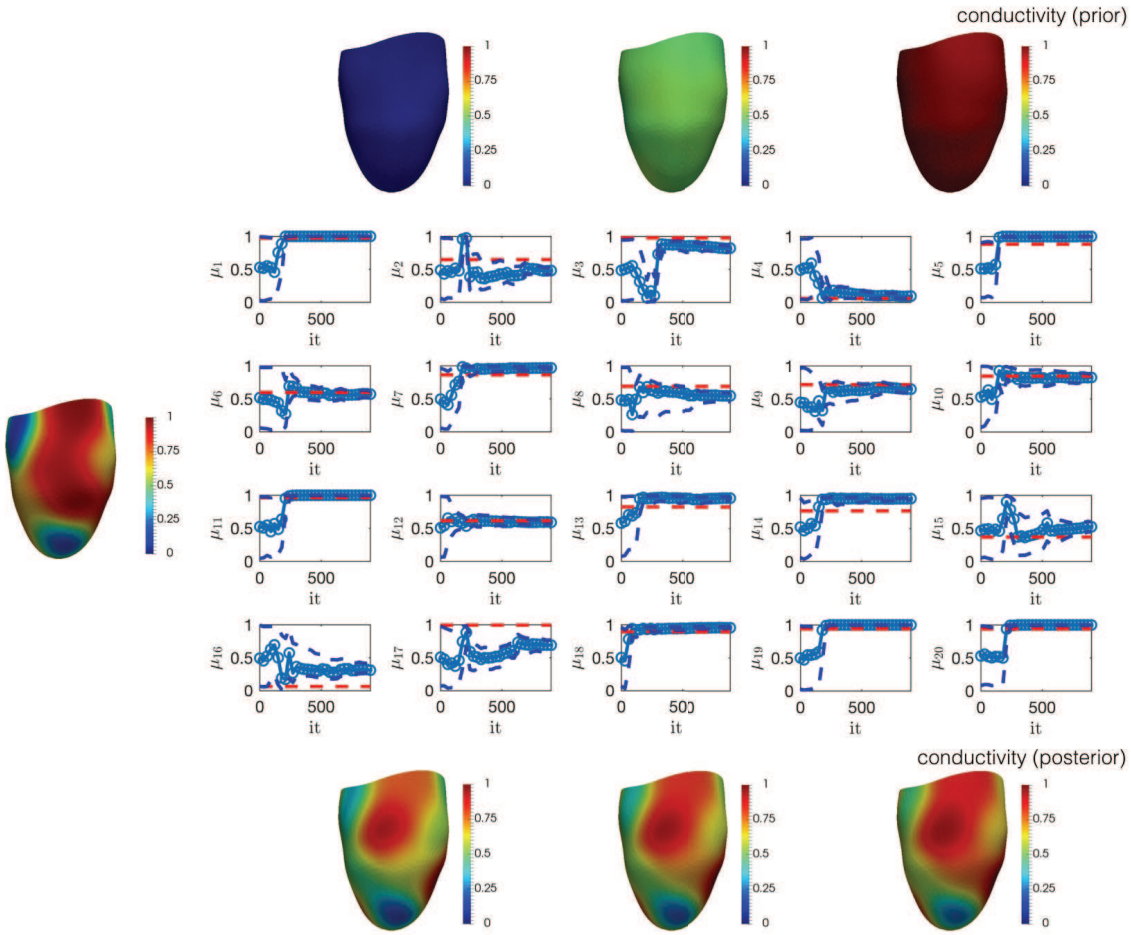

Figure 32: Top: 5% quantile, mean and 95% quantile of the uniform prior distribution of $\boldsymbol{\theta}^0$. Middle: identification of $p = 20$ parameters through the EnKF algorithm. References values θ_i^*, $i = 1, \ldots, 20$, estimates $(\bar{\theta}_e^k)_i$ and confidence intervals are reported in dot red, blue and dot blue lines, respectively. Bottom: 5% quantile, conditional mean and 95% quantile of the posterior distribution of $\boldsymbol{\theta}^K$. These numerical results are obtained using the Finite Element library *redbKIT v2.1* (github.com/redbKIT/redbKIT/releases)

stemming from the (e.g. finite element) discretization of a parametrized PDE, being $A(\boldsymbol{\mu}) \in \mathbb{R}^{N_h \times N_h}$, $M(\boldsymbol{\mu}) \in \mathbb{R}^{N_h \times N_h}$ and $F(\boldsymbol{\mu}) : \mathbb{R}^{N_h} \to \mathbb{R}^{N_h}$ three operators corresponding to the linear, the mass and the nonlinear terms of the PDE.

The dimensional reduction is made possible by exploiting the parametric dependence of the solution manifold, that is, the set $\mathcal{M}_h = \{\mathbf{y}(t; \boldsymbol{\mu}) : t \in (0, T], \boldsymbol{\mu} \in \mathcal{P}\}$, thanks to the evaluation of a database of solutions, or *snapshots*, for selected parameter values, and to a (Petrov-)Galerkin projection onto the RB space spanned by a set of RB functions. In the case of a stationary problem, these latter are the snapshots themselves if a *greedy* algorithm is used, or the first singular vectors of the snapshot matrix if *proper orthogonal*

decomposition (POD) is used; see, e.g. [471, 247, 112]. For time-dependent problems, the parameter space can still be sampled relying on one of the two mentioned techniques, whereas POD is usually exploited for reducing trajectories of the system over the time interval.

Hence, the RB method seeks an approximation $V_N \mathbf{y}_N(t;\boldsymbol{\mu}) \approx \mathbf{y}(t;\boldsymbol{\mu})$ to the solution of (162), being $\mathbf{y}_N(t;\boldsymbol{\mu})$ the reduced state vector and $V_N = [\mathbf{v}_1, \ldots, \mathbf{v}_N] \in \mathbb{R}^{N_h \times N}$ a matrix stacking by columns the RB functions. A possible RB approximation of (162) would read:

$$\begin{aligned} M_N(\boldsymbol{\mu})\frac{d\mathbf{y}_N(t;\boldsymbol{\mu})}{dt} + A_N(\boldsymbol{\mu})\mathbf{y}_N(t;\boldsymbol{\mu}) + V_N^T\mathbf{F}(V_N\mathbf{y}_N(t;\boldsymbol{\mu})) &= \mathbf{f}_N(t;\boldsymbol{\mu}), \qquad t \in (0,T] \\ \mathbf{y}_N(0;\boldsymbol{\mu}) &= \mathbf{y}_{N,0}(\boldsymbol{\mu}) \end{aligned} \tag{163}$$

where

$$A_N(\boldsymbol{\mu}) = V_N^T A(\boldsymbol{\mu}) V_N, \qquad M_N(\boldsymbol{\mu}) = V_N^T M(\boldsymbol{\mu}) V_N, \qquad \mathbf{f}_N(t;\boldsymbol{\mu}) = V_N^T \mathbf{f}(t;\boldsymbol{\mu})$$

The arrays appearing in (163) can be efficiently assembled in a rapid online phase by combining parameter-independent quantities stored during a more expensive offline phase. Suitable *hyper-reduction* techniques are instead required to manage nonlinear terms in order to make their assembling independent of the dimension N_h of the high-fidelity problem.

We emphasize that a RB method requires the solution of some full-order, and therefore very expensive, discrete equations. The key-idea is that these demanding calculations can be done offline, before the optimization with respect to the control parameters, or the parameter estimation, is attempted. As a matter of fact, the cost of each optimization step performed online is much smaller than that involving the full-order state approximation; similarly, computing the evolution of a particles set in the Ensemble Kalman Filter algorithm by querying the ROM can thus be performed in a substantially inexpensive way.

Describing the mathematical principles and the numerical algorithms on which the RB method is rooted would bring us quite far; the interested reader can refer, e.g., to [471] for a detailed presentation. We limit ourselves to cite some remarkable applications of the RB method to problems of interest in cardiovascular modeling (this list is of course incomplete). Parametrized blood flows in idealized cardiovascular geometries have been considered in [320, 357] and in [30, 113, 397] by taking into account more complex (and computationally challenging) subject-specific configurations; in all these cases, solutions of Navier-Stokes equations are computed with respect to inflow and/or geometrical parameters. Applications to PDE-constrained optimization problems arising in the context of optimal design of prosthetic devices can be found, e.g., in [358, 318]. A reduced-order model based on POD is proposed for the bidomain equations of cardiac electrophysiology in [75], yielding the efficient approximation of a restitution curve and the estimation of ionic parameters and infarction locations from synthetic electrocardiograms with an evolutionary algorithm. Alternative options in this respect have been more recently proposed in [208]. Applications of POD to parameter estimation problems with sequential filtering techniques can be found in [90], whereas an application of the RB method for the compu-

tational speedup of Bayesian inverse problems related to blood flows modeling is reported in [319, 355].

We highlight that while physical coefficients, boundary and/or initial conditions, as well as source terms can be usually described in terms of input parameters in a straightforward way, dealing with geometries of varying shape is much more involved. In this latter case, additional techniques providing flexible descriptions of complex shapes, possibly involving few parameters, are required. Notable examples are given by *volume-based* representations, which operate on a control volume and define parametric maps by introducing a set of control points over the control volume; control points displacements, actually inducing a shape deformation, can thus be treated as input parameters. Within this class, free-form deformation techniques and interpolants built over a family of radial basis functions have been successfully employed, see, e.g., [358, 357, 30] for further details. We also point out that the need of deriving flexible and low-dimensional parametrizations is not confined to the realm of RB methods for parametrized PDEs. Indeed, it also arises when dealing with random inputs or fields; in this latter case, input uncertainties are usually parametrized with respect to a finite number of random variables, corresponding to the retained terms after truncating Karhunen-Loève or Polynomial Chaos expansions.

The analysis, development and application of reduced-order modeling techniques is a very active field in the context of numerical approximation for PDEs; without any doubt, cardiovascular applications represent one of the most relevant testing environment.

Disclaimers

Despite being 200 pages long[5], several topics related to the cardiovascular system have not been addressed in this review paper. Among others, we mention the *venous system* (mandatory when one wants to consider a closed loop model of the CS and playing a crucial role in some specific pathologies, see e.g. [547]), the *metabolic system* [128], the *respiratory system* [368, 583, 550], the *cerebro-spinal fluid circulation* [179], the *nervous system* [337], and the *limphatyc system* [362]. For some of them (for example the venous and the respiratory systems) research has progressed remarkably in the last years. Yet, the mathematical investigation of these systems is still in its infancy. In particular, their coupling with CS is almost lacking. Many research avenues are open to the contribution of both pure and applied mathematicians, with the dream of bringing mathematical achievements to play a decisive role in clinical everyday's practice.

Acknowledgments

The authors would like to thank P. Biondetti, M. Domanin, L. Forzenigo (Fondazione IRCSS Ca' Granda, Ospedale Maggiore Policlinico, Milan, Italy), S. Ippolito, R. Scrofani (Ospedale Sacco, Milan, Italy), D. Catanzariti, M. Centonze (Ospedale S. Maria del

[5]By slightly rephrasing Blase Pascal's quotation, we can state that "*we were not good enough* to make it shorter."

Carmine, Rovereto (TN), Italy), for providing the radiological images; G. Aloe (Politecnico di Milano) for his help in preparing the figures; D. Bonomi, B. Guerciotti, R.M. Lancellotti, S. Pagani (Politecnico di Milano), D. Forti, F. Negri (EPFL, Lausanne, Switzerland), L. Barbarotta (Technische Universiteit Eindhoven), E. Faggiano (University of Pavia) for their help in preparing the plots of some numerical results; E. Faggiano for her fruitful suggestions. AQ acknowledges the project "Integrative HPC Framework for Coupled Cardiac Simulations" (IFCCS) within the PASC (Platform for Advanced Scientific Computing) network "Life Sciences Across Scales" and the Swiss National Supercomputing Centre (CSCS), project ID s635. CV has been partially supported by the Italian MIUR PRIN09 project no. 2009Y4RC3B 001.

References

[1] S. Abboud, O. Berenfeld, and D. Sadeh. Simulation of high-resolution QRS complex using a ventricular model with a fractal conduction system. effects of ischemia on high-frequency QRS potentials. *Circ Res*, 68(6):1751–1760, 1991.

[2] S.A. Ahmed and D.P. Giddens. Pulsatile poststenotic flow studies with laser Doppler anemometry. *J Biomech*, 17(9):695–705, 1984.

[3] I. Akkerman, Y. Bazilevs, V.M. Calo, T.J.R. Hughes, and S. Hulshoff. The role of continuity in residual-based variational multiscale modeling of turbulence. *Computational Mechanics*, 41:371–378, 2008.

[4] F. Alauzet, B. Fabréges, M.A. Fernández, and M. Landajuela. Nitsche-xfem for the coupling of an incompressible fluid with immersed thin-walled structures. *Comput. Methods Appl. Mech. Engrg.*, 301:300–335, 2016.

[5] R.R. Aliev and A.V. Panfilov. A simple two-variable model of cardiac excitation. *Chaos, Solitons & Fractals*, 7(3):293–301, 1996.

[6] A. Álvarez, F. Alonso-Atienza, J.L. Rojo-Álvarez, A. Garcia-Alberola, and M. Moscoso. Shape reconstruction of cardiac ischemia from non-contact intracardiac recordings: a model study. *Math. Computer Modeling*, 55:1770–1781, 2012.

[7] D. Ambrosi, G. Arioli, F. Nobile, and A. Quarteroni. Electromechanical coupling in cardiac dynamics: The active strain approach. *SIAM J. Appl. Math.*, 2(71):605–621, 2011.

[8] D. Ambrosi and S. Pezzuto. Active stress vs. active strain in mechanobiology: Constitutive issues. *Journal of Elasticity*, 2(107):199–212, 2012.

[9] B. Andreianov, M. Bendahmane, A. Quarteroni, and R. Ruiz-Baier. Solvability analysis and numerical approximation of linearized cardiac electromechanics. *Mathematical Models and Methods in Applied Sciences*, 25(5):959–993, 2015.

[10] L. Antiga, J. Peiró, and D.A. Steinman. From image data to computational domains. In *Cardiovascular mathematics, edited by L. Formaggia, A. Quarteroni, A. Veneziani, Chapter 4*, pages 123–175. Springer, 2009.

[11] L. Antiga, M. Piccinelli, L. Botti, B. Ene-Iordache, A. Remuzzi, and D.A. Steinman. An image-based modeling framework for patient-specific computational hemodynamics. *Med Biol Eng Comput*, 46:10971112, 2008.

[12] A. C. Antoulas. *Approximation of Large-Scale Dynamical Systems*. Society for Industrial and Applied Mathematics, Philadelphia, 2005.

[13] M. Astorino, F. Chouly, and M. Fernández. Robin based semi-implicit coupling in fluid-structure interaction: stability analysis and numerics. *SIAM J. Sci. Comput.*, 31(6):4041–4065, 2009.

[14] M. Astorino, J.F Gerbeau, O. Pantz, and K.F. Traoré. Fluid-structure interaction and multi-body contact. application to the aortic valves. *Comput. Methods Appl. Mech. Engrg.*, 116(4):721–767, 2010.

[15] M. Astorino and C. Grandmont. Convergence analysis of a projection semi-implicit coupling scheme for fluid-structure interaction problems. *Numer. Math.*, 45-46(198):3603–3612, 2009.

[16] M. Astorino, J. Hamers, C.S. Shadden, and J.F. Gerbeau. A robust and efficient valve model based on resistive immersed surfaces. *International Journal for Numerical Methods in Biomedical Engineering*, 28(9):937959, 2012.

[17] C.M. Augustin, G.A. Holzapfel, and O. Steinbach. Classical and all-floating feti methods for the simulation of arterial tissues. *International Journal for Numerical Methods in Engineering*, 99(4):290–312, 2014.

[18] F. Auricchio, A. Ferrara, and S. Morganti. Comparison and critical analysis of invariant-based models with respect to their ability in fitting human aortic valve data. *Annals of Solid and Structural Mechanics*, 4(1):1–14, 2012.

[19] F. Auricchio, F. Lefieux, A. Reali, and A. Veneziani. A locally anisotropic fluid-structure interaction remeshing strategy for thin structures with application to a hinged rigid leaflet. *International Journal for Numerical Methods in Engineering*, 107(2):155–180, 2016.

[20] A. P. Avolio. Multi-branched model of the human arterial system. *Medical and Biological Engineering and Computing*, 18:709–718, 1980.

[21] I. M. Babuška, F. Nobile, and R. Tempone. A stochastic collocation method for elliptic partial differential equations with random input data. *SIAM J. Numer. Anal.*, 45:1005–1034, 2007.

[22] I. M. Babuška, R. Tempone, and G. E. Zouraris. Galerkin finite element approximations of stochastic elliptic partial differential equations. *SIAM J. Numer. Anal.*, 42:800–825, 2004.

[23] S. Badia, F. Nobile, and C. Vergara. Fluid-structure partitioned procedures based on Robin transmission conditions. *J. Comput. Physics*, 227:7027–7051, 2008.

[24] S. Badia, F. Nobile, and C. Vergara. Robin-Robin preconditioned Krylov methods for fluid-structure interaction problems. *Comput. Methods Appl. Mech. Engrg.*, 198(33-36):2768–2784, 2009.

[25] S. Badia, A. Quaini, and A. Quarteroni. Modular vs. non-modular preconditioners for fluid-structure systems with large added-mass effect. *Comput. Methods Appl. Mech. Engrg.*, 197:4216–4232, 2008.

[26] S. Badia, A. Quaini, and A. Quarteroni. Splitting methods based on algebraic factorization for fluid-structure interaction. *SIAM J Sc Comp*, 30(4):1778–1805, 2008.

[27] E.Z. Bagci, Y. Vodovotz, T.R. Billiar, B. Ermentrout, and I. Bahar. Computational insights on the competing effects of nitric oxide in regulating apoptosis. *PLOS One*, 3(5):e2249, 2008.

[28] J. M. Ball. Constitutive inequalities and existence theorems in nonlinear elastostatics. In R.J. Knowps, editor, *Nonlinear Analysis and Mechanics*, 1997.

[29] J.M. Ball. Convexity conditions and existence theorems in nonlinear elasticity. *Archive for Rational Mechanics and Analysis*, 63(4):337–403, 1976.

[30] F. Ballarin, E. Faggiano, S. Ippolito, A. Manzoni, A. Quarteroni, G. Rozza, and R. Scrofani. Fast simulations of patient-specific haemodynamics of coronary artery bypass grafts based on a pod?galerkin method and a vascular shape parametrization. *J. Comput. Phys.*, 315:609–628, 2016.

[31] D. Balzani, D. Brands, A. Klawonn, O. Rheinbach, and J. Schroder. On the mechanical modeling of anisotropic biological soft tissue and iterative parallel solution strategies. *Archive of Applied Mechanics*, 80(5):479–488, 2010.

[32] D. Balzani, P. Neff, J. Schroder, and G.A. Holzapfel. A polyconvex framewok for soft biological tissues. adjustment to experimental data. *International Journal of Solids and Structures*, 43:6052–6070, 2006.

[33] H.T. Banks and K. Kunisch. *Estimation Techniques for Distributed Parameter Systems*. Systems & Control: Foundations & Applications. Birkhäuser Basel, 1989.

[34] J.W. Banks, W.D. Henshaw, and D.W. Schwendeman. An analysis of a new stable partitioned algorithm for fsi problems. part i: Incompressible flow and elastic solids. *J. Comput. Physics*, 269:108–137, 2014.

[35] L. Barbarotta. *A Mathematical and Numerical Study of the Left Ventricular Contraction based on the Reconstruction of a Patient Specific Geometry*. PhD thesis, MSc thesis, Mathematical Engineering, Politecnico di Milano, 2014.

[36] A. Barker and X.C. Cai. Scalable parallel methods for monolithic coupling in fluid-structure interaction with application to blood flow modeling. *J. Comput. Phys.*, 229:642–659, 2010.

[37] A. Barker and X.C. Cai. Two-level newton and hybrid schwarz preconditioners for fluid-structure interaction. *SIAM J. Sc. Comp.*, 32(4):23952417, 2010.

[38] A.C.L. Barnard, W.A. Hunt, W.P. Timlake, and E. Varley. A theory of fluid flow in compliant tubes. *Biophysical journal*, 6(6):717–724, 1966.

[39] J.D. Bayer, R.C. Blake, G. Plank, and N.A. Trayanova. A novel rule-based algorithm for assigning myocardial fiber orientation to computational heart models. *Annals of Biomedical Engineering*, 40(10):54, 2012.

[40] Y. Bazilevs, V.M Calo, Y. Zhang, and T.J.R Hughes. Isogeometric fluid-structure interaction analysis with applications to arterial blood flow. *Computational Mechanics*, 38(4–5):310–322, 2006.

[41] Y. Bazilevs, J.R. Gohean, T.J.R. Hughes, R.D. Moser, and Y. Zhang. Patient-specific isogeometric fluid–structure interaction analysis of thoracic aortic blood flow due to implantation of the jarvik 2000 left ventricular assist device. *Computer Methods in Applied Mechanics and Engineering*, 198(45):3534–3550, 2009.

[42] Y. Bazilevs, K. Takizawa, and T.E. Tezduyar. *Computational fluid-structure interaction: methods and applications*. John Wiley & Sons, 2012.

[43] G.W. Beeler and H. Reuter. Reconstruction of the action potential of ventricular myocardial fibres. *J Physiol*, 268(1):177–210, 1977.

[44] H. Beirao da Veiga. On the existence of strong solutions to a coupled fluid-structure evolution problem. *Journal of Mathematical Fluid Mechanics*, 6(1):21–52, 2004.

[45] P. Benner, S. Gugercin, and K. Willcox. A survey of model reduction methods for parametric dynamical systems. *SIAM Review*, 57(4):483–531, 2015.

[46] J.L. Bentley and J.H. Friedman. Data structures for range searching. *ACM Computing Surveys*, 11(4):397–409, 1979.

[47] M. Benzi, G.H. Golub, and J. Liesen. Numerical solution of saddle point problems. *Acta Numerica*, 14:1–137, 2005.

[48] M. Benzi, H. G.H. Golub, and J. Liesen. Numerical solution of saddle point problems. *Acta Numerica*, pages 1–137, 2005.

[49] L. Bertagna, M. D'Elia, M. Perego, and A. Veneziani. Data assimilation in cardiovascular fluid–structure interaction problems: An introduction. In T. Bodnár, P. G. Galdi, and Š. Nečasová, editors, *Fluid-Structure Interaction and Biomedical Applications*, pages 395–481. Springer Basel, Basel, 2014.

[50] L. Bertagna and A. Veneziani. A model reduction approach for the variational estimation of vascular compliance by solving an inverse fluid–structure interaction problem. *Inverse Problems*, 30(5), 2014.

[51] C. Bertoglio, P. Moireau, and J.F. Gerbeau. Sequential parameter estimation for fluid-structure problems: Application to hemodynamics. *Int. J. Numer. Meth. Biomed. Engng.*, 28(4):434–455, 2012.

[52] F. Bertrand, P.A. Tanguy, and F. Thibault. A three-dimensional fictitious domain method for incompressible fluid flow problems. *International Journal for Numerical Methods in Fluids*, 25(6):719–736, 1997.

[53] R.L.T. Bevan, P. Nithiarasu, R. Van Loon, I. Sazonov, H. Luckraz, and A. Garnham. Application of a locally conservative galerkin (lcg) method for modelling blood flow through a patient-specific carotid bifurcation. *International Journal for Numerical Methods in Fluids*, 64:1274–1295, 2010.

[54] J. Biehler, M.W. Gee, and W.A. Wall. Towards efficient uncertainty quantification in complex and large-scale biomechanical problems based on a Bayesian multi-fidelity scheme. *Biomech. Model. Mechanobiol.*, 14(3):489–513, 2015.

[55] P.J. Blanco, S. Deparis, and A.C.I. Malossi. On the continuity of mean total normal stress in geometrical multiscale cardiovascular problems. *J Comp Phys*, 51:136–155, 2013.

[56] P.J. Blanco and R.A. Feijóo. A dimensionally-heterogeneous closed-loop model for the cardiovascular system and its applications. *Medical Engineering & Physics*, 35(5):652–667, 2013.

[57] P.J. Blanco, R.A. Feijòo, and S.A. Urquiza. A unified variational approach for coupling 3d-1d models and its blood flow applications. *Comput. Methods Appl. Mech. Engrg.*, 196:4391–4410, 2007.

[58] P.J. Blanco, M.R. Pivello, S.A. Urquiza, and R.A. Feijòo. On the potentialities of 3d-1d coupled models in hemodynamics simulations. *J. Biomech.*, 42:919–930, 2009.

[59] P.J. Blanco, S.M. Watanabe, and R.A. Feijóo. Identification of vascular territory resistances in one-dimensional hemodynamics simulations. *J. Biomech.*, 45(12):2066–2073, 2012.

[60] P.J. Blanco, S.M. Watanabe, M.A.R.F. Passos, Lemos P., Feijoo R.A., et al. An anatomically detailed arterial network model for one-dimensional computational hemodynamics. *Biomedical Engineering, IEEE Transactions on*, 62(2):736–753, 2015.

[61] J. Blum, F.-X. Le Dimet, and I.M. Navon. Data assimilation for geophysical fluids. In P.G. Ciarlet, editor, *Handbook of Numerical Analysis*, volume 14 of *Handbook of Numerical Analysis*, pages 385–441. Elsevier, 2009.

[62] T. Bodnár, G.P. Galdi, and Š. Nečasová. *Fluid-Structure Interaction and Biomedical Applications*. Springer, 2014.

[63] J.M. Boese, M. Bock, S.O. Schoenberg, and L.R. Schad. Estimation of aortic compliance using magnetic resonance pulse wave velocity measurement. *Physics in Medicine and Biology*, 45(6):1703–1713, 2000.

[64] D. Boffi, F. Brezzi, and M. Fortin. *Mixed Finite Element Methods and Applications*. Springer, 2013.

[65] D. Boffi and L. Gastaldi. A finite element approach for the immersed boundary method. *Comp. and Struct*, 81(8-11):491–501, 2003.

[66] D. Boffi, L. Gastaldi, and L. Heltai. Numerical stability of the finite element immersed boundary method. *Mathematical Models and Methods in Applied Sciences*, 17(10):1479–1505, 2007.

[67] D. Boffi, L. Gastaldi, L. Heltai, and C. Peskin. On the hyper-elastic formulation of the immersed boundary method. *Computer Methods in Applied Mechanics and Engineering*, 197(25–28):2210–2231, 2008.

[68] E. Boileau, P. Nithiarasu, P.J. Blanco, L.O. Muller, F.E. Fossan, L.R. Hellevik, W.P. Donders, W. Huberts, M. Willemet, and J. Alastruey. A benchmark study of numerical schemes for one-dimensional arterial blood flow modelling. *International journal for numerical methods in biomedical engineering*, DOI: 10.1002/cnm.2732, 2015.

[69] C. Boldak, Y. Rolland, and C. Toumoulin. An improved model-based vessel tracking algorithm with application to computed tomography angiography. *Biocybern. Biomed.*, 23:41–63, 2003.

[70] D. Bonomi, C. Vergara, E. Faggiano, M. Stevanella, C. Conti, A. Redaelli, G. Puppini, G. Faggian, L. Formaggia, and G.B. Luciani. Influence of the aortic valve leaflets on the fluid-dynamics in aorta in presence of a normally functioning bicuspid valve. *Biomechanics and Modeling in Mechanobiology*, 6(14):1349–1361, 2015.

[71] I. Borazjani, L. Ge, and F. Sotiropoulos. Curvilinear immersed boundary method for simulating fluid structure interaction with complex 3d rigid bodies. *Journal of Computational Physics*, 227(16):7587–7620, 2008.

[72] R.M. Bordas, K. Gillow, D. Gavaghan, B. Rodríguez, and D. Kay. A Bidomain model of the ventricular specialized conduction system of the heart. *SIAM J. Appl. Math.*, 72(5):1618–1643, 2012.

[73] A. Borzì and V. Schulz. *Computational optimization of systems governed by partial differential equations*. Society for Industrial and Applied Mathematics, Philadephia, PA, 2011.

[74] M. Boulakia, M. A. Fernandez, J. F. Gerbeau, and N. Zemzemi. Direct and inverse problems in electrocardiography. *AIP Conference Proceedings*, 1048(1):113–117, 2008.

[75] M. Boulakia, E. Schenone, and J-F. Gerbeau. Reduced-order modeling for cardiac electrophysiology. application to parameter identification. *Int. J. Numer. Meth. Biomed. Engng.*, 28(6–7):727–744, 2012.

[76] Y. Bourgault, Y. Coudière, and C. Pierre. Existence and uniqueness of the solution for the bidomain model used in cardiac electrophysiology. *Nonlinear Analysis: Real World Applications*, 10(1):458–482, 2006.

[77] Y. Bourgault, M. Ethier, and V.G. LeBlanc. Simulation of electrophysiological waves with an unstructured finite element method. *ESAIM: Math. Modelling Numer. Anal.*, 37(4):649–661, 2003.

[78] A. Bueno-Orovio, E.M. Cherry, and F.H. Fenton. Minimal model for human ventricular action potentials in tissue. *J Theor Biol*, 3(253):544–560, 2008.

[79] E. Burman, S. Claus, P. Hansbo, M.G. Larson, and A. Massing. Cutfem: Discretizing geometry and partial differential equations. *International Journal of Numerical Methods for Engineering*, 104(7):472501, 2015.

[80] E. Burman and M.A. Fernández. Stabilization of explicit coupling in fluidstructure interaction involving fluid incompressibility. *Comput. Methods Appl. Mech. Engrg.*, 198:766–784, 2009.

[81] E. Burman and M.A. Fernández. An unfitted nitsche method for incompressible fluidstructure interaction using overlapping meshes. *Comput. Methods Appl. Mech. Engrg.*, 279:497–514, 2014.

[82] I.C. Campbell, J. Ries, S.S. Dhawan, A.A. Quyyumi, W.R. Taylor, and J.N. Oshinski. Effect of inlet velocity profiles on patient-specific computational fluid dynamics simulations of the carotid bifurcation. *J Biomech Eng*, 134(5):051001, 2012.

[83] T.E. Carew, R.N. Vaishnav, and D.J. Patel. Compressibility of the arterial wall. *Circ Res*, 23:61–68, 1968.

[84] J.C. Carr, W. Fright, and R.K. Beatson. Surface interpolation with radial basis functions for medical imaging. *IEEE Transactions on Medical Imaging*, 16(1):96–107, 1997.

[85] P. Causin, J.F. Gerbeau, and F. Nobile. Added-mass effect in the design of partitioned algorithms for fluid-structure problems. *Comput. Methods Appl. Mech. Engrg.*, 194(42-44):4506–4527, 2005.

[86] I.B. Celik, U. Ghia, P.J. Roache, C.J. Freitas, and H. Coleman P.E. Raad. Procedure for estimation and reporting of uncertainty due to discretization in cfd applications. *J Fluids Eng Trans ASME*, 130(7):078001, 2008.

[87] R. Chabiniok, Moireau P., Lesault P.-F., A. Rahmouni, J.-F. Deux, and D. Chapelle. Estimation of tissue contractility from cardiac cine-mri using a biomechanical heart model. *Biomech. Model. Mechanobiol.*, 11:609–630, 2012.

[88] R. Chabiniok, V.Y. Wang, M. Hadjicharalambous, L. Asner, J. Lee, M. Sermesant, E. Kuhl, A.A. Young, P. Moireau, M.P. Nash, D. Chapelle, and D. A. Nordsletten. Multiphysics and multiscale modelling, datamodel fusion and integration of organ physiology in the clinic: ventricular cardiac mechanics. *Interface Focus*, 6(2):20150083, 2016.

[89] D. Chapelle, M. Fragu, V. Mallet, and P. Moireau. Fundamental principles of data assimilation underlying the Verdandi library: applications to biophysical model personalization within euheart. *Med. Biol. Eng. Comput.*, 51(11):1221–1233, 2013.

[90] D. Chapelle, A. Gariah, P. Moireau, and J. Sainte-Marie. A galerkin strategy with proper orthogonal decomposition for parameter-dependent problems: Analysis, assessments and applications to parameter estimation. *ESAIM: Math. Modelling Numer. Anal.*, 47(6):1821–1843, 2013.

[91] J.J. Charonko, R. Kumar, K. Stewart, W.C. Little, and P.P. Vlachos. Vortices formed on the mitral valve tips aid normal left ventricular filling. *Annals of Biomedical Engineering*, 41(5):10491061, 2013.

[92] G. Chavent. *Nonlinear Least Squares for Inverse Problems. Theoretical Foundations and Step-by-Step Guide for Applications*. Scientific Computation. Springer Netherlands, 2010.

[93] J Chen, X-Y Lu, and W Wang. Non-newtonian effects of blood flow on hemodynamics in distal vascular graft anastomoses. *J. Biomech.*, 39:1983–1995, 2006.

[94] P. Chen, A. Quarteroni, and G. Rozza. Simulation-based uncertainty quantification of human arterial network hemodynamics. *Int. J. Numer. Methods Biomed. Engng.*, 29(6):698–721, 2013.

[95] P. Chen and C. Schwab. Sparse-grid, reduced-basis Bayesian inversion. *Comput. Methods Appl. Mech. Engrg.*, 297:84–115, 2015.

[96] L.K. Cheng, J.M. Bodley, and A. Pullan. Comparison of potential- and activation-based formulations for the inverse problem of electrocardiology. *IEEE Trans. Biomed. Eng.*, 50(1):11–22, 2003.

[97] Y. Cheng, H. Oertel, and T. Schenkel. Fluid-structure coupled cfd simulation of the left ventricular flow during filling phase. *Annals of Biomedical Engineering*, 5(33):567–576, 2005.

[98] C. Cherubini, S. Filippi, P. Nardinocchi, and L. Teresi. An electromechanical model of cardiac tissue: Constitutive issues and electrophysiological effects. *Progress in Biophysics and Molecular Biology*, 2–3(97):562–573, 2008.

[99] S.C.P. Cheung, Kelvin K. L. Wong, Guan Heng Yeoh, William Yang, Jiyuan Tu, Richard Beare, and Thanh Phan. Experimental and numerical study on the hemodynamics of stenosed carotid bifurcation. *Australasian Physical & Engineering Sciences in Medicine*, 33(4):319–328, 2010.

[100] P. Chinchapatnam, K.S. Rhode, M. Ginks, C.A. Rinaldi, P. Lambiase, R. Razavi, S. Arridge, and M. Sermesant. Model-based imaging of cardiac apparent conductivity and local conduction velocity for diagnosis and planning of therapy. *IEEE Trans. Med. Imaging*, 27(11):1631–1642, 2008.

[101] J. Ching, J.L. Beck, and K.A. Porter. Bayesian state and parameter estimation of uncertain dynamical systems. *Probabilist. Eng. Mech.*, 21(1):81–96, 2006.

[102] C. Chnafa, S. Mendez, and F. Nicoud. Image-based large-eddy simulation in a realistic left heart. *Computers & Fluids*, 94:173–187, 2014.

[103] Y.J. Choi, J. Constantino, V. Vedula, N. Trayanova, and R. Mittal. A new mri-based model of heart function with coupled hemodynamics and application to normal and diseased canine left ventricles. *Front Bioeng Biotechnol*, 3:140, 2015.

[104] A.J. Chorin. Numerical solution of the Navier–Stokes equations. *Mathematics of Computation*, 22:745–762, 1968.

[105] J. Chung and G. M. Hulbert. A time integration algorithm for structural dynamics with improved numerical dissipation: the generalized-α method. *Trans. ASME J. Appl. Mech.*, 60(2):371–375, 1993.

[106] P.G. Ciarlet. *Mathematical Elasticity, Volume 1: Three Dimensional Elasticity.* Elsevier Science Publishers, North-Holland, 1988.

[107] P.G. Ciarlet and J. Necas. Unilateral problems in nonlinear, three-dimensional elasticity. *Archive for Rational Mechanics and Analysis*, 87(4):319–338, 1985.

[108] R.H. Clayton, O. Bernus, E.M. Cherry, H. Dierckx, F.H. Fenton, L. Mirabella, A.V. Panfilov, F.B. Sachse, G. Seemann, and H. Zhang. Models of cardiac tissue electrophysiology: Progress, challenges and open questions. *Progress in Biophysics and Molecular Biology*, 104:22–48, 2011.

[109] R.H. Clayton and A.V. Panfilov. A guide to modelling cardiac electrical activity in anatomically detailed ventricles. *Progress in Biophysics and Molecular Biology*, 96(1-3):19–43, 2008.

[110] C.A. Cocosco, T. Netsch, J. Sénǵas, D. Bystrov, W.J. Niessen, and M.A. Viergever. Automatic cardiac region-of-interest computation in cine 3d structural mri. *Computer Assisted Radiology and Surgery. Proceedings of the 18th International Congress and Exhibition*, 1268:1126–1131, 2004.

[111] R. Codina and S. Badia. On some pressure segregation methods of fractional-step type for the finite element approximation of incompressible flow problems. *Comput. Methods Appl. Mech. Engrg.*, 195:2900–2918, 2006.

[112] A. Cohen and R. DeVore. Approximation of high-dimensional parametric pdes. *Acta Numerica*, 24:1–159, 2015.

[113] C.M. Colciago, S. Deparis, and A. Quarteroni. Comparisons between reduced order models and full 3d models for fluid-structure interaction problems in haemodynamics. *J. Comput. Appl. Math.*, 2754:120–138, 2014.

[114] P. Colli Franzone and L. Guerri. Spreading excitation in 3-d models of the anisotropic cardiac tissue, I. validation of the Eikonal model. *Math Biosci*, 113:145–209, 1993.

[115] P. Colli Franzone, L. Guerri, and S. Rovida. Wavefront propagation in an activation model of the anisotropic cardiac tissue: asymptotic analysis and numerical simulations. *Journal of Mathematical Biology*, 28(2):121–176, 1990.

[116] P. Colli Franzone, L. Guerri, C. Viganotti, and B. Taccardi. Finite element approximation of regularized solution of the inverse potential problem of electrocardiography and applications to experimental data. *Calcolo*, 12(1):91–186, 1985.

[117] P. Colli Franzone and L.F. Pavarino. A parallel solver for reaction-diffusion systems in computational electrocardiology. *Mathematical Models and Methods in Applied Sciences*, 14(6):883–911, 2004.

[118] P. Colli Franzone, L.F. Pavarino, and S. Scacchi. *Mathematical Cardiac Electrophysiology*. Springer, 2014.

[119] P. Colli Franzone, L.F. Pavarino, and S. Scacchi. Bioelectrical effects of mechanical feedbacks in a strongly coupled cardiac electro-mechanical model. *Mathematical Models and Methods in Applied Sciences*, 26(1):27–57, 2016.

[120] P. Colli Franzone, L.F. Pavarino, and B. Taccardi. Simulating patterns of excitation, repolarization and action potential duration with cardiac bidomain and monodomain models. *Math. Biosci.*, 197(1):35–66, 2005.

[121] P. Colli Franzone and G. Savaré. Degenerate evolution systems modeling the cardiac electric field at micro- and macroscopic level. In A. Lorenzi and B. Ruf, editors, *Evolution Equations, Semigroups and Functional Analysis: In Memory of Brunello Terreni*, pages 49–78. Birkhäuser Basel, 2002.

[122] P. Colli Franzone, B. Taccardi, and C. Viganotti. An approach to inverse calculation of epicardial potentials from body surface maps. *Adv. Cardiol.*, 21:50–54, 1978.

[123] C. Corrado, J.-F. Gerbeau, and P. Moireau. Identification of weakly coupled multiphysics problems. application to the inverse problem of electrocardiography. *J. Comput. Phys.*, 283:271 – 298, 2015.

[124] K.D. Costa, J.W. Holmes, and A.D. Mcculloch. Modelling cardiac mechanical properties in three dimensions. *American Journal of PhysiologyPHILOSOPHICAL TRANSACTIONS of the Royal society A*, 359(6):1233–1250, 2001.

[125] P. Crosetto, S. Deparis, G. Fourestey, and A. Quarteroni. Parallel algorithms for fluid-structure interaction problems in haemodynamics. *SIAM J. Sci. Comput.*, 33:1598–1622, 2011.

[126] T. Cui, Y. Marzouk, and K. Willcox. Data-driven model reduction for the Bayesian solution of inverse problems. *Int. J. Numer. Methods Engng*, 102(5):966–990, 2015.

[127] B. Dacorogna. *Direct Methods in the Calculus of Variations - Applied Mathematical Science (vol 78)*. Springer, New York, 2000.

[128] C. D'Angelo. *Multiscale modelling of metabolism and transport phenomena in living tissues*. PhD thesis, Ecole Polytechnique Fédérale de Lausanne, 2007.

[129] J De Hart, FPT Baaijens, GWM Peters, and PJG Schreurs. A computational fluid-structure interaction analysis of a fiber-reinforced stentless aortic valve. *Journal of biomechanics*, 36(5):699–712, 2003.

[130] J. Degroote. On the similarity between dirichletneumann with interface artificial compressibility and robinneumann schemes for the solution of fluid-structure interaction problems. *J. Comput. Physics*, 230:6399640363996403, 2011.

[131] J. Degroote, A. Swillens, P. Bruggeman, Haelterman, P. Segers, and J. Vierendeels. Simulation of fluidstructure interaction with the interface artificial compressibility method. *International Journal for Numerical Methods in Biomedical Engineering*, 26(3-4):276–289, 2010.

[132] J. Degroote and J. Vierendeels. Multi-solver algorithms for the partitioned simulation of fluidstructure interaction. *Comput. Methods Appl. Mech. Engrg.*, 25–28(200):21952210, 2011.

[133] M. D'Elia, M. Perego, and A. Veneziani. A variational data assimilation procedure for the incompressible navier-stokes equations in hemodynamics. *J. Sc. Comp.*, 52(2):340–359, 2012.

[134] M. D'Elia and A. Veneziani. Uncertainty quantification for data assimilation in a steady incompressible navier-stokes problem. *ESAIM: Math. Modelling Numer. Anal.*., 47(04):1037–1057, 2013.

[135] H. Delingette, F. Billet, K.C. Wong, M. Sermesant, K. Rhode, M. Ginks, C.A Rinaldi, R. Razavi, and N. Ayache. Personalization of cardiac motion and contractility from images using variational data assimilation. *IEEE Trans. Biomed. Engng.*, 59(1):20–24, 2012.

[136] S. Deparis. *Numerical analysis of axisymmetric flows and methods for fluid-structure interaction arising in blood flow simulation.* PhD thesis, École Polytechnique Fédérale de Lausanne, 2004.

[137] S. Deparis, M. Discacciati, G. Fourestey, and A. Quarteroni. Fluid-structure algorithms based on Steklov-Poincaré operators. *Comput. Methods Appl. Mech. Engrg.*, 195(41-43):5797–5812, 2006.

[138] S. Deparis, D. Forti, G. Grandperrin, and A. Quarteroni. Facsi: A block parallel preconditioner for fluid-structure interaction in hemodynamics. *J. Comput. Physics*, (327):700–718, 2016.

[139] S. Deparis, G. Grandperrin, and A. Quarteroni. Parallel preconditioners for the unsteady Navier–Stokes equations and applications to hemodynamics simulations. *Computer & Fluids*, 92:253–273, 2014.

[140] D. Di Francesco and D. Noble. A model of cardiac electrical activity incorporating ionic pumps and concentration changes. *Phil. Trans. R. Soc. B*, 307(1133):353–398, 1985.

[141] J. Dick, F. Kuo, and I. Sloan. High-dimensional integration: the quasi-Monte Carlo way. *Acta Numerica*, 22:133–288, 2013.

[142] M. Dihlmann and B. Haasdonk. A reduced basis Kalman filter for parametrized partial differential equations. *SAIM: Control Optim. Calc. Var.*, 22(3):625–669, 2016.

[143] F.-X. Dimet and O. Talagrand. Variational algorithms for analysis and assimilation of meteorological observations: theoretical aspects. *Tellus A*, 38A(2):97–110, 1986.

[144] H. Do, A. A. Owida, W. Yang, and Y.S. Morsi. Numerical simulation of the haemodynamics in end-to-side anastomoses. *Int. J. Numer. Meth. Fluids*, 67(5):638–650, 2011.

[145] C.R. Dohrmann and O.B. Widlund. An overlapping schwarz algorithm for almost incompressible elasticity. *SIAM J. Num. Anal.*, 4(47):8811–8823, 2009.

[146] S. Dokos, B.H. Smaill, A.A. Young, and I.J. LeGrice. Shear properties of passive ventricular myocardium. *American Journal of Physiology*, 283(6):H2650–H2659, 2002.

[147] W. P. Donders, W. Huberts, F. N. van de Vosse, and T. Delhaas. Personalization of models with many model parameters: an efficient sensitivity analysis approach. *Int. J. Numer. Methods Biomed. Engng.*, 31(10):e02727, 2015.

[148] J. Donea. An arbitrary Lagrangian-Eulerian finite element method for transient dynamic fluid-structure interaction. *Comput. Methods Appl. Mech. Engrg.*, 33:689–723, 1982.

[149] O. Dur, S.T. Coskun, K.O. Coskun, D. Frakes, L.B. Kara, and K. Pekkan. Computer-aided patient-specific coronary artery graft design improvements using CFD coupled shape optimizer. *Cardiovasc. Engr. Tech.*, pages 1–13, 2011.

[150] D. Durrer, R.R. van Dam, G.E. Freud, M.J. Janse, F.L. Meijler, and R.C. Arzbaecher. Total excitation of the isolated human heart. *Circulation*, 41(6):899–912, 1970.

[151] V.G. Eck, W.P. Donders, J. Sturdy, J. Feinberg, T. Delhaas, L.R. Hellevik, and W. Huberts. A guide to uncertainty quantification and sensitivity analysis for cardiovascular applications. *Int. J. Numer. Methods Biomed. Engng.*, page in press, 2015.

[152] D.R. Einstein, K.S. Kunzelman, P.G. Reinhall, M.A. Nicosia, and R.P. Cochran. The effects of cellular contraction on aortic valve leaflet flexural stiffness. *J Heart Valve Disease*, 14:376–385, 2005.

[153] C. Eitel, G. Hindricks, N. Dagres, P. Sommer, and C. Piorkowski. Ensite velocity^{TM} cardiac mapping system: a new platform for 3d mapping of cardiac arrhythmias. *Expert Rev Med Devices*, 7(2):185–192, 2010.

[154] H. Elman, D. Silvester, and A. Wathen. *Finite Elements and Fast Iterative Solvers*. Oxford Science Publications, 2005.

[155] H.C. Elman and D.J. Silvester. Fast nonsymmetric iterations and preconditioning for navierstokes equations. *SIAM J. Sci. Comp.*, 17(1):33–46, 1996.

[156] G. Enden and A. Popel. A numerical study of the shape of the surface separating flow into branches in microvascular bifurcations. *J Biomech Eng*, 114:398405., 1992.

[157] T.S.E. Eriksson, A.J. Prassl, G. Plank, and G.A. Holzapfel. Modeling the dispersion in electromechanically coupled myocardium. *International Journal for Numerical Methods in Biomedical Engineering*, 29(11):1267–1284, 2013.

[158] O.G. Ernst, B. Sprungk, and H.-J. Starkloff. Bayesian inverse problems and Kalman filters. In *Extraction of Quantifiable Information from Complex Systems*, volume 102 of *Lecture Notes in Computational Science and Engineering*, pages 133–159. Springer International Publishing, 2014.

[159] V.J. Ervin and H. Lee. Numerical approximation of a quasi-newtonian stokes flow problem with defective boundary conditions. *SIAM J. Numer. Anal.*, 45(5):21202140, 2007.

[160] C.R. Ethier, D.A. Steinman, X. Zhang, S.R. Karpik, and M. Ojha. Flow waveform effects on end-to-side anastomotic flow patterns. *J. Biomech.*, 31(7):609–617, 1998.

[161] M. Ethier and Y. Bourgault. Semi-implicit time-discretization schemes for the bidomain model. *SIAM J. Numer. Anal.*, 5(46):2443–2468, 2008.

[162] L. Euler. Principia pro motu sanguinis per arterias determinando. *Opera posthuma mathematica et physica anno 1844 detecta. Ediderunt P.H. Fuss et N. Fuss Petropoli; Apund Eggers et Socios.*, 1:814–823, 1775.

[163] G. Evensen. Sequential data assimilation with a nonlinear quasi-geostrophic model using Monte Carlo methods to forecast error statistics. *J. Geophys. Res.*, 9:10143–10162, 1994.

[164] G. Evensen. The Ensemble Kalman Filter: theoretical formulation and practical implementation. *Ocean Dynamics*, 53:343–367, 2003.

[165] G. Evensen. The ensemble Kalman filter for combined state and parameter estimation. *IEEE Control Syst. Mag.*, 29(3):83–104, 2009.

[166] E. Faggiano, A. Antiga, G. Puppini, A. Quarteroni, G.B. Luciani, and C Vergara. Helical flows and asymmetry of blood jet in dilated ascending aorta with normally functioning bicuspid valve. *Biomechanics and Modeling in Mechanobiology*, 4(12):801–813, 2013.

[167] E. Faggiano, T. Lorenzi, and A. Quarteroni. Metal artefact reduction in computed tomography images by a fourth-order total variation flow. *Computer Methods in Biomechanics and Biomedical Engineering: Imaging & Visualization*, 3-4(4):202–213, 2014.

[168] C. Farhat and F.X. Roux. A method of finite element tearing and interconnecting and its parallel solution algorithm. *International Journal for Numerical Methods in Engineering*, 32(6):1205–1227, 1991.

[169] A. Fasano, R.F. Santos, and A. Sequeira. Blood coagulation: A puzzle for biologists, a maze for mathematicians. In *Modeling of Physiological Flows, edited by D. Ambrosi, A. Quarteroni, G. Rozza, Chapter 3*, pages 41–75. Springer, 2012.

[170] M. Fedele, E. Faggiano, L. Barbarotta, F. Cremonesi, L. Formaggia, and S. Perotto. Semi-automatic three-dimensional vessel segmentation using a connected component localization of the region-scalable fitting energy. In *2015 9th International Symposium on Image and Signal Processing and Analysis (ISPA)*, pages 72–77. IEEE, 2015.

[171] M. Fedele, E. Faggiano, L Dedè, and A. Quarteroni. A patient-specific aortic valve model based on moving resistive immersed implicit surfaces. MOX-Report n. 23-2016, Department of Mathematics, Politecnico di Milano, Italy, 2016.

[172] F. Fenton and A. Karma. Vortex dynamics in three-dimensional continuous myocardium with fiber rotation: Filament instability and fibrillation. *Chaos*, 8(1), 1998.

[173] M.A. Fernández. Incremental displacement-correction schemes for incompressible fluid-structure interaction - stability and convergence analysis. *Numerische Mathematik*, 123(1):21–65, 2013.

[174] M.A. Fernández, J.F. Gerbeau, and C. Grandmont. A projection semi-implicit scheme for the coupling of an elastic structure with an incompressible fluid. *Int. J. Num. Methods Engrg.*, 69(4):794–821, 2007.

[175] M.A. Fernàndez, V. Milisic, and A. Quarteroni. Analysis of a geometrical multiscale blood flow model based on the coupling of odes and hyperbolic pdes. *Multiscale Model Simul*, 4(1):215–236, 2005.

[176] M.A. Fernández and M. Moubachir. A Newton method using exact Jacobians for solving fluid-structure coupling. *Computers & Structures*, 83(2-3):127–142, 2005.

[177] M.A. Fernandez and N. Zemzemi. Decoupled time-marching schemes in computational cardiac electrophysiology and ecg numerical simulation. *Mathematical Biosciences*, 226(1):58–75, 2010.

[178] C.A. Figueroa, I.E. Vignon-Clementel, K.E. Jansen, T.J.R Hughes, and C.A. Taylor. A coupled momentum method for modeling blood flow in three-dimensional deformable arteries. *Computer Methods in Applied Mechanics and Engineering*, 195(41–43):5685–5706, 2006.

[179] L. Fin and R. Grebe. Three dimensional modeling of the cerebrospinal fluid dynamics and brain interactions in the aqueduct of sylvius. *Computer Methods in Biomechanics and Biomedical Engineering*, 3(6):163–170, 2003.

[180] P.F. Fischer, F. Loth, S.E. Lee, S.W. Lee, D.S. Smith, and H.S. Bassiouny. Simulation of high-Reynolds number vascular flows. *Comput. Methods Appl. Mech. Engrg.*, 196:3049–3060, 2007.

[181] G. Fishman. *Monte Carlo. Concepts, Algorithms, and Applications*. Springer Series in Operations Research and Financial Engineering. Springer-Verlag New York, 1996.

[182] R. FitzHugh. Impulses and physiological states in theoretical models of nerve membrane. *Biophys J*, 1(6):445–466, 1961.

[183] L. Formaggia, J.F. Gerbeau, F. Nobile, and A. Quarteroni. On the coupling of 3D an 1D Navier-Stokes equations for flow problems in compliant vessels. *Comput. Methods Appl. Mech. Engrg.*, 191(6-7):561–582, 2001.

[184] L. Formaggia, J.F. Gerbeau, F. Nobile, and A. Quarteroni. Numerical treatment of defective boundary conditions for the Navier-Stokes equation. *SIAM J. Numer. Anal.*, 40(1):376–401, 2002.

[185] L. Formaggia, D. Lamponi, and A. Quarteroni. One-dimensional models for blood flow in arteries. *Journal of Engineering Mathematics*, 47(3-4):251–276, 2003.

[186] L. Formaggia, A. Moura, and F. Nobile. On the stability of the coupling of 3d and 1d fluid-structure interaction models for blood flow simulations. *M2AN Math. Model. Numer. Anal.*, 41(4):743–769, 2007.

[187] L. Formaggia, F. Nobile, A. Quarteroni, and A. Veneziani. Multiscale modelling of the circulatory system: a preliminary analysis. *Comput and Visual in Science*, 2:75–83, 1999.

[188] L. Formaggia, A. Quarteroni, and A. Veneziani (Eds.). *Cardiovascular Mathematics - Modeling and simulation of the circulatory system.* Springer-Verlag Milan, 2009.

[189] L. Formaggia, A. Quarteroni, and C. Vergara. On the physical consistency between three-dimensional and one-dimensional models in haemodynamics. *J. Comput. Physics*, 244:97–112, 2013.

[190] L. Formaggia, A. Veneziani, and C. Vergara. A new approach to numerical solution of defective boundary value problems in incompressible fluid dynamics. *SIAM J. Numer. Anal.*, 46(6):2769–2794, 2008.

[191] L. Formaggia, A. Veneziani, and C. Vergara. Flow rate boundary problems for an incompressible fluid in deformable domains: formulations and solution methods. *Comput. Methods Appl. Mech. Engrg.*, 199 (9-12):677–688, 2009.

[192] L. Formaggia and C. Vergara. Prescription of general defective boundary conditions in fluid-dynamics. *Milan Journal of Mathematics*, 80(2):333–350, 2012.

[193] M. Fornefett, K. Rohr, and H.S. Stiehl. Radial basis functions with compact support for elastic registration of medical images. *Image and Vision Computing*, 19(1–2):87–96, 2001.

[194] C. Forster, W. Wall, and E. Ramm. Artificial added mass instabilities in sequential staggered coupling of nonlinear structures and incompressible viscous flow. *Comput. Methods Appl. Mech. Engrg.*, 196(7):1278–1293, 2007.

[195] D. Forti and L. Dedé. Semi-implicit bdf time discretization of the navier-stokes equations with vms-les modeling in a high performance computing framework. *Computer & Fluids*, 117:168–182, 2015.

[196] A.F. Frangi, W.J. Niessen, R.M. Hoogeveen, T. Van Walsum, and M.A. Viergever. Model-based quantitation of 3-d magnetic resonance angiographic images. *IEEE Transactions on Medical Imaging*, 18(10):946–956, 1999.

[197] D.W. Frazier, W. Krassowska, P.S. Chen, P.D. Wolf, N.D. Danieley, W.M. Smith, and R.E. Ideker. Transmural activations and stimulus potentials in three-dimensional anisotropic canine myocardium. *Circ Res*, 63(1):135–146, 1988.

[198] T. Fritz, C. Wieners, G. Seemann, H. Steen, and O. Dossel. Simulation of the contraction of the ventricles in a human heart model including atria and pericardium. *Biomechanics and Modeling in Mechanobiology*, 13(3):627–641, 2014.

[199] Y. Fung. *Biomechanics: mechanical properties of living tissues*. Springer, 1993.

[200] Y. C. Fung, K. Fronek, and P. Patitucci. Pseudoelasticity of arteries and the choice of its mathematical expression. *American Journal of Physiology*, 237(5):H620–H631, 1979.

[201] K. Galvin and H. Lee. Analysis and approximation of the cross model for quasi-newtonian flows with defective boundary conditions. *Appl. Math. Comp.*, 222:244254, 2013.

[202] K. Galvin, H. Lee, and L.G. Rebholz. Approximation of viscoelastic flows with defective boundary conditions. *J. Non Newt. Fl. Mech.*, 169-170:104113, 2012.

[203] M.W. Gee, U. Kuttler, and W.A. Wall. Truly monolithic algebraic multigrid for fluid-structure interaction. *Int. J. Num. Methods Engrg.*, 85(8):987–1016, 2011.

[204] B. Geiger. Three-dimensional modeling of human organs and its application to diagnosis and surgical planning. Technical Report RR-2105, INRIA, 1993.

[205] S.E. Geneser, R.M. Kirby, and R.S. MacLeod. Application of stochastic finite element methods to study the sensitivity of ecg forward modeling to organ conductivity. *IEEE Trans. Biomed. Engng.*, 55(1):31–40, 2008.

[206] L. Gerardo Giorda, L. Mirabella, F. Nobile, M. Perego, and A. Veneziani. A model-based block-triangular preconditioner for the bidomain system in electrocardiology. *Journal of Computational Physics*, 228(10):36253639, 2009.

[207] L. Gerardo Giorda, F. Nobile, and C. Vergara. Analysis and optimization of robin-robin partitioned procedures in fluid-structure interaction problems. *SIAM J. Numer. Anal.*, 48(6):2091–2116, 2010.

[208] J.-F. Gerbeau, D. Lombardi, and E. Schenone. Reduced order model in cardiac electrophysiology with approximated lax pairs. *Adv. Comput. Math.*, 41(5):1103–1130, 2015.

[209] P. Gervasio, F. Saleri, and A. Veneziani. Algebraic fractional-step schemes with spectral methods for the incompressible Navier-Stokes equations. *J. Comput. Physics*, 214(1):347–365, 2006.

[210] R. Ghanem and P. D. Spanos. *Stochastic Finite Elements: A Spectral Ap- proach, revised edition*. Dover, 2003. Reprint of the Springer-Verlag, New York, 1991 edition.

[211] G. Gigante and C. Vergara. Analysis and optimization of the generalized schwarz method for elliptic problems with application to fluid-structure interaction. *Numer. Math.*, 131(2):369–404, 2015.

[212] M.B. Giles. Multilevel Monte Carlo methods. *Acta Numerica*, 24:259–328, 2015.

[213] S. Giordana, S.J. Sherwin, J. Peiró, D.J. Doorly, J.S. Crane, K.E. Lee, N.J.W. Cheshire, and C.G. Caro. Local and global geometric influence on steady flow in distal anastomoses of peripheral bypass grafts. *J. Biomech. Engr.*, 127:1087, 2005.

[214] V. Girault and P.A. Raviart. *Finite element methods for Navier-Stokes equations*. Springer–Verlag, 1986.

[215] S. Glagov, C. Zarins, D.P. Giddens, and D.N. Ku. Hemodynamics and atherosclerosis. insights and perspectives gained from studies of human arteries. *Archives of Pathology & Laboratory Medicine*, 112(10):1018–1031, 1988.

[216] R. Glowinski, T.W. Pan, and J. Periaux. A lagrange multiplier/fictitious domain method for the numerical simulation of incompressible viscous flow around moving rigid bodies: (i) case where the rigid body motions are known a priori. *Comptes Rendus de l'Acadmie des Sciences - Series I - Mathematics*, 324(3):361–369, 1997.

[217] R. Gnyaneshwar, R.K. Kumar, and K.R. Balakrishnan. Dynamic analysis of the aortic valve using a finite element model. *Ann Thorac Surg*, 73(4):1122–1129, 2002.

[218] S. Goktepe and E. Kuhl. Electromechanics of the heart: a unified approach to the strongly coupled excitationcontraction problem. *Computational Mechanics*, 45(2):227–243, 2010.

[219] A. Goshtasby and D. Turner. Segmentation of cardiac cine mr images for extraction of right and left ventricular chambers. *IEEE Transactions on Medical Imaging*, 14(1):56–64, 1995.

[220] C. Grandmont. *Analyse Mathematique et Numerique de Quelques Problemes d Interaction Fluide-Structure*. PhD thesis, Laboratoire d Analyse Numrique de Paris VI, 1998.

[221] B.E. Griffith, R.D. Hornung, D.M. McQueen, and C.S. Peskin. An adaptive, formally second order accurate version of the immersed boundary method. *Journal of Computational Physics*, 223(1):10–419, 2007.

[222] B.E. Griffith, X. Luo, D.M. McQueen, and C.S. Peskin. Simulating the fluid dynamics of natural and prosthetic heart valves using the immersed boundary method. *International Journal of Applied Mechanics*, 1:137–176, 2009.

[223] L. Grinberg, E. Cheever, T. Anor, J.R. Madsen, and G.E. Karniadakis. Modeling blood flow circulation in intracranial arterial networks: a comparative 3d/1d simulation study. *Annals of Biomed Eng*, 39(1):297–309, 2010.

[224] L. Grinberg, A. Yakhot, and G.E. Karniadakis. Analyzing Transient Turbulence in a Stenosed Carotid Artery by Proper Orthogonal Decomposition. *Annals of Biomedical Engineering*, 37(11):2200–2217, 2009.

[225] J. M. Guccione, A. D. McCulloch, and L. K. Waldman. Passive material properties of intact ventricular myocardium determined from a cylindrical model. *Journal of Biomechanical Engineering*, 113(1):42–55, 1991.

[226] B. Guerciotti, C. Vergara, L. Azzimonti, L. Forzenigo, A. Buora, P. Biondetti, and M. Domanin. Computational study of the fluid-dynamics in carotids before and after endarterectomy. *J. Biomech.*, 195:2088–2099, 2015.

[227] B. Guerciotti, C. Vergara, S. Ippolito, A. Quarteroni, C. Antona, and R. Scrofani. Computational study of the risk of restenosis in coronary bypasses. *Biomechanics and Modeling in Mechanobiology, DOI:10.1007/s10237-016-0818-x*, 2016.

[228] J.L. Guermond, P. Minev, and J. Shen. Error analysis of pressure-correction schemes for the time-dependent stokes equations with open boundary conditions. *SIAM J. Numer. Anal.*, 43(1):239–258, 2005.

[229] J.L. Guermond, P. Minev, and J. Shen. An overview of projection methods for incompressible flows. *Comput. Methods Appl. Mech. Engrg.*, 195:6011–6045, 2006.

[230] J.L. Guermond and L. Quartapelle. On the approximation of the unsteady Navier-Stokes equations by finite element projection methods. *Numer. Math.*, 80:207–238, 1998.

[231] J.L. Guermond and J. Shen. Velocity-correction projection methods for incompressible flows. *SIAM J. Numer. Anal.*, 41:112–134, 2003.

[232] J.L. Guermond and J. Shen. An overview of projection methods for incompressible flows. *Comput. Methods Appl. Mech. Engrg.*, 195:6011–6045, 2006.

[233] G. Guidoboni, R. Glowinski, N. Cavallini, and S. Canic. Stable loosely-coupled-type algorithm for fluidstructure interaction in blood flow. *J. Comput. Physics*, 228:69166937, 2009.

[234] O. Gultekin, G. Sommer, and G.A. Holzapfel. An orthotropic viscoelastic model for the passive myocardium: continuum basis and numerical treatment. *Computer Methods in Biomechanics and Biomedical Engineering*, 19(15):1647–1664, 2016.

[235] M.D. Gunzburger. *Perspectives in Flow Control and Optimization*. Advances in Design and Control. Society for Industrial and Applied Mathematics, Philadephia, PA, 2003.

[236] M.D. Gunzburger, C.G. Webster, and G. Zhang. Stochastic finite element methods for partial differential equations with random input data. *Acta Numerica*, 23:521–650, 2014.

[237] A. Gupta, L. von Kurowski, A. Singh, D. Geiger, C.C. Liang, M.Y. Chiu, L. Adler, M. Haacke, and D. Wilson. Cardiac mr image segmentation using deformable models. *Computers in Cardiology, Proceedings*, pages 747–750, 1993.

[238] V. Gurev, P. Pathmanathan, J.L. Fattebert, H.F. Wen, J. Magerlein, R.A. Gray, D.F. Richards, and J.J. Rice. A high-resolution computational model of the deforming human heart. *Biomechanics and Modeling in Mechanobiology*, 14(4):132–140, 2015.

[239] C.M. Haggerty, L. Mirabella, M. Restrepo, D. A de Zélicourt, J. Rossignac, F. Sotiropoulos, T.L. Spray, K.R. Kanter, M.A. Fogel, and A.P. Yoganathan. Patient-specific surgery planning for the fontan procedure. In *Computer Models in Biomechanics*, pages 217–228. Springer, 2013.

[240] A. Hansbo and P. Hansbo. An unfitted finite element method, based on nitsche's method, for elliptic interface problems. *Comput. Methods Appl. Mech. Engrg.*, 191(47–48):5537–5552, 2002.

[241] A. Hansbo, P. Hansbo, and M.G. Larson. An unfitted finite element method, based on nitsche's method, for elliptic interface problems. *ESAIM: Math. Modelling Numer. Anal.*, 37(3):495 – 514, 2003.

[242] I. Hariton, G. de Botton, T.C. Gasser, and G.A. Holzapfel. Stress-driven collagen fiber remodeling in arterial walls. *Biomechanics and Modeling in Mechanobiology*, 3(6):163–175, 2006.

[243] J. De Hart, G.W.M. Peters, P.J.G. Schreurs, and F.P.T. Baaijens. A two-dimensional fluidstructure interaction model of the aortic value. *Journal of biomechanics*, 33(9):10791088, 2000.

[244] H. Haruguchi and S. Teraoka. Intimal hyperplasia and hemodynamic factors in arterial bypass and arteriovenous grafts: a review. *J. Artif. Organs*, 6(4):227–235, 2003.

[245] X. He, D.N. Ku, and J.E. Moore Jr. Simple calculation of the velocity profiles for pulsatile flow in a blood vessel using mathematica. *Ann Biomed Eng*, 21:45–49, 1993.

[246] M. Heil. An efficient solver for the fully coupled solution of large-displacement fluid-structure interaction problems. *Comput. Methods Appl. Mech. Engrg.*, 193:1–23, 2004.

[247] J.S. Hesthaven, G. Rozza, and B. Stamm. *Certified Reduced Basis Methods for Parametrized Partial Differential Equations*. SpringerBriefs in Mathematics. Springer, 2016.

[248] J.G. Heywood, R. Rannacher, and S. Turek. Artificial boundaries and flux and pressure conditions for the incompressible Navier-Stokes equations. *Int. J. Num. Methods Fluids*, 22:325–352, 1996.

[249] D.W. Hilgemann and D. Noble. Excitation-contraction coupling and extracellular calcium transients in rabbit atrium: reconstruction of basic cellular mechanisms. *Proc R soc Lond B*, 230:163–205, 1987.

[250] B. Hillen, H.W. Hoogstraten, and L. Post. A wave propagation model of blood flow in large vessels using an approximate velocity profile function. *J Biomech*, 19:187–194, 1986.

[251] M. Hintermüller, K. Kunisch, Y. Spasov, and S. Volkwein. Dynamical systems-based optimal control of incompressible fluids. *Int. J. Numer. Meth. Fluids*, 46(4):345–359, 2004.

[252] M. Hinze, R. Pinnau, M. Ulbrich, and S. Ulbrich. *Optimization with PDE Constraints*, volume 23 of *Mathematical Modelling: Theory and Applications*. Springer, 2009.

[253] C.W. Hirt, A.A. Amsden, and J.L. Cook. An arbitrary lagrangian eulerian computing method for all flow speeds. *J. Comput. Physics*, 69:277–324, 1974.

[254] A.L. Hodgkin and A.F. Hukley. A quantitative description of membrane current and its application to conduction and excitation in nerve. *J Physiol*, 117(4):500–544, 1952.

[255] G.A. Holzapfel. *Nonlinear Solid Mechanics: a ContinuumApproach for Engineering*. John Wiley & Sons Ltd, England, 2000.

[256] G.A. Holzapfel and T.C. Gasser. A viscoelastic model for fiber-reinforced composites at finite strains: continuumbasis, computational aspects, and applications. *Comput. Methods Appl. Mech. Engrg.*, 190:4379–4403, 2001.

[257] G.A. Holzapfel, T.C. Gasser, and R.W. Ogden. A new constitutive framework for arterial wall mechanics and a comparative study of material models. *J Elast*, 61:1–48, 2000.

[258] G.A. Holzapfel and R.W. Ogden. Constitutive modelling of passive myocardium: a structurally based framework for material characterization. *PHILOSOPHICAL TRANSACTIONS of the Royal society A*, 367:3445–3475, 2009.

[259] G.A. Holzapfel and R.W. Ogden. Constitutive modelling of arteries. *Proc. R. Soc. Lond. Ser. A Math. Phys. Eng. Sci.*, 466(2118):1551–1596, 2010.

[260] E. Hopf. Uber die aufangswertaufgabe für die hydrodynamischen grundgliechungen. *Mathematische Nachrichten*, 4:213–231, 1951.

[261] I. Hoteit, D.T. Pham, and J. Blum. A simplified reduced order kalman filtering and application to altimetric data assimilation in tropical pacific. *J. Mar. Syst.*, 36(1–2):101–127, 2002.

[262] M.C. Hsu, D. Kamensky, Y. Bazilevs, M.S. Sacks, and T.J.R. Hughes. Fluidstructure interaction analysis of bioprosthetic heart valves: significance of arterial wall deformation. *Comp Mech*, 54(4):10551071, 2014.

[263] W. Huberts, C. de Jonge, W.P.M. van der Linden, M. Inda, K. Passera, J.H.M. Tordoir, F.N. van de Vosse, and E.M.H Bosboom. A sensitivity analysis of a personalized pulse wave propagation model for arteriovenous fistula surgery. part b: identification of possible generic model parameters. *Med. Eng. Phys.*, 35(6):827–837, 2013.

[264] W. Huberts, C. de Jonge, W.P.M. van der Linden, M. Inda, J.H.M. Tordoir, F.N. van de Vosse, and E.M.H Bosboom. A sensitivity analysis of a personalized pulse wave propagation model for arteriovenous fistula surgery. part a: identification of most influential model parameters. *Med. Eng. Phys.*, 35(6):810–826, 2013.

[265] T.J.R. Hughes. *A Study of the One-Dimensional Theory of Arterial Pulse Propagation*. PhD thesis, University of California, Berkeley, 1974.

[266] T.J.R. Hughes. Multiscale phenomena: Green's function, the Dirichlet-to-Neumann formulation, subgrid scale models, bubbles and the origins of stabilized formulations. *Comput. Methods Appl. Mech. Engrg.*, 127:387–401, 1995.

[267] T.J.R. Hughes and J. Lubliner. On the one-dimensional theory of blood flow in the larger vessels. *Mathematical Biosciences*, 18(1-2):161–170, 1973.

[268] T.J.R. Hughes, L. Mazzei, and K.E. Jansen. Large eddy simulation and the variational multiscale method. *Computing and Visualization in Science*, 3(1):47–59, 2000.

[269] G. Huiskamp. Simulation of depolarization in a membrane- equations-based model of the anisotropic ventricle. *IEEE Transaction on Biomedical Engineering*, 45(7):847–855, 1998.

[270] J. Humpherys, P. Redd, and J. West. A fresh look at the kalman filter. *SIAM Review*, 54(4):801–823, 2012.

[271] J.D. Humphrey and F.C.P. Yin. On constitutive relations and finite deformations of passive cardiac tissue: I. a pseudostrain-energy function. *Journal of Biomechanical Engineering*, 109(4):298–304, 1987.

[272] P.J. Hunter, M.P. Nash, and G.B. Sands. Computational electromechanics of the heart. *Computational biology of the heart (eds. Panfilov, Holden)*, pages 345–407, 1997.

[273] Paul A Iaizzo. *Handbook of cardiac anatomy, physiology, and devices*. Springer, 2009.

[274] K. Ide, P. Courtier, M. Ghil, and A. C. Lorenc. Unified notation for data assimilation: Operational, sequential and variational. *J. Met. Soc. Japan*, 75(1B):181–189, 1997.

[275] M.A Iglesias, K.J.H. Law, and A.M Stuart. Ensemble Kalman methods for inverse problems. *Inverse Problems*, 29(4):045001, 2013.

[276] T. Ijiri, T. Ashihara, T. Yamaguchi, K. Takayama, T. Igarashi, T. Shimada, T. Namba, R. Haraguchi, and K. Nakazawa. A procedural method for modeling the purkinje fibers of the heart. *J Physiol Sci*, 58(7):90–100, 2008.

[277] J.G. Isaksen, Y. Bazilevs, T. Kvamsdal, Y. Zhang, J.H. Kaspersen, K. Waterloo, B. Romner, and T. Ingebrigtsen. Determination of wall tension in cerebral artery aneurysms by numerical simulation. *Stroke*, 39:3172–3178, 2008.

[278] R.H. Johnstone, E.T. Chang, R. Bardenet, T.P. de Boer, D.J. Gavaghan, P. Pathmanathan, R.H. Clayton, and G.R. Mirams. Uncertainty and variability in models of the cardiac action potential: Can we build trustworthy models? *J. Mol. Cell. Cardiol.*, 96:49–62, 2016.

[279] S. Julier and J. Uhlmann. Unscented filtering and nonlinear estimation. *Proceedings of the IEEE*, 92(3):401?422, 2004.

[280] S. Julier, J. Uhlmann, and H. Durrant-Whyte. A new method for the nonlinear transformation of means and covariance in filters and estimators. *IEEE Trans. on Automatic Control*, 45(3):477–482, 2000.

[281] S.J. Julier, J.K. Uhlmann, and H.F. Durrant-Whyte. A new approach for filtering nonlinear systems. In *American Control Conference, Proceedings of the 1995*, volume 3, pages 1628–1632, 1995.

[282] M. Juntunen and R. Stenberg. Nitsche's method for general boundary conditions. *Math. Comp.*, 78:1353–1374, 2009.

[283] J. Kaipio and E. Somersalo. *Statistical and computational inverse problems*, volume 160 of *Applied Mathematical Sciences*. Springer Science+Business Media, Inc., 2005.

[284] R.E. Kalman. A new approach to linear filtering and prediction problems. *ASME. J. Basic Eng.*, 82(1):35–45, 1960.

[285] G.E. Karniadakis, M. Israeli, and S.E. Orszag. High order splitting methods for the incompressible Navier-Stokes equations. *J. Comput. Physics*, 59:414–443, 1991.

[286] J.P. Keener. An eikonal-curvature equation for action potential propagation in myocardium. *J Math Biol*, 29(7):629–651, 1991.

[287] J.P. Keener and K. Bogar. A numerical method for the solution of the bidomain equations in cardiac tissue. *Chaos*, 8:234–241, 1998.

[288] S. Kefayati, D.W. Holdsworth, and T.L. Poepping. Turbulence intensity measurements using particle image velocimetry in diseased carotid artery models: Effect of stenosis severity, plaque eccentricity, and ulceration. *Journal of Biomechanics*, 47:253–263, 2014.

[289] R.H. Keldermann, M.P. Nash, and A.V. Panfilov. Modeling cardiac mechano-electrical feedback using reaction-diffusion-mechanics systems. *Physica D: Nonlinear Phenomena*, 238(11-12):1000–1007, 2009.

[290] C. Kelley. *Iterative Methods for Optimization*. Society for Industrial and Applied Mathematics, 1999.

[291] D.T.B. Kelly, K.J.H. Law, and A.M. Stuart. Well-posedness and accuracy of the ensemble Kalman filter in discrete and continuous time. *Nonlinearity*, 27(10):2579, 2014.

[292] M. Kennedy and A. O'Hagan. Predicting the output from a complex computer code when fast approximations are available. *Biometrika*, 87:1–13, 2000.

[293] B. Kerckoffs, O.P. Faris, P.H. Boveenderd, F.W. Prinzen, K. Smits, and T. Arts. Timing of depolarization and contraction in the paced canine left ventricle:. *J. Cardiovasc. Electrophysiol.*, 14:S188–S195, 2003.

[294] R.S. Keynton, M.M. Evancho, R.L. Sims, N.V. Rodway, A. Gobin, and S.E. Rittgers. Intimal hyperplasia and wall shear in arterial bypass graft distal anastomoses: an in vivo model study. *J. Biomech. Engr.*, 123:464, 2001.

[295] S.S. Khalafvand, L. Zhong, and E.Y.K. Ng. Three-dimensional cfd/mri modeling reveals that ventricular surgical restoration improves ventricular function by modifying intraventricular blood flow. *International Journal for Numerical Methods in Biomedical Engineering*, 30(10):1044–1056, 2014.

[296] H. Kim, J. Lu, M.S. Sacks, and K.B. Chandran. Dynamic simulation of bioprosthetic heart valves using a stress resultant shell model. *Journal of Biomechanics*, 36(2):262–275, 2008.

[297] H. Kim, I.E. Vignon-Clementel, C. Figueroa, J. Ladisa, K. Jansen, J. Feinstein, and C. Taylor. On coupling a lumped parameter heart model and a three-dimensional finite element aorta model. *Ann Biomed Eng*, 37:2153–2169, 2009.

[298] C. Kleinstreuer. *Biofluid Dynamics: Principles and Selected Applications*. CRC Press, 2006.

[299] P. Kohl, P. Hunter, and D. Noble. Stretch-induced changes in heart rate and rhythm: clinical observations, experiments and mathematical models. *Progress in Biophysics and Molecular Biology*, 71(1):91–138, 1999.

[300] P. Kohl and F. Sachs. Stretch-induced changes in heart rate and rhythm: clinical observations, experiments and mathematical models. *PHILOSOPHICAL TRANSACTIONS of the Royal society A*, 359:1173–1185, 2001.

[301] E. Konukoglu, J. Relan, U. Cilingir, B.H. Menze, P. Chinchapatnam, A. Jadidi, H. Cochet, M. Hocini, H. Delingette, P. Jaïs, M. Haïssaguerre, N. Ayache, and

M. Sermesant. Efficient probabilistic model personalization integrating uncertainty on data and parameters: Application to eikonal-diffusion models in cardiac electrophysiology. *Progress Biophys. Molec. Biology*, 107(1):134–146, 2011.

[302] T. Korakianitis and Y. Shi. A concentrated parameter model for the human cardiovascular system including heart valve dynamics and atrioventricular interaction. *Medical Engineering & Physics*, 28(7):613–628, 2006.

[303] T. Korakianitis and Y. Shi. Numerical simulation of cardiovascular dynamics with healthy and diseased heart valves. *J Biomech*, 39(11):1964–1982, 2006.

[304] P. Koutsourelakis. Accurate uncertainty quantification using inaccurate models. *SIAM J. Sci. Comput.*, 31(5):3274–3300, 2009.

[305] A. Krishnamurthy, C.T. Villongco, J. Chuang, L.R. Frank, V. Nigam, E. Belezzuoli, P. Stark, D.E. Krummen, S. Narayan, J.H. Omens, A.D. McCulloch, and R.C.P. Kerckhoffs. Patient-specific models of cardiac biomechanics. *J. Comput. Phys.*, 244:4–21, 2013.

[306] R.H. Kufahl and M.E. Clark. A circle of willis simulation using distensible vessels and pulsatile flow. *J Biomech Eng*, 107(2):112–122, 1985.

[307] E. Kuhl and G.A. Holzapfel. A continuum model for remodeling in living structures. *Journal of Materials Science*, 21(42):8811–8823, 2006.

[308] K. Kunisch and A. Rund. Time optimal control of the monodomain model in cardiac electrophysiology. *IMA J. Appl. Math.*, 80(6):1664–1683, 2015.

[309] K. Kunisch and B. Vexler. Optimal vortex reduction for instationary flows based on translation invariant cost functionals. *SIAM J. Control Optim*, 46(4):1368–1397, 2007.

[310] K.S. Kunzelman and R.P. Cochran. Mechanical properties of basal and marginal mitral valve chordae tendineae. *ASAIO Trans.*, 36:M405, 1990.

[311] K.S. Kunzelman, R.P. Cochran, C. Chuong, W.S. Ring, Verrier, and R.D. Eberhart. Finite element analysis of the mitral valve. *J. Heart Valve Dis.*, 2:326–340, 1993.

[312] U. Kuttler, M. Gee, C. Forster, A. Comerford, and W.A. Wall. Coupling strategies for biomedical fluid-structure interaction problems. *Int. J. Numer. Meth. Biomed. Engng.*, 26:305–321, 2010.

[313] U. Kuttler and W.A. Wall. Fixed-point fluidstructure interaction solvers with dynamic relaxation. *Comp. Mech*, 43(1):61–72, 2008.

[314] A. Laadhari and A. Quarteroni. Aortic valve dynamics using a fluid structure interaction model - the physiology of opening and closing. *International Journal for Numerical Methods in Biomedical Engineering*, 32(5):, 2016.

[315] R. Lal, B. Mohammadi, and F. Nicoud. Data assimilation for identification of cardiovascular network characteristics. *Int. J. Numer. Methods Biomed. Engrg.*, pages n/a–n/a, 2016.

[316] R.M. Lancellotti, C. Vergara, L. Valdettaro, S. Bose, and A. Quarteroni. Large eddy simulations for blood fluid-dynamics in real stenotic carotids. MOX-Report n. 63-2015, Department of Mathematics, Politecnico di Milano, Italy, 2015.

[317] S. Land, S.A. Niederer, J.M. Aronsen, E.S. Espe, L. Zhang, W.E. Louch, I.Sjaastad, O.M. Sejersted, and N.P. Smith. An analysis of deformation-dependent electromechanical coupling in the mouse heart. *The Journal of Physiology*, 590(18):4553–4569, 2012.

[318] T. Lassila, A. Manzoni, A. Quarteroni, and G. Rozza. Boundary control and shape optimization for the robust design of bypass anastomoses under uncertainty. *ESAIM: Math. Modelling Numer. Anal.*, 47(4):1107–1131, 2013.

[319] T. Lassila, A. Manzoni, A. Quarteroni, and G. Rozza. A reduced computational and geometrical framework for inverse problems in haemodynamics. *Int. J. Numer. Methods Biomed. Engng.*, 29(7):741–776, 2013.

[320] T. Lassila, A. Quarteroni, and G. Rozza. A reduced basis model with parametric coupling for fluid-structure interaction problem. *SIAM J. Sci. Comput.*, 34(2):A1187–A1213, 2012.

[321] K. Law, A. Stuart, and K. Zygalakis. *Data Assimilation. A Mathematical Introduction*, volume 62 of *Texts in Applied Mathematics*. Springer International Publishing Switzerland, 2015.

[322] T.B. Le and F. Sotiropoulos. Fluidstructure interaction of an aortic heart valve prosthesis driven by an animated anatomic left ventricle. *Journal of Computational Physics*, 224(1):4162, 2013.

[323] O.P. Le Maître and O. Knio. *Spectral Methods for Uncertainty Quantification With Applications to Computational Fluid Dynamics*. Springer Netherlands, 2010.

[324] H. Lee. Optimal control for quasi-newtonian flows with defective boundary conditions. *Comput. Methods Appl. Mech. Engrg.*, 200:24982506, 2011.

[325] J. Lee, A. Cookson, I. Roy, E. Kerfoot, L. Asner, G. Vigueras, T. Sochi, S. Deparis, C. Michler, N. P. Smith, and D. A. Nordsletten. Multiphysics computational modeling in cheart. *SIAM J. Sci. Comput.*, 38(3):C150C178, 2016.

[326] S.E. Lee, S.W. Lee, P.F. Fischer, H.S. Bassiouny, and F. Loth. Direct numerical simulation of transitional flow in a stenosed carotid bifurcation. *J Biomech*, 41(11):2551–2561, 2008.

[327] M.J. Legato. Ultrastructure of the atrial, ventricular, and purkinje cell, with special reference to the genesis of arrhythmias. *Circulation*, 47:178–189, 1973.

[328] C.A.D. Leguy, A.S.Z. Bosboom, E.M.H. abd Belloum, A.P.G. Hoeks, and F.N. van de Vosse. Global sensitivity analysis of a wave propagation model for arm arteries. *Med. Eng. Phys.*, 33(8):1008–1016, 2011.

[329] M. Lei, J. Archie, and C. Kleinstreuer. Computational design of a bypass graft that minimizes wall shear stress gradients in the region of the distal anastomosis. *J. Vasc. Surg.*, 25(4):637–646, 1997.

[330] J.S. Leiva, P.J. Blanco, and G.C. Buscaglia. Partitioned analysis for dimensionally-heterogeneous hydraulic networks. *Mult Model Simul*, 9:872–903, 2011.

[331] J. Leray. Sur les mouvements d'un liquide visqueux emplissant l'espace. *Acta Mathematica*, 63:193–248, 1934.

[332] D. Lesagea, E.D. Angelini, I. Blochb, and G. Funka-Lea. A review of 3d vessel lumen segmentation techniques: Models, features and extraction schemes. *Medical Image Analysis*, 13:819845, 2009.

[333] A. Leuprecht, K. Perktold, Martin Prosi, T. Berk, W. Trubel, and H. Schima. Numerical study of hemodynamics and wall mechanics in distal end-to-side anastomoses of bypass grafts. *Journal of Biomechanics*, 2(35):225–236, 2002.

[334] R.J. LeVeque. *Numerical methods for conservation laws*, volume 132. Birkhäuser Basel, 1992.

[335] C. Li and C. Vuik. Eigenvalue analysis of the simple preconditioning for incompressible flow. *Numerical Linear Algebra with Applications*, 11(5-6):511–523, 2004.

[336] D. Li and A.M. Robertson. A structural multi-mechanism damage model for cerebral arterial tissue. *Journal of Biomechanical Engineering*, 131(10):101013, 2013.

[337] F. Liang and H. Liu. Simulation of hemodynamic responses to the valsalva maneuver: An integrative computational model of the cardiovascular system and the autonomic nervous system. *The Journal of Physiological Sciences*, 1(56):45–65, 2006.

[338] J.L. Lions and G. Prodi. Un theoreme d'existence et d'unicite dans les equations de navier-stokes en dimension 2. *C.R. Acad. Sci. Paris*, 248:3519–3521, 1959.

[339] Y. Liu, C. Charles, M. Gracia, H. Gregersen, and G. S. Kassab. Surrounding tissues affect the passive mechanics of the vessel wall: theory and experiment. *Am J Physiol Heart Circ Physiol*, 293:H3290–H3300, 2007.

[340] D. Lombardi. Inverse problems in 1d hemodynamics on systemic networks: A sequential approach. *Int. J. Numer. Meth. Biomed. Engng*, 30(2):160–179, 2014.

[341] M. Lorenzo-Valdés, G.I. Sanchez-Ortiz, A.G. Elkington, R.H. Mohiaddin, and D. Rueckert. Segmentation of 4d cardiac mr images using a probabilistic atlas and the em algorithm. *Medical Images Analysis*, 8(3):255265, 2004.

[342] F. Loth, P.F. Fischer, and H.S. Bassiouny. Blood flow in end-to-side anastomoses. *Annu. Rev. Fluid. Mech.*, 40:367–393, 2008.

[343] C.H. Luo and Y. Rudy. A model of the ventricular cardiac action potential. depolarization, repolarization, and their interaction. *Circ Res*, 68:1501–1526, 1991.

[344] C.H. Luo and Y. Rudy. A dynamic model of the cardiac ventricular action potential. i. simulations of ionic currents and concentration changes. *Circ Res*, 74:1071–1096, 1994.

[345] C.H. Luo and Y. Rudy. A dynamic model of the cardiac ventricular action potential. ii. afterdepolarizations, triggered activity, and potentiation. *Circ Res*, 74:1097–1113, 1994.

[346] M. Lykaser and B.F. Nielsen. Towards a level set framework for infarction modeling: an inverse problem. *Int. J. Numer. Anal. Model.*, 3(4):377–394, 2006.

[347] M.C. MacLachlan, B.F. Nielsen, m. Lysaker, and A. Tveito. Computing the size and location of myocardial ischemia using measurements of ST-segment shift. *IEEE Trans. Biomed. Engng.*, 53(6):1024–1031, 2006.

[348] Y. Maday. Analysis of coupled models for fluid-structure interaction of internal flows. In *Cardiovascular mathematics, edited by A. Quarteroni, L. Formaggia, A. Veneziani, Chapter 8*, pages 279–306. Springer, 2009.

[349] A. Mahmoud, A. El-Barkouky, H.E. Farag, J. Graham, and A. Farag. A non-invasive method for measuring blood flow rate in superficial veins from a single thermal image. In *Computer Vision and Pattern Recognition Workshops (CVPRW), 2013 IEEE Conference on*, pages 354–359. IEEE, 2013.

[350] A.C.I. Malossi. *Partitioned Solution of Geometrical Multiscale Problems for the Cardiovascular System: Models, Algorithms, and Applications.* PhD thesis, École Polytechnique Fédérale de Lausanne, 2012. Thesis n° 5453.

[351] A.C.I. Malossi, P.J. Blanco, P. Crosetto, S. Deparis, and A. Quarteroni. Implicit coupling of one-dimensional and three-dimensional blood flow models with compliant vessels. *Multiscale Model Simul*, 11(2):474–506, 2013.

[352] A.C.I. Malossi, P.J. Blanco, and S. Deparis. A two-level time step technique for the partitioned solution of one-dimensional arterial networks. *Comput. Methods Appl. Mech. Engrg.*, 237–240:212–226, 2012.

[353] T. Mansi, I. Voigt, B. Georgescu, X. Zheng, E.A. Mengue, M. Hackl, R.I. Ionasec, T. Noack, J. Seeburger, and D. Comaniciu. An integrated framework for finite-element modeling of mitral valve biomechanics from medical images: Application to mitralclip intervention planning. *Medical Image Analysis*, 16(7):13301346, 2012.

[354] A. Manzoni. *Reduced Models for optimal control, shape optimization and inverse problems in haemodynamics*. PhD thesis, Ecole Polytechnique Fédérale de Lausanne, 2012.

[355] A. Manzoni, T. Lassila, A. Quarteroni, and G. Rozza. A reduced-order strategy for solving inverse bayesian shape identification problems in physiological flows. In G.H. Bock, P.X. Hoang, R. Rannacher, and P.J. Schlöder, editors, *Modeling, Simulation and Optimization of Complex Processes - HPSC 2012: Proceedings of the Fifth International Conference on High Performance Scientific Computing, March 5-9, 2012, Hanoi, Vietnam*, pages 145–155. Springer International Publishing, Cham, 2014.

[356] A. Manzoni, S. Pagani, and T. Lassila. Accurate solution of bayesian inverse uncertainty quantification problems combining reduced basis methods and reduction error models. *SIAM/ASA J. Uncert. Quant.*, 4:380–412, 2016.

[357] A. Manzoni, A. Quarteroni, and G. Rozza. Model reduction techniques for fast blood flow simulation in parametrized geometries. *Int. J. Numer. Methods Biomed. Engng.*, 28(6–7):604–625, 2012.

[358] A. Manzoni, A. Quarteroni, and G. Rozza. Shape optimization of cardiovascular geometries by reduced basis methods and free-form deformation techniques. *Int. J. Numer. Methods Fluids*, 70(5):646–670, 2012.

[359] S. Marchesseau, H. Delingette, M. Sermesant, and N. Ayache. Fast parameter calibration of a cardiac electromechanical model from medical images based on the unscented transform. *Biomech. Model. Mechanobiol.*, 12(4):815–831, 2012.

[360] S. Marchesseau, H. Delingette, M. Sermesant, R. Cabrera-Lozoya, C. Tobon-Gomez, P. Moireau, R.M. Figueras i Ventura, K. Lekadir, A. Hernandez, M. Garreau, E. Donal, C. Leclercq, S.G. Duckett, K. Rhode, C.A. Rinaldi, A.F. Frangi, R. Razavi, D. Chapelle, and N. Ayache. Personalization of a cardiac electromechanical model using reduced order unscented kalman filtering from regional volumes. *Medical Image Analysis*, 17(7):816–829, 2013.

[361] K.A. Mardal, B.F. Nielsen, X. Cai, and A. Tveito. Semi-implicit time-discretization schemes for the bidomain modelan order optimal solver for the discretized bidomain equations. *Numerical Linear Algebra with Applications*, 14(2):83–98, 2007.

[362] K.N. Margaris and R.A. Black. Modelling the lymphatic system: challenges and opportunities. *J. R. Soc. Interface*, 69(9):601–612, 2012.

[363] G. Marom. Numerical Methods for Fluid–Structure Interaction Models of Aortic Valves. *Arch Computat Methods Eng*, 22(4):595–620, 2015.

[364] A.L. Marsden. Optimization in cardiovascular modeling. *Annual Review of Fluid Mechanics*, 46(1):519–546, 2014.

[365] A.L. Marsden, J.A. Feinstein, and C.A. Taylor. A computational framework for derivative-free optimization of cardiovascular geometries. *Comput. Methods Appl. Mech. Engrg.*, 197(21–24):1890–1905, 2008.

[366] V. Martin, F. Clément, A. Decoene, and J.-F. Gerbeau. Parameter identification for a one-dimensional blood flow model. *ESAIM: Proc.*, 14:174–200, 2005.

[367] K.S. Matthys, J. Alastruey, J. Peiró, A.W. Khir, P. Segers, P.R. Verdonck, K.H. Parker, and S.J. Sherwin. Pulse wave propagation in a model human arterial network: Assessment of 1-d numerical simulations against in vitro measurements. *J Biomech*, 40(15):3476–3486, 2007.

[368] B. Maury. *The Respiratory System in Equations*. Springer-Verlag Italia, 2013.

[369] K. May-Newman, C. Lam, and F.C.P. Yin. A hyperelastic constitutive law for aortic valve tissue. *J Biomech Eng*, 131:081009, 2009.

[370] K. May-Newman and F.C.P. Yin. A constitutive law for mitral valve tissue. *J Biomech Eng*, 120(1):38–47, 1998.

[371] W.D. Merryman, H.Y.S. Huang, F.J. Schoen, and M.S. Sacks. The effects of cellular contraction on aortic valve leaflet flexural stiffness. *Journal of Biomechanics*, 39(1):88–96, 2006.

[372] F. Migliavacca, R. Balossino, G. Pennati, G. Dubini, T.Y. Hsia, M.R. de Leval, and E.L. Bove. Multiscale modelling in biofluidynamics: application to reconstructive paediatric cardiac surgery. *J Biomech*, 39:1010–1020, 2006.

[373] F. Migliavacca and G. Dubini. Computational modeling of vascular anastomoses. *Biomech. Model. Mechanobiol.*, 3(4):235–250, 2005.

[374] R. Mittal and G. Iaccarino. Immersed boundary methods. *Annual Review of Fluid Mechanics*, 37:239–261, 2005.

[375] R. Mittal, J.H. Seo, V. Vedula, Y.J. Choi, H. Liu, H.H. Huang, S. Jain, L. Younes, T. Abraham, and R.T. George. Computational modeling of cardiac hemodynamics: Current status and future outlook. *Journal of Computational Physics*, 305:1065–1082, 2016.

[376] P. Moireau, C. Bertoglio, N. Xiao, C. A. Figueroa, C. A. Taylor, D. Chapelle, and J.-F. Gerbeau. Sequential identification of boundary support parameters in a fluid-structure vascular model using patient image data. *Biomech. Model. Mechanobiol.*, 12(3):475–496, 2013.

[377] P. Moireau and D. Chapelle. Reduced-order unscented kalman filtering with application to parameter identification in large-dimensional systems. *ESAIM: Control Optim. Calc. Var.*, 17(2):380–405, 2011.

[378] P. Moireau, D. Chapelle, and P. Le Tallec. Joint state and parameter estimation for distributed mechanical systems. *Comput. Methods Appl. Mech. Engrg.*, 197(6–8):659–677, 2008.

[379] P. Moireau, D. Chapelle, and P.L. Tallec. Filtering for distributed mechanical systems using position measurements: perspectives in medical imaging. *Inverse Problems*, 25:035010, 2009.

[380] P. Moireau, N. Xiao, M. Astorino, C. A. Figueroa, D. Chapelle, C. A. Taylor, and J.F. Gerbeau. External tissue support and fluid–structure simulation in blood flows. *Biomechanics and Modeling in Mechanobiology*, 11(1–2):1–18, 2012.

[381] J.A. Moore, D.A. Steinman, and C.R. Ethier. Computational blood flow modelling: Errors associated with reconstructing finite element models from magnetic resonance images. *Journal of Biomechanics*, 31(2):179–184, 1997.

[382] H. Moradkhani, S. Sorooshian, H.V. Gupta, and P.R. Houser. Dual state-parameter estimation of hydrological models using ensemble kalman filter. *Adv. Water Resour.*, 28(2):135–147, 2005.

[383] U. Morbiducci, R. Ponzini, G. Rizzo, M. Cadioli, A. Esposito, F. De Cobelli, A. Del Maschio, F.M. Montevecchi, and A. Redaelli. In vivo quantification of helical blood flow in human aorta by time-resolved three-dimensional cine phase contrast magnetic resonance imaging. *Ann Biomed Eng*, 37(3):516–531, 2009.

[384] D. Mozaffarian, E.J. Benjamin, A.S. Go, D.K. Arnett, M.J. Blaha, M. Cushman, S.R. Das, S. de Ferranti, J.-P. Després, H.J. Fullerton, V.J. Howard, M.D. Huffman, C.R. Isasi, M.C. Jiménez, S.E. Judd, B.M. Kissela, J.H. Lichtman, L.D. Lisabeth, S. Liu, R.H. Mackey, D.J. Magid, D.K. McGuire, E.R. Mohler, C.S. Moy, P. Muntner, M.E. Mussolino, K. Nasir, R.W. Neumar, G. Nichol, L. Palaniappan, D.K. Pandey, M.J. Reeves, C.J. Rodriguez, W. Rosamond, P.D. Sorlie, J. Stein, A. Towfighi, T.N. Turan, S.S. Virani, D. Woo, R.W. Yeh, and M.B. Turner. Heart disease and stroke statistics—2016 update. *Circulation*, 132, 2015.

[385] J. Muller, O. Sahni, X. Lia, K.E. Jansen, M. S. Shephard, and C.A. Taylor. Anisotropic adaptive finite element method for modelling blood flow. *Computer Methods in Biomechanics and Biomedical Engineering*, 8(5):295–305, 2005.

[386] L. Muller and E.F. Toro. Well-balanced high-order solver for blood flow in networks of vessels with variable properties. *Int J Num Meth Biomed Eng*, 29(12):1388–1411, 2013.

[387] L. Muller and E.F. Toro. A global multiscale mathematical model for the human circulation with emphasis on the venous system. *Int J Num Meth Biomed Eng*, 30(7):681–725, 2014.

[388] M. Munteanu, L.F. Pavarino, and S. Scacchi. A scalable newton–krylov–schwarz method for the bidomain reaction-diffusion system. *SIAM J. Sci. Comput.*, 31(5):3861–3883, 2009.

[389] M. Murillo and X.C. Cai. A fully implicit parallel algorithm for simulating the non-linear electrical activity of the heart. *Numerical Linear Algebra with Applications*, 2-3(11):261–277, 2004.

[390] A. Muszkiewicz, O.J. Britton, P. Gemmell, E. Passini, C. Sánchez, X. Zhou, A. Carusi, T.A. Quinn, K. Burrage, A. Bueno-Orovio, and B. Rodriguez. Variability in cardiac electrophysiology: Using experimentally-calibrated populations of models to move beyond the single virtual physiological human paradigm. *Progress Biophys. Molec. Biology*, 120(1-3):115–127, 2016.

[391] Ch. Nagaiah, K. Kunisch, and G. Plank. Numerical solution for optimal control of the reaction-diffusion equations in cardiac electrophysiology. *Comput. Optim. Appl.*, 49:149–178, 2011.

[392] Ch. Nagaiah, K. Kunisch, and G. Plank. On boundary stimulation and optimal boundary control of the bidomain equations. *Mathem. Biosciences*, 245(2):206–215, 2013.

[393] Ch. Nagaiah, K. Kunisch, and G. Plank. Optimal control approach to termination of re-entry waves in cardiac electrophysiology. *J. Math. Biol.*, 67(2):1–30, 2013.

[394] Ch. Nagaiah, K. Kunisch, and G. Plank. Pde constrained optimization of electrical defibrillation in a 3d ventricular slice geometry. *Int. J. Numer. Meth. Biomed. Engng.*, 32(4):e02742, 2016.

[395] A. Nagler, C. Bertoglio, M. Gee, and W. Wall. Personalization of cardiac fiber orientations from image data using the unscented kalman filter. *Functional Imaging and Modeling of the Heart*, 7945:132–140, 2013.

[396] M.P. Nash and A.V. Panfilov. Electromechanical model of excitable tissue to study reentrant cardiac arrhythmias. *Progress in Biophysics and Molecular Biology*, 2-3(85):501–522, 2004.

[397] F. Negri. *Efficient Reduction Techniques for the Simulation and Optimization of Parametrized Systems: Analysis and Applications*. PhD thesis, Ecole Polytechnique Fédérale de Lausanne, 2016.

[398] M.G.C. Nestola, E. Faggiano, C Vergara, R.M. Lancellotti, S. Ippolito, C. Antona, A. Quarteroni, and R. Scrofani. Computational comparison of aortic root stresses in presence of stentless and stented aortic valve bio-prostheses. *Computer Methods in Biomechanics and Biomedical Engineering, DOI:10.1080/10255842.2016.1207171*, 2016.

[399] N.M Newmark. A method of computation for structural dynamics. *Journal of Engineering Mechanics*, 85:67–94, 1959.

[400] N. K. Nichols. Mathematical concepts of data assimilation. In W. Lahoz, B. Khattatov, and R. Menard, editors, *Data Assimilation: Making Sense of Observations*, pages 13–39. Springer Berlin Heidelberg, Berlin, Heidelberg, 2010.

[401] W.W. Nichols and M.F. O'Rourke, editors. *McDonald's Blood Flow in Arteries*. Hodder Arnold, 2005.

[402] S.A. Niederer, P.J. Hunter, and N.P. Smith. A quantitative analysis of cardiac myocyte relaxation: A simulation study. *Biophysical Journal*, 90(5):1697–1722, 2006.

[403] S.A. Niederer, E. Kerfoot, A.P. Benson, M.O. Bernabeu, O. Bernus, C. Bradley, E..M Cherry, R. Clayton, F.H. Fenton, A. Garny, et al. Verification of cardiac tissue electrophysiology simulators using an n-version benchmark. *Phil. Trans. R. Soc. A*, 369(1954):4331–4351, 2011.

[404] S.A. Niederer and N.P Smith. A mathematical model of the slow force response to stretch in rat ventricular myocytes. *Biophysical Journal*, 92(11):4030–4044, 2007.

[405] S.A. Niederer and N.P Smith. An improved numerical method for strong coupling of excitation and contraction models in the heart. *Progress in Biophysics and Molecular Biology*, 96(1–3):90–111, 2008.

[406] B.F. Nielsen, X. Cai, and M. Lykaser. On the possibility for computing the transmembrane potential in the heart with a one shot method: an inverse problem. *Math. Biosciences*, 210:523–553, 2007.

[407] B.F. Nielsen, M. Lykaser, and A. Tveito. On the use of the resting potential and level set methods for identifying ischemic heart disease: An inverse problem. *J. Comput. Phys.*, 220:772–790, 2007.

[408] J.A. Nitsche. Uber ein variationsprinzip zur lozung von dirichlet-problemen bei verwendung von teilraumen, die keinen randbedingungen unterworfen sind. *Abhandlungen aus dem Mathematischen Seminar der Universitat Hamburg*, 36:9–15, 1970/71.

[409] F. Nobile. *Numerical approximation of fluid-structure interaction problems with application to haemodynamics*. PhD thesis, École Polytechnique Fédérale de Lausanne, 2001. Thesis n° 2458.

[410] F. Nobile, M. Pozzoli, and C. Vergara. Time accurate partitioned algorithms for the solution of fluid-structure interaction problems in haemodynamics. *Computer & Fluids*, 86:470–482, 2013.

[411] F. Nobile, M. Pozzoli, and C. Vergara. Inexact accurate partitioned algorithms for fluid-structure interaction problems with finite elasticity in haemodynamics. *Journal of Computational Physics*, 273:598–617, 2014.

[412] F. Nobile, R. Tempone, and C. G. Webster. A sparse grid stochastic collocation method for partial differential equations with random input data. *SIAM J. Numer. Anal.*, 46:2309–2345, 2008.

[413] F. Nobile and C. Vergara. An effective fluid-structure interaction formulation for vascular dynamics by generalized Robin conditions. *SIAM J Sc Comp*, 30(2):731–763, 2008.

[414] F. Nobile and C. Vergara. Partitioned algorithms for fluid-structure interaction problems in haemodynamics. *Milan Journal of Mathematics*, 80(2):443–467, 2012.

[415] J. Nocedal. Theory of algorithms for unconstrained optimization. *Acta Numerica*, 1:199–242, 1992.

[416] D.A. Nordsletten, M. McCormick, P.J. Kilner, P. Hunter, D. Kayand, and N.P. Smith. Fluid–solid coupling for the investigation of diastolic and systolic human left ventricular function. *International Journal for Numerical Methods in Biomedical Engineering*, 27(7):1017–1039, 2011.

[417] D.A. Nordsletten, S.A. Niederer, M.P. Nash, P.J. Hunter, and N.P. Smith. Coupling multi-physics models to cardiac mechanics. *Progress in Biophysics and Molecular Biology*, 104(1-3):77–88, 2011.

[418] A. A. Oberai, N. H. Gokhale, and G. R. Feijoo. Solution of inverse problems in elasticity imaging using the adjoint method. *Inverse Problems*, 19(2):297–313, 2003.

[419] T. O'Donnell, M.P.D. Jolly, and A. Gupta. A cooperative framework for segmentation using 2d active contours and 3d hybrid models as applied to branching cylindrical structures. *Proc. IEEE Int. Conf. Computer Vision*, pages 454 – 459, 1998.

[420] M.S. Olufsen, C.S. Peskin, W.Y. Kim, E.M. Pedersen, A. Nadim, and J. Larsen. Numerical simulation and experimental validation of blood flow in arteries with structured-tree outflow conditions. *Ann Biomed Eng*, 28(11):1281–1299, 2000.

[421] S.A. Orszag, M. Israeli, and M. Deville. Boundary conditions for incompressible flows. *J. Sci. Comput.*, 1:75–111, 1986.

[422] H. Osnes and J. Sundnes. Uncertainty analysis of ventricular mechanics using the probabilistic collocation method. *IEEE Trans. Biomed. Engng.*, 59(8):2171–2179, 2012.

[423] A.A. Owida, H. Do, and Y.S. Morsi. Numerical analysis of coronary artery bypass grafts: an over view. *Comput. Methods Programs Biomed.*, 108(2):689–705, 2012.

[424] M. Padala, M.S. Sacks, S.W. Liou, K. Balachandran, Z. He, and A.P. Yoganathan. Mechanics of the mitral valve strut chordae insertion region. *Journal of Biomechanical Engineering*, 132(8):081004, 2010.

[425] S. Pagani. *Reduced order models for inverse problems and uncertainty quantification in cardiac electrophysiology.* PhD thesis, Mathematical Models and Methods in Engineering, Dipartimento di Matematica, Politecnico di Milano, 2016.

[426] S. Pagani, A. Manzoni, and A. Quarteroni. A reduced basis ensemble Kalman filter for state/parameter identification in large-scale nonlinear dynamical systems. MOX-Report n. 24-2016, Department of Mathematics, Politecnico di Milano, Italy, 2016.

[427] S. Palamara, C. Vergara, D. Catanzariti, E. Faggiano, M. Centonze, C. Pangrazzi, M. Maines, and A. Quarteroni. Computational generation of the Purkinje network driven by clinical measurements: the case of pathological propagations. *Int. J. Numer. Meth. Biomed. Engng.*, 30(12):1558–1577, 2014.

[428] S. Palamara, C. Vergara, E. Faggiano, and F. Nobile. An effective algorithm for the generation of patient-specific purkinje networks in computational electrocardiology. *J. Comp. Phys.*, 283:495–517, 2015.

[429] A.V. Panfilov. Three-dimensional organization of electrical turbulence in the heart. *Phys. Rev. E*, 59:R6251–R6254, 1999.

[430] S. Pant, B. Fabréges, J-F. Gerbeau, and I. E. Vignon-Clementel. A methodological paradigm for patient-specific multi-scale cfd simulations: from clinical measurements to parameter estimates for individual analysis. *Int. J. Numer. Meth. Biomed. Engng.*, 30(12):1614–1648, 2014.

[431] G. Papadakis. Coupling 3d and 1d fluid–structure-interaction models for wave propagation in flexible vessels using a finite volume pressure-correction scheme. *Comm Numer Meth Eng*, 25(5):533–551, 2009.

[432] S.V. Patankar and D.B. Spalding. A calculation procedure for heat, mass and momentum transfer in three-dimensional parabolic flows. *International Journal of Heat and Mass Transfer*, 15(10):1787–1806, 1972.

[433] P. Pathmanathan, S. J. Chapman, D. J. Gavaghan, and J.P. Whiteley. Cardiac electromechanics: The effect of contraction model on the mathematical problem and accuracy of the numerical scheme. *Quarterly Jnl of Mechanics & Applied Math*, 63(3):375–399, 2010.

[434] P. Pathmanathan, G.R. Mirams, J. Southern, and J.P. Whiteley. The significant effect of the choice of ionic current integration method in cardiac electro-physiological simulations. *International Journal for Numerical Methods in Biomedical Engineering*, 27(11):1751–1770, 2011.

[435] L.F. Pavarino and S. Scacchi. Multilevel additive schwarz preconditioners for the bidomain reaction-diffusion system. *SIAM J. Sci. Comput*, 31(1):420–443, 2008.

[436] L.F. Pavarino, S. Scacchi, and S. Zampini. Newton–krylov-bddc solvers for nonlinear cardiac mechanics. *Computer Methods in Applied Mechanics and Engineering*, 295:562–580, 2015.

[437] T.J. Pedley. *The fluid mechanics of large blood vessels*. Cambridge monographs on mechanics and applied mathematics: Cambridge University Press, 1980.

[438] J. Peiró, L. Formaggia, M. Gazzola, A. Radaelli, and V. Rigamonti. Shape reconstruction from medical images and quality mesh generation via implicit surfaces. *International Journal for Numerical Methods in Fluids*, 53(8):1339–1360, 2007.

[439] J. Peiró and A. Veneziani. Reduced models of the cardiovascular system. In *Cardiovascular mathematics, edited by A. Quarteroni, L. Formaggia, A. Veneziani, Chapter 10*, pages 347–394. Springer, 2009.

[440] M. Pennacchio and V. Simoncini. Efficient algebraic solution of reaction-diffusion systems for the cardiac excitation process. *Journal of Computational and Applied Mathematics*, 145(1):49–70, 2002.

[441] P. Perdikaris and G.E. Karniadakis. Model inversion via multi-fidelity bayesian optimization: a new paradigm for parameter estimation in haemodynamics, and beyond. *J. R. Soc. Interface*, 13:20151107, 2015.

[442] M. Perego, A. Veneziani, and C. Vergara. A variational approach for estimating the compliance of the cardiovascular tissue: An inverse fluid-structure interaction problem. *SIAM J. Sci. Comput.*, 33(3):1181–1211, 2011.

[443] K. Perktold and D. Hilbert. Numerical simulation of pulsatile flow in a carotid bifurcation model. *Journal of biomedical engineering*, 8(3):193–199, 1986.

[444] K. Perktold, E. Thurner, and T. Kenner. Flow and stress characteristics in rigid walled and compliant carotid artery bifurcation models. *Medical and Biological Engineering and Computing*, 32(1):19–26, 1994.

[445] P. Perona and J. Malik. Scale-space and edge detection using anisotropic diffusion. *IEEE Transactions on Pattern Analysis and Machine Intelligence*, 12(7):629–639, 1990.

[446] C. Peskin. Flow patterns around heart valves: A numerical method. *J. Comput. Physics*, 10(2):252–271, 1972.

[447] C. Peskin. Fiber architecture of the left ventricular wall: An asymptotic analysis. *Communications on Pure and Applied Mathematics*, 42(1):1126–1131, 1989.

[448] C. Peskin. The immersed boundary method. *Acta Numerica*, 11:479–517, 2002.

[449] C. Petitjean and J.-N. Dacher. A review of segmentation methods in short axis cardiac mr images. *Medical Image Analysis*, 15(2):169184, 2011.

[450] S. Pezzuto. *Mechanics of the Heart. Constitutive Issues and Numerical Experiments*. PhD thesis, Mathematical Models and Methods in Engineering, Dipartimento di Matematica, Politecnico di Milano, 2013.

[451] D.L. Pham, C. Xu, and J.L. Prince. Current methods in medical image segmentation. *Annual Review of Biomedical Engineering*, 2:315–337, 2000.

[452] D.T. Pham. Stochastic methods for sequential data assimilation in strongly nonlinear systems. *Mon. Weather Rev.*, 129(5):1194–1207, 2001.

[453] M. Piccinelli, C. Vergara, L. Antiga, L. Forzenigo, P. Biondetti, and M. Domanin. Impact of hemodynamics on lumen boundary displacements in abdominal aortic aneurysms by means of dynamic computed tomography and computational fluid dynamics. *Biomech Model Mechanobiol*, 2013.

[454] C. Pierre. Preconditioning the bidomain model with almost linear complexity. *Journal of Computational Physics*, 231(1):8297, 2012.

[455] S. Piperno and C. Farhat. Partitioned prodecures for the transient solution of coupled aeroelastic problems-Part II: energy transfer analysis and three-dimensional applications. *Comput. Methods Appl. Mech. Engrg.*, 190:3147–3170, 2001.

[456] G. Plank, M. Liebmann, R. Weber dos Santos, E.J. Vigmond, and G. Haase. Algebraic multigrid preconditioner for the cardiac bidomain model. *IEEE Transaction on Biomedical Engineering*, 54(4):585–596, 2007.

[457] R. Ponzini, C. Vergara, A. Redaelli, and A. Veneziani. Reliable cfd-based estimation of flow rate in haemodynamics measures. *Ultrasound in Med. and Biol.*, 32(10):1545–1555, 2006.

[458] R. Ponzini, C. Vergara, G. Rizzo, A. Veneziani, A. Roghi, A. Vanzulli, O. Parodi, and A. Redaelli. Womersley number-based estimates of blood flow rate in doppler analysis: In vivo validation by means of phase contrast magnetic resonance imaging. *IEEE Transaction on Biomedical Engineering*, 57(7):1807–1815, 2010.

[459] A. Porpora, P. Zunino, C. Vergara, and M. Piccinelli. Numerical treatment of boundary conditions to replace lateral branches in haemodynamics. *Int. J. Numer. Meth. Biomed. Eng.*, 28(12):1165–1183, 2012.

[460] M. Potse, B. Dubé, J. Richer, A. Vinet, and R.M. Gulrajani. A comparison of monodomain and bidomain reaction-diffusion models for action potential propagation in the human heart. *IEEE Transaction on Biomedical Engineering*, 53(12):2425–2435, 2006.

[461] S.F. Pravdin, V.I. Berdyshev, A.V. Panfilov, L.B. Katsnelson, O. Solovyova, and V.S. Markhasin. Mathematical model of the anatomy and fibre orientation field of the left ventricle of the heart. *Biomedical Engineering OnLine*, 12:54, 1989.

[462] G. Prodi. Teoremi di tipo locale per il sistema di navier-stokes e stabilitá delle soluzioni stazionarie. *Rendiconti del Seminario Matematico della Universitá di Padova*, 32:374–397, 1962.

[463] V. Prot, B. Skallerud, and G.A. Holzapfel. Transversely isotropic membrane shells with application to mitral valve mechanics. constitutive modelling and finite element implementation. *International Journal for Numerical Methods in Engineering*, 71:987–1008, 2007.

[464] A.J. Pullan, L.K. Cheng, M.P. Nash, C.P. Bradley, and D.J. Paterson. Noninvasive electrical imaging of the heart: Theory and model development. *Ann. Biomed. Eng*, 29:817–836, 2001.

[465] A.J. Pullan, L.K. Cheng, M.P. Nash, A. Ghodrati, R. MacLeod, and D.H. Brooks. The inverse problem of electrocardiography. In P.W. Macfarlane, A. van Oosterom, O. Pahlm, P. Kligfield, M. Janse, and J. Camm, editors, *Comprehensive Electrocardiology*, pages 299–344. Springer London, 2010.

[466] S. Puwal and B.J. Roth. Forward euler stability of the bidomain model of cardiac tissue. *IEEE Transaction on Biomedical Engineering*, 5(54):951–953, 2007.

[467] Z. Qu and A. Garfinkel. An advanced algorithm for solving partial differential equation in cardiac conduction. *IEEE Transaction on Biomedical Engineering*, 46(9):1166–1168, 1998.

[468] A. Quarteroni, editor. *Modeling the Heart and the Circulatory System*. Springer, 2015.

[469] A. Quarteroni and L. Formaggia. Mathematical modelling and numerical simulation of the cardiovascular system. In *Computational Models for the Human Body*, volume 12 of *Handbook of Numerical Analysis*, pages 3–127. Elsevier, 2004.

[470] A. Quarteroni, T. Lassila, S. Rossi, and R. Ruiz-Baier. Integrated heart - coupling multiscale and multiphysics models for the simulation of the cardiac function. *Comput. Methods Appl. Mech. Eng.*, page in press, 2016.

[471] A. Quarteroni, A. Manzoni, and F. Negri. *Reduced Basis Methods for Partial Differential Equations. An Introduction*, volume 92 of *Unitext*. Springer, 2016.

[472] A. Quarteroni, S. Ragni, and A. Veneziani. Coupling between lumped and distributed models for blood flow problems. *Comp Vis Sc*, 4(2):111–124, 2001.

[473] A. Quarteroni and G. Rozza. Optimal control and shape optimization of aorto-coronaric bypass anastomoses. *Math. Models Meth. Appl. Sci.*, 13(12):1801–1823, 2003.

[474] A. Quarteroni and G. Rozza, editors. *Reduced Order Methods for Modeling and Computational Reduction*, volume 9 of *Modeling, Simulation and Applications (MS&A)*. Springer International Publishing, Switzerland, 2014.

[475] A. Quarteroni, R. Sacco, and F. Saleri. *Numerical mathematics*. Springer Berlin, 2000.

[476] A. Quarteroni, F. Saleri, and A. Veneziani. Analysis of the Yosida method for the incompressible Navier-Stokes equations. *Journal de Mathématiques Pures et Appliquées*, 78:473–503, 1999.

[477] A. Quarteroni, F. Saleri, and A. Veneziani. Factorization methods for the numerical approximation of Navier-Stokes equations. *Comput. Methods Appl. Mech. Engrg.*, 188:505–526, 2000.

[478] A. Quarteroni, M. Tuveri, and A. Veneziani. Computational vascular fluid dynamics: Problems, models and methods. *Computing and Visualisation in Science*, 2:163–197, 2000.

[479] A. Quarteroni and A. Valli. *Numerical approximation of partial differential equations*. Springer, 1994.

[480] A. Quarteroni and A. Veneziani. Modeling and simulation of blood flow problems. Technical report, Bristeau, M.-O.(ed.) et al. Chichester: John Wiley & Sons., 1997.

[481] A. Quarteroni and A. Veneziani. Analysis of a geometrical multiscale model based on the coupling of ode and pde for blood flow simulations. *Multiscale Model. Simul.*, 1(2):173–195, 2003.

[482] A. Quarteroni, A. Veneziani, and C. Vergara. Geometric multiscale modeling of the cardiovascular system, between theory and practice. *Comput. Methods Appl. Mech. Engrg.*, 302:193–252, 2016.

[483] G. Querzoli, S. Fortini, and A. Cenedese. Effect of the prosthetic mitral valve on vortex dynamics and turbulence of the left ventricular flow. *Phys. Fluids*, 22:041901, 2010.

[484] M. Raghavan and D. Vorp. Towards a biomechanical tool to evaluate rupture potential of abdominal aortic aneurysm: identification of a finite strain constitutive model and evaluation of its applicability. *Journal of Biomechanics*, 33:475–482, 2000.

[485] R. Rannacher. *On Chorin's projection method for incompressible Navier-Stokes equations,* Lecture Notes in Mathematics, volume 1530, pages 167–183. Springer, Berlin, 1992.

[486] S.P. Raya and J.K. Udupa. Shape-based interpolation of multidimensional objects . *IEEE Transactions on Medical Imaging*, 9(1):32–42, 1990.

[487] V.L. Rayz, S.A. Berger, and D. Saloner. Transitional flows in arterial fluid dynamics. *Computer Methods in Applied Mechanics and Engineering*, 196(31–32):3043–3048, 2007.

[488] T. Rees, H. S. Dollar, and A. J. Wathen. Optimal Solvers for PDE-Constrained Optimization. *SIAM J. Sci. Comput.*, 32:271–298, 2010.

[489] J. Relan, P. Chinchapatnam, M. Sermesant, K. Rhode, M. Ginks, H. Delingette, C.A. Rinaldi, R. Razavi, and N. Ayache. Coupled personalization of cardiac electrophysiology models for prediction of ischaemic ventricular tachycardia. *Interface Focus*, 1(3):396–407, 2011.

[490] P. Reymond, F. Merenda, F.Perren, D. Rufenacht, and N. Stergiopulos. Validation of a one-dimensional model of the systemic arterial tree. *Am J Physiol Heart Circ Physiol*, 297:H208–H222, 2009.

[491] C.P. Robert and G. Casella. *Monte Carlo Statistical Methods*. Springer, 2nd edition, 2004.

[492] A.M. Robertson, A. Sequeira, and R.G. Owens. Rheological models for blood. In *Cardiovascular mathematics, edited by L. Formaggia, A. Quarteroni, A. Veneziani, Chapter 6*, pages 211–241. Springer, 2009.

[493] D.D. Robertson, J. Yuan, G. Wang, and M.W. Vannier. Total hip prosthesis metal-artifact suppression using iterative deblurring reconstruction. *J Comput Assist Tomogr*, 21(2):293–298, 1997.

[494] J.M. Rogers and A.D. McCulloch. A collocation-galerkin finite element model of cardiac action potential propagation. *Biophys JIEEE Transaction on Biomedical Engineering*, 41(8):743–757, 1994.

[495] S. Rossi. *Anisotropic Modeling of Cardiac Mechanical Activation*. PhD thesis, Ecole Polytechnique Fédérale de Lausanne, 2014.

[496] S. Rossi, T. Lassila, R. Ruiz-Baier, Adélia Sequeira, and A. Quarteroni. Thermodynamically consistent orthotropic activation model capturing ventricular systolic wall thickening in cardiac electromechanics. *European Journal of Mechanics - A/Solids*, 48(1):129–142, 2014.

[497] B.J. Roth. Action potential propagation in a thick strand of cardiac muscle. *Circ Res*, 68:162–173, 1991.

[498] Bradley J. Roth. Electrical conductivity values used with the bidomain model of cardiac tissue. *IEEE transactions on bio-medical engineering*, 44(4):326–328, 1997.

[499] O. Rousseau. *Geometrical modeling of the heart*. PhD thesis, Université de Ottawa, 2010.

[500] Y. Rudy and B.J. Messinger-Rapport. The inverse problem in electrocardiography: solutions in terms of epicardial potentials. *Crit. Rev. Biomed. Eng.*, 16(3):215–268, 1988.

[501] Y. Rudy and J.R. Silva. Computational biology in the study of cardiac ion channels and cell electrophysiology. *Quarterly Reviews of Biophysics*, 39(1):57–116, 2006.

[502] A. Saltelli, M. Ratto, T. Andres, F. Campolongo, J. Cariboni, D. Gatelli, M. Salsana, and S. Tarantola. *Global sensitivity analysis - The primer*. Wiley, 2008.

[503] S. Sankaran, L. Grady, and C.A. Taylor. Impact of geometric uncertainty on hemodynamic simulations using machine learning. *Comput. Methods Appl. Mech. Engrg.*, 297:167–190, 2015.

[504] S. Sankaran, H.J. Kim, G. Choi, and C.A. Taylor. Uncertainty quantification in coronary blood flow simulations: Impact of geometry, boundary conditions and blood viscosity. *J. Biomech.*, 49(12):2540–2547, 2016.

[505] S. Sankaran and A.L. Marsden. The impact of uncertainty on shape optimization of idealized bypass graft models in unsteady flow. *Phys. Fluids*, 22:121902, 2010.

[506] S. Sankaran and A.L Marsden. A stochastic collocation method for uncertainty quantification and propagation in cardiovascular simulations. *J. Biomech. Eng.*, 133(3):031001, 2011.

[507] R. Weber Dos Santos, G. Plank, S. Bauer, and E.J. Vigmond. Preconditioning techniques for the bidomain equations. In T.J. Barth, M. Field, M. Griebel, D.E. Keyes, R.M. Nieminen, D. Roose, and T. Schlick, editors, *Proceedings of the XV International Symposium on Domain Decomposition Methods for PDE's - Lecture Notes in Computational Science and Engineering*, pages 571–580. Springer, 2004.

[508] S. Särkkä. *Bayesian Filtering and Smoothing*. Cambridge University Press, 2013.

[509] S.J. Savader, G.B. Lund, and F.A. Osterman. Volumetric evaluation of blood flow in normal renal arteries with a doppler flow wire: A feasibility study. *J Vasc Interventional Radiol*, 8(2):209–214, 1997.

[510] I. Sazonov, S.Y. Yeo, R.L.T. Bevan, X. Xie, R. van Loon, and P. Nithiarasu. Modelling pipeline for subject-specific arterial blood flow: A review. *International Journal for Numerical Methods in Biomedical Engineering*, 27:1868–1910, 2011.

[511] D.E. Schiavazzi, G. Arbia, C. Baker, A.M. Hlavacek, T.Y. Hsia, A.L. Marsden, I.E. Vignon-Clementel, and The Modeling Of Congenital Hearts Alliance (MOCHA) Investigators. Uncertainty quantification in virtual surgery hemodynamics predictions for single ventricle palliation. *Int. J. Numer. Methods Biomed. Engng.*, 32(3):02737, 2016.

[512] R. J. Schilling, N. S. Peters, and D. W. Davies. Simultaneous endocardial mapping in the human left ventricle using a noncontact catheter comparison of contact and reconstructed electrograms during sinus rhythm. *Circulation*, 98(9):887–?898, 1998.

[513] R. Sebastian, V. Zimmerman, D. Romero, and A.F. Frangi. Construction of a computational anatomical model of the perpheral cardiac conduction system. *IEEE Transaction on Biomedical Engineering*, 58(12):90–100, 2011.

[514] J.H. Seo, V. Vedula, T. Abraham, A.C. Lardo, F. Dawoud, H. Luo, and R. Mittal. Effect of the mitral valve on diastolic flow patterns. *Physics of fluids*, 26(12):121901, 2014.

[515] M. Sermesant, R. Chabiniok, P. Chinchapatnam, T. Mansi, F. Billet, P. Moireau, J.M. Peyrat, K. Wong, J. Relan, K. Rhode, M. Ginks, P. Lambiase, H. Delingette, M. Sorine, C.A. Rinaldi, D. Chapelle, R. Razavi, and N. Ayache. Patient-specific electromechanical models of the heart for the prediction of pacing acute effects in crt: a preliminary clinical validation. *Med Image Anal*, 16(1):201–215, 2012.

[516] M. Sermesant, P. Moireau, O. Camara, J. Sainte-Marie, R. Andriantsimiavona, R. Cimrman, D.L.G. Hill, D. Chapelle, and R. Razavi. Cardiac function estimation from {MRI} using a heart model and data assimilation: Advances and difficulties. *Medical Image Analysis*, 10(4):642–656, 2006.

[517] J.A. Sethian. *Level set methods and fast marching methods*. Cambridge University, 1999.

[518] S.J. Sherwin, L. Formaggia, J. Peiró, and V. Franke. Computational modelling of 1d blood ow with variable mechanical properties and its application to the simulation of wave propagation in the human arterial system. *Int J Num Meth Fluids*, 43:673–700, 2003.

[519] S.J. Sherwin, V. Franke, J. Peiró, and K. Parker. One-dimensional modelling of a vascular network in space-time variables. *Journal of Engineering Mathematics*, 47(3-4):217–259, 2003.

[520] D. Simon. *Optimal State Estimation: Kalman, H-infinity, and Nonlinear Approaches*. John Wiley and Sons, 2006.

[521] N. P. Smith, D. P. Nickerson, E. J. Crampin, and P. J. Hunter. Multiscale computational modelling of the heart. *Acta Numerica*, 13:371–431, 2004.

[522] R.L. Spilker and C.A. Taylor. Tuning multidomain hemodynamic simulations to match physiological measurements. *Ann. Biomed. Engng.*, 38(8):2635–2648, 2010.

[523] T Stankovičová, V Bito, F Heinzel, K Mubagwa, and KR Sipido. Isolation and morphology of single purkinje cells from the porcine heart. *Gen. Physiol. Biophys*, 22:329–340, 2003.

[524] B.N. Steele, J. Wan, J.P. Ku, T.J.R Hughes, and C.A. Taylor. In vivo validation of a one-dimensional finite-element method for predicting blood flow in cardiovascular bypass grafts. *IEEE Trans Biomed Eng*, 50:649–656, 2003.

[525] D.A. Steinman, J.B. Thomas, H.M. Ladak, J.S. Milner, B.K. Rutt, and J.D. Spence. Reconstruction of carotid bifurcation hemodynamics and wall thickness using computational fluid dynamics and mri. *Magnetic Resonance in Medicine*, 47(1):149–159, 2001.

[526] N. Stergiopulos, B.E. Westerhof, J.J. Meister, and N. Westerhof. The four-element windkessel model. In *Engineering in Medicine and Biology Society, 1996. Bridging Disciplines for Biomedicine. Proceedings of the 18th Annual International Conference of the IEEE*, volume 4, pages 1715–1716, Oct 1996.

[527] N. Stergiopulos, B.E. Westerhof, and N. Westerhof. Total arterial inertance as the fourth element of the windkessel model. *American Journal of Physiology-Heart and Circulatory Physiology*, 276(1):H81–H88, 1999.

[528] J.M.A. Stijnen, J. de Hart, P.H.M. Bovendeerd, and F.N. van de Vosse. Evaluation of a fictitious domain method for predicting dynamic response of mechanical heart valves. *International Journal for Numerical Methods in Fluids*, 19(6):835–850, 2004.

[529] J.S. Stroud, S.A. Berger, and D. Saloner. Numerical Analysis of Flow Through a Severely Stenotic Carotid Artery Bifurcation. *J Biomech Eng*, 124(1):9–20, 2002.

[530] A.M. Stuart. Inverse problems: A Bayesian perspective. *Acta Numerica*, 19:451–559, 2010.

[531] T.J. Sullivan. *Introduction to Uncertainty Quantification*, volume 63 of *Texts in Applied Mathematics*. Springer International Publishing Switzerland, 2015.

[532] W. Sun, B. Starly, J. Nam, and A. Darling. Bio-cad modeling and its applications in computer-aided tissue engineering. *Computer-Aided Design*, 11:1097–1114, 2005.

[533] G.B.K. Sundaram, K.R. Balakrishnan, and R.K. Kumar. Aortic valve dynamics using a fluid structure interaction model - the physiology of opening and closing. *Journal of Biomechanics*, 48(10):1737–1744, 2015.

[534] J. Sundnes, G.T. Lines, and A. Tveito. An operator splitting method for solving the bidomain equations coupled to a volume conductor model for the torso. *Mathematical Biosciences*, 2(194):233–248, 2005.

[535] J. Sundnes, S. Wall, H. Osnes, T. Thorvaldsen, and A.D. McCulloch. Improved discretisation and linearisation of active tension in strongly coupled cardiac electromechanics simulations. *Computer Methods in Biomechanics and Biomedical Engineering*, 6(17):604–615, 2014.

[536] E.W. Swim and P. Seshaiyer. A nonconforming finite element method for fluid-structure interaction problems. *Comput. Methods Appl. Mech. Engrg.*, 195(17–18):2088–2099, 2006.

[537] A. Tagliabue, L Dedè, and A. Quarteroni. Fluid dynamics of an idealized left ventricle: the extended nitsche's method for the treatment of heart valves as mixed time varying boundary conditions. MOX-Report n. 61-2015, Department of Mathematics, Politecnico di Milano, Italy, 2015.

[538] H. Talbot, S. Cotin, R. Razavi, C. Rinaldi, and H. Delingette. Personalization of Cardiac Electrophysiology Model using the Unscented Kalman Filtering. In *Computer Assisted Radiology and Surgery (CARS 2015)*, Barcelona, Spain, 2015.

[539] A. Tarantola. *Inverse Problem Theory and Methods for Model Parameter Estimation.* Society for Industrial and Applied Mathematics, Philadelphia, USA, 2004.

[540] C.A. Taylor and C.A. Figueroa. Patient-specific modeling of cardiovascular mechanics. *Annual Review of Biomedical Engineering*, 11:109–134, 2009.

[541] C.A. Taylor, T.J.R. Hughes, and C.K. Zarins. Finite element analysis of pulsatile flow in the abdominal aorta under resting and exercise conditions. *American Society of Mechanical Engineers, Bioengineering Division*, 33:81–82, 1996.

[542] C.A. Taylor, T.J.R. Hughes, and C.K. Zarins. Finite element modeling of blood flow in arteries. *Computer Methods in Applied Mechanics and Engineering*, 158(1-2):155–196, 1998.

[543] R. Temam. Sur l'approximation de la solution des équations de Navier–Stokes par la méthode des pas fractionaires (I). *Archives for Rational Mechanics and Analysis*, 32:135–153, 1969.

[544] T.E. Tezduyar, S. Sathe, T. Cragin, B. Nanna, B.S. Conklin, J. Pausewang, and M. Schwaab. Modelling of fluid-structure interactions with the space-time finite elements: arterial fluid mechanics. *Int. J. Num. Methods Fluids*, 54:901–922, 2007.

[545] L.J.P. Timmermans, P.D. Minev, and F.N. Van de Vosse. An approximate projection scheme for incompressible flow using espectral elements. *Int. J. Num. Methods Fluids*, 22:673–688, 1996.

[546] K.A. Tomlinson, P.J. Hunter, and A.J. Pullan. A finite element method for an eikonal equation model of myocardial excitation wavefront propagation. *SIAM J. Appl. Math*, 1(63):324–350, 2002.

[547] E.F. Toro. Brain venous haemodynamics, neurological diseases and mathematical modelling. a review. *Applied Mathematics and Computation*, 272(2):542579, 2016.

[548] N.A. Trayanova. Defibrillation of the heart: insights into mechanisms from modelling studies Authors. *Experimental physiology*, 91(2):323–337, 2006.

[549] N.A. Trayanova, W. li, J. Eason, and P. Kohl. Effect of stretch-activated channels on defibrillation efficacy. *Heart Rhythm*, 1(1):67–77, 2004.

[550] P.R. Trenhago, L.G Fernandes, L.O. Müller, P.J. Blanco, and R.A. Feijóo. An integrated mathematical model of the cardiovascular and respiratory systems. *Int. J. Numer. Meth. Biomed. Engng.*, 32(1):e02736–n/a, 2016. e02736 cnm.2736.

[551] F. Tröltzsch. *Optimal control of partial differential equations: theory, methods and applications*, volume 112 of *Graduate Studies in Mathematics*. American Mathematical Society, Providence, 2010.

[552] C. Tu and C. Peskin. Stability and instability in the computation of flows with moving immersed boundaries: A comparison of three methods. *SIAM J. Sci. and Stat. Comput.*, 6(13):13611376, 1992.

[553] S. Turek. *Efficient Solvers for Incompressible Flow Problems*. Lecture Notes in Computational Science and Engineering. Springer, 1999.

[554] K.H.W.J. Ten Tusscher and A.V. Panfilov. Cell model for efficient simulation of wave propagation in human ventricular tissue under normal and pathological conditions. *Physics in Medicine and Biology*, 51(23):6141–6156, 2006.

[555] M. Unser. Splines: a perfect fit for signal and image processing. *IEEE Transactions on Signal Processing Magazine*, 16(6):22–38, 1999.

[556] T.P. Usyk, I.J. LeGrice, and A.D. McCulloch. Computational model of three-dimensional cardiac electromechanics. *Computing and Visualization in Science*, 4(4):249–257, 2002.

[557] R.J. van der Geest, E. Jansen, V. Buller, and J. Reiber. Automated detection of left ventricular epi- and endocardial contours in short-axis mr images. *Computers in Cardiology, Proceedings*, pages 33–36, 1994.

[558] A. Veneziani. Boundary conditions for blood flow problems. *Proceedings of ENUMATH, Rannacher et al. eds., World Sci. Publishing, River Edge, NJ*, 1998.

[559] A. Veneziani. *Mathematical and Numerical Modeling of Blood Flow Problems*. PhD thesis, University of Milan, 1998.

[560] A. Veneziani. Block factorized preconditioners for high-order accurate in time approximation of the navier-stokes equations. *Numerical Methods for Partial Differential Equations*, 19(4):487–510, 2003.

[561] A. Veneziani and C. Vergara. Flow rate defective boundary conditions in haemodinamics simulations. *Int. J. Num. Methods Fluids*, 47:803–816, 2005.

[562] A. Veneziani and C. Vergara. An approximate method for solving incompressible Navier-Stokes problems with flow rate conditions. *Comput. Methods Appl. Mech. Engrg.*, 196(9-12):1685–1700, 2007.

[563] A. Veneziani and C. Vergara. Inverse problems in Cardiovascular Mathematics: toward patient-specific data assimilation and optimization. *Int. J. Numer. Meth. Biomed. Engng.*, 29(7):723–725, 2013.

[564] A. Veneziani and U. Villa. Aladins: An algebraic splitting time adaptive solver for the incompressible navierstokes equations. *J Comp Phys*, 238:359–375, 2013.

[565] C. Vergara. Nitsche's method for defective boundary value problems in incompressibile fluid-dynamics. *J Sci Comp*, 46(1):100–123, 2011.

[566] C. Vergara, M. Lange, S. Palamara, T. Lassila, A.F. Frangi, and A. Quarteroni. A coupled 3D-1D numerical monodomain solver for cardiac electrical activation in the myocardium with detailed Purkinje network. *J. Comput. Phys*, 308:218–238, 2016.

[567] C. Vergara, S. Palamara, D. Catanzariti, F. Nobile, E. Faggiano, C. Pangrazzi, M. Centonze, M. Maines, A. Quarteroni, and G. Vergara. Patient-specific generation of the Purkinje network driven by clinical measurements of a normal propagation. *Med. Biol. Eng. Comput.*, 52(10):813–826, 2014.

[568] C. Vergara, R. Ponzini, A. Veneziani, A. Redaelli, D. Neglia, and O. Parodi. Womersley number-based estimation of flow rate with doppler ultrasound: Sensitivity analysis and first clinical application. *Computer Methods and Programs in Biomedicine*, 98(2):151–160, 2010.

[569] C. Vergara, F. Viscardi, L. Antiga, and G.B. Luciani. Influence of bicuspid valve geometry on ascending aortic fluid-dynamics: a parametric study. *Artificial Organs*, 36(4):368–378, 2012.

[570] J. A. Vierendeels, K. Riemslagh, E. Dick, and P.R. Verdonck. Computer simulation of intraventricular flow and pressure gradients during diastole. *Journal of Biomechanical Engineering*, 6(122):667–674, 2000.

[571] E.J. Vigmond, F. Aguel, and N.A. Trayanova. Computational techniques for solving the bidomain equations in three dimensions. *IEEE Transaction on Biomedical Engineering*, 49(11):1260–1269, 2002.

[572] E.J. Vigmond and C. Clements. Construction of a computer model to investigate sawtooth effects in the Purkinje system. *IEEE Trans Biomed Eng*, 54(3):389–399, 2007.

[573] E.J. Vigmond, R. Weber dos Santos, A.J. Prassl, M. Deo, and G. Plank. Solvers for the cardiac bidomain equations. *Progress in Biophysics and Molecular Biology*, 96(1–3):3–18, 2008.

[574] I.E. Vignon-Clementel, C.A. Figueroa, K. Jansen, and C. Taylor. Outflow boundary conditions for three-dimensional finite element modeling of blood flow and pressure waves in arteries. *Comput. Methods Appl. Mech. Engrg.*, 195:3776–3996, 2006.

[575] N. Virag, V. Jacquemet, C.S. Henriquez, S. Zozor, O. Blanc, J.-M. Vesin, E. Pruvot, and L. Kappenberger. Study of atrial arrhythmias in a computer model based on magnetic resonance images of human atria. *Chaos*, 12:754, 2002.

[576] F. Viscardi, C. Vergara, L. Antiga, S. Merelli, A. Veneziani, G. Puppini, G. Faggian, A. Mazzucco, and G.B. Luciani. Comparative finite element model analysis of ascending aortic flow in bicuspid and tricuspid aortic valve. *Artificial organs*, 34(12):1114–20, December 2010.

[577] H. U. Voss, J. Timmer, and J. Kurths. Nonlinear dynamical system identification from uncertain and indirect measurements. *Int. J. Bifurc. Chaos*, 14(6):1905–1933, 2004.

[578] J. Voss. *An introduction to Statistical Computing: A Simulation-Based Approach.* Wiley, 2013.

[579] J. Vossoughi, R.N. Vaishnav, and D.J. Patel. Compressibility of the myocardial tissue. *Adv Bioeng (ed V.C. Mow)*, pages 45–48, 1980.

[580] E. Votta, T.B. Le, M. Stevanella, L. Fusinic, E.G. Caiani, A. Redaelli, and F. Sotiropoulos. Toward patient-specific simulations of cardiac valves: State-of-the-art and future directions. *Journal of Biomechanics*, 46(2):217–228, 2013.

[581] E. Votta, F. Maisano, S.F. Bolling, O. Alfieri, F.M. Montevecchi, and A. Redaelli. The geoform disease-specific annuloplasty system: a finite element study. *The Annals of Thoracic Surgery*, 84(1):92–101, 2007.

[582] G.D. Waiter, F.I. McKiddie, T.W. Redpath, S.I.K. Semple, and R.J. Trent. Determination of normal regional left ventricular function from cine-mr images using a semi-automated edge detection method. *Magnetic Resonance Imaging*, 17(1):99–107, 1999.

[583] W. Wall, L. Wiechert, A. Comerford, and S. Rausch. Towards a comprehensive computational model for the respiratory system. *International Journal for Numerical Methods in Biomedical Engineering*, 26(7):807827, 2010.

[584] M. Wallman, N.P. Smith, and B. Rodriguez. Computational methods to reduce uncertainty in the estimation of cardiac conduction properties from electroanatomical recordings. *Med. Image Anal.*, 18(1):228–240, 2014.

[585] D. Wang, R.M. Kirby, R. MacLeod, and C.R. Johnson. Inverse electrocardiographic source localization of ischemia: An optimization framework and finite element solution. *J. Comput. Phys.*, 250:403–424, 2013.

[586] K.C. Wang, R.W. Dutton, and C.A. Taylor. Improving geometric model construction for blood flow modeling. *Engineering in Medicine and Biology Magazine, IEEE*, 18(6):33–39, 1999.

[587] L. Wang, K.C. L. Wong, H. Zhang, H. Liu, and P. Shi. Noninvasive computational imaging of cardiac electrophysiology for 3-d infarct. *IEEE Trans. Biomed. Engng.*, 58(4):1033–1043, 2011.

[588] L. Wang, H. Zhang, K.C.L. Wong, and P. Shi. A reduced-rank square root filtering framework for noninvasive functional imaging of volumetric cardiac electrical activity. In *2009 IEEE International Conference on Acoustics, Speech and Signal Processing*, pages 533–536, 2009.

[589] H. Watanabe, T. Hisada, S. Sugiura, J. Okada, and H. Fukunari. Computer simulation of blood flow, left ventricular wall motion and their interrelationship by fluid-structure interaction finite element method. *JSME International Journal Series C Mechanical Systems, Machine Elements and Manufacturing*, 45(4):1003–1012, 2002.

[590] D.F. Watson. Computing the n-dimensional Delaunay tessellation with application to voronoi polytopes. *Computer Journal*, 24(2):167–172, 1981.

[591] N.P. Weatherill and O. Hassan. Efficient three-dimensional Delaunay triangulation with automatic point creation and imposed boundary constraints. *International Journal for Numerical Methods in Engineering*, 37(12):2005–2039, 1994.

[592] E.J. Weinberg and M.R. Kaazempur-Mofrad. A large-strain finite element formulation for biological tissues with application to mitral valve leaflet tissue mechanics. *Journal of Biomechanics*, 39(8):15571561, 2006.

[593] J.F. Wenk, L. Ge, Z. Zhang, M. Soleimani, D.D. Potter, A.W. Wallace, E. Tseng, M.B. Ratcliffe, and J.M. Guccione. Mechanics of the mitral valve strut chordae insertion region. *Computer Methods in Biomechanics and Biomedical Engineering*, 16(8):807–818, 2013.

[594] N. Westerhof, J.W. Lankhaar, and B.E. Westerhof. The arterial windkessel. *Medical & biological engineering & computing*, 47(2):131–141, 2009.

[595] J. Wong, S. Goktepe, and E. Kuhl. Computational modeling of chemo-electro-mechanical coupling: A novel implicit monolithic finite element approach. *International Journal for Numerical Methods in Biomedical Engineering*, 29(10):1104–1133, 2013.

[596] J. Wong and E. Kuhl. Generating fibre orientation maps in human heart models using poisson interpolation. *Computer Methods in Biomechanics and Biomedical Engineering*, 17(11):1217–1226, 2014.

[597] J. Xi, P. Lamata, J.L., P. Moireau, D. Chapelle, and N. Smith. Myocardial transversely isotropic material parameter estimation from in-silico measurements based on a reduced-order unscented kalman filter. *J. Mech. Behav. Biomed. Materials*, 4(7):1090–1102, 2011.

[598] F. Xie, Z. Qu, J. Yang, A. Baher, J.N. Weiss, and A. Garfinkel. A simulation study of the effects of cardiac anatomy in ventricular fibrillation. *J Clin Invest*, 113:686–693, 2004.

[599] F. Xiong and C. Chong. A parametric numerical investigation on haemodynamics in distal coronary anastomoses. *Medical Engineering & Physics*, 30(3):311–320, 2008.

[600] D. Xiu and J. S. Hesthaven. High-order collocation methods for differential equations with random inputs. *SIAM J. Sci. Comput.*, 27(3):1118–1139, 2005.

[601] D. Xiu and G. E. Karniadakis. Modeling uncertainty in steady state diffusion problems via generalized polynomial chaos. *Comput. Methods Appl. Mech. Engrg.*, 191:4927–494, 2002.

[602] D. Xiu and G. E. Karniadakis. The Wiener-Askey polynomial chaos for stochastic differential equations. *SIAM J. Sci. Comput.*, 24:619–644, 2002.

[603] D. Xiu and S.J. Sherwin. Parametric uncertainty analysis of pulse wave propagation in a model of a human arterial network. *J. Comput. Phys.*, 226(2):1385–1407, 2007.

[604] Y. Yamashita. Theoretical studies on the inverse problem in electrocardiography and the uniqueness of the solution. *IEEE Trans. Biomed. Eng.*, BME-29:719?–725, 1982.

[605] K. Yanagihara, A. Noma, and H. Irisawa. Reconstruction of sino-atrial node pacemaker potential based on the voltage clamp experiments. *Jpn. J. Physiol*, 30:841–857, 1980.

[606] H. Yang and A. Veneziani. Estimation of cardiac conductivities in ventricular tissue by a variational approach. *Inverse Problems*, 31:115001, 2015.

[607] P.J. Yim, J.J. Cebral, R. Mullick, H.B. Marcos, and P.L. Choyke. Vessel surface reconstruction with a tubular deformable model. *IEEE Transactions on Medical Imaging*, 20(12):1411–1421, 2001.

[608] M. Yin, X.Y. Luo, T.J. Wang, and P.N. Watton. Effects of flow vortex on a chorded mitral valve in the left ventricle. *International Journal for Numerical Methods in Biomedical Engineering*, 26(3-4):381–404, 2009.

[609] H.F. Younis, M.R. Kaazempur-Mofrad, R.C. Chan, A.G. Isasi, D.P. Hinton, A.H. Chau, L.A. Kim, and R.D. Kamm. Hemodynamics and wall mechanics in human carotid bifurcation and its consequences for atherogenesis: investigation of inter-individual variation. *Biomechanics and Modeling in Mechanobiology*, 3(1):17–32, 2004.

[610] Y. Yu, H. Baek, and G.E. Karniadakis. Generalized fictitious methods for fluid-structure interactions: Analysis and simulations. *J. Comput. Physics*, 245:317–346, 2013.

[611] S.Z. Zhao, X.Y. Xu, A.D. Hughes, S.A. Thom, A.V. Stanton, B. Ariff, and Q. Long. Blood flow and vessel mechanics in a physiologically realistic model of a human carotid arterial bifurcation. *Journal of Biomechanics*, 33(8):975–984, 2000.

[612] F. Zhu and J. Tian. Modified fast marching and level set method for medical image segmentation. *J Xray Sci Technol*, 11(4):193–204, 2003.

[613] O.C. Zienkiewicz and R.L. Taylor. *The Finite Element Method for Solid and Structural Mechanics*. Butterworth-Heinemann, 6 edition, 2005.

[614] S. Zonca, L. Formaggia, and C. Vergara. An unfitted formulation for the interaction of an incompressible fluid with a thick structure via an XFEM/DG approach. MOX-Report n. 35-2016, Department of Mathematics, Politecnico di Milano, Italy, 2016.

[615] P. Zunino. Numerical approximation of incompressible flows with net flux defective boundary conditions by means of penalty technique. *Comput. Methods Appl. Mech. Engrg.*, 198(37-40):3026–3038, 2009.

MOX Technical Reports, last issues

Dipartimento di Matematica
Politecnico di Milano, Via Bonardi 9 - 20133 Milano (Italy)

36/2016 Mancini, L.; Paganoni, A.M.
Marked Point Process models for the admissions of heart failured patients

37/2016 Tugnoli, M; Abbà, A. ; Bonaventura, L.; Restelli, M.
A locally p-adaptive approach for Large Eddy Simulation of compressible flows in a DG framework

34/2016 Menafoglio, A.; Secchi, P.
Statistical analysis of complex and spatially dependent data: a review of Object Oriented Spatial Statistics

35/2016 Zonca, S.; Formaggia, L.; Vergara, C.
An unfitted formulation for the interaction of an incompressible fluid with a thick structure via an XFEM/DG approach

33/2016 Antonietti, P. F.; Ferroni, A.; Mazzieri, I.; Quarteroni, A.
hp-version discontinuous Galerkin approximations of the elastodynamics equation

32/2016 Tarabelloni, N.; Schenone, E.; Collin, A.; Ieva, F.; Paganoni, A.M.; Gerbeau, J.-F.
Statistical Assessment and Calibration of Numerical ECG Models

30/2016 Abramowicz, K.; Häger, C.; Pini, A.; Schelin, L.; Sjöstedt de Luna, S.; Vantini, S.
Nonparametric inference for functional-on-scalar linear models applied to knee kinematic hop data after injury of the anterior cruciate ligament

31/2016 Antonietti, P.F.; Merlet, B.; Morgan, P.; Verani, M.
Convergence to equilibrium for a second-order time semi-discretization of the Cahn-Hilliard equation

29/2016 Miglio, E.; Parolini, N.; Penati, M.; Porcù, R.
GPU parallelization of brownout simulations with a non-interacting particles dynamic model

28/2016 Antonietti, P.F.; Dal Santo, N.; Mazzieri, I.; Quarteroni, A.
A high-order discontinuous Galerkin approximation to ordinary differential equations with applications to elastodynamics